

UC Berkeley

UC Berkeley Electronic Theses and Dissertations

Title

Spatially Modulated Structures in Convective Systems

Permalink

<https://escholarship.org/uc/item/1q31f6c1>

Author

Kao, Hsien-Ching

Publication Date

2013

Peer reviewed|Thesis/dissertation

Spatially Modulated Structures in Convective Systems

by

Hsien-Ching Kao

A dissertation submitted in partial satisfaction of the
requirements for the degree of
Doctor of Philosophy

in

Physics

in the

Graduate Division

of the

University of California, Berkeley

Committee in charge:

Professor Edgar Knobloch, Chair
Professor Jonathan Wurtele
Professor Oliver O'Reilly

Spring 2013

Spatially Modulated Structures in Convective Systems

Copyright 2013
by
Hsien-Ching Kao

Abstract

Spatially Modulated Structures in Convective Systems

by

Hsien-Ching Kao

Doctor of Philosophy in Physics

University of California, Berkeley

Professor Edgar Knobloch, Chair

This dissertation focuses on the study of spatially modulated structures in pattern forming systems. The work is motivated by recent interest in spatially localized states observed in convective systems. Weakly nonlinear analysis is applied to derive the modulation equations and systematic studies, both analytical and numerical, are then performed on the simplified equations. The following is a summary of this work:

Weakly Subcritical Patterns

The transition from subcritical to supercritical periodic patterns is described by the one-dimensional cubic-quintic Ginzburg-Landau equation

$$A_t = \mu A + A_{xx} + b|A|^2 A + i(a_1|A|^2 A_x + a_2 A^2 A_x^*) - |A|^4 A,$$

where $A(x, t)$ represents the pattern amplitude. The coefficients are real indicating that the system is spatially reversible. Coefficients μ and b are treated as bifurcation parameters. Properties of the equation such as well-posedness, gradient structure, and bifurcation behavior depend significantly on the parameters a_1 and a_2 . In this system, periodic patterns may in turn become unstable through one of two different mechanisms, an Eckhaus instability or an oscillatory instability. Dynamics and bifurcations near the instability thresholds are analyzed. Among the stationary solutions, the front solution which connects the zero state to a spatially periodic state plays the most important role. The location of the front in the parameter μ is treated as a Maxwell point. The spatially modulated solutions which bifurcate from the periodic solutions demonstrate protosnaking behavior near this point. These results are used to shed light on both variational and non-variational systems exhibiting homoclinic snaking.

Localized Patterns in Rotating Convection and Magnetoconvection

In two-dimensional rotating convection and magnetoconvection, the formation of spatially localized patterns is strongly affected by the interaction between convection and a large scale mode: zonal velocity in rotating convection and magnetic flux in magnetoconvection. A nonlocal fifth order Ginzburg-Landau theory is developed to describe

the localization near a codimension-two point. The study of the fifth-order Ginzburg-Landau theory gives us better understanding of the appearance of spatially modulated solutions and their subsequent bifurcation behavior. These results are used to explain the properties of spatially localized convectons in the full convection problem. The effect of boundary conditions is also analyzed which shows how the bifurcation picture is modified in the presence of mixed boundary conditions.

Exact Solutions of the Cubic-Quintic Swift-Hohenberg Equation

Meromorphic exact solutions of the cubic-quintic Swift-Hohenberg equation

$$u_t = \mu u - (1 + \partial_{xx})^2 u + bu^3 - cu^5$$

are studied and a one-parameter family of real exact solutions is derived. The solutions are of two types, differing in their symmetry properties, and are connected via an exact heteroclinic solution. These exact solutions are used as initial conditions for numerical continuation which shows that some of these lie on secondary branches while others fall on isolas. The approach substantially enhances our understanding of the solution space of this equation.

To my parents

Contents

Contents	ii
List of Figures	iv
1 Introduction	1
2 Weakly Subcritical Patterns	8
2.1 The cubic-quintic Ginzburg-Landau equation	9
2.2 Stationary solutions	10
2.3 Steady state bifurcations from primary branches	14
2.4 Temporal stability analysis	31
2.5 Dynamics of periodic wavetrains	38
2.6 Stability and dynamics of spatially localized solutions near the Maxwell point	48
2.7 Discussion	58
3 Large-scale Mode in Pattern Formation	61
3.1 Rotating convection and magnetoconvection	61
3.2 Theoretical understanding of the bifurcation	69
3.3 Modulation equations near a codimension-two point	76
3.4 Stationary nonlocal Ginzburg-Landau equation	78
3.5 Temporal stability of the stationary solutions	85
3.6 Effects of boundary conditions	87
3.7 Discussion	92
4 Exact solutions of the cubic-quintic Swift-Hohenberg equation	94
4.1 Exact meromorphic solutions	95
4.2 Meromorphic solutions of stationary SH35	96
4.3 Real meromorphic solutions	100
4.4 Numerical bifurcation analysis	104
4.5 Discussion	113
5 Conclusions	114
5.1 Summary of results	114

5.2	Ongoing work	115
5.3	Future work	119
Bibliography		121
A	The generalized Swift-Hohenberg equation near the subcritical to supercritical transition	127
B	Heteroclinic and homoclinic solutions in GL35	129
C	Bifurcation analysis near $\mu = 1$ in GL35	132
C.1	The case $a_1 = a_2 = 0$	132
C.2	Nonzero a_1 or a_2 (or both)	133
D	Calculation of $\frac{dE}{d\mu}$ and $\frac{dL}{d\mu}$ on primary branches	134
E	Derivation of the nonlinear phase equation in GL35	137
F	Branching direction of the convecton branches	138
G	Derivation of the modulation equations for magnetoconvection near the codimension-two point	140
H	Coefficients of the modulation equation for rotating convection near the codimension-two point	145
I	Direction of branching in the fifth order nonlocal Ginzburg-Landau equation	147
J	Exact real solutions of SH23 with dispersion	149

List of Figures

1.1	(a) Shadowgraph of hexagonal convection cells. (b) Hexagonal cells transform to roll pattern [5].	1
1.2	Bifurcation diagram showing Nusselt number $Nu - 1$ as a function of the Rayleigh number in binary-fluid convection [9].	3
1.3	Bifurcation diagram and sample solution profiles of SH23 [13]. Here N represents the L^2 -norm of the solution. Black line: periodic state. Blue line: localized state. The thick line indicates the solution branch is stable while the thin line indicates the solution branch is unstable.	4
1.4	Bifurcation diagram showing the average poloidal kinetic energy as a function of the Rayleigh number Ra for slanted snaking when Taylor number $Ta = 20$ and Prandtl number $\sigma = 0.1$ [17].	5
2.1	The existence region in parameter space of periodic states when (a) $a_2 - a_1 = 1$, $b = 1$, and (b) $a_2 - a_1 = 3$, $b = 1$. In both cases the state R_0^+ exists for $\mu > k^2$ if $b' < 0$, and for $\mu > k^2 - \frac{b'^2}{4}$ if $b' \geq 0$; R_0^- exists in the region between $\mu = k^2$ and $\mu = k^2 - \frac{b'^2}{4}$, but the curve $\mu = k^2 - \frac{b'^2}{4}$ in (a,b) has positive (negative) curvature depending on the sign of $(a_2 - a_1)^2 - 4$	13
2.2	Bifurcation diagrams showing R_0^2 as a function of μ for (a,b) $ a_2 - a_1 < 2$, (c,d) $ a_2 - a_1 > 2$. Panels (a,b) are for $a_2 - a_1 = 1$, $b = 1$ and show (a) $k \geq 0$, (b) $k \leq 0$. Panels (c,d) are for $a_2 - a_1 = 3$, $b = 1$ and show (c) $k \geq 0$, (d) $k \leq 0$. Solid (dashed) lines indicate solutions that are stable (unstable) in time with respect to amplitude perturbations. These correspond to R_0^+ and R_0^- , respectively. . . .	14
2.3	Bifurcation diagrams showing R_0^2 as a function of k when (a) $\mu = 1$, $a_2 - a_1 = 1$, (b) $\mu = 1$, $a_2 - a_1 = 3$, (c) $\mu = -1$, $a_2 - a_1 = 1$, and (d) $\mu = -1$, $a_2 - a_1 = 3$. Solid (dashed) lines indicate solutions that are stable (unstable) in time with respect to amplitude perturbations.	15

- 2.4 (Color online) The (a_1, a_2) plane splits into a number of regions with different behavior (see text). Black dots indicate the parameter values used in subsequent figures, with the numbers indicating the corresponding figure. The region $\beta \equiv \frac{(a_1+a_2)^2}{16} - \frac{a_2(a_1+a_2)}{6} - \frac{1}{3} < 0$ (between solid black lines) contains heteroclinic solutions between the origin and either R_0^+ (if $a_2(a_1 + a_2) < 4$) or R_0^- (if $a_2(a_1 + a_2) > 4$). The line $\alpha \equiv a_2^2 - a_1^2 = 0$ plays a role in determining the sequence of secondary bifurcations while the sign of $\alpha + 4$ plays an important role in the temporal analysis. 16
- 2.5 The potential $U(R; \mu, L)$ when $L = 0$, drawn reflected in $R = 0$. (a) $\mu = -1$, $b = 1$, $\beta = 0.9$ ($\mu < 0$, $\beta > 0$). (b) $\mu = 1$, $b = -1$, $\beta = -0.9$ ($\mu > 0$, $\beta < 0$). (c) $\mu = -1$, $b = 5$, $\beta = -1$ ($\mu, \beta < 0$ and $b > 4\sqrt{\mu\beta}$). (d) $\mu = 1$, $b = -5$, $\beta = 1$ ($\mu, \beta > 0$ and $b < -4\sqrt{\mu\beta}$). (e) $\mu = -1$, $b = 3.7$, $\beta = -1$ ($\mu, \beta < 0$ and $2\sqrt{3\mu\beta} < b < 4\sqrt{\mu\beta}$). (f) $\mu = 1$, $b = -3.7$, $\beta = 1$ ($\mu, \beta > 0$ and $-4\sqrt{\mu\beta} < b < -2\sqrt{3\mu\beta}$). (g) $\mu = -1$, $b = 3.3$, $\beta = -1$ ($\mu, \beta < 0$ and $b < 2\sqrt{3\mu\beta}$). (h) $\mu = 1$, $b = -3.3$, $\beta = 1$ ($\mu, \beta > 0$ and $b > -2\sqrt{3\mu\beta}$). 17
- 2.6 The potential $U(R; \mu, L)$ when $L = 1$. (a) $\mu = 1$, $b = 4$, $a_1 = 1$, $a_2 = 1$, ($\beta < 0$, $R_{0,-}^2 > 0$, $R_{0,-}^4 (\mu' + bR_{0,-}^2/2) > 2L^2$). (b) $\mu = 1$, $b = -1$, $a_1 = 1$, $a_2 = 1$, ($\beta < 0$ and at least one of the other conditions in (a) is violated). (c) $\mu = 40$, $b = -20$, $a_1 = 4$, $a_2 = 0.5$ ($\beta > 0$, $b < 0$, $0 < 32\beta\mu' < 3b^2$, $R_{0,+}^4 (\mu' + b'R_{0,+}^2/2) < 2L^2$). (d) $\mu = 40$, $b = 5$, $a_1 = 4$, $a_2 = 0.5$ ($\beta > 0$ and at least one of the other conditions in (c) is violated). Here $\mu' \equiv \mu + \frac{3a_2 - a_1}{2}L$ and $R_{0,\pm}^2 \equiv \frac{-b \pm \sqrt{b^2 - 32\beta\mu'/3}}{8\beta}$ 17
- 2.7 The profile $\text{Re}A(x)$ from Appendix B, Eq. (B.1), of the heteroclinic solution at $\mu = \mu_M \approx -0.0146$ when $b = 1$, $a_1 = 1$, and $a_2 = 6$ 18
- 2.8 (a) Homoclinic solution to $A = 0$ at $\mu = 0$ when $b = -2$, $\beta = 1$ and $a_1 + a_2 = 64$ (Appendix B, Eq. (B.5)). (b) Homoclinic solution to a nonzero equilibrium corresponding to a rotating wave at $\mu = -1$ with $R_0 \approx 1.1791$ and $k = -1.3903$ when $b = 3.5$, $a_1 = a_2 = 2$ (Appendix B, Eq. (B.6)). 18
- 2.9 (Color online) Bifurcation diagrams for subcritical stationary solutions with $k = 0$ with several secondary branches of nonuniform states satisfying boundary conditions (2.29). Parameters: $a_1 = 0$, $a_2 = 0$, $\Gamma = 16\pi$. (a) $b = 0.5$. (b) $b = 0.2$. (c) Sample profiles $R(x)$ along the branch bifurcating from point 1 in (a). 20
- 2.10 (Color online) Bifurcation diagrams for subcritical stationary solutions with $k = 0$ with several secondary branches of nonuniform states satisfying boundary conditions (2.29). Parameters: $a_1 = 0.6$, $a_2 = 0.1$, $\Gamma = 16\pi$. (a) $b = 0.5$. (b) $b = 0.25$. (c) Sample profiles of $\text{Re}A(x)$ (solid line) and $\text{Im}A(x)$ (dashed line) along the branch bifurcating from point 1 in (a). This branch terminates on a primary branch with $k = \pi/\Gamma \approx k_M$ 21

- 2.11 (Color online) (a) Bifurcation diagram for subcritical stationary solutions with $k = 0$ with several secondary branches of nonuniform states satisfying boundary conditions (2.29). The first three secondary branches terminate on a primary branch with $k \neq 0$. (b,c) Sample profiles of $\text{Re}A(x)$ (solid line) and $\text{Im}A(x)$ (dashed line) along the branch bifurcating from points 1 and 2, respectively, showing that both branches terminate on a primary branch with wavenumber $k = 2\pi/\Gamma \approx k_M$. Parameters: $b = 0.5$, $a_1 = 1.1$, $a_2 = 0.1$, $\Gamma = 16\pi$ 22
- 2.12 (Color online) (a) Bifurcation diagram for subcritical stationary solutions with $k = 0$ with several secondary branches of nonuniform states satisfying boundary conditions (2.29). Parameters: $b = 0.5$, $a_1 = 1.5$, $a_2 = 1.0$, $\Gamma = 16\pi$. Branches bifurcating at points 1 and 2 in (a) terminate at the same wavenumber, $k = -3/16$. (b) Sample profiles of $\text{Re}A(x)$ (solid line) and $\text{Im}A(x)$ (dashed line) along the defect branch bifurcating at point 3 in (a). 23
- 2.13 (Color online) Bifurcation diagrams for subcritical stationary solutions with $k = 0$ with several secondary branches of nonuniform states satisfying boundary conditions (2.29) showing the reconnection process that takes place with decreasing b . Branches bifurcating at points 1 and 2 in (a) terminate at the same wavenumber, $k = -1/8$. Parameters: $a_1 = 1.5$, $a_2 = 1.6$, $\Gamma = 16\pi$. (a) $b = 0.5$. (b) $b = 0.4$. (c) $b = 0.395$ 24
- 2.14 (Color online) Bifurcation diagrams for (a) subcritical and (b) supercritical stationary solutions with $k = 0$ with several secondary branches of nonuniform states satisfying boundary conditions (2.29). All secondary branches terminate at nonzero wavenumber. Parameters: $a_1 = 2.1$, $a_2 = 0.2$, $\Gamma = 16\pi$. (a) $b = 0.5$. (b) $b = -0.01$. (c) Sample profiles of $\text{Re}A(x)$ along the branch bifurcating from point 1 in (a). 25
- 2.15 (Color online) Bifurcation diagrams for subcritical stationary solutions with $k = 0$ with several secondary branches of nonuniform states satisfying boundary conditions (2.29). Some secondary branches terminate on the $k = 0$ primary branch. Parameters: $a_1 = 1.6$, $a_2 = -0.5$, $\Gamma = 16\pi$. (a) $b = 0.5$. (b) $b = 0.42$. (c) $b = 0.41$. (d) $b = 0.2$ 26
- 2.16 (Color online) Bifurcation diagrams for (a) subcritical and (b) supercritical stationary solutions with $k = 1$ with several secondary branches of nonuniform states satisfying boundary conditions (2.29). (c) Sample profiles of $\text{Re}A(x)$ (solid line) and $\text{Im}A(x)$ (dashed line) along the branch extending between points 1 and 10 in panel (a). (d) Sample profiles of $\text{Re}A(x)$ along the secondary branch bifurcating from the RW branch at point 3 in panel (a). The behavior along the branches bifurcating from points 2 and 4–7 is qualitatively similar to (d). Parameters: $a_1 = 0$, $a_2 = 0$, $\Gamma = 16\pi$. (a) $b = 0.5$. (b) $b = -0.5$ 27

- 2.17 (Color online) Bifurcation diagrams for (a) subcritical and (b) supercritical stationary solutions with $k = 1$ (RW⁺) and $k = -1$ (RW⁻) together with several secondary branches of nonuniform states satisfying boundary conditions (2.29) on a domain of length $\Gamma = 16\pi$. Parameters: (a) $b = 0.5$, $a_1 = 0.6$, and $a_2 = 0.8$. (b) $b = -0.5$, $a_1 = 1.4$, and $a_2 = 1.2$. (c) Sample profiles of $\text{Re}A(x)$ (solid line) and $\text{Im}A(x)$ (dashed line) along the branch in (a) bifurcating at point 3 showing a gradual change of wavenumber between points 3 and 7. $\text{Im}A(x)$ oscillates $\frac{\pi}{2}$ out of phase with $\text{Re}A(x)$. Similar wavenumber changes occur along the branches in (a) bifurcating at points 1 and 2. (d) Sample profiles of $\text{Re}A(x)$ (solid line) and $\text{Im}A(x)$ (dashed line) along the branch bifurcating at point 1 in (b) showing a gradual change of wavenumber between points 1 and 5. 28
- 2.18 (Color online) (a) Bifurcation diagram showing the simultaneous bifurcation at $\mu = \frac{1}{64}$ of an SW branch and a pair of RW branches with $k = \pm 0.125$. A secondary branch of spatially modulated states connects the SW and RW⁻ branches between points 1 and 3. (b) Sample profiles of $R(x)$ along the SW branch. Parameters: $b = 0.5$, $a_1 = -0.2$, $a_2 = 0.2$, $\Gamma = 16\pi$ 29
- 2.19 (Color online) (a) Bifurcation diagram showing the simultaneous bifurcation at $\mu = \frac{1}{256}$ of a branch of two-frequency states (MW: red (gray) curve) undergoing protosnaking and a pair of branches of periodic states RW[±] with $k = \pm \frac{1}{16}$. The two-frequency states terminate on RW⁻. (b) Sample profiles of $\text{Re}A(x)$ (solid line) and $\text{Im}A(x)$ (dashed line) along the MW branch in (a). Parameters: $b = 0.5$, $a_1 = 0.3$, $a_2 = 0.2$, $\Gamma = 16\pi$ 29
- 2.20 Eigenvalues σ_{\pm} as functions of q near the onset of instability. (a) Phase mode: $f = -0.2$ and $g = 1$. (b) Real and oscillatory modes: $f = 1$ and $g = -0.1$ 33
- 2.21 The (k, μ) plane when $a_1 = a_2 = 0$ and (a) $b = 1$, R_0^+ , (b) $b = 1$, R_0^- , (c) $b = -1$, R_0^+ . When $b \leq 0$ both curves lie in $\mu \geq 0$; when $b > 0$ the curves extend below $\mu = 0$ 34
- 2.22 (Color online) Bifurcation diagrams $R_0^2(k)$ when $\mu = b = 1$ showing the onset of type (i) ($f = 0$, black dashed line) and type (ii) ($g = f$, black line) instabilities. Thick blue (gray) line indicates stable solutions while the thick dashed blue (gray) line indicates the R_0^- solutions unstable with respect to instability (i) only. (a) $a_1 = 3$, $a_2 = 4$. (b) $a_1 = -3$, $a_2 = -2$. (c) $a_1 = 3$, $a_2 = 6$. (d) $a_1 = -3$, $a_2 = 0$. 36
- 2.23 (Color online) Bifurcation diagrams $R_0^2(k)$ when $\mu = -1$, $b = 3$ showing the onset of type (i) ($f = 0$, black dashed line) and type (ii) ($g = f$, black line) instabilities. Thick blue (gray) line indicates stable solutions while the thick dashed blue (gray) line indicates the R_0^- solutions unstable with respect to instability (i) only. (a) $a_1 = 3$, $a_2 = 4$. (b) $a_1 = -3$, $a_2 = -2$. (c) $a_1 = 3$, $a_2 = 6$. (d) $a_1 = -3$, $a_2 = 0$. 37

- 2.24 The parameter range ($k_b \equiv k/|b|, \mu_b \equiv \mu/b^2$) for instability (i) of R_0^+ when $b > 0$ and $a_2 > 0$. Dashed curve: saddle-node. Solid curve: $\mu = k^2$. Dash-dotted curve: Eckhaus boundary. (a) $a_1 = 1, a_2 = 2$ ($\alpha > 0$). (b) $a_1 = -1, a_2 = 2$ ($\alpha > 0$). (c) $a_1 = 1.3, a_2 = 1$ ($-4 < \alpha < 0$). (d) $a_1 = -0.6, a_2 = 0.5$ ($-4 < \alpha < 0$). (e) $a_1 = 2.8, a_2 = 1$ ($\alpha < -4$). (f) $a_1 = -2.1, a_2 = 0.5$ ($\alpha < -4$). (g) $a_1 = 3, a_2 = 1$ ($\alpha < -4$). (h) $a_1 = -2.3, a_2 = 0.5$ ($\alpha < -4$). 38
- 2.25 The parameter range ($k_b \equiv k/|b|, \mu_b \equiv \mu/b^2$) for instability (i) of R_0^+ when $b < 0$ and $a_2 > 0$. Dashed curve: saddle-node. Solid curve: $\mu = k^2$. Dash-dotted curve: Eckhaus boundary. (a) $a_1 = 0.7, a_2 = 1$ ($\alpha > 0$). (b) $a_1 = -0.7, a_2 = 1.5$ ($\alpha > 0$). (c) $a_1 = 1.8, a_2 = 1$ ($-4 < \alpha < 0$). (d) $a_1 = -2.1, a_2 = 0.5$ ($\alpha < -4$). (e) $a_1 = 2.3, a_2 = 0.5$ ($\alpha < -4$). (f) $a_1 = -2.23, a_2 = 0.5$ ($\alpha < -4$). (g) $a_1 = 2.65, a_2 = 0.5$ ($\alpha < -4$). (h) $a_1 = -2.65, a_2 = 0.5$ ($\alpha < -4$). 39
- 2.26 (Color online) The parameter range ($k_b \equiv k/|b|, \mu_b \equiv \mu/b^2$) for instability (i) and (ii) of R_0^- when $b > 0$ and $a_2 > 0$. Black dashed curve: saddle-node. Black solid curve: $\mu = k^2$. Red (gray) solid curve: boundary of instability (i). Red (gray) dashed curve: boundary of instability (ii). (a) $a_1 = 1, a_2 = 1.4$ ($\alpha > 0$). (b) $a_1 = -1, a_2 = 1.42$ ($\alpha > 0$). (c) $a_1 = 3.46, a_2 = 3$ ($-4 < \alpha < 0$). (d) $a_1 = -3.46, a_2 = 3$ ($-4 < \alpha < 0$). (e) $a_1 = 2.45, a_2 = 1$ ($\alpha < -4$). (f) $a_1 = -3, a_2 = 1.5$ ($\alpha < -4$). 40
- 2.27 (Color online) The parameter range ($k_b \equiv k/|b|, \mu_b \equiv \mu/b^2$) for instability (i) and (ii) of R_0^- when $b < 0$ and $a_2 > 0$. Black dashed curve: saddle-node. Black solid curve: $\mu = k^2$. Red (gray) solid curve: boundary of instability (i). Red (gray) dashed curve: boundary of instability (ii). (a) $a_1 = 0.45, a_2 = 2$ ($\alpha > 0$). (b) $a_1 = -1, a_2 = 2$ ($\alpha > 0$). (c) $a_1 = 2.2, a_2 = 1.4$ ($-4 < \alpha < 0$). (d) $a_1 = -2.8, a_2 = 2.2$ ($-4 < \alpha < 0$). (e) $a_1 = 3.2, a_2 = 2.2$ ($\alpha < -4$). (f) $a_1 = -3, a_2 = 1.73$ ($\alpha < -4$). 41
- 2.28 Time evolution of $\text{Re}[A]$ with PBC in a domain of size $\Gamma = 200$. Parameters: $f = -0.02, g = 1.3, k_0 = \pi/10$, and $a_1 - a_2 = 0.45$. (a) $a_1 = 0.65$. (b) $a_1 = 0.75$. (c) $a_1 = 1.25$. (d) $a_1 = 2.25$. In each case the solution has been initialized with a sinusoidal perturbation of amplitude $\sqrt{c_1^2 + c_2^2} = 0.05$ and wavenumber $q = 6\pi/\Gamma$. 43
- 2.29 Time evolution of $\text{Re}[A]$ with PBC in a domain of size $\Gamma = 200$ triggered by the Eckhaus instability. Parameter values are $a_1 = 0.75, a_2 = 0.3$, with the remaining quantities as in figure 2.28. The superposed initial perturbation is periodic with wavenumber (a) $2\pi/\Gamma$, (b) $4\pi/\Gamma$, (c) $6\pi/\Gamma$, and (d) $8\pi/\Gamma$. In each case the solution has been initialized with a sinusoidal perturbation of amplitude $\sqrt{c_1^2 + c_2^2} = 0.05$ and wavenumber $q = 6\pi/\Gamma$ 44
- 2.30 Time evolution of $\text{Re}[A]$ with PBC in a domain of size $\Gamma = 200$. Parameter values: $a_2 = 0.2, g = 1.3, \gamma = 7$. (a) $f = -0.01503$ ($\sigma_+ = 2.0847 \times 10^{-5}$). (b) $f = -0.01751$ ($\sigma_+ = 2.9261 \times 10^{-5}$). (c) $f = -0.01999$ ($\sigma_+ = 3.7680 \times 10^{-5}$). (d) $f = -0.02247$ ($\sigma_+ = 4.6105 \times 10^{-5}$). In each case the solution has been initialized with a sinusoidal perturbation of amplitude $\sqrt{c_1^2 + c_2^2} = 0.001$ and wavenumber $q = 6\pi/\Gamma$ 45

2.31	(a) The linear growth rate σ_+^{-1} as function of f from figure 2.30. (b) Time T to phase slip in figure 2.30 multiplied by σ_+ as function of σ_+^{-1}	46
2.32	Time evolution of $\text{Re}[A]$ with PBC in a domain of size $\Gamma = 200$. Parameter values: $a_1 = -2.9$, $a_2 = -0.7$, $f = -0.02$, $\gamma = 0$. The instability is initialized using an unstable mode with wavenumber (a) $4\pi/\Gamma$ and (b) $6\pi/\Gamma$	46
2.33	A 20 roll periodic wavetrain with PBC undergoing both amplitude and oscillatory instabilities. (a) Time evolution of $\text{Re}[A]$. (b) Time evolution of $\text{Re}[a]$. (c) Comparison of the evolution of the mean of the modulation mode (solid line) with the evolution of A_0 from Eq. (2.82) (dashed line). Domain size: $\Gamma = 200$. Parameter values: $a_1 = 0.3$, $a_2 = 2.2$, $b = 0.5$, and $\mu = \mu_0 + 5 \times 10^{-6}$. The initial condition is a periodic wavetrain with a superposed $q = 2\pi/\Gamma$ right-traveling wave of $O(10^{-2})$ amplitude.	48
2.34	A 20 roll periodic wavetrain with PBC undergoing both amplitude and oscillatory instabilities. (a) Time evolution of $\text{Re}[A]$. (b) Time evolution of $\text{Re}[a]$. (c) Comparison of the evolution of the mean of the modulation mode (solid line) with the evolution of A_0 from Eq. (2.82) (dashed line). Domain size: $\Gamma = 200$. Parameter values: $a_1 = 0.3$, $a_2 = 2.2$, $b = 0.5$, and $\mu = \mu_0 + 5 \times 10^{-6}$. The initial condition is a periodic wavetrain with a superposed $q = 4\pi/\Gamma$ left-traveling wave of $O(10^{-2})$ amplitude.	48
2.35	$c_{num}/c_{pre} - 1$ versus μ/μ_M for the front solutions when $a_1 = a_2 = 1$, where c_{num} is measured speed and c_{pre} is the predicted value.	51
2.36	Time evolution of the profile of a stable front with μ perturbed from μ_M . Parameter values: $a_1 = 1$, $a_2 = 1$, $b = 1$. (a) $\mu = 1.01\mu_M$. (b) $\mu = 0.99\mu_M$	52
2.37	Time evolution of the profile of an unstable front. Parameter values: $a_1 = 2$, $a_2 = 3$, $b = 1$, and $\mu = -0.0492$. The center of the front is suppressed by a factor of 0.99 in (a) and augmented by 1.01 in (b).	52
2.38	The linear spreading speed of the unstable front solution in the (a_1, a_2) plane. As (a_1, a_2) approaches the line $\beta = 0$, v^* diverges. We therefore cut off v^* at $v^* = 3$ and use black color to indicate the parameter range where $v^* \geq 3$. In addition, v^* is set equal to 0 in regions where either β or g is nonnegative (white color).	54
2.39	The potential energy $U(R, L = 0)$ when (a) $\mu > \mu_M$ and (b) $\frac{4\mu_M}{3} < \mu < \mu_M$	54
2.40	(Color online) The case $\mu = 0.99\mu_M$. Solid line: $\beta = 0$. Dashed line: $g = 0$. The quantity β is negative between the solid lines while g is positive between the dashed lines. Hole solutions are stable in the red (or gray) region.	55
2.41	Dynamics of an unstable $L = 0$ hole solution when $\mu = 0.99\mu_M$ and $(a_1, a_2) = (2, 0)$. The amplitude at center of the hole is multiplied by a factor 0.99 in (a) and by 1.01 in (b). In (a) the hole evolves to a nearby hole with $L \approx 0.01 \neq 0$ and nonzero amplitude at the center; in (b) the hole disappears.	55
2.42	(Color online) The case $\mu = 1.01\mu_M$. Solid line: $\beta = 0$. Dashed line: $g = 0$. The quantity β is negative between the solid lines while g is positive between the dashed lines. Hole solutions are stable in the red (or gray) region.	56

2.43	Dynamics of an unstable $L = 0$ hole solution when $\mu = 1.01\mu_M$ and $(a_1, a_2) = (1, 1)$. The amplitude at the center of the hole has been multiplied by a factor 0.99 in (a) and by 1.01 in (b). In (a) the hole expands; in (b) the hole decays.	57
2.44	Dynamics of an unstable $L = 0$ pulse solution when $\mu = 0.99\mu_M$ and $(a_1, a_2) = (1, 1)$. The amplitude at the center of the hole has been multiplied by a factor 0.99 in (a) and by 1.01 in (b). In (a) the pulse decays to the flat state $A = 0$; in (b) the pulse broadens into a periodic state.	57
2.45	Evolution of an unstable hole solution with $k_\infty = k_M$ when $\mu = 1.01\mu_M$ and $(a_1, a_2) = (1, 1)$. The amplitude at the center of the hole has been multiplied by a factor 0.99 in (a) and by 1.01 in (b). In (a) the hole broadens into a growing region filled with the flat state $A = 0$; in (b) the hole decays into a constant amplitude periodic state.	58
2.46	Evolution of a stable hole solution with $k_\infty = k_M$ when $\mu = 0.99\mu_M$ and $(a_1, a_2) = (1, 1.5)$. The amplitude at the center of the hole has been multiplied by a factor 0.9 in (a) and by 1.1 in (b). The oscillations decay with increasing time.	59
3.1	Bifurcation diagram showing \mathcal{E} as a function of Ra for slanted snaking when $Ta = 20$ and $\sigma = 0.1$. The branches of localized states L_{10}^\pm in a $\Gamma = 10\lambda_c$ domain are shown. They bifurcate in a secondary bifurcation on the branch P_{10} of periodic convection with 10 pairs of counter-rotating rolls in Γ and connect to P_5 , the branch of 5 pairs of counter-rotating rolls in Γ . The solutions at each saddle-node during the snaking process are shown in figure 3.2.	64
3.2	Solution profiles at successive saddle-nodes on (a) L_{10}^- , (b) L_{10}^+ in figure 3.1. Upper panels show isovalues of the streamfunction with light (dark) regions corresponding to clockwise (counterclockwise) flow. Lower panels show the profiles of $V(x)$. Topmost solutions correspond to the termination point on P_5	65
3.3	Bifurcation diagram showing \mathcal{E} as a function of Ra for the periodic states P_{10} , P_7 and for the branches L_{10}^\pm of spatially localized states. The parameters are $Ta = 40$, $\sigma = 0.6$ and $\Gamma = 10\lambda_c$	66
3.4	Same as figure 3.2 but for the localized solutions along (a) L_{10}^- and (b) L_{10}^+ in figure 3.3.	67
3.5	(a) Bifurcation diagram for the L_{10}^+ branch when $Ta = 50$. The branch bifurcates from P_{10} and terminates on P_{10} . The solid dots indicate the location of the solutions shown in (b).	68
3.6	As for figure 3.5 but for $Ta = 100$	68
3.7	Regions of super and subcriticality for primary–secondary branches in the (a) ζ - Q plane (MC) and (b) σ - Ta plane (RC) on logarithmic scales. (c) Sketches of the bifurcation diagrams characteristic of each of the four regions.	73

- 3.8 Bifurcation diagrams showing stationary solutions of Eq. (3.20) with $\phi_X = 0$ satisfying NBC for $\sigma = 0.6$ and $\Gamma = 10\lambda_c$. Thick solid lines: $k = 0$ primary state (periodic convection). Thin solid lines: modulated states (convectons). (a) $Ta = 50$ ($\xi^2 = 0.7032$, region (2)). (b) $Ta = 70$ ($\xi^2 = 0.5882$, region (2)). (c) $Ta = 120$ ($\xi^2 = 0.4269$, region (2)). (d) $Ta = 140$ ($\xi^2 = 0.3877$, region (3)). The periodic state is stable up to the secondary bifurcation; in (d) the modulated state is stable up to the saddle-node. 74
- 3.9 Sample profiles of the stationary solutions of Eq. (3.20) when $\Gamma = 10\lambda_c$. The amplitude $|A|$ is shown as function of a scaled variable while the z -average of the zonal velocity, $V(x)$, is shown in terms of the original variable x . (a,b) $\sigma = 0.1$, $Ta = 20$ ($\xi^2 = 33.3308$). (1) $Ra = 1174.3$. (2) $Ra = 1171.8$. (3) $Ra = 1166.8$. (4) $Ra = 1161.7$. (c,d) $\sigma = 0.6$, $Ta = 50$ ($\xi^2 = 0.7032$). (1) $Ra = 2573.5$. (2) $Ra = 2573.3$. (3) $Ra = 2572.6$. (4) $Ra = 2571.6$. Note that the spatial frequency of $V(x)$ is double that of $\psi(x)$ 75
- 3.10 Dependence of a_1 and a_2 on ζ for different σ when (a,b) $\tilde{c} > 0$ and (c,d) $\tilde{c} < 0$. Black line: $\sigma = 0.2$. Red line: $\sigma = 0.4$. Blue line: $\sigma = 2$. $Q_c = Q_c^+$ is indicated in a solid line while $Q_c = Q_c^-$ is indicated in a dashed line. 80
- 3.11 Coefficients (a) a_1 and (b) a_2 as functions of σ when (a,b) $\tilde{c} > 0$ and (c,d) $\tilde{c} < 0$. Solid line: $Ta_c = Ta_c^+$. Dashed line: $Ta_c = Ta_c^-$ 81
- 3.12 The existence region of Maxwell curve in (a) MC with $\zeta = 0.5$ and $\sigma = 1$ and (b) RC with $\sigma = 0.6$ 81
- 3.13 Bifurcation diagrams of $K_0 = 0$ primary branch in rotating convection with $\sigma = 0.6$ and $\Gamma = 50\lambda_c$. (a) $Ta = Ta_c = 5.1176$. (b) $Ta = 5.7176$. (c) $Ta = 5.8176$. (d) $Ta = 6.1176$ 83
- 3.14 Spatial profiles of solutions in (a) figure 3.13(b) and (b) figure 3.13(c). Solid line: $\text{Re}[\epsilon A]$. Dashed line: $\text{Im}[\epsilon A]$ 84
- 3.15 Bifurcation diagrams of $K_0 = 0$ primary branch in rotating convection. $\sigma = 0.5$. $\Gamma = 50\lambda_c$. (a) $Ta = 310.7656$. (b) $Ta = 312.7656$. (c) Spatial profiles of solutions in (b). Solid line: $\text{Re}[\epsilon A]$. Dashed line: $\text{Im}[\epsilon A]$ 85
- 3.16 Dependence of (a) Ra_c and (b) k_c on β . Solid line: $Ta = 140$. Dotted line: $Ta = 100$. Dashed line: $Ta = 60$. Dashed-dotted line: $Ta = 20$ 89
- 3.17 The dependence of μ on β . (a) $\sigma = 0.6$. Solid line: $Ta = 100$. Dashed line: $Ta = 60$. Dashed-dotted line: $Ta = 20$. (b) $Ta = 60$. Solid line: $\sigma = 1.1$. Dashed line: $\sigma = 0.6$. Dashed-dotted line: $\sigma = 0.1$ 90
- 3.18 Bifurcation diagrams of $K_0 = 0$ primary branch in rotating convection for the mixed boundary conditions (3.72). $\Gamma = 10\lambda_c$. (a) $\sigma = 0.4$, $Ta = 80$ ($\xi^2 = 1.2263$). (b) $\sigma = 0.6$, $Ta = 70$ ($\xi^2 = 0.5882$). (c) $\sigma = 0.6$, $Ta = 140$ ($\xi^2 = 0.3877$). 91
- 3.19 Bifurcation diagram showing the average poloidal kinetic energy \mathcal{E} (vertical axis) as a function of the Rayleigh number Ra (horizontal axis) for slanted snaking when $Ta = 20$, $\sigma = 0.1$, and $\Gamma = 10\lambda_c$ for the mixed boundary conditions (3.72). From left to right, the snaking branches correspond to $\beta = 0, 0.2, 0.4$, and 0.6 . These results are provided by Dr. Beaume [60]. 91

4.1	Solution profiles of the exact real elliptic solution (4.38) when $a \in I_2$ and $b = (-\frac{25a}{3} - 3)^{1/2}$. The solutions are TR_2 -symmetric. (a) $a = -0.4$. (b) $a = -0.5$. (c) $a = -1$. (d) $a = -1.4$	102
4.2	Solution profiles of the exact real elliptic solution (4.38) when $a \in I_1$ and $b = (-\frac{25a}{3} - 3)^{1/2}$. The solutions are R_1 -symmetric. (a) $a = -1.45$. (b) $a = -1.5$. (c) $a = -2$. (d) $a = -3$	103
4.3	(a) The spatial average $\langle w \rangle \equiv \frac{1}{L} \int_0^L w(x) dx$, (b) the spatial period L , and (c) the free energy F/L of the exact real solutions as functions of $\mu \equiv a + 1$	103
4.4	Exact front solution (4.40) for $a = -\frac{36}{25}$, $b = 3$	103
4.5	Time evolution of the front solution (4.40) perturbed in the middle at $t = 0$ with $O(10^{-3})$ random noise.	104
4.6	The (μ, b) plane showing the location of the exact real solutions obtained in section 4.3 (dashed line) together with the position of the saddle-node of the primary branch with $k = 1$ (solid line). The dashed-dotted line corresponds to the bound $\mu > -\frac{b^2}{6}$ for the existence of periodic or pulse-like solutions. The solid dot indicates the location of the front solution (4.40).	106
4.7	(a) Bifurcation diagram for stationary periodic solutions with $b = 0.5774$, $c = 3/2$ and period $L = 14.1492$. Point 1 corresponds to the exact real solution when $a = -0.4$. (b) Sample profiles along the black dashed line.	106
4.8	(Color online) (a) Bifurcation diagram for stationary periodic solutions with $b = 2.1213$, $c = 3/2$ and period $L = 15.9311$. Point 1 corresponds to the exact real solution with $a = -0.9$. (b) Sample profiles along the red (gray) and black dashed lines.	107
4.9	(Color online) (a) Bifurcation diagram for stationary periodic solutions with $b = 2.8723$, $c = 3/2$ and period $L = 21.1801$. Point 1 corresponds to the exact real solution with $a = -1.35$. (b) Sample profiles along the dashed and red (gray) branches. (c) Sample profiles along the dotted branch.	107
4.10	(a) Bifurcation diagrams for stationary periodic solutions with $b = 2.9861$, $c = 3/2$ and period $L = 27.9881$. Point 1 corresponds to the exact real solution with $a = -1.43 > -36/25$ and lies on an isola. The inset at top left indicates the relative position between the primary branch of 2π periodic states and the isola of periodic states with $L = 27.9881$. (b) Sample profiles along the secondary branch connecting points 2 and 5 (dashed line, panel (a)).	108
4.11	Bifurcation diagrams for stationary periodic solutions $c = 3/2$ and (a) $b = 2.9930$, $L = 30.1667$, (b) $b = 2.9965$, $L = 32.3511$, (c) 3.0035 , $L = 32.3321$, and (d) $b = 3.0069$, $L = 30.1327$. The points labeled 1, 2, 3, 4 correspond to the exact real solutions (shown in the insets with x/L as the horizontal coordinate) at (a) $a = -1.435$, (b) $a = -1.4375$, (c) $a = -1.4425$, and (d) $a = -1.445$, respectively; all lie on isolas. Secondary crosslinks consisting of asymmetric solutions are omitted.	108

- 4.12 (a) Bifurcation diagrams for stationary periodic solutions with $b = 3.0139$, $c = 3/2$ and period $L = 27.9276$. Point 1 corresponds to the real exact solution with $a = -1.45 < -36/25$. The inset at top left indicates the relative position between the primary branch of 2π periodic states and the isola of periodic states with $L = 27.9276$. (b) Bifurcation diagram for the stationary asymmetric states connecting points 2 and 7. (c) Sample profiles along the isola (solid line, panel (a)). (d) Sample profiles along the asymmetric branch connecting points 2 and 7 (solid line, panel (b)). 109
- 4.13 (a) Bifurcation diagram for stationary R_1 -symmetric solutions (solid line) with $b = 3.6968$, $c = 3/2$ and period $L = 14.8473$. Point 1 corresponds to the exact solution with $a = -2$. The inset indicates the relative position between the branch of 2π periodic states and the branch originating from the exact solution with the period held at $L = 14.8473$. The dashed line shows one of the crosslinks consisting of asymmetric solutions. (b) The branch of $R_1 \times TR_2$ -symmetric front-like states that bifurcate from the branch in panel (a) at points labeled 2 and 3 together with a second branch of $R_1 \times TR_2$ -symmetric states that bifurcates from $u = 0$ at $\mu = 0.6739$. The two branches are connected at points 8 and 14, respectively, by a branch of asymmetric states (dashed line). (c) Sample profiles at the points indicated in panel (a). (d) Sample profiles at $\mu = 1$ and $\mu = 25$ along the red (gray) branch in panel (b) (top row: upper branch; bottom row: lower branch). (e,f) Sample profiles at the points indicated in panel (b); points (2, 3), (5, 6), (9, 11), (10, 12) are connected by crosslinks (not shown). The fold labeled 7 indicates the transition to front-like states at larger μ 111
- 4.14 A blowup of the bifurcation diagram near point 3 showing the termination of the branch of R_1 -symmetric states in figure 4.13(a) on the branch of $R_1 \times TR_2$ -symmetric states shown in red (gray) in figure 4.13(b). The close passage of a part of the R_1 -symmetric branch near point 3 is a projection effect. 112
- 4.15 (a) Bifurcation diagrams for stationary periodic solutions with $b = 5.8737$, $c = 3/2$ and period $L = 9.7914$. Point 2 corresponds to the exact solution with $a = -4.5$. Point 6 on the red (gray) branch is a tertiary bifurcation point. The dashed line shows one of the R_1 -symmetric branches connecting the original periodic branch to itself, with the inset showing details of its appearance at small amplitude. (b) Sample profiles along the dashed branch. (c) Sample profiles along the red (gray) branch. 112
- 5.1 Bifurcation diagrams showing the L^2 -norm (vertical) of u as a function of r (horizontal) for even parity branches with $\alpha = \pm 0.1$, ± 0.4 , and ± 0.7 (from left to right) in SH35 with periodic forcing. Localized branches represented in a solid line have $\alpha > 0$ while those in a dashed line have $\alpha < 0$ 117

5.2	Bifurcation diagrams showing the L^2 -norm (vertical) of u as a function of r (horizontal) for odd parity branches with $\alpha = \pm 0.1, \pm 0.4$, and ± 0.7 (from left to right) in SH35 with periodic forcing. Localized branches represented in a solid line have $\alpha > 0$ while those in a dashed line have $\alpha < 0$	117
5.3	Bifurcation diagrams showing the L^2 -norm (vertical) of u as a function of r (horizontal) for the even parity branches for $\alpha = \pm 0.1$ and ± 0.7 (from left to right) in SH35 with bump forcing. Localized branches represented in a solid line have $\alpha > 0$ while those in a dashed line have $\alpha < 0$	118
J.1	Solutions of Eq. (J.1) when $\sigma \neq 0$ as given by (J.4). (a) $\sigma = 2.5$. (b) $\sigma = \sqrt{7}$. (c) $\sigma = 2.8$. The solid (dashed) line corresponds to $\text{Im}[\omega] > 0$ ($\text{Im}[\omega] < 0$). The solid and dashed lines coincide in (c).	151
J.2	Solutions of Eq. (J.1) when $\sigma = 0, \beta = 0$ as given by (J.6). (a) $\alpha = -0.4$. (b) $\alpha = \frac{11}{25}$. (c) $\alpha = 1$	151

Acknowledgments

First, I would like to thank my advisor, Prof. Edgar Knobloch, for his guidance during my graduate career. His encouragement helps me significantly and I learn a lot from his dedication on research. I also thank Prof. John Neu for his kindness on sharing his knowledge and attitude in mathematics especially on the techniques in asymptotic analysis, and Prof. Jonathan Wurtele and Prof. Oliver O'Reilly for their patience and comments during the preparation of this dissertation.

My life in Berkeley has benefited from my research collaborators and friends. It is a great experience to collaborate with Prof. Alain Bergeon and Dr. Cedric Beaume during their visit of Berkeley. I also appreciate the helpful discussions with the group members, Dr. Yiping Ma, and Jianbo Xie. Special thanks to my friends in UC Berkeley karate club. I really had a good time practicing with you.

Finally, I would like to thank my parents and other family members. It is your support that makes me have the courage to go through the hard years.

The work was supported in part by the National Science Foundation under grants DMS-0908102 and DMS-1211953.

Chapter 1

Introduction

Patterns appear naturally in a variety of systems, in particular, in fluid systems [1], chemical reactions [2], biology [3], and nonlinear optics [4]. These systems, are mostly driven dissipative systems and coherent structures like stripes, spots, spirals, labyrinths, . . . , are formed from initially homogeneous background via spontaneous symmetric-breaking bifurcations. This fascinating field of study has generated a lot of attention and also yields rich applications in fabrication, lithography, or even computer graphics. A classical and probably the best studied example of pattern formation is Rayleigh-Bénard convection [1], which occurs in a plane fluid layer heated from below. The applied temperature difference

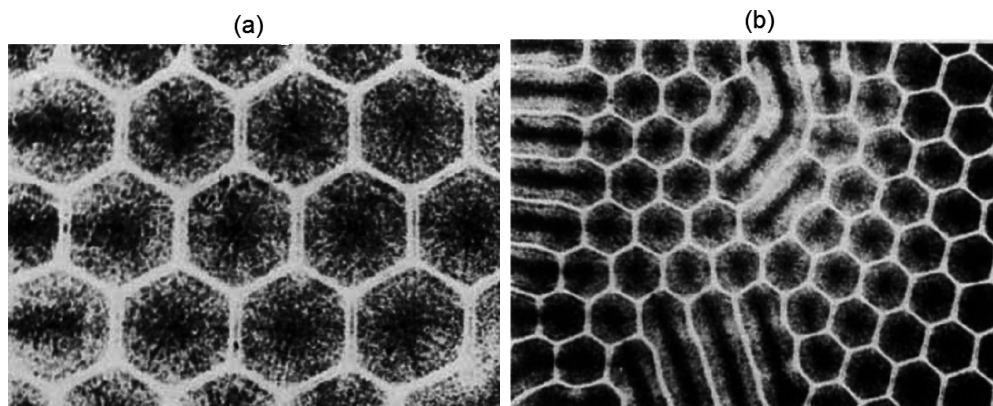


Figure 1.1: (a) Shadowgraph of hexagonal convection cells. (b) Hexagonal cells transform to roll pattern [5].

ΔT between bottom and top acts as the "driving force" which causes the uniform conduction state to lose its stability and periodic convection to appear as ΔT exceeds a certain threshold. Figure 1.1 shows the experimental observation of this phenomenon. A detailed analysis of the loss of stability to periodic convection can be found in [6].

To study the pattern forming behavior in Rayleigh-Bénard convection, a partial differ-

ential equation, the so-called Swift-Hohenberg equation

$$u_t = ru - (1 + \nabla^2)^2 u - u^3, \quad (1.1)$$

has been suggested in [7]. Here $u \equiv u(\mathbf{r}, t)$, $\mathbf{r} \in \mathbb{R}^2$, is an order parameter representing the magnitude of the slow eigenvector of the linearized system and may be identified with the temperature deviation (from the pure conduction profile) or the vertical fluid velocity at the layer mid-plane. This equation is suitable for the description of two-dimensional convection for which Eq. (1.1) becomes one-dimensional. However, in full three-dimensional convection, the nonlinear term is nonlocal in space and Eq. (1.1) then represents a model equation believed to retain the essential properties of the full convection problem.

The one-dimensional Swift-Hohenberg equation has been generalized to

$$u_t = ru - (1 + \partial_{xx})^2 u + f(u), \quad (1.2)$$

where $f(u) = o(|u|)$ as $u \rightarrow 0$ is a smooth nonlinear function of u . This equation, with different nonlinearities, has been used for modeling purposes for various systems and serves as a paradigm in pattern formation. According to linear stability analysis, the trivial state, $u = 0$, loses stability as r becomes greater than zero and a steady state bifurcation to a periodic state with wavenumber $k = 1$ occurs at $r = 0$. This bifurcation can be either supercritical or subcritical which depends on the nonlinearity $f(u)$. If $f(u)$ has the Taylor expansion

$$f(u) = f_2 u^2 + f_3 u^3 + O(u^4), \quad (1.3)$$

the bifurcation is subcritical when $38f_2^2 + 27f_3 > 0$ and supercritical when $38f_2^2 + 27f_3 < 0$ [8]. Note that in the classical Swift-Hohenberg equation, $f(u) = -u^3$, the bifurcation to periodic state is always supercritical.

The patterns introduced previously in Rayleigh-Bénard convection are spatially-extended patterns. Recent interest in convective fluid pattern formation has focused on localized patterns in coupled-convection systems. Such localized patterns appear mostly in the region of subcritical bifurcation. This bifurcation behavior has been observed in [9, 10, 11, 12] in full numerical simulations of binary-fluid convection and doubly-diffusive convection. In these systems, a bistability exists between the pure conduction state and periodic convection state. Figure 1.2 [9] shows an example of the bifurcation diagram in binary-fluid convection of water-ethanol mixture. The vertical axis corresponds to $Nu - 1$, where Nu is the dimensionless number, Nusselt number, which measures the ratio of convective to conductive heat transfer across the layer. The horizontal axis corresponds to Ra , which is the dimensionless number, Rayleigh number, that is proportional to the applied temperature difference. When the fluid mixture is heated from below, the destabilizing temperature gradient competes with a stabilizing concentration gradient that develops in response to the heating whenever the separation ratio of the mixture is negative. As demonstrated in the figure, besides the usual periodic convection structure (SOC, steady overturning convection) there are spatially periodic traveling waves (TW), chaotic states (black dots), and spatially localized states.

There are two branches of stationary localized states, each of which obeys either odd or even reflection symmetry, which enter a snaking or pinning region as the norm, $Nu - 1$, of the solution increases, and then "snake" back and forth across this region with further increase in norm. These oscillations of the localized states in the bifurcation diagram reflect the nucleation of new convection cells at either end of the localized structure and hence the process whereby the structure grows in length (and hence norm).

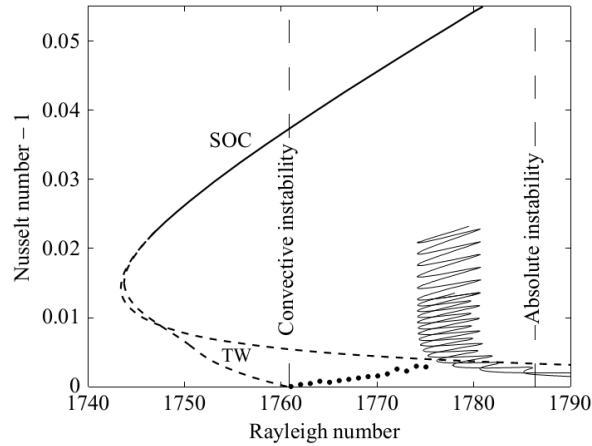


Figure 1.2: Bifurcation diagram showing Nusselt number $Nu - 1$ as a function of the Rayleigh number in binary-fluid convection [9].

The bifurcation scenario described above, so-called homoclinic snaking, has attracted much attention. This type of bifurcation scenario can be well-described within the framework of the generalized Swift-Hohenberg equation with quadratic-cubic or cubic-quintic nonlinearity

$$f_{23}(u) \equiv f_2 u^2 + f_3 u^3, \quad f_{35}(u) \equiv f_3 u^3 + f_5 u^5, \quad (1.4)$$

where the coefficients of the nonlinear terms are chosen to satisfy the condition for subcriticality. The generalized Swift-Hohenberg equation with cubic-quintic nonlinearity is equivariant under $u \rightarrow -u$ while in the quadratic-cubic case there is no such equivariance property. The choice of f_{23} or f_{35} nonlinearity depends on whether the underlying system has up-down reflection symmetry or not. Here the up-down reflection corresponds to the transformation $z \rightarrow -z$, where z is the vertical coordinate and $z = 0$ corresponds to the layer mid-plane. The bifurcation diagram for the quadratic-cubic Swift-Hohenberg equation (hereafter SH23) is shown in figure 1.3 [13]. The black line corresponds to a spatially periodic state while the blue lines, which bifurcate from the periodic branch through the Eckhaus mechanism [25], correspond to localized states. There are two types of localized states, each with a peak or a trough at its center. The localized branches switch their stability (stable to unstable or unstable to stable) as they pass through successive saddle-nodes. However, in contrast to

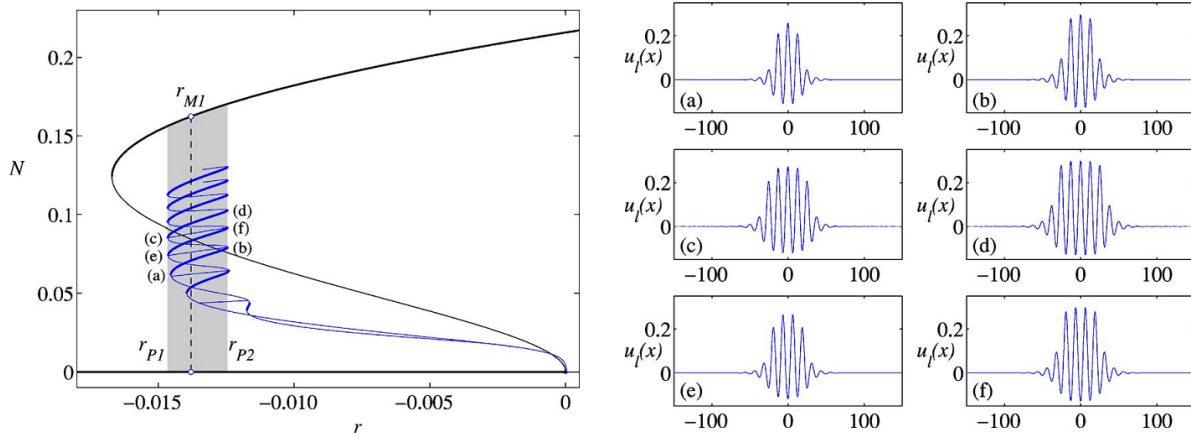


Figure 1.3: Bifurcation diagram and sample solution profiles of SH23 [13]. Here N represents the L^2 -norm of the solution. Black line: periodic state. Blue line: localized state. The thick line indicates the solution branch is stable while the thin line indicates the solution branch is unstable.

convective systems, the system described by Eq. (1.2) has gradient structure, i.e.,

$$u_t = -\frac{\delta F}{\delta u}, \quad F \equiv \int_{\Gamma} \left\{ -\frac{r}{2} u^2 + \frac{1}{2} [(1 + \partial_{xx})u]^2 - \int_0^u f(v) dv \right\} dx \quad (1.5)$$

when suitable boundary conditions are applied. Here Γ is the spatial domain and F is referred to as the free energy of the system. The Maxwell point r_M , which is the value of r such that the periodic state has the same free energy as the zero state, can therefore be defined. This point is of great value since the snaking branches exist and oscillate around it. Besides the snaking structure, there are also rung-like structures which consist of asymmetric localized states and connect the localized branches with different parity.

To study this behavior in the subcritical region, I consider the case when the bifurcation is weakly subcritical and the picture can be described by a modulation equation, the cubic-quintic Ginzburg-Landau equation (hereafter GL35) [20, 21]

$$A_t = \mu A + A_{xx} + i(a_1 |A|^2 A_x + a_2 A^2 A_x^*) + b |A|^2 A - |A|^4 A, \quad (1.6)$$

where $A(x, t)$ represents the pattern amplitude and the coefficients are all real. Equation (1.6) is the most general normal form equation for a weakly subcritical or supercritical bifurcation when the underlying system is translation invariant and reflection symmetric in x . More detailed background of this equation will be given in chapter 2. The branch of periodic states is now identified with the homogeneous state $|A| \neq 0$. Equation (1.6) is not a topological normal form but a truncated normal form at fifth order and due to the absence of higher and beyond all orders terms, the nonadiabatic effects are absent and the snaking region collapses into a point identified in gradient systems with the Maxwell point [14, 15]. The nonadiabatic

terms describe the pinning between the fronts bounding the structure on either side and the pattern within, and thereby generate homoclinic snaking centered on the Maxwell point. However, despite their absence, GL35 retains the essential properties of spatially localized states, including their origin and termination. In addition, it applies to systems that are not of gradient type. Thus, GL35 provides much useful information about the location of the pinning or snaking region in both gradient and nongradient systems, and their behavior outside of this region.

A bifurcation picture different from usual homoclinic snaking, slanted snaking, occurs when there is a large scale mode present in the system. The slanted snaking behavior can be observed in two-dimensional rotating convection and magnetoconvection with stress-free boundary conditions [16, 17]. In these two systems, the large scale modes correspond to zonal velocity and magnetic flux, respectively. These two physical variables vary on a large spatial scale despite the presence of localized structures. Furthermore, the spatial averages of these variables are constants in time and thus represent conservation laws for these systems when periodic boundary conditions are applied in the horizontal direction. In this situation, the usual nearly vertical snaking structure is replaced by a slanted snaking structure as the localized solution branch grows in norm. In contrast with homoclinic snaking, slanted snaking allows localized states to be present outside the region of bistability and indeed when spatially periodic convection sets in supercritically and no bistability is present at all. Figure 1.4 shows the bifurcation diagram for slanted snaking in a rotating convection system.

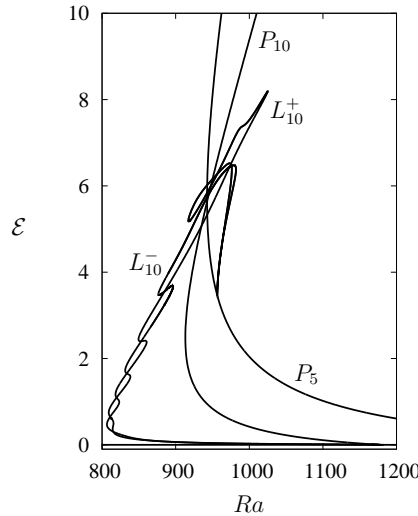


Figure 1.4: Bifurcation diagram showing the average poloidal kinetic energy as a function of the Rayleigh number Ra for slanted snaking when Taylor number $Ta = 20$ and Prandtl number $\sigma = 0.1$ [17].

The leading order modulation behavior of pattern forming systems with a large scale

mode has been studied in [18, 19] and is described by the coupled set of equations

$$\eta A_T = rA + A_{XX} - \frac{1 - \xi^2}{2} |A|^2 A - \xi A V_X, \quad (1.7)$$

$$V_T = V_{XX} + \xi (|A|^2)_X, \quad (1.8)$$

where $A(X, T)$ is the convection amplitude and $V(X, T)$ is the large scale mode. In the stationary situation, these equations reduce to a nonlocal Ginzburg-Landau equation which can be used to explain the bifurcation of a branch of modulated states. I am interested in the modulation behavior near a codimension-two point where the leading order theory becomes invalid through the vanishing of a cubic nonlinear term in the stationary equation. The pattern forming behavior near the codimension-two point is again described by a fifth order Ginzburg-Landau equation similar as GL35 except that the coefficients now contain nonlocal contributions which change the bifurcation behavior [47]. Due to the nonlocal nature, the Maxwell point is no longer present at a single value but broadens into a range of values and becomes a "Maxwell curve" in the bifurcation diagram. The connections between the nonlocal equation and the two convection problems, rotating convection and magnetoconvection, are established in this work.

All the properties described above rely heavily on the use of stress-free boundary conditions but in real physical systems these boundary conditions cannot be easily realized. A possible generalization is to break the stress-free boundary conditions weakly and see how the bifurcation behavior changes due to this effect. To study this, mixed boundary conditions between stress-free and no-slip are introduced; as a result the large scale mode becomes weakly damped and a new length scale appears in the problem. This scale decreases the range of the nonlocal coupling and permits interpolation between global and local coupling. These results shed light on numerical investigation of two-dimensional convection systems and suggest possible experimental work on probing the localized convection phenomenon in a suitable parameter region.

In the study of the generalized Swift-Hohenberg equation, I focus on the stationary case, in which the equation reduces to the fourth order ordinary differential equation

$$u'''' = (r - 1)u - 2u'' + f(u). \quad (1.9)$$

The bifurcation behavior of this ODE has been studied extensively but there remains the question whether there are nontrivial $O(1)$ solutions that are not related to the states which bifurcate from the periodic solutions that originate from the homogeneous state $u = 0$. These solutions may not be stable but can still play important roles in the understanding of transient behavior when studying time evolution properties of large amplitude initial conditions. In addition, the presence of such states may shed additional light on the bifurcation properties of this type of system. ODEs such as Eq. (1.9) can be generalized to complex ordinary differential equations so techniques from complex analysis can be applied in searching for solutions. I focus on the class of meromorphic functions to construct exact meromorphic solutions of the cubic-quintic Swift-Hohenberg equation (hereafter SH35) and show these are

the only meromorphic solutions that can be found. Based on these results, an one-parameter family of real exact solutions is obtained and the solutions are then used as initial conditions for numerical continuation [80]. The procedure enables us to uncover, for example, a series of complex isolas of solutions, which would otherwise be extremely difficult to detect.

The stationary equations studied in this thesis can be understood as finite-dimensional dynamical systems using spatial dynamics interpretation. This allows the use of numerical continuation package, AUTO [36], which is developed for the study of bifurcation behavior in finite-dimensional algebraic and ODE systems.

This dissertation is organized as follows. Chapter 2 explains how I arrive at Eq. (1.6) and its relation with one-dimensional weakly subcritical patterns. The discussions of spatial structures and time-dependent behavior are both given in this chapter. Chapter 3 is devoted to the study of two-dimensional rotating convection and magnetoconvection, focusing on slanted snaking and modulation behavior. A detailed weakly nonlinear analysis is provided and the resulting equation, the nonlocal Ginzburg-Landau equation, is studied. The results can be compared with full numerical simulations and suggest possible directions of future investigation. Chapter 4 is a study of exact meromorphic solutions of SH35 and their bifurcations. In chapter 5, the conclusions, I give a brief summary of my thesis and show some results from ongoing work. Several possible topics and directions for future research inspired by these works are given at the end. For ease of reading, most of the calculational details are rendered in appendices.

Chapter 2

Weakly Subcritical Patterns

The generic bifurcation of a homogeneous state to a one-dimensional stationary periodic pattern is described by the cubic real Ginzburg-Landau equation

$$A_t = \mu A + A_{xx} - b|A|^2 A. \quad (2.1)$$

Eckhaus instability is of fundamental importance in the supercritical region ($b > 0$) since it determines the wavenumber interval around the band center k_c within which spatially periodic solutions are stable. On the real line, this interval shrinks to zero as the closer one approaches the primary bifurcation [22], i.e., the threshold for instability of the trivial state $|A| = 0$. The theory has been extended to periodic domains with a finite period [23, 24]. In this case the allowed wavenumbers are discrete and the wavenumber closest to band center is stable, with the wavenumbers on either side Eckhaus-unstable. Lecture notes on the Eckhaus instability in the cubic real Ginzburg-Landau equation can be found in [25].

Equation (2.1) fails, however, in the vicinity of subcritical to supercritical transition, i.e., when b is small. In this case the equation must be augmented by fifth order terms, and generically one finds that three additional terms enter into the description of the problem and the resulting equation takes the form as Eq. (1.6). This equation was proposed in [26] and studied in [27, 28, 29]; its validity was analyzed rigorously in [30]. A generalization to two-dimensional systems with anisotropy, for example, for instabilities in a nematic liquid crystal, is given in [31].

Equation (1.6) describes the transition in a number of physical systems of interest, including the Blasius boundary layer [26], binary fluid convection [9] and doubly diffusive convection [12], and can be used to predict the location of the snaking region in these systems within which spatially localized states are present.

This chapter builds upon works that appear in [20, 21].

2.1 The cubic-quintic Ginzburg-Landau equation

Consider the evolution of the complex amplitude A of a wavetrain $u(x, t)$ with wavenumber k_c near a steady state pattern-forming instability of a homogeneous state

$$u(x, t) = \epsilon \{ A(\epsilon^2 x, \epsilon^4 t) e^{ik_c x} + c.c. \} + h.o.t., \quad (2.2)$$

where $\epsilon \ll 1$ determines simultaneously the distance from the primary bifurcation and the degree of subcriticality of the primary bifurcation. The scaling of the amplitude A is a consequence of choosing the coefficient of the term $|A|^2 A$ to be $O(\epsilon^2)$, a condition that permits us to bring fifth order terms self-consistently into the theory. These terms are in turn required to stabilize solutions when the primary bifurcation is subcritical and the resulting theory is thus a codimension-two description of the bifurcation of steady wavetrains. If the underlying system is translation- and reflection-invariant in x , the fifth order terms can only belong to $|A|^2 A_x$, $A^2 A_x^*$, and $|A|^4 A$. Multiple scale analysis now leads to an amplitude equation of the form as Eq. (1.6). Here μ and b are real $O(1)$ unfolding parameters, a_1 and a_2 are two real $O(1)$ coefficients which can be positive or negative, and the variables x and t now refer to $\epsilon^2 x$ and $\epsilon^4 t$, respectively. The coefficients of A , A_{xx} , and of the quintic term can always be set equal to 1 by a suitable rescaling of t , x , and A . However, μ represents the bifurcation parameter and hence is retained in what follows. In unscaled variables all terms in this equation are of fifth order, with $\epsilon^4 \mu$ denoting the distance from the bifurcation point. Terms proportional to iA_x may be present which reflect the shift of band center in multiple scale expansions but these can be eliminated by the change of variable $A \rightarrow Ae^{-i\delta x}$ for a suitably chosen δ .

An equation of this type can be derived from the generalized Swift-Hohenberg equation near the primary pattern-forming instability [32, 33] and a sketch of the derivation is provided in Appendix A. The envelope description is valid provided $|A| > 0$ throughout the domain since the spatial phase of the wavetrain (2.2) becomes undefined at zeros of $|A|$; thus zeros of $|A|$ are generally associated with the presence of phase jumps. Equation (1.6) is equivariant under the three operations:

- (i) $x \rightarrow x, A \rightarrow Ae^{i\phi_0}$,
- (ii) $x \rightarrow x + x_0, A \rightarrow A$,
- (iii) $x \rightarrow x_1 - x, A \rightarrow A^*$,

where ϕ_0 , x_0 and x_1 are arbitrary constants. The first two operations are a consequence of translation invariance of the underlying problem, while the third arises when the underlying system is invariant under reflection of x . In this case the coefficients μ , a_1 , a_2 and b must all be real. The symmetry (iii) renders Eq. (1.6) spatially reversible.

When $a_2 = 0$, Eq. (1.6) has gradient structure,

$$A_t = -\frac{\delta F(A, A^*)}{\delta A^*}, \quad (2.3)$$

where

$$F(A, A^*) = \int_{\Gamma} \left\{ |A_x|^2 - \mu|A|^2 - \frac{b|A|^4}{2} + \frac{|A|^6}{3} + \frac{ia_1}{4}|A|^2 (AA_x^* - A^*A_x) \right\} dx, \quad (2.4)$$

and Γ is either the whole real line or a finite closed interval. In particular in the latter case all solutions approach a time-independent state corresponding to a local minimum of the free energy $F(A, A^*)$ provided F is bounded from below. However, this is not necessarily the case. In fact the lower bound on F is finite only when $|a_1| < \frac{4}{\sqrt{3}}$ and in this case Eq. (1.6) is well-posed. This result follows from the estimate

$$F \geq \int_{\Gamma} \left\{ |A_x|^2 - \mu|A|^2 - \frac{b|A|^4}{2} + \frac{|A|^6}{3} - \frac{|a_1|}{2}|A|^3|A_x| \right\} dx, \quad (2.5)$$

which in turn implies, using Young's inequality, that

$$F \geq \int_{\Gamma} \left\{ \left(1 - \frac{|a_1|}{4\delta}\right) |A_x|^2 + \left(\frac{1}{3} - \frac{|a_1|\delta}{4}\right) |A|^6 - \mu|A|^2 - \frac{b|A|^4}{2} \right\} dx \quad (2.6)$$

for all $\delta > 0$. If the domain size is finite and the coefficients of $|A_x|^2$ and $|A|^6$ are both positive in inequality 2.6 are both positive then F is bounded from below. This condition is only true when $|a_1| < \frac{4}{\sqrt{3}}$. However when $|a_1| > \frac{4}{\sqrt{3}}$, the integrand for periodic wavetrains of the form $A = R_0 \exp(ikx)$, where R_0 is a constant, reduces to

$$R_0^2 k^2 - \mu R_0^2 - \frac{b}{2} R_0^4 + \frac{R_0^6}{3} + \frac{a_1 k R_0^4}{2} \approx R_0^2 \left(k + \frac{a_1 R_0^2}{4} \right)^2 + \left(\frac{1}{3} - \frac{a_1^2}{16} \right) R_0^6$$

for large R_0 . Thus for $|a_1| > \frac{4}{\sqrt{3}}$ the free energy F of wavetrains with $k = -\frac{1}{4}a_1 R_0^2$ diverges to negative infinity as $R_0 \rightarrow \infty$ thereby permitting the existence of runaway solutions.

The situation is yet more interesting when a_2 is nonzero since no free energy then exists and the time evolution of the system need not be monotonic. Thus the presence of the terms $ia_1|A|^2 A_x$ and $ia_2 A^2 A_x^*$ in the amplitude equation changes qualitatively the evolution of the system near the pattern forming bifurcation. In particular, oscillations may now be present [29], and these may be expected near the saddle-node on the primary solution branch, where the growth rates of the amplitude and phase modes are both small and hence comparable. In the general case with nonzero a_2 , global existence of smooth solutions has only been proved for $(a_2 - a_1)^2 < 4$ [34]. Remark that for the quadratic-cubic Swift-Hohenberg equation $(a_1, a_2) = \left(\frac{4}{21\sqrt{5}}, 0\right)$ thus F is bounded from below and oscillations are absent. The latter is of course a consequence of the gradient structure of the equation.

2.2 Stationary solutions

Stationary solutions of Eq. (1.6) satisfy the equation

$$A_{xx} + i(a_1|A|^2 A_x + a_2 A^2 A_x^*) + \mu A + b|A|^2 A - |A|^4 A = 0. \quad (2.7)$$

In the following, we view this equation as a dynamical system in space. In view of the two continuous symmetries associated with translations and phase shifts the equation has two conserved quantities [27]

$$E \equiv (\mu + 2a_2L) |A|^2 + |A_x|^2 + \frac{b}{2} |A|^4 - \left[\frac{1}{3} + \frac{a_2(a_1 + a_2)}{6} \right] |A|^6, \quad (2.8)$$

$$L \equiv \frac{i}{2} (AA_x^* - A^*A_x) + \frac{a_1 + a_2}{4} |A|^4. \quad (2.9)$$

In terms of $A(x) = R(x)e^{i\phi(x)}$, where $R(x)$ and $\phi(x)$ are real-valued functions, these take the form

$$E = (\mu + 2a_2L) R^2 + (R_x^2 + R^2\phi_x^2) + \frac{b}{2} R^4 - \left[\frac{1}{3} + \frac{a_2(a_1 + a_2)}{6} \right] R^6, \quad (2.10)$$

$$L = R^2\phi_x + \frac{a_1 + a_2}{4} R^4. \quad (2.11)$$

Thus

$$R_x^2 + U = E, \quad (2.12)$$

where

$$U(R; \mu, L) \equiv \frac{L^2}{R^2} + \left(\mu + \frac{3a_2 - a_1}{2} L \right) R^2 + \frac{b}{2} R^4 + \beta R^6 \quad (2.13)$$

and $\beta \equiv \frac{(a_1 + a_2)(3a_1 - 5a_2)}{48} - \frac{1}{3}$. The problem (2.7) has thus been reduced to that of a particle of energy E in a potential U . The form of the potential depends on the integral L as well as on the bifurcation parameter μ . Thus solutions of Eq. (2.12) come in two-parameter families, specified by the values of E and L . In general the solution of Eq. (2.12) will be a periodic function of x . In view of the fact that $\phi_x = (L/R^2) + \frac{1}{4}(a_1 + a_2)R^2$, this solution corresponds to a complex amplitude $A(x)$ with two frequencies, one associated with oscillations in the amplitude $R(x)$ and the other with oscillations in the spatial phase $\phi(x)$. In the following we refer to such solutions as two frequency states, while noting that in periodic domains with finite spatial period the two frequencies must be rationally related. In the following we write $k \equiv \phi_x$ and refer to k as the wavenumber. Of particular interest are equilibria of Eq. (2.12) with $R = R_0$, where R_0 is a constant. If the associated $k \neq 0$ such a solution corresponds to a wave of constant amplitude R_0 . We call such solutions rotating waves (RW) by analogy with the corresponding solution in the time domain, cf. [35]. Likewise, periodic solutions of Eq. (2.12) with $k = 0$ will be called standing waves (SW). Both solution types are single frequency states. We mention that equilibria with $k = 0$ correspond in the original problem (2.2) to periodic wavetrains with wavenumber k_c , while equilibria with $k \neq 0$ (i.e., RW) correspond to periodic wavetrains with wavenumber $k_c + \epsilon^2 k$. In contrast, SW correspond to spatially modulated wavetrains. Finally, homoclinic and heteroclinic orbits correspond to pulses, holes, and fronts, respectively.

The notion of stability within Eq. (2.7) refers to spatial stability. In particular, the loss of stability of an equilibrium corresponds to the appearance of new steady states with an x -dependent amplitude R and phase ϕ . Such bifurcations occur at amplitudes R_0 defined by $U_R = 0$ and satisfying $U_{RR} > 0$, where

$$U_{RR} = 8k^2 + 4[b + (a_1 + a_2)k]R_0^2 + 2(a_1^2 - a_2^2 - 4)R_0^4 \quad (2.14)$$

and k is the corresponding wavenumber. To demonstrate this result, we write

$$A = (R_0 + r) \exp i(kx + \phi_0 + \psi) \quad (2.15)$$

with $|r|, |\psi| \ll 1$. The linearized system of equations governing the evolution of the perturbations r and ψ is then given by

$$\frac{d}{dx} \begin{pmatrix} r \\ s \\ \psi \\ q \end{pmatrix} = \begin{pmatrix} 0 & 1 & 0 & 0 \\ -\frac{1}{2}(U_{RR} + U_{RL}\frac{\partial L}{\partial R}) & 0 & 0 & -\frac{U_{RL}}{2}\frac{\partial L}{\partial k} \\ 0 & 0 & 0 & 1 \\ 0 & -\frac{1}{R^2}\frac{\partial L}{\partial R} & 0 & 0 \end{pmatrix} \begin{pmatrix} r \\ s \\ \psi \\ q \end{pmatrix}, \quad (2.16)$$

where the coefficients are all evaluated at $R = R_0$ and $\phi_x = k$. The associated spatial eigenvalues and eigenvectors are

$$\lambda_{1,2} = 0, \quad v_{1,2} = \begin{pmatrix} 0 \\ 0 \\ 1 \\ 0 \end{pmatrix}; \quad \lambda_{3,4} = \pm \sqrt{-\frac{U_{RR}}{2}}, \quad v_{3,4} = \begin{pmatrix} \pm \sqrt{-U_{RR}/2} \\ -U_{RR}/2 \\ -\frac{1}{R^2}\frac{\partial L}{\partial R} \\ \mp \frac{1}{R^2}\frac{\partial L}{\partial R} \sqrt{-U_{RR}/2} \end{pmatrix}.$$

The equilibrium is elliptic when $U_{RR} > 0$ and hyperbolic when $U_{RR} < 0$. The degenerate solution with $U_R = U_{RR} = 0$ is in general a saddle but can be elliptic if $U_{RRR} = 0, U_{RRRR} > 0$. Such an equilibrium is given by $R_0^2 = -\frac{b}{8\beta}$ and occurs when $b = -8(L^2\beta^3)^{1/4} < 0$ and $\mu + \frac{3a_2 - a_1}{2}L = 6(L^2\beta)^{1/2}$, where $\beta > 0$. When the energy E is increased above that for a local minimum, periodic solutions bifurcate from the elliptic equilibrium, and these correspond to quasiperiodic wavetrains whose amplitude oscillates with spatial period close to $2\pi\sqrt{2/U_{RR}}$.

We begin with the equilibria (R_0, k) . With $\phi_x \equiv k$ these satisfy the polynomial equation

$$\mu - k^2 + [b + k(a_2 - a_1)]R_0^2 - R_0^4 = 0. \quad (2.17)$$

Thus homogeneous states with $k = 0$ set in first as μ increases, followed by RW with $k \neq 0$ at $\mu = k^2$. The amplitude R_0 of these states is given by the roots R_0^\pm of this equation,

$$(R_0^\pm)^2 \equiv \frac{1}{2} \left[b' \pm \sqrt{b'^2 + 4(\mu - k^2)} \right], \quad (2.18)$$

where $b' \equiv b + k(a_2 - a_1)$. Thus when $b' \leq 0$ (the supercritical case), only the R_0^+ solution exists and it bifurcates supercritically from the trivial state at $\mu = k^2$. This solution is

temporally stable with respect to amplitude perturbations, i.e., perturbations with the same wavenumber k as the solution. When $b' > 0$ (the subcritical case), a saddle-node bifurcation occurs at $\mu_{sn}(k) \equiv k^2 - \frac{b'^2}{4}$ creating both R_0^- and R_0^+ solutions, with R_0^- unstable and R_0^+ stable. The R_0^- branch connects to the trivial state at $\mu = k^2$ via a subcritical bifurcation. When $(a_2 - a_1)^2 - 4 < 0$, the curve $\mu = \mu_{sn}(k)$ has positive curvature leading to a modest interval of bistability (figure 2.1(a)) and under this condition the global existence of solutions has been proved [34]. In contrast, when $(a_2 - a_1)^2 - 4 > 0$ the curve $\mu = \mu_{sn}(k)$ has negative curvature leading to a subcritical region that broadens rapidly with increasing wavenumber k (figure 2.1(b)). These differences are reflected in the bifurcation diagrams at fixed k shown in figure 2.2 and more dramatically in bifurcation diagrams constructed for fixed $\mu > 0$ (figures 2.3(a,b)) and $\mu < 0$ (figures 2.3(c,d)). The curves $|a_2 - a_1| = 2$ in the (a_1, a_2) plane are shown in figure 2.4 and are tangent to the curve $\beta = 0$ at the points $(a_1, a_2) = \pm(\sqrt{3}, 1)$.

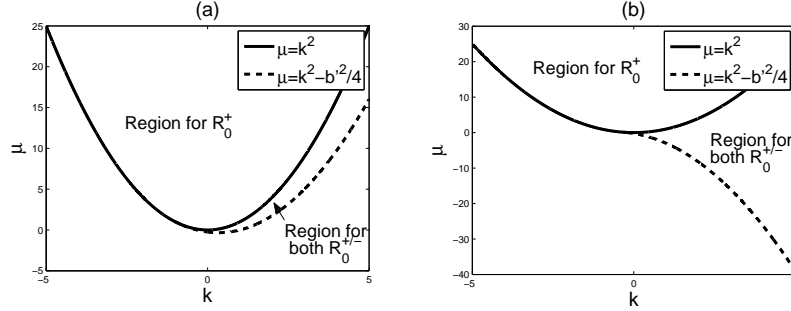


Figure 2.1: The existence region in parameter space of periodic states when (a) $a_2 - a_1 = 1$, $b = 1$, and (b) $a_2 - a_1 = 3$, $b = 1$. In both cases the state R_0^+ exists for $\mu > k^2$ if $b' < 0$, and for $\mu > k^2 - \frac{b'^2}{4}$ if $b' \geq 0$; R_0^- exists in the region between $\mu = k^2$ and $\mu = k^2 - \frac{b'^2}{4}$, but the curve $\mu = k^2 - \frac{b'^2}{4}$ in (a,b) has positive (negative) curvature depending on the sign of $(a_2 - a_1)^2 - 4$.

Different types of spatially modulated states can be determined by examining the shape of the potential $U(R; \mu, L)$. Figures 2.5 and 2.6 classify the possibilities for $L = 0$ and $L > 0$, respectively. The $L < 0$ case can be obtained from $L > 0$ by changing the signs of a_1 and a_2 . These results allow us to identify different types of homoclinic and heteroclinic orbits which play an important role in what follows. Explicit expressions for these orbits may be found in Appendix B.

Of these the heteroclinic orbits play the most important part. Owing to the shape of $U(R; \mu, L)$ such orbits necessarily involve the trivial state $A = 0$ and require the conditions $E = L = 0$. In addition we require that the potential $U(R; \mu, 0)$ has a pair of local maxima, one at $R = 0$, one at $R = R_M \neq 0$, both of the same height. This condition defines the equivalent of a Maxwell point $\mu_M = \frac{b^2}{16\beta} < 0$ for the present system, and requires $b > 0$, $\beta < 0$. The resulting heteroclinic orbit connects the trivial state $R = 0$ to a periodic wavetrain with $R_M^2 = -\frac{b}{4\beta}$ and $k_M = \frac{(a_1 + a_2)b}{16\beta}$, and hence corresponds to a front between the

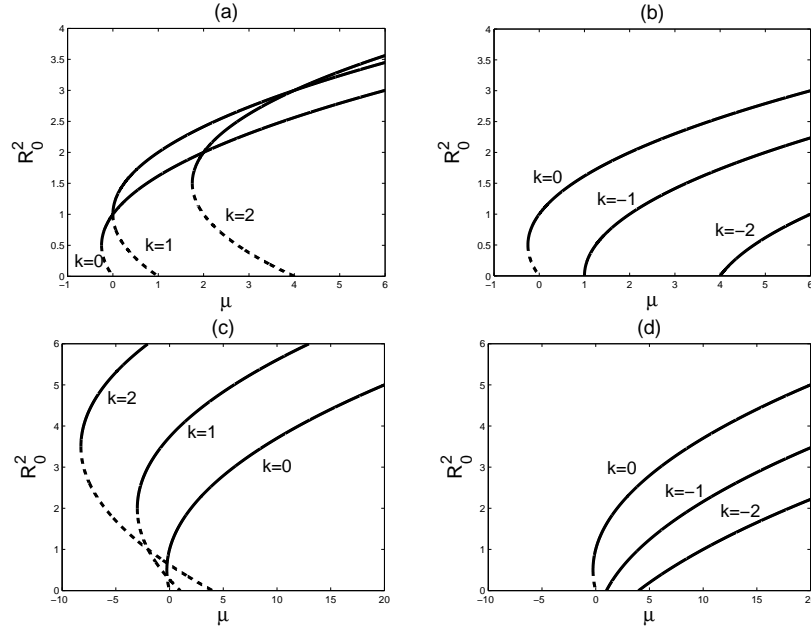


Figure 2.2: Bifurcation diagrams showing R_0^2 as a function of μ for (a,b) $|a_2 - a_1| < 2$, (c,d) $|a_2 - a_1| > 2$. Panels (a,b) are for $a_2 - a_1 = 1$, $b = 1$ and show (a) $k \geq 0$, (b) $k \leq 0$. Panels (c,d) are for $a_2 - a_1 = 3$, $b = 1$ and show (c) $k \geq 0$, (d) $k \leq 0$. Solid (dashed) lines indicate solutions that are stable (unstable) in time with respect to amplitude perturbations. These correspond to R_0^+ and R_0^- , respectively.

trivial state and a spatially periodic pattern (see figure 2.7 and Appendix B). One can check that $\mu_{sn}(k_M) \leq \mu_M < 0$ with equality when

$$a_2(a_1 + a_2) = 4. \quad (2.19)$$

It follows that if $a_2(a_1 + a_2) < 4$, then the amplitude R_M belongs to the $R_0^+(k_M)$ branch and is then referred to as R_M^+ ; if $a_2(a_1 + a_2) > 4$, the amplitude R_M belongs to the $R_0^-(k_M)$ branch and is then referred to as R_M^- . In figure 2.8, we show for comparison two different homoclinic orbits, the first homoclinic to the trivial state ($A = 0$) and the second to a nontrivial state ($A \neq 0$).

2.3 Steady state bifurcations from primary branches

From the discussion in section 2.2, we know that quasiperiodic solutions can bifurcate from the primary branch with fixed wavenumber k when the equilibrium point corresponding to the amplitude $R_0(k)$ is elliptic. The period of the associated amplitude modulation is approximately equal to $2\pi\sqrt{2/U_{RR}}$ near the original periodic state.

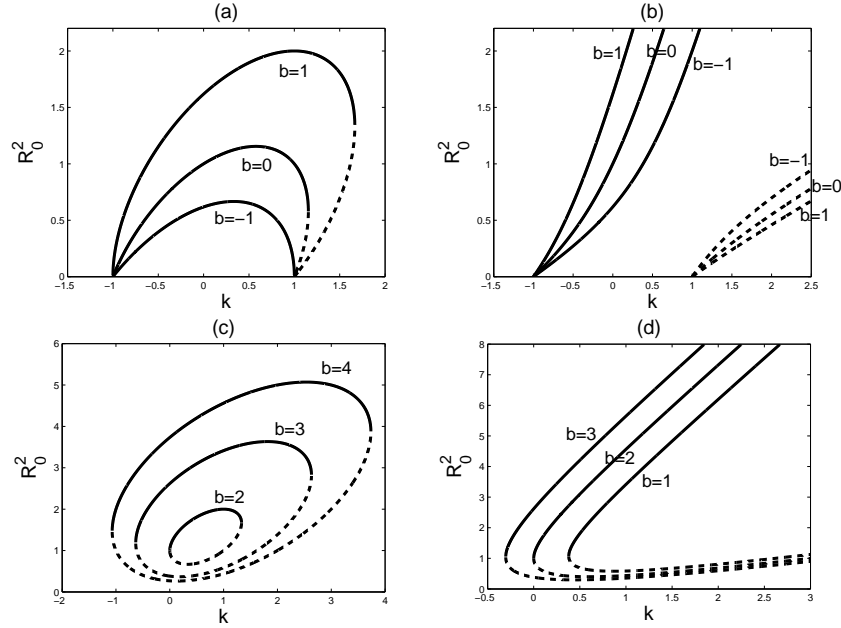


Figure 2.3: Bifurcation diagrams showing R_0^2 as a function of k when (a) $\mu = 1$, $a_2 - a_1 = 1$, (b) $\mu = 1$, $a_2 - a_1 = 3$, (c) $\mu = -1$, $a_2 - a_1 = 1$, and (d) $\mu = -1$, $a_2 - a_1 = 3$. Solid (dashed) lines indicate solutions that are stable (unstable) in time with respect to amplitude perturbations.

If the domain size is infinite, the first modulation branch occurs when $U_{RR} = 0$. To describe the initial stages of this bifurcation we fix the coefficients a_1 , a_2 , and b , and treat μ as the primary bifurcation parameter. The instability is triggered by a change in the potential U as μ varies, and takes place when U_{RR} passes through zero, subject to the requirement that k_0 , the asymptotic wavenumber at infinity, remains fixed. Thus $U = U(R; \mu, L(\mu)) \equiv \tilde{U}(R; \mu)$ and the instability sets in at

$$R_0(k)^2 = \frac{b' + 2ka_1 \pm \sqrt{(b' + 2ka_1)^2 + 4(4 + a_2^2 - a_1^2)k^2}}{4 + a_2^2 - a_1^2} > 0, \quad \mu_0 = R_0^4 - b'R_0^2 + k^2. \quad (2.20)$$

The branching direction of the stationary modulated states that result can be readily determined by a local expansion of U around (R_0, μ_0) . We write $(R, \mu) = (R_0 + \delta R, \mu_0 + \delta \mu)$ and suppose that generically $\tilde{U}_{RRR,0}\tilde{U}_{R\mu,0} \neq 0$. Thus

$$\tilde{U}(R; \mu) = \tilde{U}(R_0; \mu) + \tilde{U}_{R\mu,0}\delta\mu\delta R + \frac{\tilde{U}_{RRR,0}}{6}(\delta R)^3 + h.o.t., \quad (2.21)$$

where $\delta R = O(|\delta\mu|^{1/2})$ and the subscript 0 indicates that the quantity is evaluated at the bifurcation point. The bifurcation occurs as μ increases (decreases) provided $\tilde{U}_{RRR,0}\tilde{U}_{R\mu,0}$ is

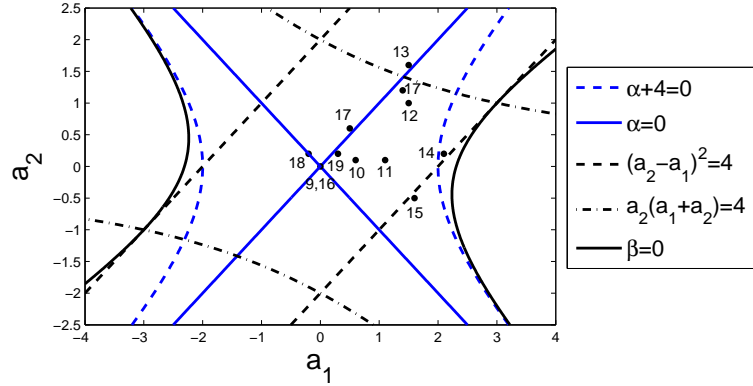


Figure 2.4: (Color online) The (a_1, a_2) plane splits into a number of regions with different behavior (see text). Black dots indicate the parameter values used in subsequent figures, with the numbers indicating the corresponding figure. The region $\beta \equiv \frac{(a_1+a_2)^2}{16} - \frac{a_2(a_1+a_2)}{6} - \frac{1}{3} < 0$ (between solid black lines) contains heteroclinic solutions between the origin and either R_0^+ (if $a_2(a_1 + a_2) < 4$) or R_0^- (if $a_2(a_1 + a_2) > 4$). The line $\alpha \equiv a_2^2 - a_1^2 = 0$ plays a role in determining the sequence of secondary bifurcations while the sign of $\alpha + 4$ plays an important role in the temporal analysis.

negative (positive); the corresponding stationary solution is given by

$$\delta R \equiv \pm \left(-\frac{2\tilde{U}_{R\mu,0}\delta\mu}{\tilde{U}_{RRR,0}} \right)^{1/2} [3\text{sech}^2(hx) - 1] + O(|\delta\mu|), \quad h \equiv \frac{1}{2} \left(-\frac{1}{2}\tilde{U}_{RRR,0}\tilde{U}_{R\mu,0}\delta\mu \right)^{1/4}, \quad (2.22)$$

which corresponds to a pulse or hole solutions according to whether $\tilde{U}_{RRR,0} > 0$ or $\tilde{U}_{RRR,0} < 0$ (see Eq. (2.21)). In the present case Eq. (2.13) together with the fact that $\tilde{U}_{RR,0} = 0$ at the bifurcation point imply that

$$\tilde{U}_{R\mu,0} = 2R_0, \quad \tilde{U}_{RRR,0} = 24R_0(b + 8\beta R_0^2). \quad (2.23)$$

Thus $\tilde{U}_{R\mu,0}$ is always positive and the bifurcated solution is a hole with branching to the right (or pulse with branching to the left) whenever $b + 8\beta R_0^2$ is negative (or positive).

When the periodic wavetrain lies at the band center, i.e., $k = 0$, the bifurcation is now located at

$$(R_0^2, \mu_0) = \left(\frac{2b}{4 + a_2^2 - a_1^2}, \frac{2b^2(a_1^2 - a_2^2 - 2)}{(4 + a_2^2 - a_1^2)^2} \right) \quad (2.24)$$

and hence lies close to the saddle-node $(R^2, \mu) = (b/2, -b^2/4)$ whenever $|a_1^2 - a_2^2| \ll 1$, $b > 0$. Since $\tilde{U}_{RRR,0}$ is now equal to $-8R_0^3[2 + a_2(a_1 + a_2)]$ it follows that the bifurcating solution is a hole branching to the right when $2 + a_2(a_1 + a_2) > 0$, or a pulse branching to the left when $2 + a_2(a_1 + a_2) < 0$.

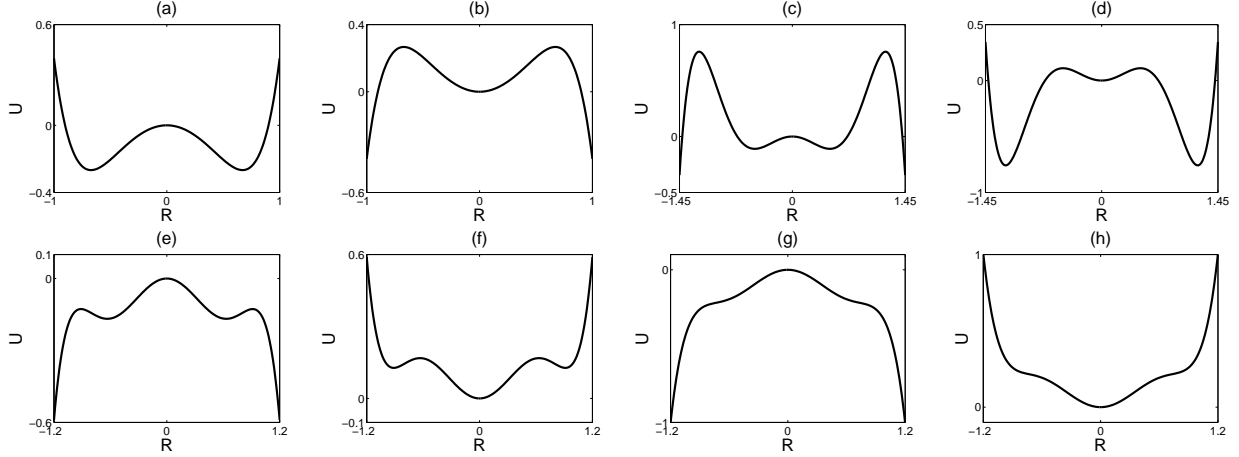


Figure 2.5: The potential $U(R; \mu, L)$ when $L = 0$, drawn reflected in $R = 0$. (a) $\mu = -1$, $b = 1$, $\beta = 0.9$ ($\mu < 0$, $\beta > 0$). (b) $\mu = 1$, $b = -1$, $\beta = -0.9$ ($\mu > 0$, $\beta < 0$). (c) $\mu = -1$, $b = 5$, $\beta = -1$ ($\mu, \beta < 0$ and $b > 4\sqrt{\mu\beta}$). (d) $\mu = 1$, $b = -5$, $\beta = 1$ ($\mu, \beta > 0$ and $b < -4\sqrt{\mu\beta}$). (e) $\mu = -1$, $b = 3.7$, $\beta = -1$ ($\mu, \beta < 0$ and $2\sqrt{3\mu\beta} < b < 4\sqrt{\mu\beta}$). (f) $\mu = 1$, $b = -3.7$, $\beta = 1$ ($\mu, \beta > 0$ and $-4\sqrt{\mu\beta} < b < -2\sqrt{3\mu\beta}$). (g) $\mu = -1$, $b = 3.3$, $\beta = -1$ ($\mu, \beta < 0$ and $b < 2\sqrt{3\mu\beta}$). (h) $\mu = 1$, $b = -3.3$, $\beta = 1$ ($\mu, \beta > 0$ and $b > -2\sqrt{3\mu\beta}$).

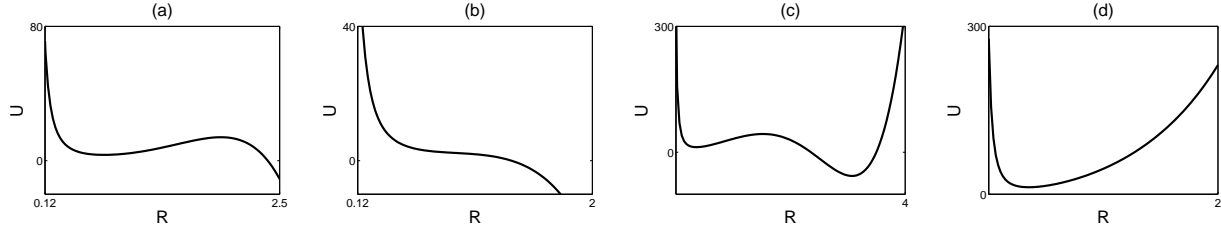


Figure 2.6: The potential $U(R; \mu, L)$ when $L = 1$. (a) $\mu = 1$, $b = 4$, $a_1 = 1$, $a_2 = 1$, ($\beta < 0$, $R_{0,-}^2 > 0$, $R_{0,-}^4 (\mu' + bR_{0,-}^2/2) > 2L^2$). (b) $\mu = 1$, $b = -1$, $a_1 = 1$, $a_2 = 1$, ($\beta < 0$ and at least one of the other conditions in (a) is violated). (c) $\mu = 40$, $b = -20$, $a_1 = 4$, $a_2 = 0.5$ ($\beta > 0$, $b < 0$, $0 < 32\beta\mu' < 3b^2$, $R_{0,+}^4 (\mu' + b'R_{0,+}^2/2) < 2L^2$). (d) $\mu = 40$, $b = 5$, $a_1 = 4$, $a_2 = 0.5$ ($\beta > 0$ and at least one of the other conditions in (c) is violated). Here $\mu' \equiv \mu + \frac{3a_2 - a_1}{2}L$ and $R_{0,\pm}^2 \equiv \frac{-b \pm \sqrt{b^2 - 32\beta\mu'/3}}{8\beta}$.

The bifurcation also sets in at $R = 0$ when $k = 0$ which the previous discussion is invalid. We expect a bifurcation to periodic RW together with pulse states. Suppose that $\mu = O(\epsilon^2)$, where $\epsilon \ll 1$. The RW take the form

$$A = \epsilon R \exp(ikx) + O(\epsilon^2), \quad (2.25)$$

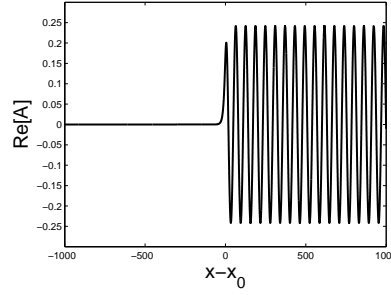


Figure 2.7: The profile $\text{Re}A(x)$ from Appendix B, Eq. (B.1), of the heteroclinic solution at $\mu = \mu_M \approx -0.0146$ when $b = 1$, $a_1 = 1$, and $a_2 = 6$.

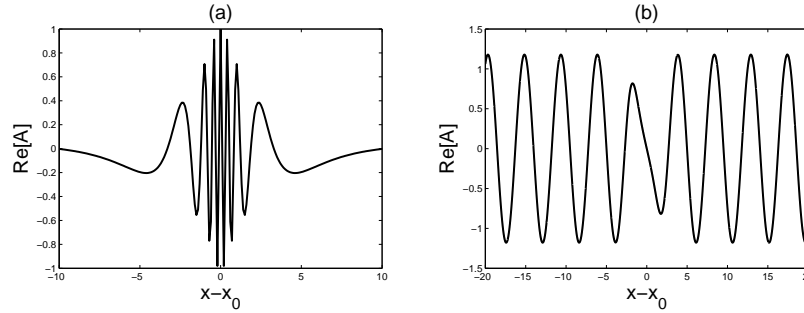


Figure 2.8: (a) Homoclinic solution to $A = 0$ at $\mu = 0$ when $b = -2$, $\beta = 1$ and $a_1 + a_2 = 64$ (Appendix B, Eq. (B.5)). (b) Homoclinic solution to a nonzero equilibrium corresponding to a rotating wave at $\mu = -1$ with $R_0 \approx 1.1791$ and $k = -1.3903$ when $b = 3.5$, $a_1 = a_2 = 2$ (Appendix B, Eq. (B.6)).

where $k = O(\epsilon)$, while the pulse states take the different form

$$A = \epsilon R(X, \epsilon) \exp i\epsilon\phi(X, \epsilon) + O(\epsilon^2), \quad (2.26)$$

where $X \equiv \epsilon x$ is a slow spatial scale. Substituting this ansatz into Eq. (2.7) with $R(X, \epsilon) = R^{(0)}(X) + \epsilon R^{(1)}(X) + \dots$, $\phi(X, \epsilon) = \phi^{(0)}(X) + \epsilon\phi^{(1)}(X) + \dots$, $\mu = \epsilon^2\mu_2$, we obtain at $O(\epsilon^3)$

$$R_{XX}^{(0)} + \mu_2 R^{(0)} + bR^{(0)3} = 0 \quad (2.27)$$

and at $O(\epsilon^4)$

$$\phi_X^{(0)} = -\frac{1}{4}(a_1 + a_2)R^{(0)2} \neq 0. \quad (2.28)$$

Thus RW and pulse states bifurcate simultaneously from $A = 0$ at $\mu = 0$, much as in the Swift-Hohenberg equation. However, owing to the absence of pinning, there is a one-parameter family of pulse solutions, parametrized by an arbitrary phase. In finite domains, however large, the modulated solutions are expected to bifurcate from the RW at small but finite amplitude.

If the domain size is finite, boundary conditions select a discrete set of branches from the continuous family of such solutions parametrized by the constants of integration E and L . Since Eq. (2.7) is spatially reversible, solutions satisfying periodic boundary conditions (PBC) on a domain of period 2Γ satisfy boundary conditions

$$\operatorname{Re}[A_x] = 0, \quad \operatorname{Im}[A] = 0 \quad (2.29)$$

on a domain of length Γ , we focus in the following on stationary solutions satisfying the boundary conditions (2.29). We mention that more generally periodic boundary conditions on $u(x)$, ie., $u(x + 2\Gamma) = u(x)$ for all x , imply the boundary condition

$$A(\epsilon^2(x + 2\Gamma)) \exp 2ik_c\Gamma = A(\epsilon^2x), \quad (2.30)$$

for all x on the amplitude A .

In the following we plot bifurcation diagrams showing the solution amplitude measured by the quantity $\| \cdot \|_{H_1}$ as a function of the parameter μ , where

$$\|A\|_{H_1} \equiv \left(\frac{1}{\Gamma} \int_0^\Gamma |A_x|^2 + |A|^2 dx \right)^{1/2}. \quad (2.31)$$

Bifurcations from the $k = 0$ primary branch

Since the $k = 0$ branch is the first of the (subcritical) primary branches to set in for $b > 0$ as μ increases, we present in figures 2.9–2.15 the $k = 0$ branch together with a number of secondary branches, computed using the continuation software AUTO [36]. These consist of states with spatially varying amplitude $R(x)$ and phase $\phi(x)$ and bifurcate from the $k = 0$ branch in secondary bifurcations we refer to as Eckhaus bifurcations (see section 2.4). These secondary branches either terminate on the same $k = 0$ branch, or do so on a different primary branch ($k \neq 0$) or not at all. Figure 2.9 reveals that when $a_1 = a_2 = 0$ [37] the secondary branches originate and terminate on the same $k = 0$ primary branch. Each branch can be labeled by a pair of integers (n, m) specifying the number of half wavelengths of $R(x)$ and $\phi(x)$ within the domain Γ . Solutions with $n = 1$ (the first secondary branch) bifurcate nearest to the primary bifurcation at $\mu = 0$ and terminate nearest to the saddle-node. Figure 2.10(a) shows typical results when $a_1 a_2 \neq 0$. In this case, unless b is too small (figure 2.10(b)), the $n = 1$ branch no longer terminates on the $k = 0$ primary branch but terminates instead on the primary branch with $k = \pi/\Gamma$. However, since an $n = 1$ Eckhaus instability near the $k = 0$ saddle-node remains, a new $n = 1$ branch bifurcates from the $k = 0$ branch near the saddle-node bifurcation and this time extends monotonically to larger amplitudes. States of this type represent a defect in the original wavetrain with wavenumber k_c that may be located either in the center of the domain or at its boundary, e.g. figure 2.12(b), and we refer to them as defect states [38]. These states resemble those familiar from studies of the Eckhaus instability for the supercritical Ginzburg-Landau equation [23, 24] but are present here even for $k = 0$. The figures show that the defect states bifurcate from the $k = 0$ branch either

below or above the saddle-node, depending on parameters; for increasingly negative b the bifurcation point moves to larger and larger amplitude, leaving behind stable supercritical periodic states. The termination points of the smaller amplitude secondary branches may likewise lie below or above the saddle-node. Figures 2.11–2.13 show that these basic effects of the presence of the coefficients a_1, a_2 persist to other values provided $a_1^2 - a_2^2 - 4 < 0$ (see Eq. (2.14) with $k = 0$). In contrast, when $a_1^2 - a_2^2 - 4 > 0$ (figures 2.14–2.15) the secondary branches are all strongly subcritical and all terminate on branches with $k \neq 0$. The curves $a_1^2 - a_2^2 - 4 = 0$ are also shown in figure 2.4.

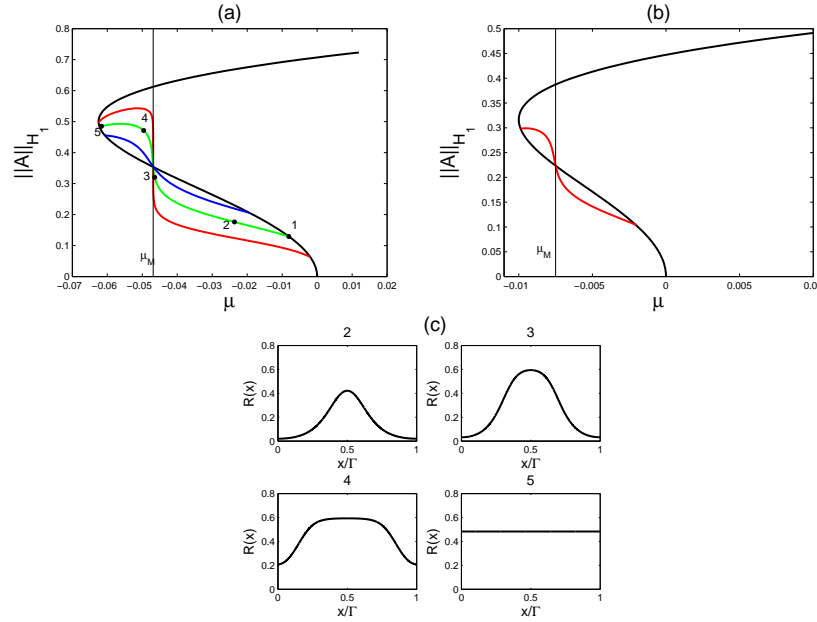


Figure 2.9: (Color online) Bifurcation diagrams for subcritical stationary solutions with $k = 0$ with several secondary branches of nonuniform states satisfying boundary conditions (2.29). Parameters: $a_1 = 0$, $a_2 = 0$, $\Gamma = 16\pi$. (a) $b = 0.5$. (b) $b = 0.2$. (c) Sample profiles $R(x)$ along the branch bifurcating from point 1 in (a).

It will have been noticed that all secondary branches bifurcating from R_0^- , except those bifurcating close to the saddle-node, develop a protosnaking region with a sudden increase of H_1 norm located near the Maxwell point $\mu_M = \frac{b^2}{16\beta} < 0$. This point plays a fundamental role in understanding the behavior shown in figures 2.9–2.15. We have seen that at $\mu = \mu_M$, a heteroclinic connection between $A = 0$ and $A = R_M \exp(ik_M x)$ is present (figure 2.7). Although one might expect the presence of homoclinic snaking extending over a finite interval whenever $k_M \neq 0$, this is not the case here owing to the absence of a coupling between the front and the spatial oscillations with wavenumber k_M . As a result the snaking region collapses to a single point $\mu = \mu_M$. Despite this, the presence of this point determines the branch on which the secondary branches involved terminate. This is because the presence of the heteroclinic orbit at $\mu = \mu_M$ determines the wavenumber k_M , and this wavenumber

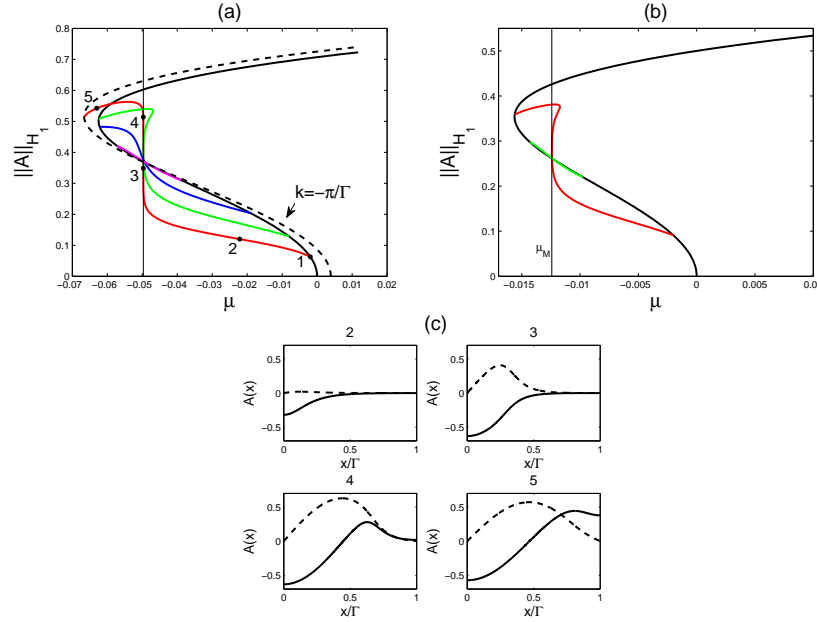


Figure 2.10: (Color online) Bifurcation diagrams for subcritical stationary solutions with $k = 0$ with several secondary branches of nonuniform states satisfying boundary conditions (2.29). Parameters: $a_1 = 0.6$, $a_2 = 0.1$, $\Gamma = 16\pi$. (a) $b = 0.5$. (b) $b = 0.25$. (c) Sample profiles of $\text{Re}A(x)$ (solid line) and $\text{Im}A(x)$ (dashed line) along the branch bifurcating from point 1 in (a). This branch terminates on a primary branch with $k = \pi/\Gamma \approx k_M$.

in turn determines the primary branch on which the branches terminate. For example, in figure 2.9, the selected wavenumber $k_M = 0$ and all secondary branches terminate on the $k = 0$ branch from which they first bifurcated. In figure 2.10, the wavenumber $k_M \approx -0.0696$ and indeed the $n = 1$ branch no longer terminates on a $k = 0$ branch and instead terminates on a primary branch with wavenumber closest to k_M that is compatible with the imposed boundary conditions (2.29) and domain length Γ , viz. $|k| = \pi/\Gamma = 0.0625$ ($m = 1$). The secondary branches with $n \geq 2$ do not come sufficiently close to forming the heteroclinic orbit and so continue to terminate on the $k = 0$ branch. In figures 2.11 and 2.12 the corresponding wavenumbers are $k_M = -0.1424$ ($m = 2$) and $k_M = -0.2174$ ($m = 3$) and these wavenumbers determine the type of change that must take place before the different secondary solutions can approach the heteroclinic connection. These changes are illustrated clearly in the lower panels in figure 2.11 which show that the branches bifurcating at points 1 ($n = 1$) and 2 ($n = 2$) both become $m = 2$ states despite bifurcating at different locations from the $k = 0$ branch. Since phase has to be added along these secondary branches for these changes to take place it follows that the quantity L in the potential $U(R; \mu, L)$ must either pass through zero in order that the phase may jump by π , or remain identically zero so that multiple phase changes can take place.

In figures 2.9–2.12 the heteroclinic orbit that forms at μ_M connects the states $R = 0$ and

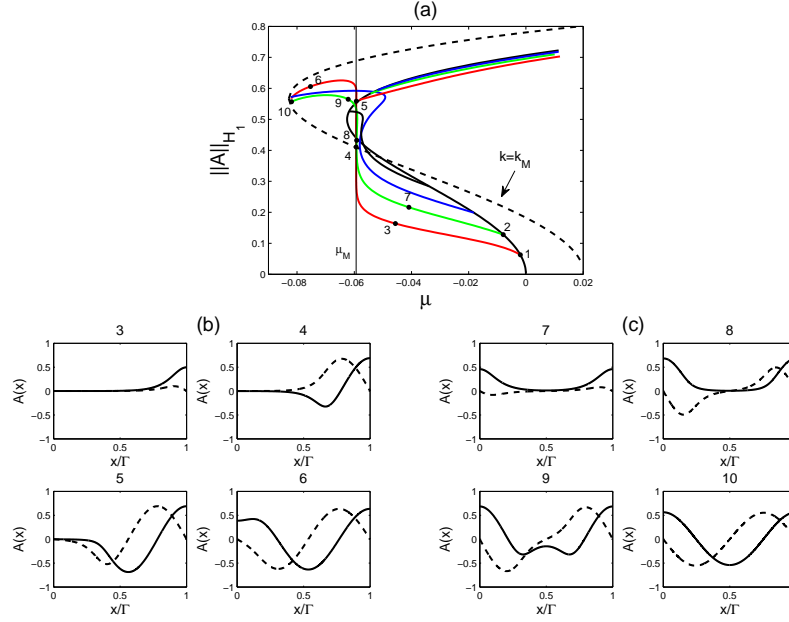


Figure 2.11: (Color online) (a) Bifurcation diagram for subcritical stationary solutions with $k = 0$ with several secondary branches of nonuniform states satisfying boundary conditions (2.29). The first three secondary branches terminate on a primary branch with $k \neq 0$. (b,c) Sample profiles of $\text{Re}A(x)$ (solid line) and $\text{Im}A(x)$ (dashed line) along the branch bifurcating from points 1 and 2, respectively, showing that both branches terminate on a primary branch with wavenumber $k = 2\pi/\Gamma \approx k_M$. Parameters: $b = 0.5$, $a_1 = 1.1$, $a_2 = 0.1$, $\Gamma = 16\pi$.

R_M^+ . In figure 2.13 it connects instead the states $R = 0$ and R_M^- , i.e., a stable state $R = 0$ to an amplitude-unstable state R_M^- . In such a situation the associated front will move, allowing the stable state to invade the unstable state. For the cases $a_1^2 - a_2^2 - 4 > 0$ with $(a_1 - a_2)^2 - 4 < 0$ (figure 2.14) and $a_1^2 - a_2^2 - 4 < 0$ with $(a_1 - a_2)^2 - 4 > 0$ (figure 2.15) the predictions $\mu_M \approx -0.197$, $R_M^+ \approx 1.255$, $k_M \approx -0.906$ (figure 2.14) and $\mu_M \approx -0.0941$, $R_M^+ \approx 0.8677$, $k_M \approx -0.207$ (figure 2.15) continue to agree well with the numerical computations shown in the figures. Thus the wavenumber selection process via the formation of a heteroclinic connection continues to determine the termination points of the secondary branches even when the $k \neq 0$ primary branches are highly subcritical.

The above bifurcation diagrams have all been obtained for a domain of one given length, $\Gamma = 16\pi$. When Γ is increased, the termination points of the secondary branches must switch to branches containing extra wavelengths of the Maxwell wavelength $\lambda_M = 2\pi/k_M$. The mechanism whereby this occurs has been studied in detail in gradient systems [38, 37]. Similar behavior has also been found in nongradient systems such as the partial differential equations describing natural doubly diffusive convection [38].

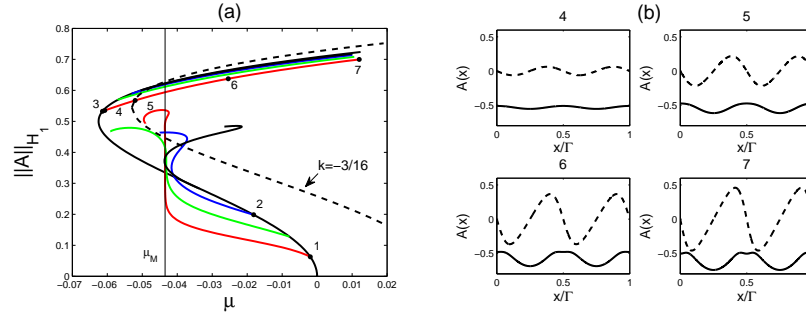


Figure 2.12: (Color online) (a) Bifurcation diagram for subcritical stationary solutions with $k = 0$ with several secondary branches of nonuniform states satisfying boundary conditions (2.29). Parameters: $b = 0.5$, $a_1 = 1.5$, $a_2 = 1.0$, $\Gamma = 16\pi$. Branches bifurcating at points 1 and 2 in (a) terminate at the same wavenumber, $k = -3/16$. (b) Sample profiles of $\text{Re}A(x)$ (solid line) and $\text{Im}A(x)$ (dashed line) along the defect branch bifurcating at point 3 in (a).

Bifurcations from the $k = 1$ primary branch

In figures 2.16 and 2.17 we show the corresponding results for the primary $k = 1$ bifurcation. As shown in Appendix C when $a_1 = a_2 = 0$ two steady state branches bifurcate together from $\mu = 1$. The prediction follows from a careful analysis of the symmetry of the problem when periodic boundary conditions are imposed and is confirmed in figure 2.16. The larger amplitude branch consists of RW states of the form $A = R_0 \exp i(x + \phi_0)$, where R_0 is a constant, while the smaller amplitude branch consists of SW states of the form $A = R(x) \exp i\phi_0$, where $R(x)$ is x -dependent and near $\mu = 1$ resembles $\cos x$. Here ϕ_0 is an arbitrary phase. Both states of course satisfy periodic boundary conditions in space, and can be translated in x so as to satisfy the imposed boundary conditions (2.29). Figure 2.16(a) also shows that the RW and SW branches may be connected by a secondary branch of time-independent states, of the form $A = R(x) \exp i(\phi(x) + \phi_0)$, while other secondary branches bifurcating from the RW branch develop into defect states and extend monotonically to large amplitude (figure 2.16(d)). Figure 2.16 shows that the former are periodic since both $R(x)$ and $\phi(x)$ oscillate with same frequency, while along the latter $R(x)$ and $\phi(x)$ oscillate with different frequencies and the solutions appear quasiperiodic.

Once either a_1 or a_2 is nonzero, a similar analysis shows that the RW branch splits into two distinct rotating waves RW^\pm both of which continue to bifurcate simultaneously from $\mu = 1$. In addition when $0 < |k(a_1 + a_2)| < |b|$ the SW state turns into a mixed mode (MW) state that bifurcates from the $A = 0$ state simultaneously with the RW^\pm . The MW are no longer present as a primary branch once $|k(a_1 + a_2)| > |b|$ (see Appendix C). Figure 2.17(a) shows the RW^\pm in the subcritical case when $a_1 = 0.6$, $a_2 = 0.8$, $b = 0.5$. Thus in this case no MW are present as a primary branch although the figure reveals the presence of two types of finite amplitude secondary branches resembling states of this type. The first type bifurcates from the $k = 1$ RW^+ branch below the saddle-node and terminates on a primary branch

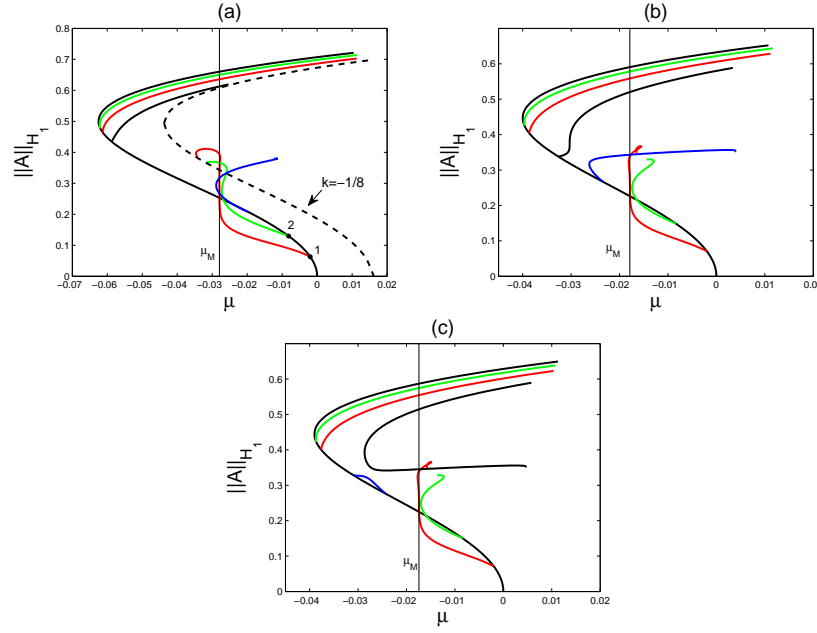


Figure 2.13: (Color online) Bifurcation diagrams for subcritical stationary solutions with $k = 0$ with several secondary branches of nonuniform states satisfying boundary conditions (2.29) showing the reconnection process that takes place with decreasing b . Branches bifurcating at points 1 and 2 in (a) terminate at the same wavenumber, $k = -1/8$. Parameters: $a_1 = 1.5$, $a_2 = 1.6$, $\Gamma = 16\pi$. (a) $b = 0.5$. (b) $b = 0.4$. (c) $b = 0.395$.

with $k \neq 0, 1$. The second type represents defect states that extend to large amplitudes without termination. These secondary branches are outside of the range of validity of the weakly nonlinear theory in Appendix C but are found in a higher codimension analysis of the $a_1 = a_2 = 0$ degeneracy [39]. Only the defect states are present in the supercritical case (figure 2.17(b), $a_1 = 1.4$, $a_2 = 1.2$, $b = -0.5$).

In the special case $a_1 + a_2 = 0$ the MW states degenerate into SW and bifurcate from $\mu = 1$ together with the RW^\pm . Figure 2.18 shows an example of the resulting bifurcation diagram. Finally, figure 2.19 shows an example with $0 < |k(a_1 + a_2)| < |b|$ in which the MW are present and bifurcate together with the RW^\pm . However, at larger amplitudes the two sets of branches behave quite differently, with the MW terminating on RW^- .

Theoretical interpretation

It is possible to develop, to a certain extent, a theoretical understanding of the above results. The understanding is based on the presence of the conserved quantities E and L , and the shape of the potential $U(R; \mu, L)$ (Eqs. (2.10)–(2.13)). With boundary conditions (2.29), secondary bifurcations to two-frequency states can only occur on a primary branch

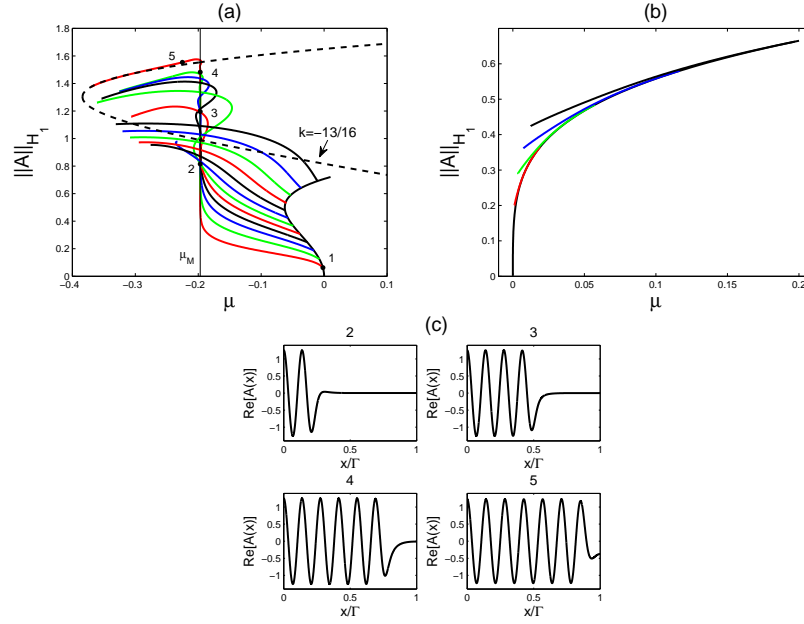


Figure 2.14: (Color online) Bifurcation diagrams for (a) subcritical and (b) supercritical stationary solutions with $k = 0$ with several secondary branches of nonuniform states satisfying boundary conditions (2.29). All secondary branches terminate at nonzero wavenumber. Parameters: $a_1 = 2.1$, $a_2 = 0.2$, $\Gamma = 16\pi$. (a) $b = 0.5$. (b) $b = -0.01$. (c) Sample profiles of $\text{Re}A(x)$ along the branch bifurcating from point 1 in (a).

at locations where

$$U_{RR} = \frac{2\pi^2 n^2}{\Gamma^2}, \quad n \in \mathbb{N}. \quad (2.32)$$

Explicit expression for U_{RR} can be found in Eq. (2.14). Since stationary solutions are determined up to translation in x and phase rotation by the integrals E and L , the behavior of a branch of two-frequency states is determined by a set of implicit functions containing E and L with μ as a bifurcation parameter. These relations capture the requirement that an integer number of half-wavelengths of both $R(x)$ and $\phi(x)$ fit in the domain Γ and take the form

$$\frac{\Gamma}{n} = \int_{R_{\min}}^{R_{\max}} \frac{dR}{\sqrt{E - U(R; \mu, L)}}, \quad n \in \mathbb{N}; \quad (2.33)$$

$$\frac{m\pi}{n} = \int_{R_{\min}}^{R_{\max}} \frac{L/R^2 - \frac{a_1 + a_2}{4} R^2}{\sqrt{E - U(R; \mu, L)}} dR, \quad m \in \mathbb{Z}. \quad (2.34)$$

Here R_{\min} and R_{\max} are the roots of $E = U(R; \mu, L)$ corresponding to the turning points of the trajectory in the potential. Thus each branch of two-frequency states is determined by a pair of integers n and m . In particular, on the primary $k = 0$ branch, the secondary

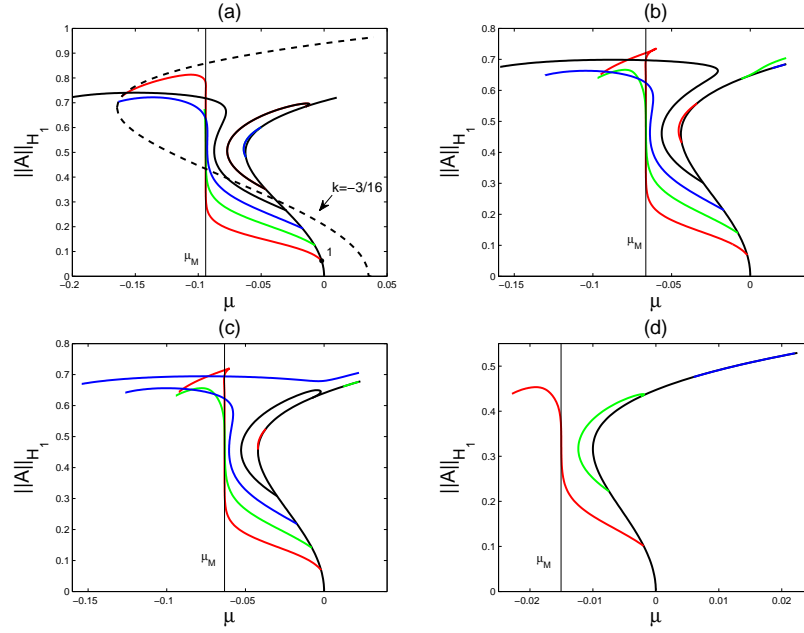


Figure 2.15: (Color online) Bifurcation diagrams for subcritical stationary solutions with $k = 0$ with several secondary branches of nonuniform states satisfying boundary conditions (2.29). Some secondary branches terminate on the $k = 0$ primary branch. Parameters: $a_1 = 1.6$, $a_2 = -0.5$, $\Gamma = 16\pi$. (a) $b = 0.5$. (b) $b = 0.42$. (c) $b = 0.41$. (d) $b = 0.2$.

bifurcation points satisfy

$$U_{RR} = 4bR_0^2 + 2(a_1^2 - a_2^2 - 4)R_0^4 = 2\pi^2 n^2 / \Gamma^2, \quad (2.35)$$

cf. Eq. (2.14). Thus in the supercritical case ($b < 0$), $U_{RR} < 0$ when $a_1^2 - a_2^2 - 4 \leq 0$ and no secondary bifurcations are present. However, if $a_1^2 - a_2^2 - 4 > 0$ the quantity U_{RR} becomes positive at sufficiently large R triggering secondary bifurcations. In contrast, in the subcritical case ($b > 0$) U_{RR} increases monotonically with R_0 provided $a_1^2 - a_2^2 - 4 \geq 0$, and consequently secondary bifurcations for each n appear exactly once along the branch. However, when $a_1^2 - a_2^2 - 4 < 0$ U_{RR} first increases with R_0 but then decreases. When $a_2^2 - a_1^2 = 0$, $U_{RR} \geq 0$ along the whole R_0^- branch; if $-4 < a_2^2 - a_1^2 < 0$ the region where $U_{RR} \geq 0$ extends above the saddle-node, but it shrinks below the saddle-node if $a_2^2 - a_1^2 > 0$. If $a_2^2 - a_1^2$ is so large that the maximum of U_{RR} falls below π^2 / Γ^2 , no bifurcation point is present. These results are reflected in the properties of figures 2.9–2.15. In the case $a_1^2 - a_2^2 < 4$, if we increase the domain size Γ , the number of bifurcation points scales as Γ . The bifurcation points accumulate near $U_{RR} = 0$, i.e., at $R_0^2 = 0$ and $R_0^2 = \frac{2b}{4+a_2^2-a_1^2}$. If we let μ_n be the n th bifurcation point in the sequence that accumulates at $R_0 = 0$ when Γ is large (i.e., at $\mu = 0$), then the μ_n scale as n^2 / Γ^2 and a similar scaling holds at the other accumulation point unless this point coincides with the saddle-node. In the latter case $a_1^2 = a_2^2$ and the

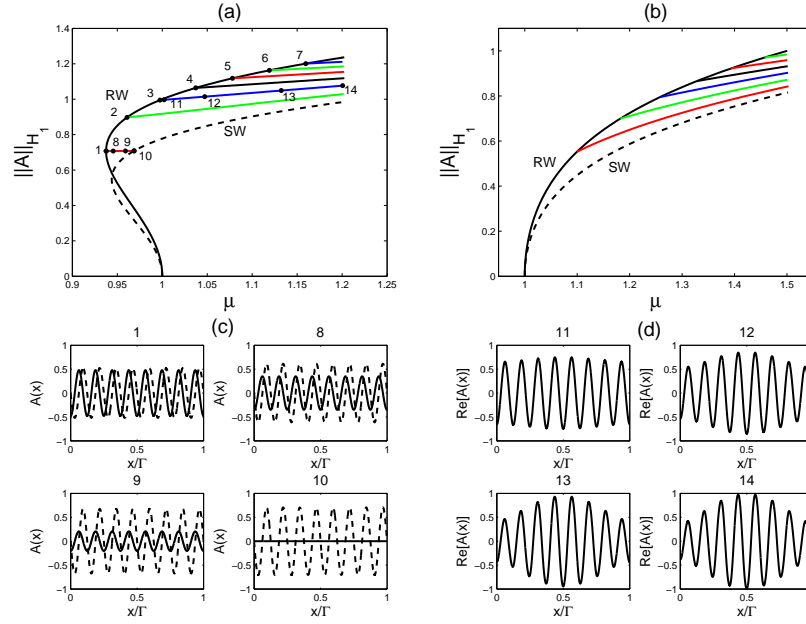


Figure 2.16: (Color online) Bifurcation diagrams for (a) subcritical and (b) supercritical stationary solutions with $k = 1$ with several secondary branches of nonuniform states satisfying boundary conditions (2.29). (c) Sample profiles of $\text{Re}A(x)$ (solid line) and $\text{Im}A(x)$ (dashed line) along the branch extending between points 1 and 10 in panel (a). (d) Sample profiles of $\text{Re}A(x)$ along the secondary branch bifurcating from the RW branch at point 3 in panel (a). The behavior along the branches bifurcating from points 2 and 4–7 is qualitatively similar to (d). Parameters: $a_1 = 0$, $a_2 = 0$, $\Gamma = 16\pi$. (a) $b = 0.5$. (b) $b = -0.5$.

distance $\delta\mu_n$ from the saddle-node scales as n^4/Γ^4 . Note that since the integer n represents the mode number, the accumulation point is reached in the limit $n \rightarrow 1$, with n/Γ , $n = 1$, representing the smallest wavenumber allowed by the boundary conditions. Such scaling laws are also found in the Swift-Hohenberg equation, and arise in studies of natural doubly diffusive convection as well [38]. As shown in Appendix D, the direction of branching of the resulting quasiperiodic states is readily computable and the predictions therein agree well with our numerical computations.

When $k \neq 0$ the conditions (2.34) provide implicit relations that determine the locations of bifurcation points. The integrals can be evaluated in terms of Jacobi elliptic functions, and the results determine the variation of E and L with the parameter μ along the secondary branch. Each branch is characterized by the integer n which is constant along the branch. This is not true for the integer m , however, which is in general only piecewise constant along the branch. This is a consequence of phase jumps that may take along place along the branch. These occur when R passes through zero at some $x \in (0, \Gamma)$ and require that

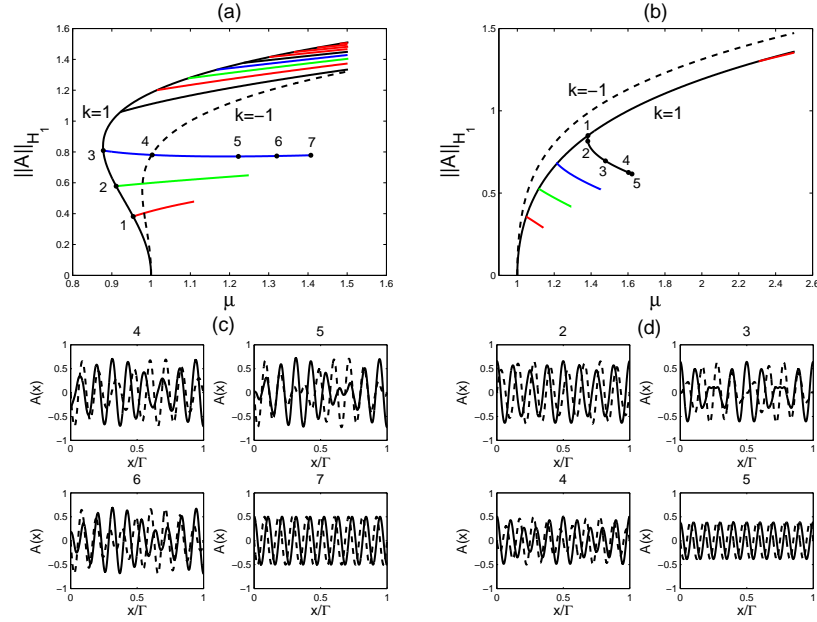


Figure 2.17: (Color online) Bifurcation diagrams for (a) subcritical and (b) supercritical stationary solutions with $k = 1$ (RW⁺) and $k = -1$ (RW⁻) together with several secondary branches of nonuniform states satisfying boundary conditions (2.29) on a domain of length $\Gamma = 16\pi$. Parameters: (a) $b = 0.5$, $a_1 = 0.6$, and $a_2 = 0.8$. (b) $b = -0.5$, $a_1 = 1.4$, and $a_2 = 1.2$. (c) Sample profiles of $\text{Re}A(x)$ (solid line) and $\text{Im}A(x)$ (dashed line) along the branch in (a) bifurcating at point 3 showing a gradual change of wavenumber between points 3 and 7. $\text{Im}A(x)$ oscillates $\frac{\pi}{2}$ out of phase with $\text{Re}A(x)$. Similar wavenumber changes occur along the branches in (a) bifurcating at points 1 and 2. (d) Sample profiles of $\text{Re}A(x)$ (solid line) and $\text{Im}A(x)$ (dashed line) along the branch bifurcating at point 1 in (b) showing a gradual change of wavenumber between points 1 and 5.

simultaneously $L = 0$. The phase jump is determined by writing

$$\int_{R_{\min}}^{R_{\max}} \frac{LdR}{R^2\sqrt{E-U}} = \int_{R_{\min}}^{R_*} \frac{LdR}{R^2\sqrt{E-U}} + \int_{R_*}^{R_{\max}} \frac{LdR}{R^2\sqrt{E-U}}, \quad (2.36)$$

and taking $R_* = O(|L|^p)$, $1/2 < p < 1$. The integral from R_* to R_{\max} ($= O(1)$) is $O(|L|/R_*)$ and so vanishes in the limit $L \rightarrow 0$. The first integral dominates because $R_{\min} = |L|/\sqrt{E} + o(|L|)$ as $L \rightarrow 0$, $E = O(1)$, and $U - L^2/R^2 = O(R^2) = o(L^2/R^2)$ in $R_{\min} < R < R_*$. Thus

$$\lim_{L \rightarrow 0} \int_{R_{\min}}^{R_*} \frac{LdR}{R^2\sqrt{E-U}} = \text{sgn}(L) \int_1^\infty \frac{dr}{r^2\sqrt{1-1/r^2}} = \text{sgn}(L) \frac{\pi}{2}, \quad (2.37)$$

where $\text{sgn}(L)$ denotes the sign of L along the branch before it reaches 0. Thus the total change of phase over the domain Γ as L crosses zero is $-\text{sgn}(L)n\pi$. The phase remains

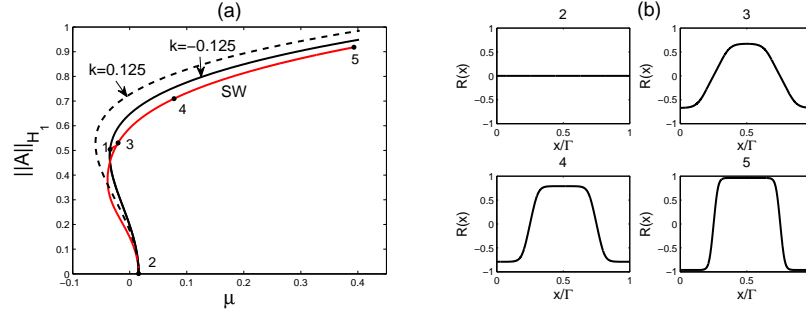


Figure 2.18: (Color online) (a) Bifurcation diagram showing the simultaneous bifurcation at $\mu = \frac{1}{64}$ of an SW branch and a pair of RW branches with $k = \pm 0.125$. A secondary branch of spatially modulated states connects the SW and RW⁻ branches between points 1 and 3. (b) Sample profiles of $R(x)$ along the SW branch. Parameters: $b = 0.5$, $a_1 = -0.2$, $a_2 = 0.2$, $\Gamma = 16\pi$.

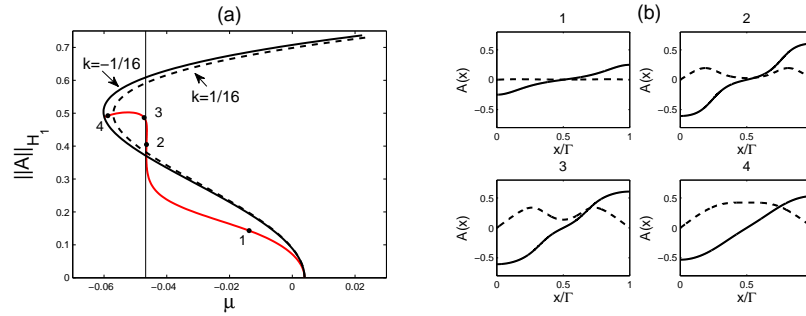


Figure 2.19: (Color online) (a) Bifurcation diagram showing the simultaneous bifurcation at $\mu = \frac{1}{256}$ of a branch of two-frequency states (MW: red (gray) curve) undergoing protosnaking and a pair of branches of periodic states RW[±] with $k = \pm \frac{1}{16}$. The two-frequency states terminate on RW⁻. (b) Sample profiles of $\text{Re}A(x)$ (solid line) and $\text{Im}A(x)$ (dashed line) along the MW branch in (a). Parameters: $b = 0.5$, $a_1 = 0.3$, $a_2 = 0.2$, $\Gamma = 16\pi$.

constant unless another phase jump takes place. It follows from Eq. (2.34b) that

$$\int_0^{R_{\max}} \frac{(a_1 + a_2)R^2}{4\sqrt{E - U}} dR = \pi \left[\frac{\text{sgn}(L)_0}{2} - \frac{m}{n} \right]. \quad (2.38)$$

This relation constrains greatly the phase jumps that may occur along the secondary branches and in particular the allowed interconnections among the primary branches. In particular, in the special case $a_1 = -a_2$, the necessary condition for a phase jump to take place is $2m = \text{sgn}(L)n$. Thus if the primary branch has nonzero wavenumber $k = \frac{m\pi}{\Gamma}$ the condition $U_{RR} = \frac{2\pi^2 n^2}{\Gamma^2}$ for a secondary bifurcation collapses to $bR_0^2 - 2R_0^4 = 0$ implying that the only secondary branch that can undergo a phase jump is the branch bifurcating at $R_0^2 = b/2$. We emphasize that these phase jumps correspond to phase jumps that occur over large scales in

the original problem; strictly, we cannot take the limit $L \rightarrow 0$ without encountering higher order terms omitted from the Ginzburg-Landau description (1.6).

Transition from subcritical to supercritical behavior

The results presented above enable us to understand the sequence of transitions that must take place as b decreases through $b = 0$ and the $k = 0$ primary branch goes from being subcritical to being supercritical. There are two fundamentally distinct scenarios, distinguished by the sign of the quantity $a_1^2 - a_2^2 - 4$. When $a_1^2 - a_2^2 - 4 < 0$ figure 2.9 shows that as b decreases the secondary bifurcation points on the $k = 0$ branch move to higher amplitude while the termination points move towards lower amplitude. In addition, since k_M is proportional to b its value decreases thereby making it more and more likely that the secondary branch originates and terminates on the same branch. The mechanism whereby the termination point switches from a primary branch with $k \approx k_M$ to the $k = 0$ branch relies on reconnection between the protosnaking branch and a defect branch originating from the $k = 0$ branch (not shown), as discussed elsewhere [38]. A similar reconnection eliminates the secondary branches one by one until none remain. Figure 2.13 shows an example of the process: as b decreases an $n = 3$ mixed mode branch approaches and reconnects with a defect branch leaving behind a short segment connecting the subcritical $k = 0$ branch to itself together with a larger amplitude, completely disconnected branch of defect-like states. With further decrease of b the endpoints of the short segment come together, eliminating the segment, while the disconnected branch moves farther away. In this particular example the protosnaking branches turn towards larger μ and undergo a twist before terminating on a periodic state but this does not occur in other cases we have examined. Thus when $a_1^2 - a_2^2 - 4 < 0$ secondary bifurcation points annihilate pairwise and there is a minimum value of b , $b_{min} \equiv (\pi/\Gamma)\sqrt{4 + a_2^2 - a_1^2}$, such for $0 < b < b_{min}$ no secondary bifurcations take place on the subcritical branch, i.e., localized states are absent.

Figure 2.15 shows that similar reconnections are responsible for successive elimination of the secondary branches in the case $a_1^2 - a_2^2 - 4 > 0$ as well. In this case the secondary branches bifurcate strongly subcritically and the Maxwell point μ_M typically falls outside the coexistence range between $A = 0$ and the $k = 0$ branch (figure 2.14(a)). As b decreases both μ_M and $\mu_{sn}(0)$ decrease as b^2 , implying that in large domains secondary branches continue to bifurcate subcritically. Moreover, when b decreases the secondary bifurcation points move up in amplitude and so move through the saddle-node to the upper $k = 0$ branch as the saddle-node moves downward. Of course the protosnaking behaviour disappears as the system becomes supercritical but the subcritical secondary branches remain (figure 2.14(b)). These terminate on periodic states that bifurcate subcritically from $A = 0$ at $\mu > 0$, cf. figure 2.2(c).

Figure 2.16(b) shows a typical result in the supercritical case $b = -0.5$ with $k = 1$ and $a_1 = a_2 = 0$. The two branches that bifurcate from $A = 0$ at $\mu = 1$ are both supercritical and only secondary branches of defect type are present, much as in the standard Eckhaus problem [24]. In contrast, once $a_1 a_2 \neq 0$ (figure 2.17(b)) the SW branch is absent and additional Eckhaus bifurcations occur on the RW branch at small amplitude with connections

to primary branches with $k \neq 0, 1$, while defect states continue to bifurcate at larger amplitudes. Observe that no protosnaking develops on any of the secondary branches bifurcating from the $k = 1$ branches, implying the absence of heteroclinic connections between $A = 0$ and $A = R_0 \exp ix$. This is a consequence of the centrifugal barrier ($L \neq 0$) in the potential $U(R; \mu, L)$ for this state, and is in turn a consequence of the fact that here $k = 1$ is selected by the boundary conditions and not by the condition for a heteroclinic connection.

2.4 Temporal stability analysis

Since R_0^+ is amplitude-stable while R_0^- is amplitude-unstable it follows that in the former case the front connects two stable states, while in the latter case it connects a stable state ($A = 0$) to an unstable state (A^-). This distinction is of great consequence for the stability and motion of the front. The curve (2.19) is also shown in figure 2.4.

In this section we examine the stability properties of primary branches with both $k = 0$ and $k \neq 0$ with respect to long wave perturbations with wavenumber $|q| \ll |k|$. The analysis performed is analogous to the classical Eckhaus analysis [22] but the results, presented in the form of stability regions in the (k, μ) plane, are substantially different owing to the subcriticality of the basic wavetrain and the presence of the coefficients a_1, a_2 , assumed to be nonzero. The problem is formally posed on the real line and no boundary conditions are imposed on the perturbations.

Stability of primary branches

Nontrivial constant-amplitude steady solutions $A = R_0 \exp i(kx + \phi_0)$ of Eq. (1.6) fall into three classes:

- (1) Supercritical case: $b' \leq 0$, R_0^+ exists in the region $\mu > k^2$.
- (2) Subcritical case: $b' > 0$, R_0^+ solution exists in the region $\mu \geq k^2 - \frac{b'^2}{4}$.
- (3) Subcritical case: $b' > 0$, R_0^- solution exists in the region $k^2 - \frac{b'^2}{4} < \mu < k^2$.

To study the stability, we calculate the spectrum of periodic solutions by writing

$$A = R_0 e^{i(kx + \phi_0)} (1 + a). \quad (2.39)$$

The perturbation $a \equiv a(x, t)$ evolves according to

$$a_t = -(2\mu - 2k^2 + b' R_0^2) (a + a^*) + 2ika_x + a_{xx} + iR_0^2 (a_1 a_x + a_2 a_x^*) + O(|a|^2). \quad (2.40)$$

The stability of the periodic solutions is determined by the eigenvalues of the linearized problem. Writing

$$a_q(x, t) = \beta_1(t) e^{iqx} + \beta_2^*(t) e^{-iqx}, \quad (2.41)$$

where $q > 0$ is a real wavenumber, we find that β_1 and β_2 are complex-valued functions of time satisfying

$$\frac{d}{dt} \begin{pmatrix} \beta_1 \\ \beta_2 \end{pmatrix} = \begin{pmatrix} C_1^+ & C_2^+ \\ C_2^- & C_1^- \end{pmatrix} \begin{pmatrix} \beta_1 \\ \beta_2 \end{pmatrix}, \quad (2.42)$$

where

$$C_1^\pm \equiv -2\mu + 3k^2 - (b' \pm a_1 q) R_0^2 - (k \pm q)^2, \quad C_2^\pm \equiv -2\mu + 2k^2 - (b' \pm a_2 q) R_0^2.$$

Thus the eigenvalues of the stability matrix are

$$\sigma_\pm = -g - q^2 \pm \sqrt{(g + q^2)^2 - q^2(f + q^2)}, \quad (2.43)$$

where

$$\begin{aligned} f(\mu, k) &\equiv (2 + a_2^2 - a_1^2) \{ \mu - k^2 + b' R_0^2 \} + 2\mu - 6k^2 - 4ka_1 R_0^2, \\ g(\mu, k) &\equiv 2(\mu - k^2) + b' R_0^2. \end{aligned}$$

When $q = 0$ there is a marginal mode $a = i$ with eigenvalue $\sigma = 0$ corresponding to translation invariance. The remaining mode is referred to as the amplitude mode and is stable when $g > 0$ (i.e., on R_0^+) and unstable when $g < 0$ (i.e., on R_0^-). The function f can be computed directly from the potential U and satisfies

$$U_{RR} = -2f \quad (2.44)$$

on periodic wavetrains. This property plays an important role in characterizing the relationship between temporal and spatial stability when $q \neq 0$.

An eigenmode of wavenumber q is unstable provided

- (i) $q^2(f + q^2) < 0$: Both eigenvalues are real and there is only one unstable eigenvalue $\sigma_+ > 0$, yielding the unstable solution

$$\tilde{a}_q(x, t) = e^{\sigma_+ t} [C_2^+ \beta e^{iqx} + (\sigma_+ - C_1^+) \beta^* e^{-iqx}],$$

where β is a complex constant.

- (ii) $g + q^2 < 0$ and $q^2(f + q^2) > 0$: The eigenvalues can be either real or complex, but both are unstable. The former case applies when $g^2 > q^2(f - 2g)$, leading to unstable solutions of the form

$$\tilde{a}_q(x, t) = e^{\sigma_\pm t} [C_2^+ \beta e^{iqx} + (\sigma_\pm - C_1^+) \beta^* e^{-iqx}],$$

where β is again a complex constant. In contrast, when $g^2 < q^2(f - 2g)$ the eigenvalues are complex, and the unstable solutions take the form

$$\tilde{a}_q(x, t) = e^{\sigma_r t} \{ C_2^+ \beta_1(t) e^{iqx} + [(\sigma_r - C_1^+) \beta_1^*(t) + \sigma_i \beta_2^*(t)] e^{-iqx} \},$$

where

$$\beta_1(t) = \beta \cos(\sigma_i t) + \gamma \sin(\sigma_i t), \quad \beta_2(t) = -\beta \sin(\sigma_i t) + \gamma \cos(\sigma_i t),$$

with β and γ are complex constants. Here $\sigma_r = -g - q^2$, $\sigma_i = \sqrt{(g + q^2)^2 - q^2(f + q^2)}$.

From the discussions above, an eigenmode of wavenumber q is stable if and only if both $q^2(f + q^2)$ and $g + q^2$ are positive. This is so for all q if and only if f and g are both nonnegative. This is so for periodic wavetrains satisfy $R = R_0^+$ whenever $U_{RR}(R_0^+) \leq 0$. In this case localized states in the form of front, pulse and hole solutions connecting to R_0^+ as $|x| \rightarrow \infty$ may be stable since the background state to which they connect is itself stable.

In the following we refer to the instability triggered by real eigenvalues as the Eckhaus instability (phase mode), since it is associated with the appearance of stationary but spatially modulated solutions (cf. section 2.3). Instability of type (ii) with complex eigenvalues will be called oscillatory instability (amplitude and oscillatory modes). To determine the regions in the (k, μ) plane corresponding to stable and unstable solutions on the real line, we determine the conditions under which at least some unstable wavenumbers q are present. In this case the conditions (i) and (ii) for instability can be rewritten as:

$$(i) \quad f < 0, \quad (ii) \quad g < \min \{0, f\}. \quad (2.45)$$

Figure 2.20 shows the eigenvalues σ_{\pm} as functions of q near the onset of instability.

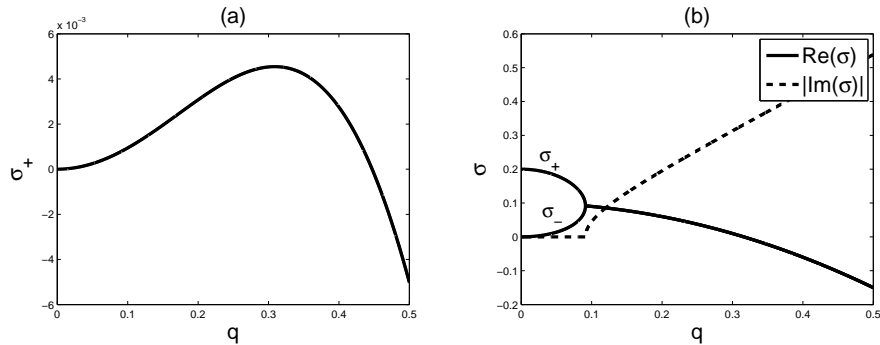


Figure 2.20: Eigenvalues σ_{\pm} as functions of q near the onset of instability. (a) Phase mode: $f = -0.2$ and $g = 1$. (b) Real and oscillatory modes: $f = 1$ and $g = -0.1$.

The case $a_1 = a_2 = 0$

In the following we use the notation (1)(i) to refer to case (1) as defined in section 2.4 and condition (i) as defined in Eq. (2.45), etc. We begin with the case $a_1 = a_2 = 0$. In this case, the range of μ within which the periodic wavetrain is unstable is

(1)(i) and (2)(i):

$$\mu < 2k^2 - \frac{b^2}{8} - \frac{b}{8}\sqrt{b^2 + 16k^2}. \quad (2.46)$$

Moreover, in order that R_0^+ be present, we also need the conditions $\mu > k^2$ (supercritical case) and $\mu \geq k^2 - b^2/4$ (subcritical case). The resulting instability regions are shown in figure 2.21(a,c).

(3)(i):

$$k^2 - \frac{b^2}{4} < \mu < k^2. \quad (2.47)$$

Condition (i) thus holds for all μ along the R_0^- branch (figure 2.21(b)), i.e., R_0^- is unstable.

The resulting bifurcation diagrams resemble those familiar from the supercritical case [24], with amplitude-stable solutions unstable with respect to the Eckhaus instability at small amplitude and stable at large amplitude.

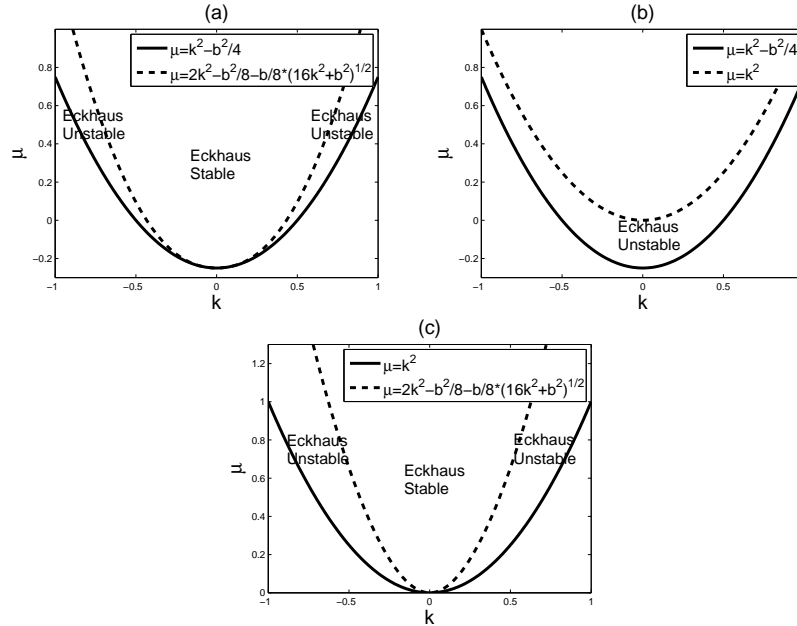


Figure 2.21: The (k, μ) plane when $a_1 = a_2 = 0$ and (a) $b = 1$, R_0^+ , (b) $b = 1$, R_0^- , (c) $b = -1$, R_0^+ . When $b \leq 0$ both curves lie in $\mu \geq 0$; when $b > 0$ the curves extend below $\mu = 0$.

The general case

In the general case with at least one of a_1 and a_2 nonzero, we let $\alpha \equiv a_2^2 - a_1^2$ and $s \equiv \sqrt{b'^2 + 4(\mu - k^2)}$. To find the range of μ for instability of type (i), we rewrite the condition $f < 0$ as a condition on s . When $\alpha + 4 \neq 0$,

(1)(i) and (2)(i):

$$(4 + \alpha) \left\{ \left[s + \frac{(2 + \alpha)b' - 4ka_1}{4 + \alpha} \right]^2 - \frac{4(b' + 2a_1k)^2 + 16(4 + \alpha)k^2}{(4 + \alpha)^2} \right\} < 0. \quad (2.48)$$

(3)(i):

$$(4 + \alpha) \left\{ \left[s - \frac{(2 + \alpha)b' - 4ka_1}{4 + \alpha} \right]^2 - \frac{4(b' + 2a_1k)^2 + 16(4 + \alpha)k^2}{(4 + \alpha)^2} \right\} < 0. \quad (2.49)$$

When $4 + \alpha = 0$, these relations become

(1)(i) and (2)(i):

$$(b' + 2a_1k)(b' + s) + 4k^2 > 0. \quad (2.50)$$

(3)(i):

$$(b' + 2a_1k)(b' - s) + 4k^2 > 0. \quad (2.51)$$

We summarize these results in two different types of plots. In the first we superpose the curves $f = 0$ and $g = f$ on the bifurcation diagram in figure 2.3 showing the amplitude R_0 of a periodic wavetrain as a function of the wavenumber k for different values of b and $\mu = 1$ (figure 2.22) and $\mu = -1$ (figure 2.23). Plots of this type determine the range of stable periodic states. We show the same information in the (k, μ) plane in figure 2.24 for $b > 0$ (the subcritical case) and figure 2.25 for $b < 0$ (the supercritical case), in both cases focusing on the stability properties of the R_0^+ state. In both cases a_2 has been taken to be positive. In each plot we indicate the regions in which a wavetrain with wavenumber k is stable with respect to the Eckhaus instability and where it is unstable. These regions are delimited by the union of two curves, the curve $\mu = \mu_{sn}(k)$ for $|k|$ small (near band center) and the curve $\mu = k^2$ for those wavenumbers for which the primary bifurcation is supercritical (larger $|k|$), and by the curve $f = 0$ corresponding to the Eckhaus instability. The resulting plots should be compared with figure 2.21 computed for $a_1 = a_2 = 0$. We see that when $a_1 \neq 0$, $a_2 \neq 0$ the stability region becomes asymmetrical with respect to $k \rightarrow -k$, and may either grow or shrink. Indeed for some coefficient values the region of stability is suppressed altogether.

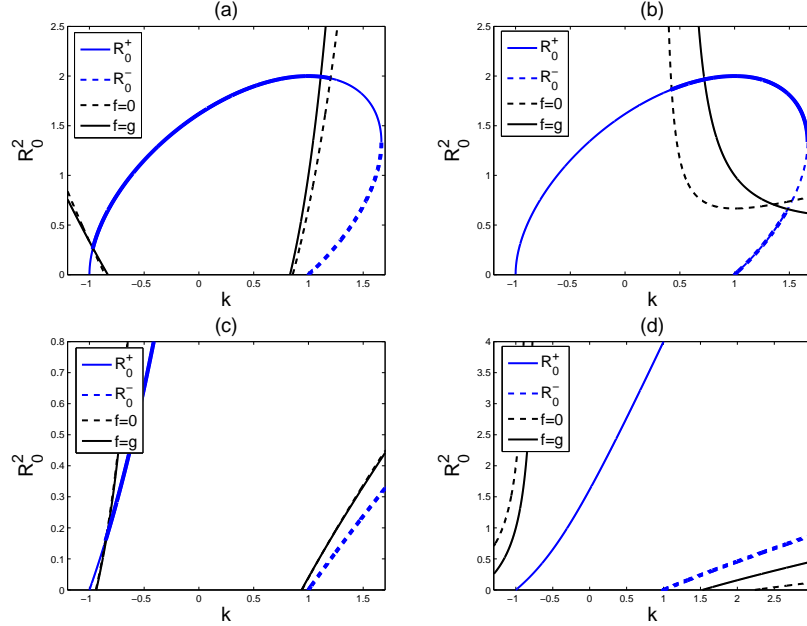


Figure 2.22: (Color online) Bifurcation diagrams $R_0^2(k)$ when $\mu = b = 1$ showing the onset of type (i) ($f = 0$, black dashed line) and type (ii) ($g = f$, black line) instabilities. Thick blue (gray) line indicates stable solutions while the thick dashed blue (gray) line indicates the R_0^- solutions unstable with respect to instability (i) only. (a) $a_1 = 3$, $a_2 = 4$. (b) $a_1 = -3$, $a_2 = -2$. (c) $a_1 = 3$, $a_2 = 6$. (d) $a_1 = -3$, $a_2 = 0$.

The instability regions for the R_0^- branch are more complex since in addition to instability (i), we may also have instability (ii), with either two real positive eigenvalues or a pair of unstable complex eigenvalues. The condition for instability (ii) is

$$\left(1 + \frac{\alpha}{2}\right) s^2 - [(1 + \alpha)b' - 4a_1k]s + \frac{\alpha b'^2 - 8a_1kb' - 16k^2}{2} > 0, \quad (2.52)$$

subject to the requirement $s < b'$ that defines the existence range for R_0^- . We show the location of complex eigenvalues on the subcritical branch R_0^- for $b > 0$ in figure 2.26 and for $b < 0$ in figure 2.27. Note that complex eigenvalues are only present close to the saddle-node where the time scales for the growth of amplitude and phase perturbations become comparable. We also mention that the quantity $f - 2g = a_2^2 R_0^4 - (a_1 R_0^2 + 2k)^2$ is negative whenever $a_2 = 0$. In this case, the condition for the presence of complex eigenvalues, $g^2 < q^2(f - 2g)$, cannot be satisfied. This is as expected since Eq. (1.6) is then of gradient type. We leave to future work the possibility that the unstable oscillations present when $a_2 \neq 0$ acquire stability at finite amplitude and the role played by the complex eigenvalues in the stability properties of the various secondary states identified in section 2.3.

Additional light can be shed on the plots in figures 2.24–2.27 by examining the special (and simpler) case $k = 0$ (the band center), starting with instability (i). In the supercritical

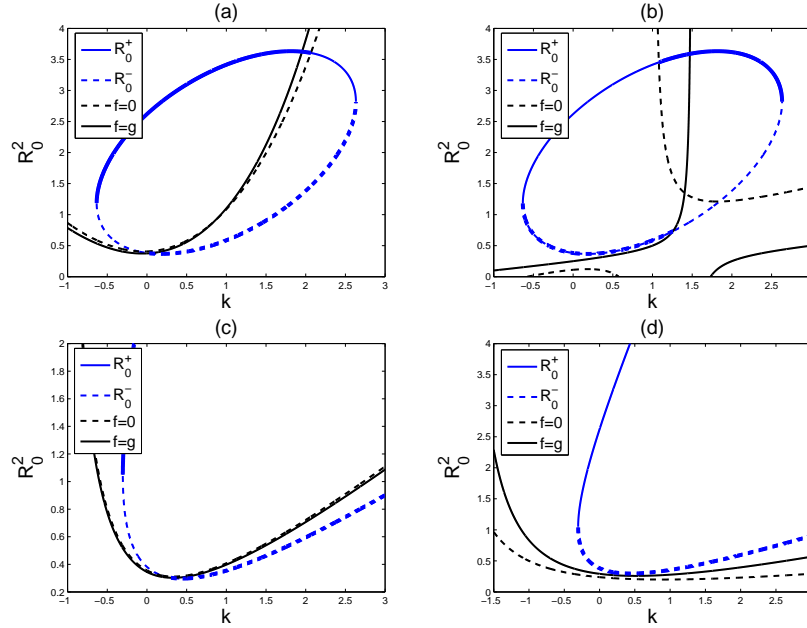


Figure 2.23: (Color online) Bifurcation diagrams $R_0^2(k)$ when $\mu = -1$, $b = 3$ showing the onset of type (i) ($f = 0$, black dashed line) and type (ii) ($g = f$, black line) instabilities. Thick blue (gray) line indicates stable solutions while the thick dashed blue (gray) line indicates the R_0^- solutions unstable with respect to instability (i) only. (a) $a_1 = 3$, $a_2 = 4$. (b) $a_1 = -3$, $a_2 = -2$. (c) $a_1 = 3$, $a_2 = 6$. (d) $a_1 = -3$, $a_2 = 0$.

regime the R_0^+ branch is unstable only when $4 + \alpha < 0$, within the range $\mu > -\frac{2(2+\alpha)b^2}{(4+\alpha)^2}$. In the subcritical regime the R_0^+ branch is unstable for all μ when $4 + \alpha \leq 0$. When $-4 < \alpha < 0$ there is a range of instability, $-\frac{b^2}{4} < \mu < -\frac{2(2+\alpha)b^2}{(4+\alpha)^2}$ which shrinks as α increases towards $\alpha = 0$ and vanishes when α reaches zero. The subcritical R_0^- branch is always unstable. The instability (ii) only appears on the R_0^- branch, and then only when $\alpha > 0$ with $-\frac{b^2}{4} < \mu < -\frac{(1+\alpha)b^2}{(2+\alpha)^2}$. These results are reflected in figures 2.24–2.27.

Finite size effects

In the presence of restrictions on q , e.g., due to a finite domain size, the allowed wavenumber q limits the range of unstable μ . For example, for periodic boundary conditions with period 2Γ , the wavenumbers $k+k_c$ and q must be integer multiples of $\frac{\pi}{\Gamma}$. With $k_c = \frac{\pi}{\Gamma}(N+l)$, where N is a nonnegative integer and $0 \leq l < 1$, the possible values of k and q are $k_n = \frac{\pi}{\Gamma}(n-l)$ and $q_m = \frac{\pi m}{\Gamma}$ with $n \in \mathbb{Z}$ and $m \in \mathbb{N}$, respectively. The smallest unstable wavenumber q_m is therefore finite, cf. [23, 24], resulting in a slight decrease in the range of instability.

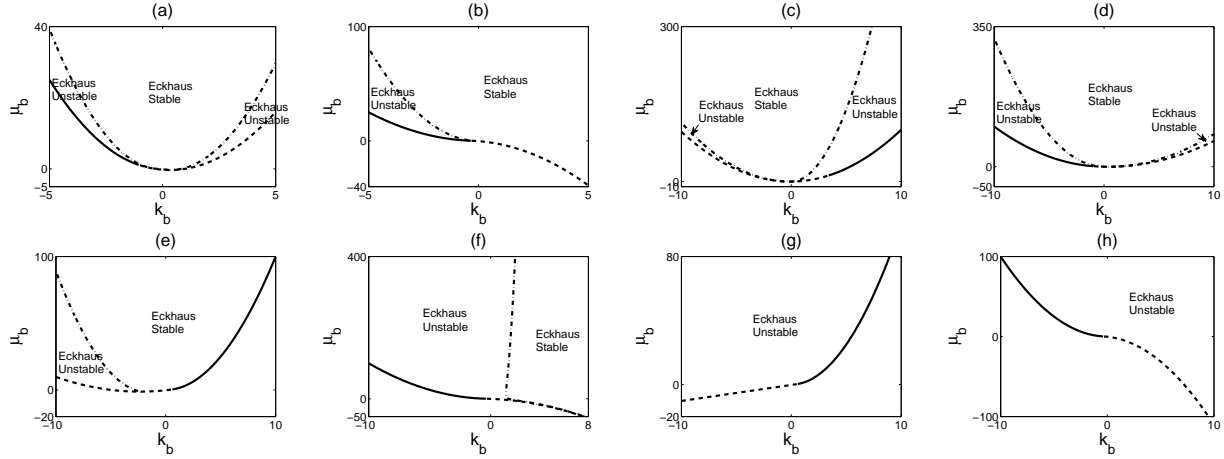


Figure 2.24: The parameter range ($k_b \equiv k/|b|, \mu_b \equiv \mu/b^2$) for instability (i) of R_0^+ when $b > 0$ and $a_2 > 0$. Dashed curve: saddle-node. Solid curve: $\mu = k^2$. Dash-dotted curve: Eckhaus boundary. (a) $a_1 = 1, a_2 = 2$ ($\alpha > 0$). (b) $a_1 = -1, a_2 = 2$ ($\alpha > 0$). (c) $a_1 = 1.3, a_2 = 1$ ($-4 < \alpha < 0$). (d) $a_1 = -0.6, a_2 = 0.5$ ($-4 < \alpha < 0$). (e) $a_1 = 2.8, a_2 = 1$ ($\alpha < -4$). (f) $a_1 = -2.1, a_2 = 0.5$ ($\alpha < -4$). (g) $a_1 = 3, a_2 = 1$ ($\alpha < -4$). (h) $a_1 = -2.3, a_2 = 0.5$ ($\alpha < -4$).

Stability of secondary branches

We have also examined the stability of the secondary branches by computing numerically the temporal spectrum σ , and examining the behavior of the leading eigenvalues along the various branches, focusing primarily on the secondary branches bifurcating from the $k = 0$ branch. Figures 2.9–2.15 show that the bifurcation to the first of these is always supercritical when $b > 0$, implying that the first secondary branch has initially a single unstable eigenvalue. When the branch enters the protosnaking region this eigenvalue becomes very small. If the branch remains monotonic this eigenvalue remains positive but if the branch undergoes folds it can become negative thereby stabilizing the branch. This is so in figures 2.10(b), 2.12(a), and 2.14(a). In figure 2.12(a) there are in fact four folds on the first secondary branch, the first three of which are not visible on the scale of the figure. In other cases, however, the portion of the branch with positive slope remains unstable. This is the case, for example, in figures 2.13(b,c).

2.5 Dynamics of periodic wavetrains

In this section we derive modulation equations describing the dynamics near the onset of each type of secondary instability and compare the resulting dynamics with results obtained via direct numerical simulation of Eq. (1.6). The time-stepping used here and in the subsequent sections employs the Fourier-based method ETD4RK [40]. Dealiasing is achieved via

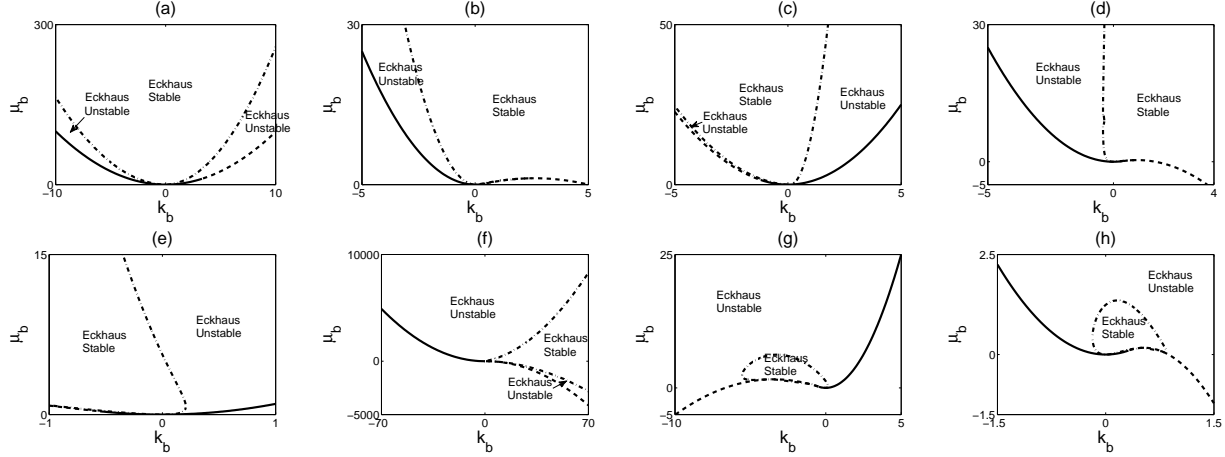


Figure 2.25: The parameter range ($k_b \equiv k/|b|, \mu_b \equiv \mu/b^2$) for instability (i) of R_0^+ when $b < 0$ and $a_2 > 0$. Dashed curve: saddle-node. Solid curve: $\mu = k^2$. Dash-dotted curve: Eckhaus boundary. (a) $a_1 = 0.7, a_2 = 1$ ($\alpha > 0$). (b) $a_1 = -0.7, a_2 = 1.5$ ($\alpha > 0$). (c) $a_1 = 1.8, a_2 = 1$ ($-4 < \alpha < 0$). (d) $a_1 = -2.1, a_2 = 0.5$ ($\alpha < -4$). (e) $a_1 = 2.3, a_2 = 0.5$ ($\alpha < -4$). (f) $a_1 = -2.23, a_2 = 0.5$ ($\alpha < -4$). (g) $a_1 = 2.65, a_2 = 0.5$ ($\alpha < -4$). (h) $a_1 = -2.65, a_2 = 0.5$ ($\alpha < -4$).

mode truncation.

Phase mode (Eckhaus instability)

Here we assume that the periodic state $R_0^+(k_0)$ is such that $g = O(1) > 0$ and $f \approx 0$, i.e., $R_0^+(k_0)$ is close to the onset of instability. Figure 2.20(a) shows the eigenvalue σ_+ versus the perturbation wavenumber q when f is slightly negative. The unstable modes are phase modes and result in Eckhaus instability, i.e., in phase slips [23].

To describe the dynamics that result we use multiple scale analysis to derive an evolution equation for the phase of the pattern. Define μ_0 be the value of μ which $f(\mu_0, k_0) = 0$ and let R_0^+ be evaluated at $(\mu, k) = (\mu_0, k_0)$. When $\partial_\mu f(\mu_0, k_0)$, f can be approximated as

$$f = \partial_\mu f|_{\mu=\mu_0} \delta\mu + o(|\delta\mu|) = \frac{[(4 + a_2^2 - a_1^2)(R_0^+)^2 + 4k_0^2/(R_0^+)^2]}{\sqrt{b^2 + 4(\mu_0 - k_0^2)}} \delta\mu + o(|\delta\mu|), \quad (2.53)$$

where R_0^+ is evaluated at $(\mu, k) = (\mu_0, k_0)$. If $a_1^2 - a_2^2 < 4$, $\partial_\mu f|_{\mu=\mu_0}$ is always positive implying that $R_{0,+}$ is Eckhaus-stable for $\mu > \mu_0$. In contrast, if $a_1^2 - a_2^2 > 4$, the quantity $\partial_\mu f|_{\mu=\mu_0}$ can be negative in an appropriate region of the (a_1, a_2) plane and this allows the phase mode to be unstable when $\mu > \mu_0$. There is no instability when $\mu < \mu_0$.

In the nondegenerate case $\partial_\mu f(\mu_0, k_0) = O(1)$ we assume that $\delta\mu = O(\epsilon^2)$ and the q^2 term in Eq. (2.43) is comparable with f , i.e., $q = O(\epsilon)$. The corresponding timescale is determined by the magnitude of the most unstable eigenvalue which is $O(\epsilon^{-4})$. For eigenmodes near

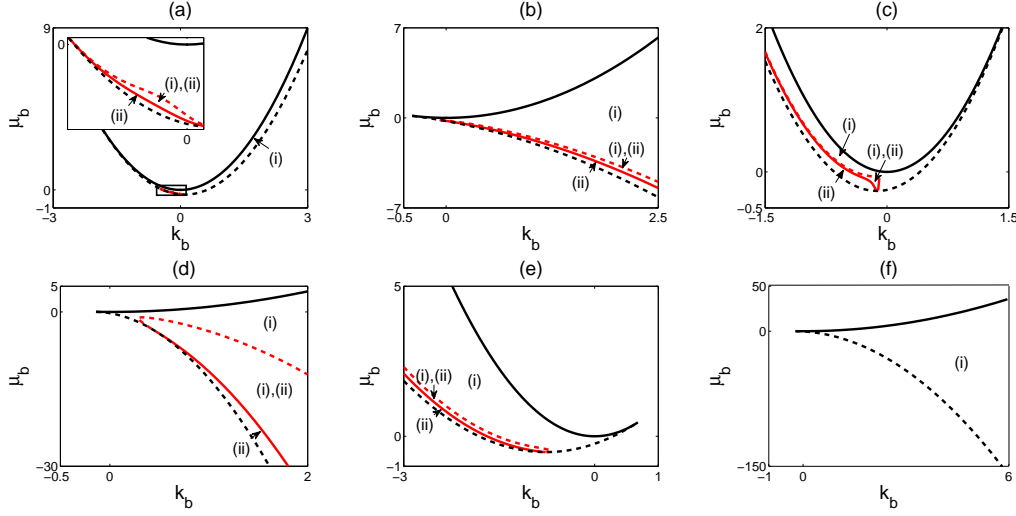


Figure 2.26: (Color online) The parameter range ($k_b \equiv k/|b|$, $\mu_b \equiv \mu/b^2$) for instability (i) and (ii) of R_0^- when $b > 0$ and $a_2 > 0$. Black dashed curve: saddle-node. Black solid curve: $\mu = k^2$. Red (gray) solid curve: boundary of instability (i). Red (gray) dashed curve: boundary of instability (ii). (a) $a_1 = 1$, $a_2 = 1.4$ ($\alpha > 0$). (b) $a_1 = -1$, $a_2 = 1.42$ ($\alpha > 0$). (c) $a_1 = 3.46$, $a_2 = 3$ ($-4 < \alpha < 0$). (d) $a_1 = -3.46$, $a_2 = 3$ ($-4 < \alpha < 0$). (e) $a_1 = 2.45$, $a_2 = 1$ ($\alpha < -4$). (f) $a_1 = -3$, $a_2 = 1.5$ ($\alpha < -4$).

$q = 0$, the real part of the eigenvector is $O(\epsilon)$ smaller than its imaginary part implying that the instability results primarily in phase modulation. We therefore write

$$\begin{aligned} \delta\mu &= \epsilon^2\mu_2, \quad T = \epsilon^4t, \quad X = \epsilon x, \\ A &= R_0^+(1 + \epsilon^2r^{(0)} + \epsilon^4r^{(1)} + \dots)e^{i(k_0x + \epsilon\phi^{(0)} + \epsilon^3\phi^{(1)} + \dots)}, \end{aligned} \quad (2.54)$$

where $r^{(n)}$ and $\phi^{(n)}$ are real functions of X and T . It can now be shown that with this scaling the phase perturbation $\phi^{(0)}$ satisfies the nonlinear phase equation [22]

$$2g_0\phi_T^{(0)} = -\phi_{XXX}^{(0)} + f_2\phi_{XX}^{(0)} + 2\gamma\phi_X^{(0)}\phi_{XX}^{(0)}, \quad (2.55)$$

where $f = \epsilon^2f_2$, $g_0 = g|_{\mu_0, k_0}$ and

$$\gamma = \frac{U_{RRR,0}R_0}{4b_+}, \quad b_{\pm} \equiv a_2R_0^2 \pm (a_1R_0^2 + 2k_0). \quad (2.56)$$

The perturbed amplitude $r^{(0)}$ is slaved to $\phi_X^{(0)}$,

$$2g_0r^{(0)} = b_-\phi_X^{(0)}. \quad (2.57)$$

These results can also be written in terms of the perturbation wavenumber $\kappa \equiv \phi_X^{(0)}$,

$$2g_0\kappa_T = (-\kappa_{XX} + f_2\kappa + \gamma\kappa^2)_{XX}. \quad (2.58)$$

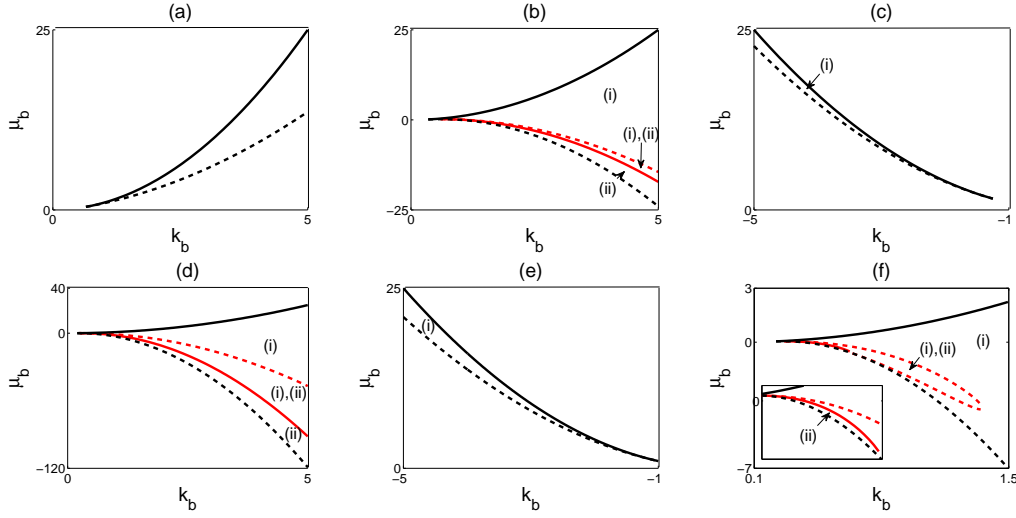


Figure 2.27: (Color online) The parameter range ($k_b \equiv k/|b|$, $\mu_b \equiv \mu/b^2$) for instability (i) and (ii) of R_0^- when $b < 0$ and $a_2 > 0$. Black dashed curve: saddle-node. Black solid curve: $\mu = k^2$. Red (gray) solid curve: boundary of instability (i). Red (gray) dashed curve: boundary of instability (ii). (a) $a_1 = 0.45$, $a_2 = 2$ ($\alpha > 0$). (b) $a_1 = -1$, $a_2 = 2$ ($\alpha > 0$). (c) $a_1 = 2.2$, $a_2 = 1.4$ ($-4 < \alpha < 0$). (d) $a_1 = -2.8$, $a_2 = 2.2$ ($-4 < \alpha < 0$). (e) $a_1 = 3.2$, $a_2 = 2.2$ ($\alpha < -4$). (f) $a_1 = -3$, $a_2 = 1.73$ ($\alpha < -4$).

A sketch of the derivation is given in Appendix E.

Equation (2.58) has stationary spatially localized solutions in the Eckhaus-stable regime $f_2 > 0$. In the stationary case, the phase equation can be integrated twice, yielding

$$-\kappa_{XX} + f_2\kappa + \gamma\kappa^2 = 0. \quad (2.59)$$

The integration constants are set to zero by the requirement that the asymptotic wavenumber outside the structure remains unchanged. Bifurcation to localized solutions takes place as f_2 becomes positive and the resulting solution takes the form

$$\kappa_0(X) = -\frac{3f_2}{2\gamma}\text{sech}^2\left(\frac{\sqrt{f_2}}{2}X\right). \quad (2.60)$$

Within the phase description the stability properties of this solution follow from the fact that Eq. (2.58) has a Lyapunov functional,

$$G[\kappa] = \int_{\mathbb{R}} \left(\frac{\kappa_X^2}{2} + \frac{f_2}{2}\kappa^2 + \frac{\gamma}{3}\kappa^3 \right) dX, \quad (2.61)$$

i.e., $G[\kappa]$ decreases monotonically with time. Consider $\tilde{G}(s) = G[\kappa_0 + sw]$, where w is an arbitrary smooth function that tends to 0 as $|X| \rightarrow \infty$. Locally around $s = 0$, we have

$$\tilde{G}(s) = \tilde{G}(0) + \frac{1}{2}\tilde{G}''(0)s^2 + O(s^3), \quad (2.62)$$

where $\tilde{G}''(0)$ takes the form

$$\tilde{G}''(0) = \frac{\sqrt{f_2}}{2} \int_{\mathbb{R}} \left\{ \frac{w_{X'}^2}{2} + (2 - 6\text{sech}^2 X') w^2 \right\} dX', \quad X' = \frac{\sqrt{f_2}}{2} X. \quad (2.63)$$

Consider now the eigenvalue problem,

$$-w'' + (4 - 12\text{sech}^2 X') w = \lambda w. \quad (2.64)$$

It is known [41] that Eq. (2.64) has one negative eigenvalue $\lambda = -5$. It follows that $\tilde{G}''(0) < 0$ for a suitable choice of w and hence that the solution given in Eq. (2.60) is unstable. The presence of an unstable localized state for $f > 0$ is consistent with the well-known fact that the Eckhaus instability is subcritical.

We now turn to the study of the dynamical evolution of the Eckhaus instability that takes place when $f < 0$ using direct numerical integration of Eq. (1.6) for different choices of (a_1, a_2) with $a_1 - a_2$, k_0 , $g > 0$ and $f < 0$ fixed. The reason for fixing f and g is to ensure that the spectrum of the linearized equation remains unchanged for different choices of (a_1, a_2) and this can be done by modifying the values μ and b . We pick $a_1 - a_2 = 0.45$, $f = -0.02$, $g = 1.3$, $k_0 = \pi/10$ with domain size $\Gamma = 200$ and periodic boundary conditions. The number of grid points, here and elsewhere, is 512 with time step equal to 0.01. We examine the cases $a_1 = 0.65, 0.75, 1.25$, and 2.25 with $\gamma \approx -7.3351, -6.1736, -4.3349$, and -3.9596 . The initial condition we choose is a periodic wavetrain with a superimposed perturbation $a = c_1 e^{iqx} + c_2 e^{-iqx}$, $q = 6\pi/\Gamma$, corresponding to the most unstable mode in the given domain. Time evolution of the profile of $\text{Re}[A]$ is shown in figure 2.28 initialized with perturbation amplitude $\sqrt{c_1^2 + c_2^2} = 0.05$. With the given initial condition, the number of rolls changes from 10 to 7 as a result of phase slips triggered by the Eckhaus instability, and it is clear that the time for a phase slip to occur is smaller when $|\gamma|$ is larger. Phase slips occur at $t = T \approx 1860, 2465, 4380$ and 5075 , respectively; for the perturbation amplitude $\sqrt{c_1^2 + c_2^2} = 0.05$ the time T is determined largely by nonlinear processes and not by the linear growth phase of the instability.

In figure 2.29 we examine the dependence of these results on initial conditions. The figure shows the dynamics of an Eckhaus unstable 10-roll periodic wavetrain with a superimposed unstable mode with perturbation wavenumber (a) $2\pi/\Gamma$, (b) $4\pi/\Gamma$, (c) $6\pi/\Gamma$, and (d) $8\pi/\Gamma$. The simulation shows that the number of rolls decreases by 1, 2, 3 and 4. Here $a_1 = 0.75$, $a_2 = 0.3$ and the remaining quantities are as in figure 2.28.

We also investigate the dependence of the time to phase slip on the linear growth rate $\sigma_+(q)$. Here we fix $a_2 = 0.2$, $g = 1.3$, $\gamma = -7$, and choose the wavenumber of the periodic wavetrain $k_0 = \pi/10$. Values of the parameters a_1 , μ , and b are adjusted so that the numerical value of f is approximately equal to $-0.01503, -0.01751, -0.01999$, and -0.02247 . In each case the most unstable mode corresponds to $q = 6\pi/\Gamma$ with the corresponding temporal eigenvalue $\sigma_+ \approx 2.0847 \times 10^{-5}, 2.9261 \times 10^{-5}, 3.7680 \times 10^{-5}$, and 4.6105×10^{-5} , respectively. Figure 2.30 shows the time evolution resulting from an initial perturbation with $\sqrt{c_1^2 + c_2^2} = 0.001$; figure 2.31 confirms that for these small amplitudes the time T to phase

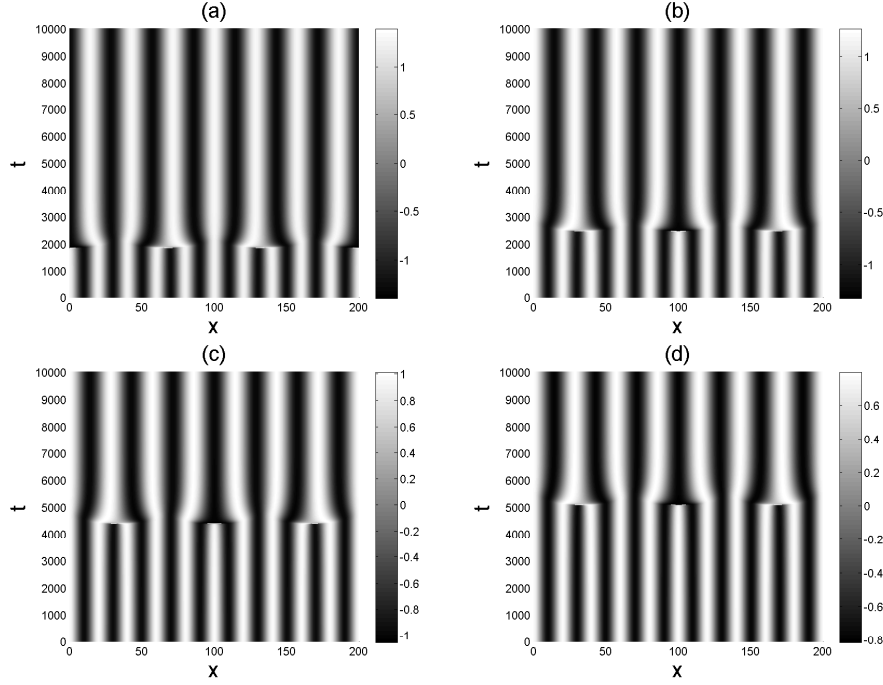


Figure 2.28: Time evolution of $\text{Re}[A]$ with PBC in a domain of size $\Gamma = 200$. Parameters: $f = -0.02$, $g = 1.3$, $k_0 = \pi/10$, and $a_1 - a_2 = 0.45$. (a) $a_1 = 0.65$. (b) $a_1 = 0.75$. (c) $a_1 = 1.25$. (d) $a_1 = 2.25$. In each case the solution has been initialized with a sinusoidal perturbation of amplitude $\sqrt{c_1^2 + c_2^2} = 0.05$ and wavenumber $q = 6\pi/\Gamma$.

slip is determined by the linear growth rate σ_+^{-1} . This is no longer the case for perturbations with amplitude $\sqrt{c_1^2 + c_2^2} \gtrsim 0.01$, cf. figure 2.29.

The degenerate situation $f|_{\mu=\mu_0} = \partial_\mu f|_{\mu=\mu_0} = 0$ arises when $a_1^2 - a_2^2 > 4$ and is always present in the supercritical case ($b' < 0$). In the subcritical case ($b' > 0$) $|a_1|$ must be smaller than $|a_2| + 2/|a_2|$ for this degeneracy to occur. At this degenerate point R_0^+ and b are given by

$$(R_0^+)^2 = 2|k_0|(a_1^2 - a_2^2 - 4)^{-1/2}, \quad b = -2|k_0|(a_1^2 - a_2^2 - 4)^{1/2} - k_0(a_1 + a_2). \quad (2.65)$$

It can be shown that at this point $\partial_\mu^2 f(\mu_0)$ is always negative implying that the periodic state is always unstable when μ is slightly perturbed from μ_0 . The derivation of the phase equation corresponding to this case is similar to the nondegenerate case except that $\delta\mu = O(\epsilon)$ instead of $O(\epsilon^2)$, and also results in Eq. (2.55).

The degeneracy $\gamma = 0$ is of greater interest. This degeneracy only arises when $\beta > 0$ implying that (a_1, a_2) must lie in the range $|a_1 - a_2| > 2$. We remark that Eq. (1.6) may not be well-posed in this regime. From Eq. (2.58), we can see that in order for the next higher order term $(\kappa^3)_{XX}$ to come in, the scaling must be modified:

$$X = \epsilon x, \quad T = \epsilon^4 t, \quad \kappa = O(\epsilon), \quad \gamma = \epsilon \gamma_1. \quad (2.66)$$

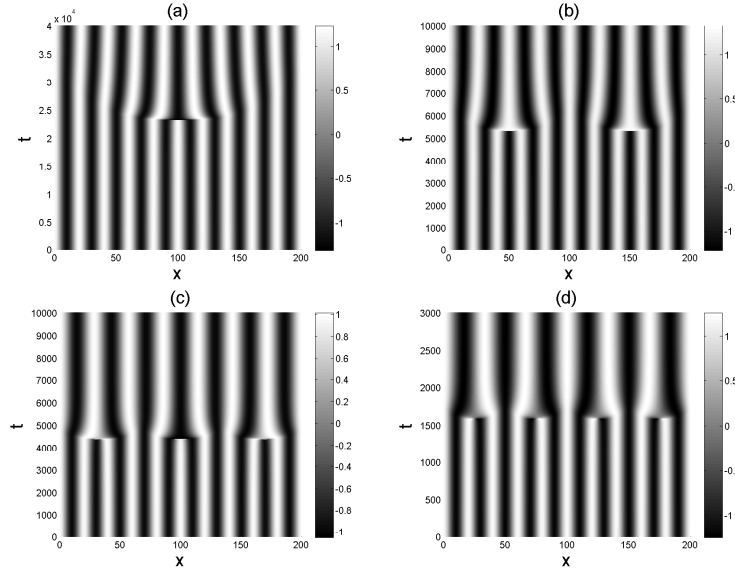


Figure 2.29: Time evolution of $\text{Re}[A]$ with PBC in a domain of size $\Gamma = 200$ triggered by the Eckhaus instability. Parameter values are $a_1 = 0.75$, $a_2 = 0.3$, with the remaining quantities as in figure 2.28. The superposed initial perturbation is periodic with wavenumber (a) $2\pi/\Gamma$, (b) $4\pi/\Gamma$, (c) $6\pi/\Gamma$, and (d) $8\pi/\Gamma$. In each case the solution has been initialized with a sinusoidal perturbation of amplitude $\sqrt{c_1^2 + c_2^2} = 0.05$ and wavenumber $q = 6\pi/\Gamma$.

The size of γ is controlled by varying b . Since κ is $O(\epsilon)$, the perturbations of the phase and amplitude will be $O(1)$ and $O(\epsilon)$, respectively, so that

$$A = R_0^+ (1 + \epsilon r^{(0)} + \epsilon^3 r^{(1)} + \dots) e^{i(k_0 x + \phi^{(0)} + \epsilon^2 \phi^{(1)} + \dots)}. \quad (2.67)$$

Following the procedure in the nondegenerate case, one can show that the perturbed wavenumber κ satisfies the Cahn-Hilliard equation but with a negative cubic coefficient,

$$2g_0 \kappa_T = [-\kappa_{XX} + f_2 \kappa + \gamma_1 \kappa^2 - 2(1 + 2k_0/b_+)^2 \kappa^3]_{XX}. \quad (2.68)$$

When this is the case solutions of Eq. (2.68) exhibit finite time blow up [42]; the blow up time corresponds to the occurrence of a phase slip, i.e., the breakdown of the phase description. In numerical simulations, solutions of Eq. (1.6) always blow up owing to the generation of high frequency modes in this regime. This result is consistent with the failure of well-posedness when $|a_1 - a_2| > 2$. In figure 2.32 we present numerical results before blow up occurs. In contrast with the generic situation when $|\gamma| = O(1) > 0$, the rolls narrow right before a phase slip.

Amplitude and oscillatory modes

We now assume that the periodic state satisfies $f = O(1) > 0$ and that $g \approx 0$. The instability sets in when g becomes slightly negative and only occurs for periodic wavetrains

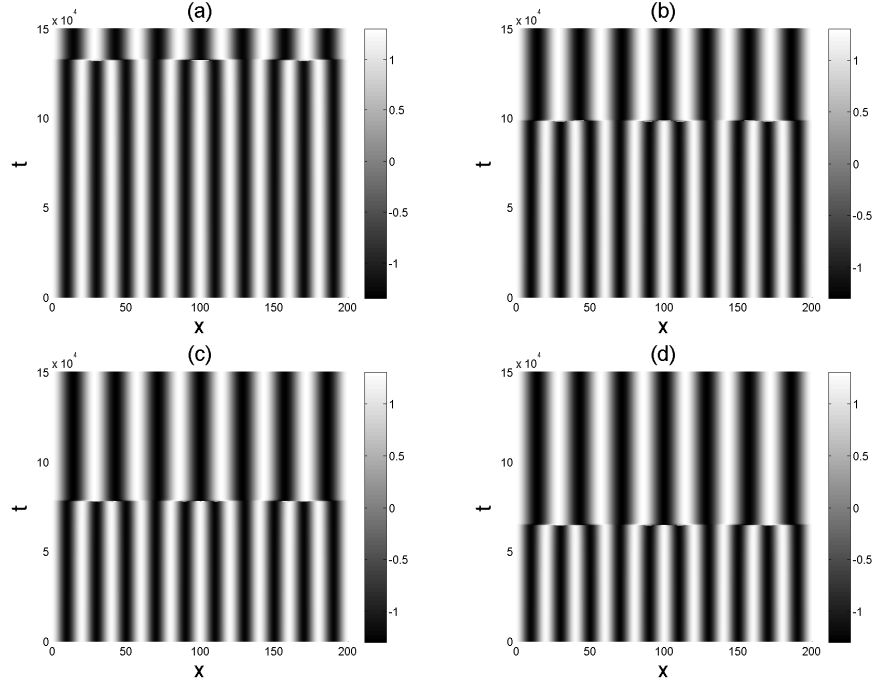


Figure 2.30: Time evolution of $\text{Re}[A]$ with PBC in a domain of size $\Gamma = 200$. Parameter values: $a_2 = 0.2$, $g = 1.3$, $\gamma = 7$. (a) $f = -0.01503$ ($\sigma_+ = 2.0847 \times 10^{-5}$). (b) $f = -0.01751$ ($\sigma_+ = 2.9261 \times 10^{-5}$). (c) $f = -0.01999$ ($\sigma_+ = 3.7680 \times 10^{-5}$). (d) $f = -0.02247$ ($\sigma_+ = 4.6105 \times 10^{-5}$). In each case the solution has been initialized with a sinusoidal perturbation of amplitude $\sqrt{c_1^2 + c_2^2} = 0.001$ and wavenumber $q = 6\pi/\Gamma$.

slightly below the saddle-node ($\mu_0 = k_0^2 - b'^2/4$). The spectrum as a function of the perturbed wavenumber q is shown in figure 2.20(b) and indicates that the eigenvalues are real and unstable when q is close to zero and become complex unstable as q exceeds a certain limit. Since $f = f_0 \equiv \frac{a_2^2 b'^2}{4} - \left(2k_0 + \frac{a_1 b'}{2}\right)^2$ when $\mu = \mu_0$ the coefficient a_2 must be nonzero and large enough for f to be positive. Thus this type of instability is only present when the system is sufficiently far from a gradient system.

When μ is close to the onset of instability, the dependence of g on $\mu - \mu_0$ is

$$g(\mu) = 2(\mu - \mu_0) - b'\sqrt{\mu - \mu_0} \approx -b'\sqrt{\mu - \mu_0}. \quad (2.69)$$

Let $\delta\mu \equiv \mu - \mu_0 = O(\epsilon^4)$. In order for g to compete with the q^2 term in the temporal eigenvalue, the amplitude must vary on $O(\epsilon^{-1})$ scales. But there is another spatial scale which comes from the modes with real unstable eigenvalues. These modes lie within a narrow region around $q = 0$ of ϵ^2 width. The inclusion of this spatial scale is important when the domain size is relatively large. We refer these modes as amplitude modes while the modes in the region of unstable complex eigenvalues are oscillatory modes. With the given scaling, the magnitude of the real and the imaginary parts of the eigenvalues are of different

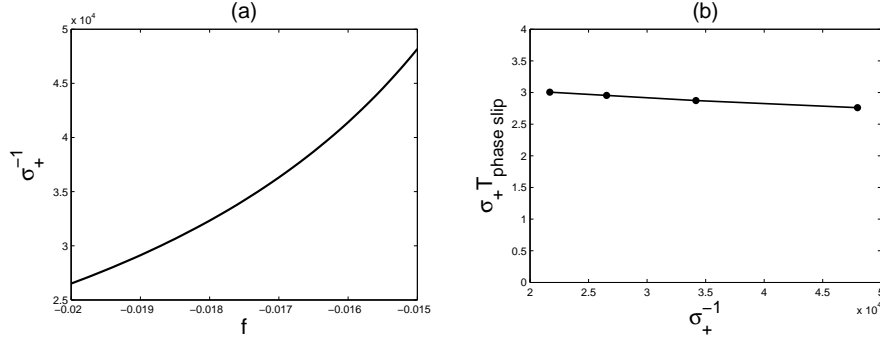


Figure 2.31: (a) The linear growth rate σ_+^{-1} as function of f from figure 2.30. (b) Time T to phase slip in figure 2.30 multiplied by σ_+ as function of σ_+^{-1} .

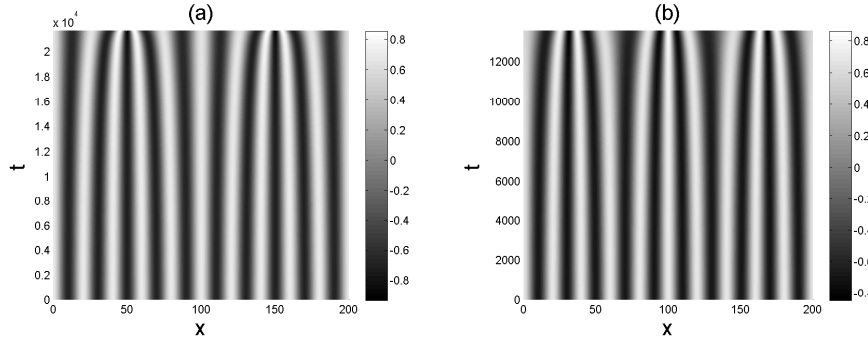


Figure 2.32: Time evolution of $\text{Re}[A]$ with PBC in a domain of size $\Gamma = 200$. Parameter values: $a_1 = -2.9$, $a_2 = -0.7$, $f = -0.02$, $\gamma = 0$. The instability is initialized using an unstable mode with wavenumber (a) $4\pi/\Gamma$ and (b) $6\pi/\Gamma$.

order, $O(\epsilon^{-2})$ for the real part and $O(\epsilon^{-1})$ for the imaginary part. These facts suggest the following choice of multiscale scaling:

$$\begin{aligned} X_1 &= \epsilon x, & X_2 &= \epsilon^2 x, & T_1 &= \epsilon t, & T_2 &= \epsilon^2 t, \\ \delta\mu &= \epsilon^4 \mu_1^2, & a &= \epsilon^2 a^{(0)} + \epsilon^3 a^{(1)} + \dots \end{aligned} \quad (2.70)$$

Here $\delta\mu \geq 0$ since μ_0 is already at the saddle-node.

In the following we write $a^{(n)} \equiv a_r^{(n)} + ia_i^{(n)}$. The first two orders in ϵ then yield the equations

$$a_{r,T_1}^{(0)} - b_- a_{i,X_1}^{(0)} = 0, \quad (2.71)$$

$$a_{i,T_1}^{(0)} - b_+ a_{r,X_1}^{(0)} = 0, \quad (2.72)$$

$$a_{r,T_1}^{(1)} - b_- a_{i,X_1}^{(1)} = b_- a_{i,X_2}^{(0)} - a_{r,T_2}^{(0)} + a_{r,X_1 X_1}^{(0)} - b'^2 a_r^{(0)2} + 2b' \mu_1 a_r^{(0)}, \quad (2.73)$$

$$a_{i,T_1}^{(1)} - b_+ a_{r,X_1}^{(1)} = b_+ a_{r,X_2}^{(0)} - a_{i,T_2}^{(0)} + a_{i,X_1 X_1}^{(0)}. \quad (2.74)$$

Thus $a_r^{(0)}$ and $a_i^{(0)}$ both satisfy a one-dimensional wave equation on $O(\epsilon^{-1})$ scales with wave speed $\sqrt{f_0}$. We therefore introduce the comoving variables $\xi \equiv X_1 - \sqrt{f_0}T_1$ and $\eta \equiv X_1 + \sqrt{f_0}T_1$ and look for solutions of the form

$$a_r^{(0)} = A_1(\xi, X_2, T_2) + A_2(\eta, X_2, T_2) + A_0(X_2, T_2), \quad (2.75)$$

$$a_i^{(0)} = (b_+/b_-)^{1/2} \left[-A_1(\xi, X_2, T_2) + A_2(\eta, X_2, T_2) + \tilde{A}_0(X_2, T_2) \right]. \quad (2.76)$$

Combining Eqs. (2.73) and (2.74) together gives

$$2\sqrt{f_0}a_{r,\xi\eta}^{(1)} = (\partial_{T_2} - b'\mu_1 + b'^2a_r^{(0)}) (A_{2,\eta} - A_{1,\xi}) + A_{1,\xi\xi\xi} - A_{2,\eta\eta\eta} - \sqrt{f_0} (A_{1,\xi} + A_{2,\eta})_{X_2} \quad (2.77)$$

Requiring that A_1 and A_2 remain bounded as $|\xi| \rightarrow \infty$, $|\eta| \rightarrow \infty$, we obtain the following coupled equations for the slow evolution of the amplitudes A_1 and A_2 ,

$$(\partial_{T_2} + \sqrt{f_0}\partial_{X_2}) A_{1,\xi} = A_{1,\xi\xi\xi} + b'\mu_1 A_{1,\xi} - b'^2 (A_1 + A_0) A_{1,\xi}, \quad (2.78)$$

$$(\partial_{T_2} - \sqrt{f_0}\partial_{X_2}) A_{2,\eta} = A_{2,\eta\eta\eta} + b'\mu_1 A_{2,\eta} - b'^2 (A_2 + A_0) A_{2,\eta}. \quad (2.79)$$

Since the spatial average of A_1 and A_2 can be absorbed into A_0 and \tilde{A}_0 , we may assume $\langle A_1 \rangle = \langle A_2 \rangle = 0$, where $\langle \cdot \rangle$ indicates the average over the comoving space variables. Integrating both Eqs. (2.78) and (2.79) once and averaging Eqs. (2.73) and (2.74) with respect to ξ and η , respectively, we obtain finally a pair of equations that describe the interaction between the amplitude and oscillatory modes,

$$(\partial_{T_2} + \sqrt{f_0}\partial_{X_2}) A_1 = A_{1,\xi\xi} + (\mu_1 - A_0)A_1 - \frac{A_1^2 - \langle A_1^2 \rangle}{2}, \quad (2.80)$$

$$(\partial_{T_2} - \sqrt{f_0}\partial_{X_2}) A_2 = A_{2,\eta\eta} + (\mu_1 - A_0)A_2 - \frac{A_2^2 - \langle A_2^2 \rangle}{2}, \quad (2.81)$$

$$\tilde{A}_{0,T_2} - \sqrt{f_0}A_{0,X_2} = 0, \quad A_{0,T_2} - \sqrt{f_0}\tilde{A}_{0,X_2} = 2\mu_1 A_0 - \langle A_1^2 + A_2^2 \rangle - A_0^2. \quad (2.82)$$

Here the coefficient b' has been scaled out by suitably redefining A_1 , A_2 , A_0 , \tilde{A}_0 , and μ_1 . These equations generalize those derived by Knobloch and De Luca for counterpropagating waves on a trivial background [43] to the case of a nontrivial background.

Figures 2.33 and 2.34 show plots of the time evolution of Eq. (1.6) in a periodic domain of size $\Gamma = 200$ for $a_1 = 0.3$, $a_2 = 2.2$, $b = 0.5$, and $\mu = \mu_0 + 5 \times 10^{-6}$. The initial 20 roll periodic wavetrain is perturbed with a right-traveling wave with $q = 2\pi/\Gamma$ (figure 2.33) or a left-traveling wave with $q = 4\pi/\Gamma$ (figure 2.34). Both perturbations are of order 10^{-2} . Under these conditions, the wavetrain eventually collapses to 0 although a growing traveling modulation is visible in the demodulated solution as shown in figures 2.33(b) and 2.34(b). A comparison between the dynamics of the full equation (1.6) and the modulation equations is shown in (c), which demonstrates that the time dependence of $(b'^2/\epsilon^2)\text{Re}[\langle a \rangle]$ (solid line) is well approximated by the time evolution of the mean mode A_0 (dashed line).

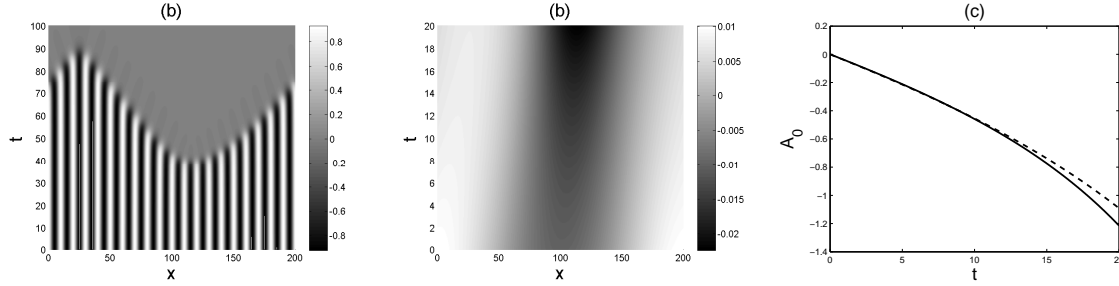


Figure 2.33: A 20 roll periodic wavetrain with PBC undergoing both amplitude and oscillatory instabilities. (a) Time evolution of $Re[A]$. (b) Time evolution of $Re[a]$. (c) Comparison of the evolution of the mean of the modulation mode (solid line) with the evolution of A_0 from Eq. (2.82) (dashed line). Domain size: $\Gamma = 200$. Parameter values: $a_1 = 0.3$, $a_2 = 2.2$, $b = 0.5$, and $\mu = \mu_0 + 5 \times 10^{-6}$. The initial condition is a periodic wavetrain with a superposed $q = 2\pi/\Gamma$ right-traveling wave of $O(10^{-2})$ amplitude.

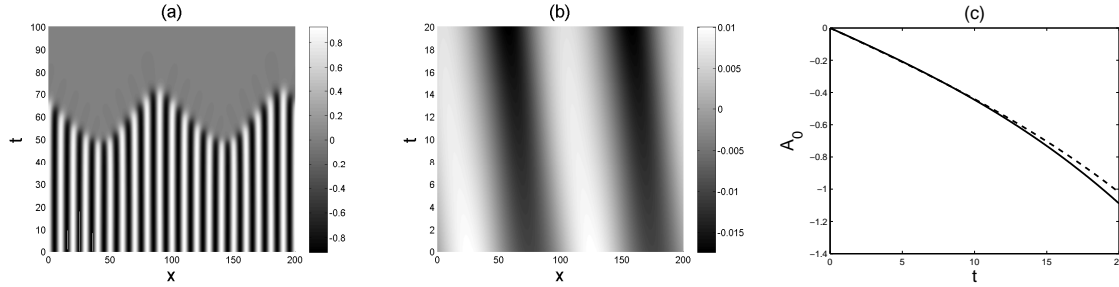


Figure 2.34: A 20 roll periodic wavetrain with PBC undergoing both amplitude and oscillatory instabilities. (a) Time evolution of $Re[A]$. (b) Time evolution of $Re[a]$. (c) Comparison of the evolution of the mean of the modulation mode (solid line) with the evolution of A_0 from Eq. (2.82) (dashed line). Domain size: $\Gamma = 200$. Parameter values: $a_1 = 0.3$, $a_2 = 2.2$, $b = 0.5$, and $\mu = \mu_0 + 5 \times 10^{-6}$. The initial condition is a periodic wavetrain with a superposed $q = 4\pi/\Gamma$ left-traveling wave of $O(10^{-2})$ amplitude.

2.6 Stability and dynamics of spatially localized solutions near the Maxwell point

In this section we study the stability and dynamics of spatially localized solutions near the Maxwell point. Dynamical properties of these solutions are important for understanding the location of the snaking region and the process of nucleation of periodic patterns in convective systems.

Stationary and nonstationary fronts

Among the spatially localized solutions, the front solutions determine the location of the Maxwell point and the associated protosnaking behavior. With the coefficients a_1 , a_2 , and b fixed, there is at most one stationary front solution to within the symmetries given in section 2.2. This solution connects the trivial state $A = 0$ to one of the periodic states. As shown in section 2.2, the front solution exists when $E = L = 0$ with coefficients $b > 0$, $\mu = \mu_M \equiv b^2/(16\beta) < 0$. In order to simplify the discussion that follows, we set without loss of generality $b = 1$ and obtain the explicit solution

$$R^2 = \frac{-4\mu_M}{e^{\pm 2\sqrt{-\mu_M}x} + 1}, \quad \phi_x = \frac{(a_1 + a_2)\mu_M}{e^{\pm 2\sqrt{-\mu_M}x} + 1}. \quad (2.83)$$

The selected wavenumber k_M at the Maxwell point is given by $k_M = (a_1 + a_2)\mu_M$.

The front solution can only be stable when the asymptotic states as $x \rightarrow \pm\infty$ are both stable and no unstable point eigenvalue is present [45]. The same argument also applies to other spatially extended solutions. Since μ is negative, the zero asymptotic state is always linearly stable. The stability of the competing periodic state is determined by the sign of the coefficient g here given by $g = \frac{8\mu_M^2}{3} [4 - a_2(a_1 + a_2)]$. Thus the competing periodic state is unstable when $a_2(a_1 + a_2) > 4$ and stable when $a_2(a_1 + a_2) < 4$. To check for the existence of unstable point eigenvalues when $g > 0$, we solve an eigenvalue problem analogous to Eq. (2.40), viz.

$$\begin{aligned} a_t = & a_{xx} + \left[2R^{-1}R_x + i \left(\frac{a_1 - a_2}{2} R^2 + \frac{2L}{R^2} \right) \right] a_x + i a_2 R^2 a_x^* \\ & + \left[bR^2 + \left(\frac{a_1^2 - a_2^2}{4} - 2 \right) R^4 + (a_2 - a_1)L + i(a_1 + a_2)RR_x \right] (a + a^*). \end{aligned} \quad (2.84)$$

We solve this problem using the Ansatz $a(x, t) = (u + v)e^{\sigma t} + (u^* - v^*)e^{\sigma^* t}$, where u and v are functions of x . The resulting eigenvalue problem takes the form

$$\sigma \begin{pmatrix} u \\ v \end{pmatrix} = \begin{pmatrix} \partial_{xx} + A\partial_x + C & i(B - a_2 R^2)\partial_x \\ i(B + a_2 R^2)\partial_x + iD & \partial_{xx} + A\partial_x \end{pmatrix} \begin{pmatrix} u \\ v \end{pmatrix}. \quad (2.85)$$

where

$$\begin{aligned} A &= 2R_x/R, \quad B = \frac{a_1 - a_2}{2} R^2 + \frac{2L}{R^2}, \\ C &= 2bR^2 + \left(\frac{a_1^2 - a_2^2}{2} - 4 \right) R^4 + 2(a_2 - a_1)L, \quad D = (a_1 + a_2) (R^2)_x. \end{aligned}$$

The temporal stability of the front solution depends on the coefficients a_1 and a_2 ; since $L = 0$ the stability of the solution with coefficients (a_1, a_2) is identical to that with coefficients $(-a_1, -a_2)$. The problem is solved using a spectral method with cosine and sine basis

functions with wavenumbers equal to integer multiples of π/Γ , where $\Gamma = 50/\sqrt{-\mu_M}$. The spectral matrix is truncated after the first 512 modes. The same procedure is also used for the stability calculation for the other spatially localized solutions examined below. The numerical results indicate that there is no unstable point eigenvalue for solutions with stable asymptotic states within the range $|a_1|, |a_2| \leq 10$, suggesting that this family of solutions is linearly stable. This results holds independently of the value of b provided only that $b > 0$.

Motion of the stable front can be generated by shifting the parameter μ slightly from the Maxwell point, i.e., by introducing a difference in “energy” between the two competing states. The existence of these moving front solutions has only been proved in the case $|a_1 + a_2| \ll 1$ [28] but our numerical simulations indicate that these traveling front solutions continue to exist when $|a_1 + a_2| = O(1)$. When $\mu < \mu_M$ the trivial state has the lower “energy” and the front therefore moves to eliminate the periodic wavetrain. The opposite occurs for $\mu > \mu_M$. The time evolution of such moving fronts with coefficients $a_1 = 1, a_2 = 1$ is shown in figure 2.36. Here we give the details of an asymptotic calculation of the resulting front speed when $|\mu - \mu_M| \ll 1$.

Equation (1.6), written in terms of R and $k \equiv \phi_x$, takes the form

$$R_t = (\mu - k^2)R + R_{xx} + [b + k(a_2 - a_1)] R^3 - R^5, \quad (2.86)$$

$$k_t = \left(k + \frac{a_1 + a_2}{2} R^2 \right)_{xx} + \left(\frac{2kR_x}{R} \right)_x. \quad (2.87)$$

According to the numerical results, both R and k drift slowly with certain speed c . In the comoving frame, we have

$$-cR_x = (\mu - k^2)R + R_{xx} + [b + k(a_2 - a_1)] R^3 - R^5, \quad (2.88)$$

$$-ck_x = \left(k + \frac{a_1 + a_2}{2} R^2 \right)_{xx} + \left(\frac{2kR_x}{R} \right)_x, \quad (2.89)$$

where x now refers to the space variable in the comoving frame. Equation (2.88) can also be written as

$$-cR_x = R_{xx} + \frac{1}{2}U_R, \quad (2.90)$$

where U is defined in Eq. (2.13). Integrating Eq. (2.89) once and multiplying it by R^2 leads to

$$L_x = R^2 c(k_\infty - k), \quad (2.91)$$

where k_∞ is the wavenumber of the periodic state as $x \rightarrow -\infty$. Assuming that the trivial solution is present at $x \rightarrow \infty$ we have

$$L = c \int_x^\infty R^2 (k - k_\infty) dx, \quad (2.92)$$

indicating that L is proportional to the speed of the front c , at least when c is small. Let $R = R_f + r$, where R_f is the amplitude of the stationary front solution and r is a small

perturbation. Substituting $R = R_f + r$ into Eq. (2.90) and collecting leading order terms yield

$$-cR_{f,x} \approx (\mu - \mu_M)R_f + \frac{3a_2 - a_1}{2}LR_f + r_{xx} + \frac{1}{2}U_{RR}(R_f; \mu_M, 0)r. \quad (2.93)$$

Multiplying this equation by $-2R_{f,x}$ and integrating over the spatial domain we obtain

$$2c \int_{\mathbb{R}} R_{f,x}^2 dx \approx (\mu - \mu_M) R_f^2|_{x=-\infty} + (a_1 - 3a_2) \int_{\mathbb{R}} LR_f R_{f,x} dx. \quad (2.94)$$

The contribution of the terms proportional to r vanishes since $R_{f,x}$ corresponds to the infinitesimal translation mode in the stationary case. After evaluating the integrals we have

$$c \approx \frac{3(\mu - \mu_M)}{2(-\mu_M)^{3/2}} [4 - a_2(a_1 + a_2)]^{-1}. \quad (2.95)$$

This expression reduces to the front speed as calculated in [28] when $a_1 + a_2 = 0$. The coefficient in the denominator is always positive for stable stationary front solutions and the sign of c is then in agreement with the energy argument. The approximate front speed agrees well with the numerical results when μ is close to μ_M as shown in figure 2.35.

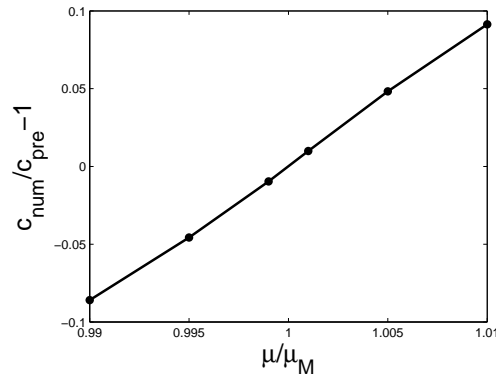


Figure 2.35: $c_{num}/c_{pre} - 1$ versus μ/μ_M for the front solutions when $a_1 = a_2 = 1$, where c_{num} is measured speed and c_{pre} is the predicted value.

For unstable fronts, we perform numerical simulations initialized with the stationary front solution and a superposed small amplitude localized perturbation at the center. Since the unstable part of the front lies in between the stable trivial state and stable periodic state, the perturbation can either grow or decay, depending on the details of the initial condition. If the front solution is initially slightly suppressed at the center, simulations reveal that the adjacent unstable part collapses, allowing the trivial state to invade the unstable state. Figure 2.37(a) shows this behavior when $a_1 = 2$, $a_2 = 3$; the speed of the resulting front is approximately 1.14. In figure 2.37(b), the coefficients used are the same as in figure 2.37(a) but the initial profile is slightly augmented at the center instead. This perturbation leads to

the growth of an unstable periodic state followed by a transition to a stable periodic state which then invades both the stable zero state and the unstable periodic state. The measured front speed between the stable and unstable periodic states is approximately 1.27 while that between stable periodic state and $A = 0$ is approximately 0.24.

In all these simulations domain truncation has been applied. In order to implement suitable boundary conditions we compute the dynamical behavior of $\tilde{A}(x, t) \equiv A(x, t)e^{-ik_M x}$, where $k_M = (a_1 + a_2)\mu_M$ is the asymptotic wavenumber as $x \rightarrow \pm\infty$, instead of dealing with A . Thus \tilde{A} tends to a constant as $x \rightarrow -\infty$ and this constant can be chosen to be a real number. Cosine and sine functions are applied as the basis functions with wavenumbers equal to integer multiples of π/Γ . A similar method is also used in the simulation of the dynamics of perturbed hole and pulse solutions discussed below.

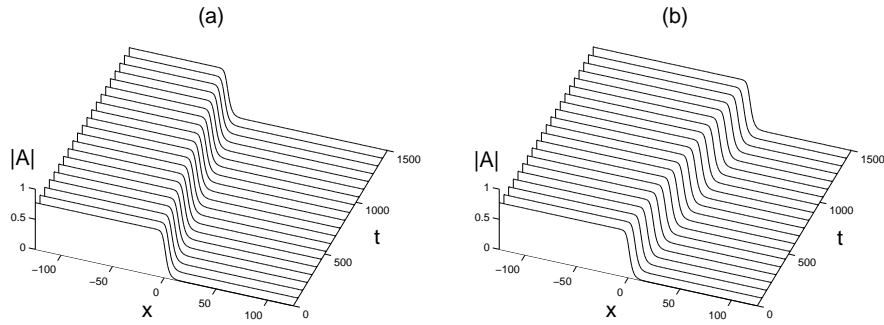


Figure 2.36: Time evolution of the profile of a stable front with μ perturbed from μ_M . Parameter values: $a_1 = 1$, $a_2 = 1$, $b = 1$. (a) $\mu = 1.01\mu_M$. (b) $\mu = 0.99\mu_M$.

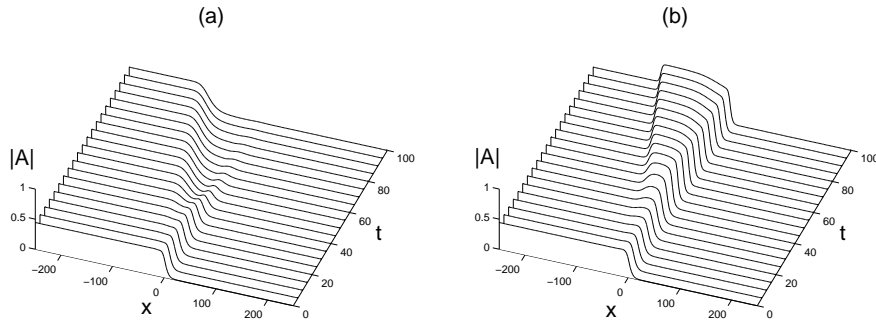


Figure 2.37: Time evolution of the profile of an unstable front. Parameter values: $a_1 = 2$, $a_2 = 3$, $b = 1$, and $\mu = -0.0492$. The center of the front is suppressed by a factor of 0.99 in (a) and augmented by 1.01 in (b).

The front motion presented in figure 2.37 is an example of front propagation into an unstable state. In many cases the speed of the resulting front is selected by the marginal

stability condition [46, 32]. This prediction focuses on modes of the form

$$a_{\tilde{q},\lambda} \sim \beta_1 e^{i\tilde{q}x} + \beta_2^* e^{-i\tilde{q}^*x}, \quad (2.96)$$

where \tilde{q} is now a complex wavenumber, $\tilde{q} \equiv q + i\lambda$. Thus λ represents the spatial decay or growth rate of the mode. This mode has the dispersion relation $\sigma_{\pm}(\tilde{q})$, where σ_{\pm} is given in Eq. (2.43). In the present case it is the $+$ branch of the dispersion relation that is relevant. The linear spreading speed is thus given by the relation

$$v^* \equiv i \frac{d\sigma_+}{d\tilde{q}} = \frac{\text{Re}[\sigma_+(\tilde{q})]}{\lambda}, \quad (2.97)$$

or equivalently

$$v^* = \min_{\lambda} \max_q \left\{ \frac{\text{Re}[\sigma_+(\tilde{q})]}{\lambda} \right\}. \quad (2.98)$$

Pinch point analysis in the complex \tilde{q} plane [32] now leads to the prediction

$$q = 0, \quad \lambda^{*2} = \frac{g}{2(2g - f)} \left(2f - 3g + \sqrt{9g^2 - 4fg} \right), \quad (2.99)$$

and hence, from Eq. (2.98), to the explicit result

$$v^* = \frac{\lambda^*}{1 + g/\lambda^{*2}}. \quad (2.100)$$

For the parameter values of figure 2.37 this expression predicts that $v^* = 1.1642$, compared with the measured speeds $v^* = 1.14$ in figure 2.37(a) and $v^* = 1.27$ in figure 2.37(b). Moreover, since $q = 0$ the wavenumber k^* selected by the invading front [46]

$$k^* \equiv \frac{\text{Im}[\sigma_+(\tilde{q}) + i\tilde{q}v^*]}{v^*} = 0. \quad (2.101)$$

Figure 2.38 shows these results in the (a_1, a_2) plane.

Note that figure 2.37(b) shows a second front as well, in which the stable large amplitude state invades the stable trivial state $A = 0$. The speed of this type of front cannot be obtained from the linear stability analysis described above [32].

Stationary holes and pulses

Equation (1.6) possesses several other spatially localized solutions of interest, in addition to the front solutions just described. We focus here on the case $b = 1$, $\beta < 0$ for which the potential energy $U(R, L = 0)$ takes the form shown in figure 2.39. Thus hole solutions exist for μ both greater and less than μ_M .

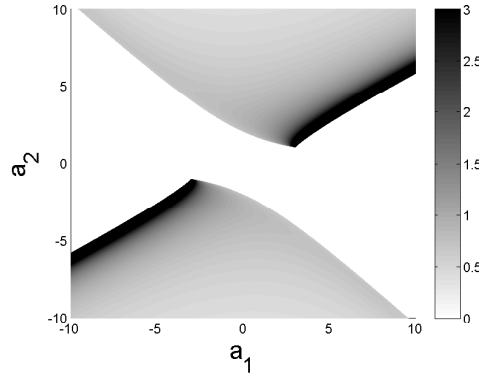


Figure 2.38: The linear spreading speed of the unstable front solution in the (a_1, a_2) plane. As (a_1, a_2) approaches the line $\beta = 0$, v^* diverges. We therefore cut off v^* at $v^* = 3$ and use black color to indicate the parameter range where $v^* \geq 3$. In addition, v^* is set equal to 0 in regions where either β or g is nonnegative (white color).

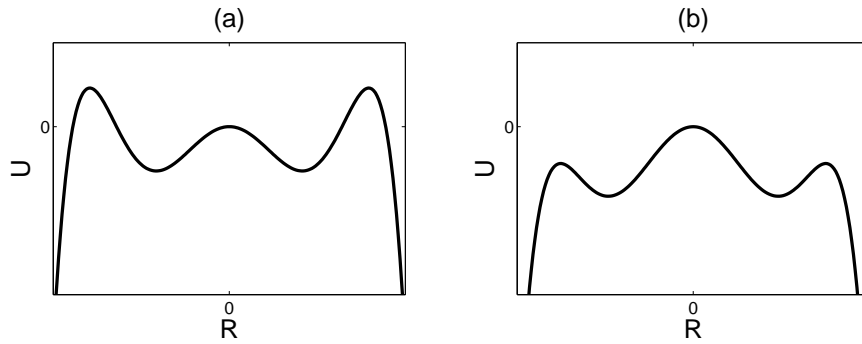


Figure 2.39: The potential energy $U(R, L = 0)$ when (a) $\mu > \mu_M$ and (b) $\frac{4\mu_M}{3} < \mu < \mu_M$.

When $\mu > \mu_M$ the holes take the form

$$R^2 = \frac{\xi_1 \xi_2 \sinh^2 \left(\sqrt{\mu + \frac{\xi_1}{2}} x \right)}{\xi_2 \cosh^2 \left(\sqrt{\mu + \frac{\xi_1}{2}} x \right) - \xi_1} \quad (2.102)$$

with asymptotic wavenumber $k_\infty = -(a_1 + a_2)\xi_1/4$ as $x \rightarrow \pm\infty$, where

$$\xi_1 = -\frac{4\mu_M}{3} \left(2 + \sqrt{4 - \frac{3\mu}{\mu_M}} \right), \quad \xi_2 = \frac{8\mu_M}{3} \left(-1 + \sqrt{4 - \frac{3\mu}{\mu_M}} \right). \quad (2.103)$$

The region of stability of these solutions in parameter space is shown in figure 2.40 for the case $\mu = 0.99\mu_M > \mu_M$ and indicated by red (or gray) color. Most of the solutions with stable

asymptotic states are stable except those with $\beta \approx 0$, as indicated in the figure. Figure 2.41 shows the dynamical evolution in the unstable case $(a_1, a_2) = (2, 0)$, starting from an initial condition with $L = 0$. For these coefficients the asymptotic states $x \rightarrow \pm\infty$ are stable but the hole state is nevertheless unstable. To reveal the instability the amplitude $|A|$ in a small interval around the center of the hole has been multiplied by a factor 0.99 in (a) and by 1.01 in (b), and the results used as initial conditions in a time evolution code. In the former case the solution converges quickly to a nearby stationary hole solution with $L \neq 0$. In the latter case the solution relaxes to the stable asymptotic state.

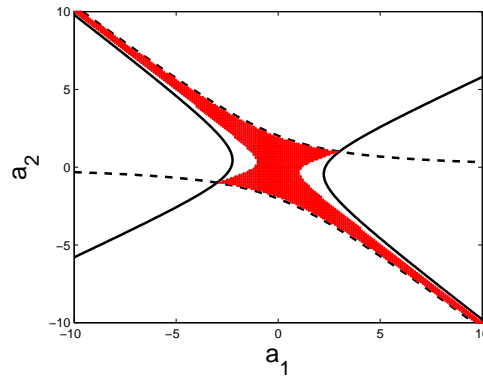


Figure 2.40: (Color online) The case $\mu = 0.99\mu_M$. Solid line: $\beta = 0$. Dashed line: $g = 0$. The quantity β is negative between the solid lines while g is positive between the dashed lines. Hole solutions are stable in the red (or gray) region.

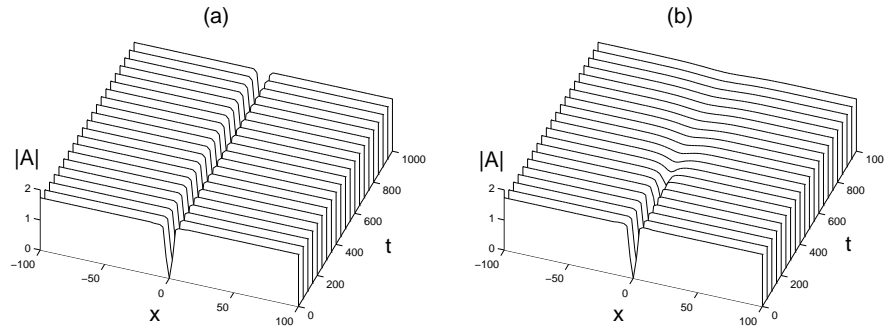


Figure 2.41: Dynamics of an unstable $L = 0$ hole solution when $\mu = 0.99\mu_M$ and $(a_1, a_2) = (2, 0)$. The amplitude at center of the hole is multiplied by a factor 0.99 in (a) and by 1.01 in (b). In (a) the hole evolves to a nearby hole with $L \approx 0.01 \neq 0$ and nonzero amplitude at the center; in (b) the hole disappears.

When $\frac{4\mu_M}{3} < \mu < \mu_M$ the stationary hole solutions take the form

$$R^2 = \frac{\xi_1 \xi_2 \cosh^2 \left(\sqrt{\mu + \frac{\xi_1}{2}} x \right)}{\xi_1 + \xi_2 \sinh^2 \left(\sqrt{\mu + \frac{\xi_1}{2}} x \right)}. \quad (2.104)$$

Here ξ_1 and ξ_2 are as defined in Eq. (2.103) and the asymptotic wavenumber remains $k_\infty = -(a_1 + a_2)\xi_1/4$. The region of stability of these hole solutions in parameter space is shown in figure 2.42 for the case $\mu = 1.01\mu_M < \mu_M$ and indicated by red (or gray) color. In contrast with the case $\mu > \mu_M$, almost all of the solutions are now unstable except for those with $\beta \approx 0$. Figure 2.43 shows the dynamical evolution in the unstable case $(a_1, a_2) = (1, 1)$ with stable asymptotic states. To generate the initial condition the amplitude at the center of the hole has been multiplied by a factor 0.99 in (a) and by 1.01 in (b). If the solution is initially suppressed at the center the central part collapses to zero and invades the periodic structure in both directions as expected. However, if the solution is initially augmented at the center the amplitude at the central part overshoots the amplitude of the periodic state but then decays back. This behavior is a consequence of the non-gradient nature of the system when $a_2 \neq 0$.

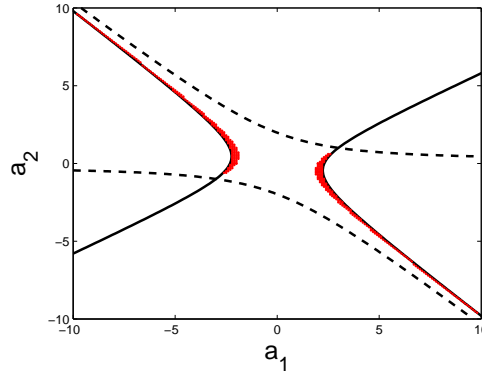


Figure 2.42: (Color online) The case $\mu = 1.01\mu_M$. Solid line: $\beta = 0$. Dashed line: $g = 0$. The quantity β is negative between the solid lines while g is positive between the dashed lines. Hole solutions are stable in the red (or gray) region.

Pulses connecting the trivial state to itself exist only when $\mu_M < \mu < 0$. These solutions take the form

$$R^2 = \frac{\xi_1 \xi_2}{\xi_1 + (\xi_2 - \xi_1) \cosh^2(\sqrt{-\mu} x)}, \quad (2.105)$$

where

$$\xi_1 = -4\mu_M \left(1 - \sqrt{1 - \frac{\mu}{\mu_M}} \right), \quad \xi_2 = -4\mu_M \left(1 + \sqrt{1 - \frac{\mu}{\mu_M}} \right).$$

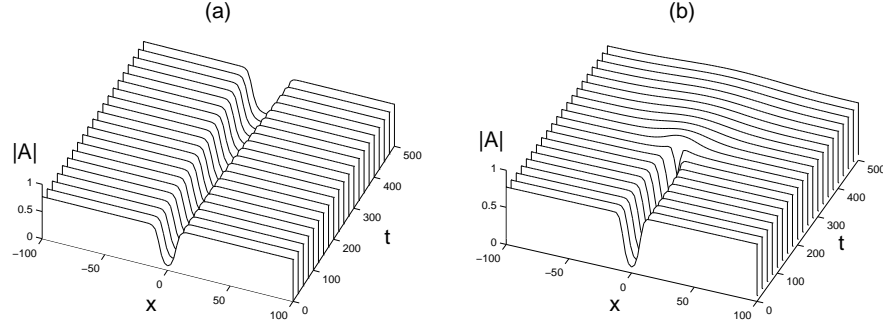


Figure 2.43: Dynamics of an unstable $L = 0$ hole solution when $\mu = 1.01\mu_M$ and $(a_1, a_2) = (1, 1)$. The amplitude at the center of the hole has been multiplied by a factor 0.99 in (a) and by 1.01 in (b). In (a) the hole expands; in (b) the hole decays.

All such solutions appear to be unstable when $\mu = 0.99\mu_M$ at least within $|a_1|, |a_2| \leq 10$. Dynamical evolution of the unstable case $(a_1, a_2) = (1, 1)$ is shown in figure 2.44. Depending on the perturbation applied initially, the solution either collapses to $A = 0$ or broadens into a periodic state.

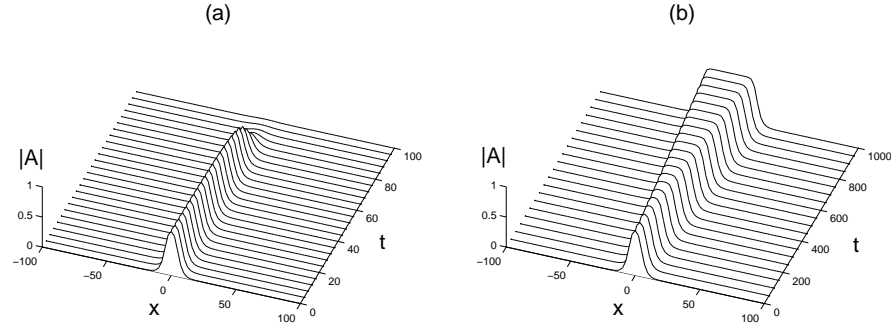


Figure 2.44: Dynamics of an unstable $L = 0$ pulse solution when $\mu = 0.99\mu_M$ and $(a_1, a_2) = (1, 1)$. The amplitude at the center of the hole has been multiplied by a factor 0.99 in (a) and by 1.01 in (b). In (a) the pulse decays to the flat state $A = 0$; in (b) the pulse broadens into a periodic state.

In the previous discussion we focused on localized states with $L = 0$. Also of interest is the case when k_∞ , the asymptotic wavenumber of the localized state as $x \rightarrow \pm\infty$, is equal to k_M , the wavenumber at $\mu = \mu_M$. When μ is perturbed from μ_M , L becomes nonzero but remains small. The only stationary spatially localized states allowed are holes and these take the explicit form

$$R^2 = \xi_1 + \frac{(\xi_2 - \xi_1)(\xi_3 - \xi_1)}{\xi_2 - \xi_1 + (\xi_3 - \xi_2)\cosh^2 \left[\sqrt{\beta(\xi_3 - \xi_1)(\xi_1 - \xi_2)}x \right]},$$

where ξ_1 is the square of the amplitude of the asymptotic periodic state, ξ_2 is the square of the minimum amplitude of the solution, and $\xi_3 \neq \xi_1, \xi_2$ is the remaining root of the polynomial $\xi [E - U(\sqrt{\xi})]$. We computed the stability properties of these solutions at $\mu = 1.01\mu_M$ and $0.99\mu_M$ and found no stable solution when $\mu = 1.01\mu_M$ within $|a_1|, |a_2| \leq 10$. However, when $\mu = 0.99\mu_M$ the solutions are stable within $|a_1|, |a_2| \leq 10$.

To examine the dynamics that result from the instability, we set $\mu = 1.01\mu_M$ and choose an unstable solution with $(a_1, a_2) = (1, 1)$. The resulting time evolution is shown in figure 2.45 and resembles that in figure 2.43 in which the solution either collapses to $A = 0$ or approaches a periodic state in an oscillatory fashion. When $\mu = 0.99\mu_M$, we choose $(a_1, a_2) = (1, 1.5)$; the resulting time evolution is shown in figure 2.46. This time the perturbation applied at the center is larger and generates oscillatory behavior near the center but the oscillation decays as time increases and the solution converges to the unperturbed solution.

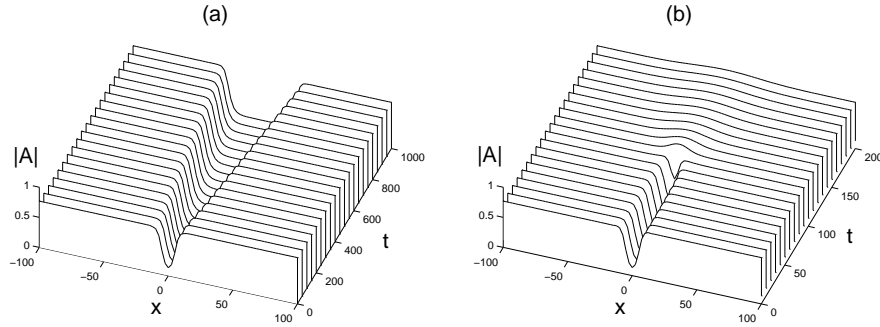


Figure 2.45: Evolution of an unstable hole solution with $k_\infty = k_M$ when $\mu = 1.01\mu_M$ and $(a_1, a_2) = (1, 1)$. The amplitude at the center of the hole has been multiplied by a factor 0.99 in (a) and by 1.01 in (b). In (a) the hole broadens into a growing region filled with the flat state $A = 0$; in (b) the hole decays into a constant amplitude periodic state.

2.7 Discussion

In this chapter, we explore in detail the properties of stationary solutions of GL35, both analytically and numerically. The presence of the coefficients a_1 and a_2 in Eq. (1.6) is responsible for a variety of new and interesting phenomena, many due to the loss of variational structure when $a_2 \neq 0$. These coefficients are readily derivable from systems at the transition between subcritical to supercritical bifurcation as shown in Appendix A. The work can be used to predict and classify the stationary and dynamical properties of weakly subcritical and supercritical pattern forming systems. Altogether, we identified four critical codimension-one curves in the (a_1, a_2) plane, corresponding to $\beta = 0$ (Eq. (2.13)), $a_1^2 - a_2^2 = 4$ (Eq. (2.14)) and $(a_2 - a_1)^2 = 4$ (Eq. (2.18)) and $a_2(a_1 + a_2) = 4$ (Eq. (2.19)). Additional codimension-one curves such as $a_1 + a_2 = 0$ and $a_2 = 0$ can also be significant.

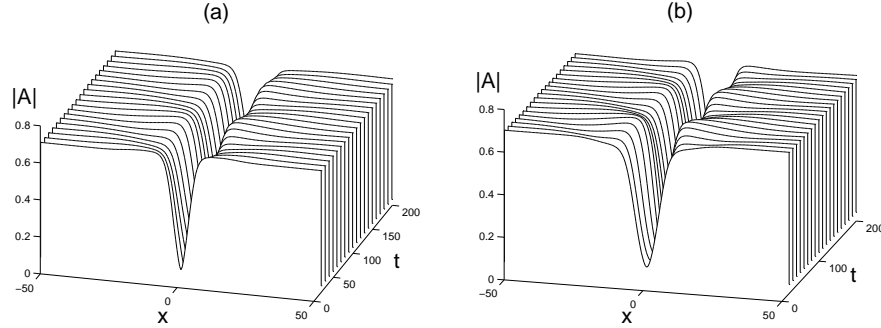


Figure 2.46: Evolution of a stable hole solution with $k_\infty = k_M$ when $\mu = 0.99\mu_M$ and $(a_1, a_2) = (1, 1.5)$. The amplitude at the center of the hole has been multiplied by a factor 0.9 in (a) and by 1.1 in (b). The oscillations decay with increasing time.

We have computed a variety of both primary solution branches corresponding to periodic patterns with either the critical wavenumber ($k = 0$, band center) or with a shifted wavenumber ($k \neq 0$, off-center) and determined their stability properties with respect to wavelength changing perturbations of Eckhaus type. We have also computed the different types of secondary branches that result. These correspond in general to quasiperiodic states, although on a finite domain both the solution amplitude and phase must of course satisfy the boundary conditions. The branches that bifurcate from the primary $k = 0$ branch exhibit protosnaking near a point $\mu = \mu_M$. At this parameter value one finds a heteroclinic connection between the trivial solution $A = 0$ and a periodic solution $A = R_M \exp(ik_M x)$ with a well-defined wavenumber k_M . The presence of these heteroclinic connections, and the associated wavenumber selection process are of particular interest since they play a large role in the interconnections between the $k = 0$ and $k \neq 0$ branches.

On the stability of periodic wavetrains, these solutions become unstable through two different mechanisms: one is the result of an unstable phase mode (Eckhaus instability) while the other is a consequence of an interaction between amplitude and oscillatory modes. In the former case we examined the bifurcations to spatially localized solutions within appropriate phase equations and investigated the evolution of the instability using direct numerical integration. The phase equation description breaks down at phase slips whereby the wavelength of the solution changes abruptly but coarsening of the structure may take place prior to this event. In the latter case the instability is oscillatory and the evolution takes the form of waves. The evolution of these waves is described by a pair of equations of Fisher-Kolmogorov type for the amplitudes of the left/right traveling waves coupled to an amplitude mode.

A systematic study of different spatially localized solutions was also performed. Solutions homoclinic to the trivial state (pulses) or to a periodic state (holes) were found near the heteroclinic connection (front) between the trivial and periodic states forms. The formation of such a front is associated with protosnaking behavior. We have found that such fronts are stable when the asymptotic states are stable and vice versa. Away from the Maxwell point

the fronts persist but move with a speed that depends on the distance from the Maxwell point. When the periodic state is unstable a wave of constant form can nonetheless be present and takes the form of a invasion front whereby a stable state invades an unstable state. We have computed the speed of such invasion fronts assuming that this speed is selected by the marginal stability criterion and showed that the resulting speed is in reasonable agreement with speeds measured in direct simulations of GL35. Stability properties of analytically determined pulse-like and hole-like solutions were found numerically and in each case the stability region in the (a_1, a_2) plane was determined.

Chapter 3

Large-scale Mode in Pattern Formation

Convection in a horizontal fluid layer rotating about the vertical or subject to an imposed vertical magnetic field provides one of the classic examples of hydrodynamic instability [6]. The system is of interest because convection can set in either via an exchange of stability (a steady state bifurcation) or via overstability. Recent interest has focused on the study of spatially localized structures in these systems. In two-dimensional convection with stress-free boundary conditions, the formation of such states is strongly influenced by the interaction between convection and a large scale mode: zonal velocity in rotating convection and magnetic flux in magnetoconvection. The localized structures are embedded within a self-generated shear layer or a magnetic field-free region with a compensating effect outside of the structure. These states are organized within a bifurcation structure called slanted snaking and are present even when periodic convection sets in supercritically.

In this chapter, I will present some numerical results and explain the observed bifurcation behavior using a modulation equation approach. The emphasis will be put on the modulation behavior near a codimension-two point where the leading order theory described in [18] becomes invalid through the vanishing of a cubic term in the stationary equation. Another aspect that will be discussed in the chapter is the breaking of stress-free boundary conditions.

Throughout this chapter, I use RC for rotating convection and MC for magnetoconvection. The chapter builds upon work that appears in [17, 47].

3.1 Rotating convection and magnetoconvection

The dimensionless equations governing two-dimensional convection in a Boussinesq fluid layer subject to a vertical magnetic field $B_0 \hat{\mathbf{z}}$ or uniform rotation with angular velocity $\Omega \hat{\mathbf{z}}$ are (MC)

$$\sigma^{-1} [\nabla^2 \psi_t + J(\psi, \nabla^2 \psi)] = Ra \theta_x + \zeta Q [\nabla^2 A_z + J(A, \nabla^2 A)] + \nabla^4 \psi, \quad (3.1)$$

$$\theta_t + J(\psi, \theta) = \psi_x + \nabla^2 \theta, \quad A_t + J(\psi, A) = \psi_z + \zeta \nabla^2 A, \quad (3.2)$$

and (RC)

$$\sigma^{-1} [\nabla^2 \psi_t + J(\psi, \nabla^2 \psi)] = Ra\theta_x - Ta v_z + \nabla^4 \psi, \quad (3.3)$$

$$\theta_t + J(\psi, \theta) = \psi_x + \nabla^2 \theta, \quad \sigma^{-1} [v_t + J(\psi, v)] = Ta\psi_z + \nabla^2 v, \quad (3.4)$$

where $J(u, v) \equiv u_x v_z - u_z v_x$. Here $\psi(x, z, t)$ is the poloidal stream function with z the vertical coordinate. The fluid velocity in the x - z plane is $\mathbf{u} = (-\psi_z, \psi_x)$. The field $A(x, z, t)$ represents the departure of the magnetic potential from that responsible for the imposed magnetic field $B_0 \hat{\mathbf{z}}$, $v(x, z, t)$ represents the zonal velocity (i.e., the y component of the velocity), while θ measures the departure of the temperature from the conduction profile. We use the height h of the layer as the unit of length, the thermal diffusion time in the vertical h^2/κ (κ is the thermal diffusivity) as the unit of time and the imposed temperature difference $\Delta\Theta$ as the unit of temperature. The resulting systems are specified by the following dimensionless numbers: the Prandtl number σ , the Rayleigh number Ra , the Chandrasekhar number Q , the Taylor number Ta , and the diffusivity ratio ζ

$$\sigma = \frac{\nu}{\kappa}, \quad Ra = \frac{g\alpha\Delta\Theta h^3}{\kappa\nu}, \quad Q = \frac{B_0^2 h^2}{\mu_0 \rho \nu \eta}, \quad Ta = \frac{2\Omega h^2}{\nu}, \quad \zeta = \frac{\eta}{\kappa}, \quad (3.5)$$

where μ_0 is the magnetic permeability, ρ is the density of the fluid, ν is the kinematic viscosity, η is the magnetic diffusivity, g is the gravitational acceleration, and α is the thermal expansion coefficient.

Stress-free and fixed temperature boundary conditions are applied at the upper and lower boundaries

$$\psi = \psi_{zz} = \theta = 0, \quad A_z \text{ or } v_z = 0 \quad (3.6)$$

with periodic boundary conditions (PBC) in the horizontal with spatial period Γ that is large compared with the onset wavelength λ_c of convection. With these boundary conditions, both systems possess a trivial solution $\psi = \theta = 0$, $A = 0$ (or $v = 0$), corresponding to the pure conduction state. The solution is present for all values of Ra and its instability is responsible for triggering convection. The onset of steady, spatially periodic convection from the conduction state can be predicted by linear stability analysis [6]. A similar analysis will be given later in section 3.6 with mixed boundary conditions. The critical Rayleigh number Ra_c is the minimum Rayleigh number for which the conduction state is marginally stable, and is equal to $2p^3/\pi^2$ in MC and $3p^2$ in RC. The corresponding critical wavenumbers k satisfy

$$Q\pi^4 = p^2(2k^2 - \pi^2), \quad Ta^2\pi^2 = p^2(2k^2 - \pi^2), \quad (3.7)$$

respectively, where $p \equiv k^2 + \pi^2$. The properties of the convection that results are in turn affected by the symmetries of Eqs. (3.1)–(3.4) together with the given boundary conditions. These include equivariance under horizontal translations, i.e., $x \rightarrow x + \ell$ with the other variables unchanged, as well as the two reflections

$$\begin{aligned} R_1 &: (x, z) \rightarrow (-x, z), \quad (\psi, \theta) \rightarrow (-\psi, \theta), \quad A \rightarrow -A \text{ or } v \rightarrow -v, \\ R_2 &: (x, z) \rightarrow (x, -z), \quad (\psi, \theta, A \text{ or } v) \rightarrow (-\psi, -\theta, A \text{ or } v). \end{aligned}$$

The stress-free boundary conditions play important roles in what follows since with these boundary conditions A and v are defined only up to a constant, i.e., A and v are phase-like variables. Moreover, owing to the PBC applied in the horizontal the spatial averages of A and v are constant in time. In the following subsections, we first show stationary solutions of RC, obtained using a numerical continuation algorithm [17].

Localized states in the subcritical regime

As Ra increases steady convection sets in at $Ra_c = 2p^3/\pi^2$. As the Taylor number Ta increases Ra_c moves to higher values: rotation stabilizes the conduction state against convection. For small Ta convection is supercritical but becomes subcritical with increasing Ta whenever the Prandtl number is sufficiently small. This is so for both stress-free and no-slip boundary conditions [51, 52].

In this subsection we describe the results for $\sigma = 0.1$ and several different values of Ta . Figure 3.1 shows the average poloidal kinetic energy,

$$\mathcal{E} \equiv \frac{1}{2\Gamma} \int_D (\psi_x^2 + \psi_z^2) dx dz \quad (3.8)$$

as a function of Ra when $Ta = 20$. Here D corresponds to the whole spatial domain. For this value of Ta convection sets in at $Ra = Ra_c \approx 1179.2$ and it does so with critical wavenumber $k_c \approx 3.1554$. The results are obtained in a periodic domain of length $\Gamma = 20\pi/k_c$. The figure shows the branch of steady periodic convection with 10 wavelengths in the domain, labeled P_{10} . The branch bifurcates subcritically but turns around at a saddle-node. The figure also shows a pair of branches of even and odd parity localized states, labeled L_{10}^\pm , that bifurcate subcritically from P_{10} at small amplitude. Initially both solutions take the form of weakly modulated wavetrains, but as Ra approaches the leftmost saddle-nodes the modulation becomes strongly nonlinear resulting in the formation of convectons of even and odd parity (figure 3.2). Beyond the leftmost saddle-nodes the two branches intertwine forming the so-called slanted snaking structure, along which the convectons gradually increase in length by nucleating new cells at either end. Because of the slant in the snaking structure the localized states move towards larger values of the Rayleigh number and their wavelength grows (figure 3.2). As a result of this Rayleigh number dependence of the convecton wavelength the domain Γ becomes almost full when the convectons have grown to 4 wavelengths. At this point the structure resembles a periodic wavetrain with defects a distance Γ apart and the snaking stops. The branches now undergo a loop required to squeeze in an extra pair of cells and terminate on P_5 with 5 wavelengths in the domain Γ (figure 3.1).

The lower panels in figure 3.2 show the profile of the depth-integrated zonal velocity

$$V(x) \equiv \int_0^1 v(x, z) dz. \quad (3.9)$$

We see that the presence of convection imprints a step-like structure on this profile. This structure turns into a saw-tooth profile by the time the branches terminate on the branch

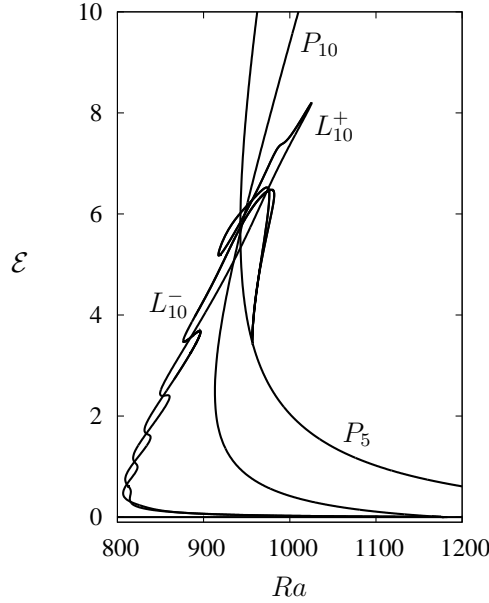


Figure 3.1: Bifurcation diagram showing \mathcal{E} as a function of Ra for slanted snaking when $Ta = 20$ and $\sigma = 0.1$. The branches of localized states L_{10}^{\pm} in a $\Gamma = 10\lambda_c$ domain are shown. They bifurcate in a secondary bifurcation on the branch P_{10} of periodic convection with 10 pairs of counter-rotating rolls in Γ and connect to P_5 , the branch of 5 pairs of counter-rotating rolls in Γ . The solutions at each saddle-node during the snaking process are shown in figure 3.2.

P_5 of periodic states. To understand this behavior we first note that the symmetry R_2 implies that clockwise and counterclockwise cells have the same effect on $V(x)$; moreover, the symmetry R_1 implies that the slope of $V(x)$ is unaffected by reflection in $x = 0$. In the periodic state (top panels) $V(x)$ varies linearly across each convection cell with steeper diffusive layers of the opposite slope between adjacent cells. These diffusive layers are quite broad since their dimensional width is $Re^{-1/2}h$, where $Re \equiv Uh/\nu$ is the Reynolds number; since the flow speed $U \sim \kappa/h$ when $Ra \sim Ra_c$ the dimensionless width $\sim \sigma^{1/2}$. The effect of the cellular motion outside these layers is most easily discussed in terms of the relation

$$\sigma \frac{dV}{dx} = - \int_0^1 \psi_z v dz, \quad (3.10)$$

obtained from the second equation in Eq. (3.4) upon integration over z followed by integration once in x . Thus nonzero values of the averaged Reynolds stress are responsible for the presence of a linear profile $V(x)$ across the cell.

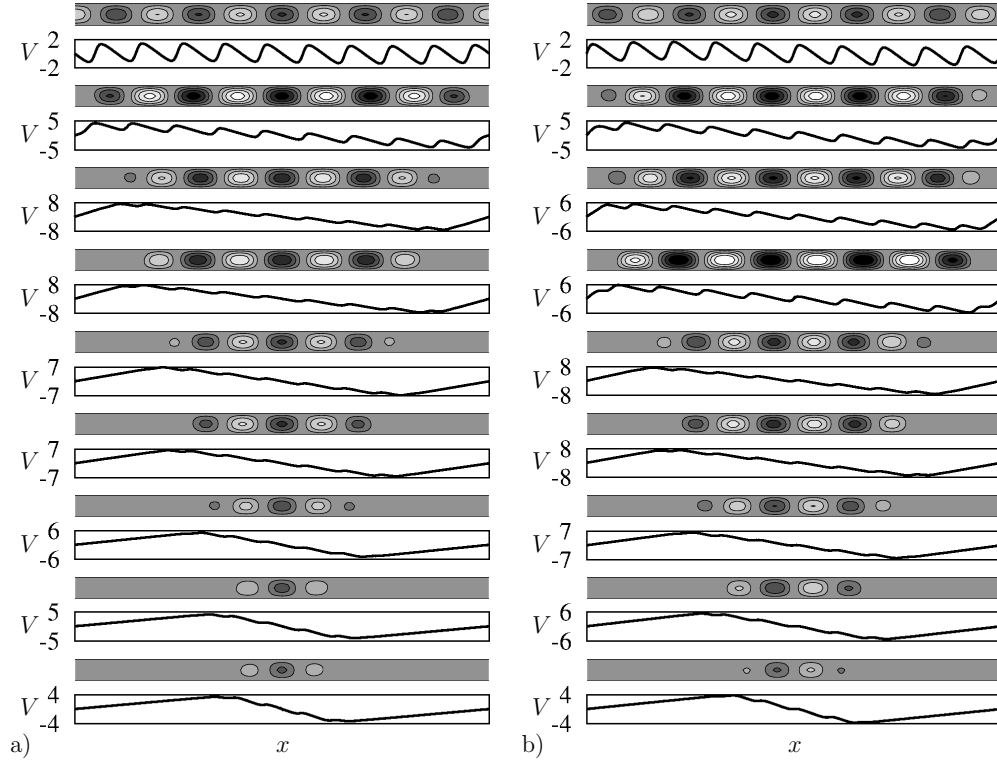


Figure 3.2: Solution profiles at successive saddle-nodes on (a) L_{10}^- , (b) L_{10}^+ in figure 3.1. Upper panels show isovals of the streamfunction with light (dark) regions corresponding to clockwise (counterclockwise) flow. Lower panels show the profiles of $V(x)$. Topmost solutions correspond to the termination point on P_5 .

Localized states in the supercritical regime

As σ is increased, the primary branch of periodic states becomes less subcritical and a transition occurs towards supercriticality. Figure 3.3 presents the bifurcation diagram for $\sigma = 0.6$ and $Ta = 40$ in a domain $\Gamma = 10\lambda_c$ where, at this Taylor number, the critical wavenumber $k_c = 4.0481$. For these parameter values the primary solution branch bifurcates supercritically at $Ra = Ra_c \approx 2068$. This branch loses stability almost immediately, creating a pair of branches of spatially modulated states. These states behave in exactly the same way as in the subcritical case. In the present case both L_{10}^\pm branches terminate together on the P_7 branch. Figure 3.4 shows the solutions along these branches using the same representation as used in figure 3.2. The solutions are qualitatively similar to those in figure 3.2 except for broader diffusive layers between adjacent cells owing to the larger σ . However, the localized states are still accompanied by strong negative shear within the structure that serves to reduce the local rotation rate, with a compensating prograde shear zone outside. Thus the convectons are embedded in a self-generated shear zone exactly as in the subcritical case.

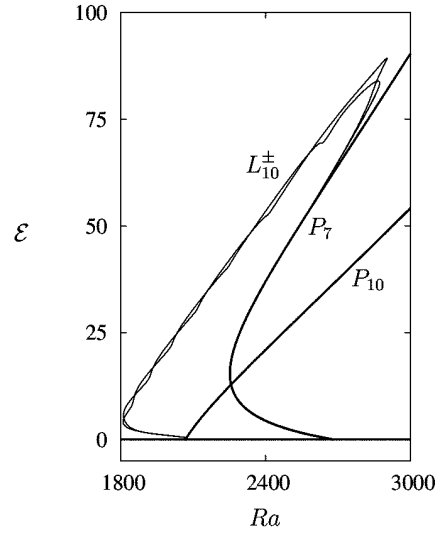


Figure 3.3: Bifurcation diagram showing \mathcal{E} as a function of Ra for the periodic states P_{10} , P_7 and for the branches L_{10}^{\pm} of spatially localized states. The parameters are $Ta = 40$, $\sigma = 0.6$ and $\Gamma = 10\lambda_c$.

We also plot in figures 3.5 and 3.6 the bifurcation diagrams and the profiles along the branches of even parity convectons for $Ta = 50$ and $Ta = 100$. While the convectons are in both cases well localized near the left saddle-nodes (albeit less so when Ta is larger) the figures reveal a significant change in the wavelength of the cells comprising them. In figure 3.5 the cells are initially broad and remain so until maximum energy is reached; thereafter the wavelength decreases rapidly and the branch terminates on P_{10} . In contrast, the wavelength of the cells when $Ta = 100$ (figure 3.6) hardly changes as \mathcal{E} increases from small values to large. At the same time the dimples representing nucleation events in figure 3.5 disappear and the convecton branch exhibits "smooth snaking" [53] with continuous and gradual appearance of new cells and no abrupt nucleation events. We surmise that the sudden change in slope of the slanted snaking that takes place is related to this change in cell wavelength and note, in particular, that broader cells are more efficient at transporting heat since in narrower cells such as those favored at larger rotation rates the rising plumes exchange more heat with falling plumes, thereby reducing their efficiency and hence the associated Nusselt number. Thus for small Ta the length scale of convection is selected primarily by thermal effects, while for large Ta the length scale is selected primarily by a competition between the tendency towards a Taylor-Proudman balance and the requirement that the flow transport heat at the level specified by the Rayleigh number. In the former regime localization is strong and nucleation of new cells occurs at well-defined Rayleigh numbers. In contrast, the latter regime is characterized by weak localization while new cells grow gradually over a range of Rayleigh numbers.

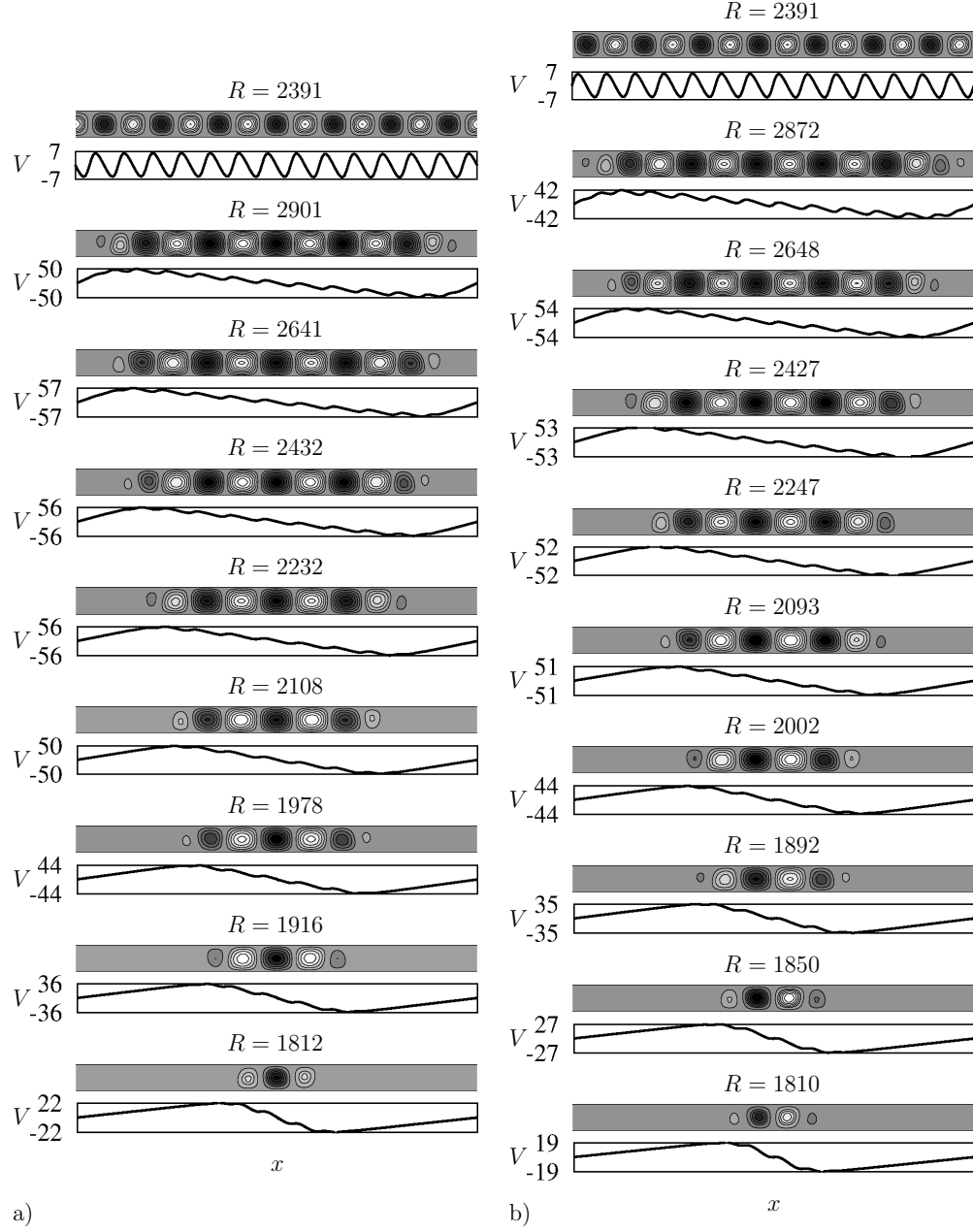


Figure 3.4: Same as figure 3.2 but for the localized solutions along (a) L_{10}^- and (b) L_{10}^+ in figure 3.3.

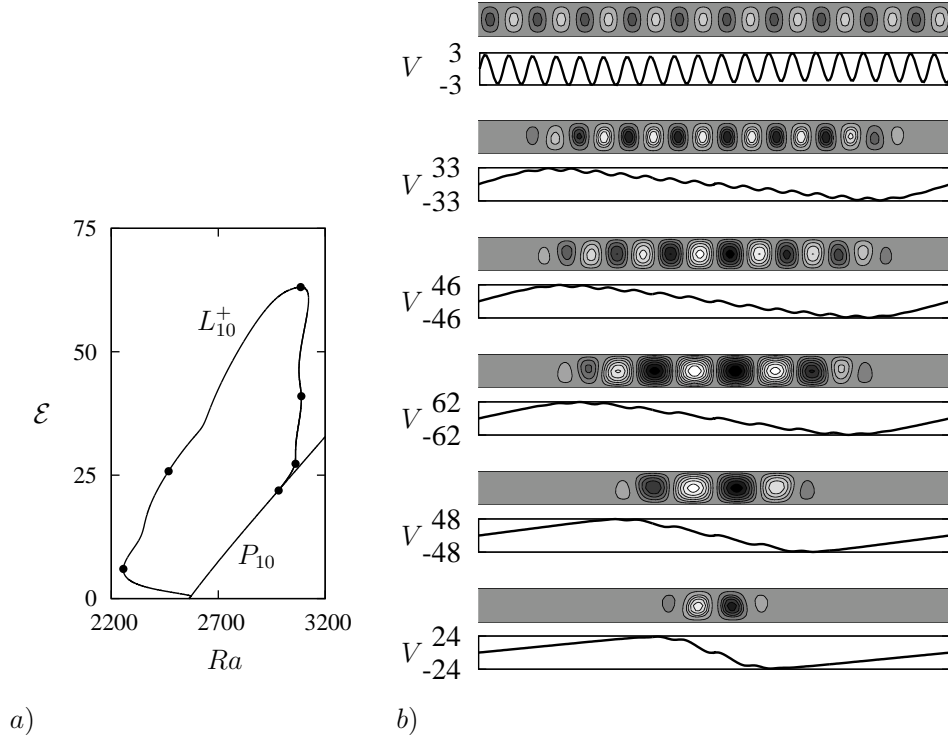


Figure 3.5: (a) Bifurcation diagram for the L_{10}^+ branch when $Ta = 50$. The branch bifurcates from P_{10} and terminates on P_{10} . The solid dots indicate the location of the solutions shown in (b).

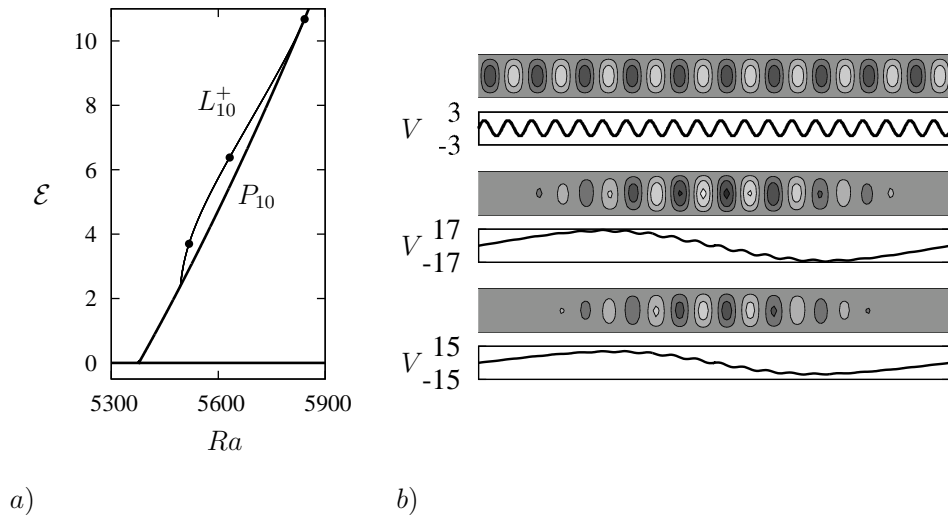


Figure 3.6: As for figure 3.5 but for $Ta = 100$.

Figures 3.2 and 3.4 also reveal a systematic trend that merits explanation: the convection cells are always broader than the corresponding cells in the periodic state. We believe that this is a reflection of the shear V' across the convection. If we suppose that this shear is smoothed out and is a linear function of x , i.e., $V(x) = sx$, where $s < 0$ (see, e.g., figure 3.2) we may include this shear in the base state and study the stability of the state $(\psi, \theta, v) = (0, 0, sx)$ instead of the state $(\psi, \theta, v) = (0, 0, 0)$. The stability of this state is described by the relations given in Eq. (3.7) with Ta^2 replaced by $Ta(Ta + \sigma^{-1}s)$. It follows that negative shear ($s < 0$) decreases both the critical Rayleigh number Ra_c and the associated critical wavenumber k_c relative to the case $s = 0$. However, this linear effect is quickly overwhelmed by the nonlinear wavelength change that takes place with increasing amplitude.

3.2 Theoretical understanding of the bifurcation

To study the modulation behavior of the resulting solutions in the weakly nonlinear regime we suppose that $Ra = Ra_c + \epsilon^2 r$, where $r = O(1)$, $\epsilon \ll 1$, and introduce a slow spatial scale $X = \epsilon x$ and a slow time scale $T_2 = \epsilon^2 t$. We follow [18] and look for solutions in the form

$$\psi = \frac{\epsilon}{2} (a(X, T_2) e^{ikx} + c.c.) \sin(\pi z) + h.o.t., \quad (3.11)$$

$$\theta = \frac{\epsilon k}{2p} (ia(X, T_2) e^{ikx} + c.c.) \sin(\pi z) + h.o.t., \quad (3.12)$$

and

$$A = \epsilon V(X, T_2) + \frac{\epsilon \pi}{2p\zeta} (a(X, T_2) e^{ikx} + c.c.) \cos(\pi z) + h.o.t. \quad (3.13)$$

for MC or

$$v = \epsilon V(X, T_2) + \frac{\epsilon T \pi}{2p} (a(X, T_2) e^{ikx} + c.c.) \cos(\pi z) + h.o.t. \quad (3.14)$$

for RC. The $O(\epsilon)$ terms are chosen as the superposition of the marginal modes. The large scale variable V is necessary to capture the shear or magnetic field that builds up across a convection; its inclusion is a consequence of the phase-like quality of the large scale modes. After simplification we obtain the equations

$$\eta A_{T_2} = rA + A_{XX} - \frac{1 - \xi^2}{2} |A|^2 A - \xi A V_X, \quad (3.15)$$

$$V_{T_2} = V_{XX} + \xi (|A|^2)_X \quad (3.16)$$

at $O(\epsilon^3)$, where r is proportional to $Ra - Ra_c$, η and ξ are coefficients rely on the physical parameters of the underlying system. The coefficient ξ takes the form $\left(\frac{2Q\pi^4 p}{Ra_c k^4 \zeta^2 + 4Q\pi^4 k^2} \right)^{1/2}$ in

MC and $\frac{Ta\pi^2}{\sqrt{3}pk^2\sigma}$ in RC. The coefficient η is crucial in determining the dynamics of Eqs. (3.15) and (3.16). In facts, it is proportional to $Ra_H - Ra_c$ where Ra_H is the Rayleigh number for the onset of Hopf mode at the same wavenumber as the steady convection. Here we are interested in the case in which the conduction state loses stability at a steady state bifurcation thus in this case $\eta > 0$.

Equations (3.15) and (3.16) can also be written in the form

$$A_{T_2} = -\eta^{-1} \frac{\delta F}{\delta A^*}, \quad V_{T_2} = -\frac{\delta F}{\delta V}, \quad (3.17)$$

where F is defined as

$$F[A, A^*, V] = \int_{\Gamma' \equiv \epsilon \Gamma} \left\{ -r|A|^2 + |A_X|^2 + \frac{1}{2}|V_X|^2 + \frac{1-\xi^2}{4}|A|^4 + \xi|A|^2 V_X \right\} dX. \quad (3.18)$$

The functional $F[A, A^*, V]$ is bounded from below when $\xi^2 < 1/3$. It follows that in this case the system (3.15)-(3.16) has gradient structure provided only that $\eta > 0$. This is not the case for the original system (3.1)-(3.4).

In the stationary case with PBC on the large scale X Eq. (3.16) implies that

$$V_X = \xi (\langle |A|^2 \rangle - |A|^2), \quad (3.19)$$

where $\langle \cdot \rangle$ represents a spatial average over the domain. Thus $V_X > 0$ if $|A|^2 < \langle |A|^2 \rangle$, i.e., outside the convecton, while $V_X < 0$ if $|A|^2 > \langle |A|^2 \rangle$, i.e., inside the convecton, exactly as found in figures 3.2 and 3.4. Moreover, using Eq. (3.19) to eliminate V_X from Eq. (3.15) we obtain the nonlocal equation [18]

$$rA + A_{XX} - \frac{1}{2}(1 - 3\xi^2)|A|^2 A - \xi^2 \langle |A|^2 \rangle A = 0. \quad (3.20)$$

Let $A = \rho e^{i\phi}$ with $\rho, \phi \in \mathbb{R}$ and $\rho > 0$. If ρ is independent of X , i.e., the solution is periodic, then $\langle |A|^2 \rangle = \rho^2 = 2(r - q^2)/(1 - \xi^2)$, where $q \equiv \phi_X$, and the solution is supercritical when $\xi^2 < 1$ and subcritical when $\xi^2 > 1$, as determined already by [54]. Equation (3.19) shows that the inclusion of amplitude modulation on the scale $X = O(1)$ alters this picture dramatically. In particular, the codimension two point for modulated wavetrains occurs at a different location, as determined next. This shift is a consequence of the nonlinear interaction between the unstable mode and the marginally stable longwave mode V .

Nonlocal equations of the form (3.20) have been studied before [55, 56, 57, 58, 59]. We summarize first the stability properties of the periodic solution $A = \rho e^{iqX}$, $V = 0$, corresponding to a wavetrain (ψ, θ, v) with wavenumber $k + \epsilon q$. We write $A = \rho e^{iqX}(1 + \tilde{A})$, where $|\tilde{A}| \ll 1$, and let V be the associated zonal velocity perturbation. The linearized equations are

$$\eta \tilde{A}_{T_2} = \tilde{A}_{XX} + 2iq\tilde{A}_X - (1 - \xi^2)\rho^2 \text{Re}[\tilde{A}] - \xi V_X, \quad (3.21)$$

$$V_{T_2} = V_{XX} + 2\xi\rho^2 \text{Re}[\tilde{A}]_X. \quad (3.22)$$

The characteristic polynomial for the growth rate λ of a Fourier mode with wavenumber l is [18]

$$\begin{aligned} &\eta^2 \lambda^3 + \eta \lambda^2 [(1 - \xi^2) \rho^2 + (2 + \eta) l^2] + \lambda l^2 [(1 - \xi^2) \rho^2 + \eta(1 - 3\xi^2) \rho^2 - 4q^2] \\ &+ \lambda l^4 (1 + 2\eta) + l^4 [l^2 - 4q^2 + (1 - 3\xi^2) \rho^2] = 0. \end{aligned}$$

Thus when $|l| \ll 1$ there is a pure amplitude mode with $O(1)$ eigenvalue $\lambda \approx (\xi^2 - 1) \rho^2 / \eta + O(l^2)$ reflecting the supercriticality or subcriticality of the periodic state and two $O(l^2)$ eigenvalues satisfying

$$\eta \rho^2 (1 - \xi^2) \lambda^2 + [\eta \rho^2 (1 - 3\xi^2) + \rho^2 (1 - \xi^2) - 4q^2] l^2 \lambda + [\rho^2 (1 - 3\xi^2) - 4q^2] l^4 \approx 0. \quad (3.23)$$

It follows that when $q = 0$ there are two longwave modes, $\lambda = -l^2/\eta$ and $\lambda = \frac{3\xi^2-1}{1-\xi^2} l^2$. Thus when $\eta < 0$ ($Ra_H < Ra_c$) the periodic state at band center is necessarily unstable. On the other hand when $\eta > 0$ (no primary Hopf bifurcation) there is a longwave instability when $1/3 < \xi^2 < 1$ but no longwave instability when $\xi^2 < 1/3$. Thus the $q = 0$ mode loses stability as ξ^2 decreases through $\xi^2 = 1/3$ (see figure 3.7). The resulting instability generates an amplitude modulated wavetrain. When $\xi^2 > 1$ the periodic state is subcritical and therefore also unstable. Finally, when $q \neq 0$ the two longwave modes become coupled but no secondary Hopf bifurcation is possible when $\eta > 0$, which is a trivial result of the underlying gradient structure. These results apply to infinite domains; in finite domains they require modification as discussed further below [59].

The spatial dynamics of Eq. (3.20) is integrable with two conserved quantities:

$$K_1 \equiv \rho^2 \phi_X, \quad K_2 \equiv \frac{1}{2} (\rho_X)^2 + U[\rho], \quad (3.24)$$

where

$$U[\rho] \equiv \frac{1}{2} r' \rho^2 + \frac{K_1^2}{2\rho^2} - \frac{1}{8} (1 - 3\xi^2) \rho^4. \quad (3.25)$$

Here $r' \equiv r - \xi^2 \langle \rho^2 \rangle$, implying that the bifurcation parameter r is increasingly modified as the convection amplitude ρ grows. In a periodic domain with period Γ' (Γ in terms of the large scale X) PBC and the integral constraint imply

$$\frac{\Gamma'}{2n} = \int_{\rho_{min}}^{\rho_{max}} \frac{d\rho}{\sqrt{2(K_2 - U)}}, \quad \frac{\langle \rho^2 \rangle \Gamma'}{2n} = \int_{\rho_{min}}^{\rho_{max}} \frac{\rho^2 d\rho}{\sqrt{2(K_2 - U)}}, \quad (3.26)$$

where $n \in \mathbb{N}$ is the number of full periods of amplitude modulation within Γ' , and ρ_{min} (ρ_{max}) corresponds to the minimum (maximum) of ρ during amplitude modulation. The total change of phase across the domain (including the contribution from the fast oscillation with wavenumber k) must be an integer multiple of 2π implying that the change of phase across the domain must also be a constant unless a phase jump occurs. The wavenumber $q \equiv \phi_X$ is a constant along the branch of periodic states. Secondary branching occurs when

ρ attains a local minimum of U . To fit PBC, $U_{\rho\rho}$ must be equal to $4\pi^2 n^2 / \Gamma'^2$ which occurs at $r = r_n$ where

$$r_n \equiv \frac{2\pi^2 n^2}{\Gamma'^2} \frac{1 - \xi^2}{3\xi^2 - 1} + \frac{5\xi^2 - 3}{3\xi^2 - 1} q^2 \quad (3.27)$$

in both super and subcritical cases. When q is small, a secondary bifurcation is only possible when $\xi^2 > 1/3$. The branching direction at these points was calculated by [56], who shows that when $q = 0$, the secondary bifurcation is supercritical when $\xi^2 < 3/7$ and subcritical when $\xi^2 > 3/7$ (see Appendix F for an alternative derivation of this result). In summary, there are four possible scenarios for the primary–secondary bifurcations with PBC: (1) both bifurcations are subcritical ($\xi^2 > 1$), (2) the primary bifurcation is supercritical while the secondary bifurcation is subcritical ($3/7 < \xi^2 < 1$), (3) both bifurcations are supercritical ($1/3 < \xi^2 < 3/7$), and (4) the primary bifurcation is supercritical but no secondary bifurcation is present ($\xi^2 < 1/3$). Figure 3.7 shows the regions of super and subcriticality in both MC and RC.

The bifurcation diagrams and discussions below will be focused on RC. Figure 3.8 shows sample bifurcation diagrams computed from Eq. (3.20) for (some of) the Taylor numbers used in RC using the numerical continuation software AUTO [36]. Owing to translation symmetry and spatial reversibility, we perform continuation on the half domain using Neumann boundary conditions (NBC), i.e.,

$$\text{Re}[A_X] = \text{Im}[A] = 0 \quad (3.28)$$

at the boundaries. The average poloidal kinetic energy \mathcal{E} to $O(\epsilon^4)$ takes the form

$$\mathcal{E} = \frac{1}{8}\epsilon^2 p \langle |a|^2 \rangle + \frac{1}{8}i\epsilon^3 k \langle aa_X^* - a^* a_X \rangle + \frac{1}{8}\epsilon^4 \langle |a_X|^2 \rangle, \quad (3.29)$$

where the amplitude a is defined in Eq. (3.11). We use this expression to draw bifurcation diagrams \mathcal{E} - Ra for $\sigma = 0.6$. For this purpose we define ϵ using the ratio of the small and large scales, $\epsilon \equiv \lambda_c / \Gamma = 0.1$. We then solve Eq. (3.20) in the domain $\Gamma' = 2\pi/k$ varying the parameter r . Owing to the relatively small domain (large value of ϵ) the calculation requires quite large values of r in order to locate the secondary states. The resulting energy \mathcal{E} is therefore also large. Of course, as r and hence \mathcal{E} increase the amplitude equation (3.20) becomes less reliable, and comparison with the results of section 3.1 shows that in the full problem the convection branch always turns towards larger values of Ra as \mathcal{E} increases, in contrast to the predictions summarized below.

Figure 3.8 shows that for $\sigma = 0.6$ the convection branch bifurcates supercritically from the periodic states once $Ta \geq 119.2579$ (i.e., $\xi^2 < 3/7$). The bifurcation to convections is also supercritical when $Ta < 6.1108$ since for these values $\xi^2 < 3/7$ also. As ξ^2 decreases towards $\xi^2 = 1/3$ the secondary bifurcation moves to larger and larger amplitude and for $\xi^2 < 1/3$ the secondary bifurcation to convections is absent. Of course before this happens Eq. (3.20)

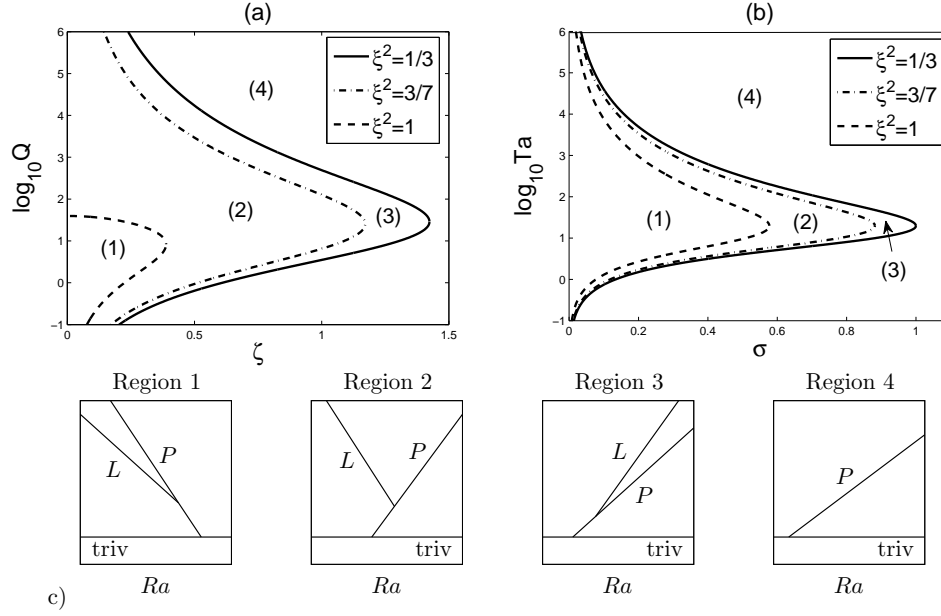


Figure 3.7: Regions of super and subcriticality for primary–secondary branches in the (a) ζ - Q plane (MC) and (b) σ - Ta plane (RC) on logarithmic scales. (c) Sketches of the bifurcation diagrams characteristic of each of the four regions.

loses validity; in particular, a different scaling is required to understand the disappearance of the convecton branch (see section 3.3).

We define the length L of a convecton as the interval where $|A|^2 > \langle |A|^2 \rangle$. This interval can be calculated explicitly by solving the nonlocal equation (3.20) in terms of elliptic functions. The explicit form of the $n = 1$ solution is

$$\rho^2/\rho_+^2 = 1 - \zeta^2 \text{sn}^2 \left[\frac{1}{2} \sqrt{\rho_+^2 (3\xi^2 - 1)} X; \zeta \right], \quad (3.30)$$

where

$$\Gamma' = \frac{4K(\zeta)}{\sqrt{\rho_+^2 (3\xi^2 - 1)}}, \quad \langle \rho^2 \rangle = \frac{E(\zeta)}{K(\zeta)} \rho_+^2. \quad (3.31)$$

The ratio L/Γ' is thus equal to $F\left(\zeta^{-1} \sqrt{1 - E(\zeta)/K(\zeta)}, \zeta\right)/K(\zeta)$. Here $\zeta \equiv \sqrt{1 - \rho_-^2/\rho_+^2}$, ρ_{\pm} are the positive roots of $U[\rho] = K_2$ with $\rho_- < \rho_+$, F is the incomplete elliptic integral of the first kind, and K and E are the complete elliptic integrals of the first and second kind. There are two limiting regimes which yield simple predictions for the parameter dependence of L . In the case of weak spatial modulation, K_2 is only slightly greater than the local minimum of U and we have

$$L/\Gamma' = \frac{1}{2} - \frac{\Gamma'}{2\pi^2} \sqrt{\frac{(3\xi^2 - 1)(r - r_1)}{3 - 7\xi^2}} + O(|r - r_1|). \quad (3.32)$$

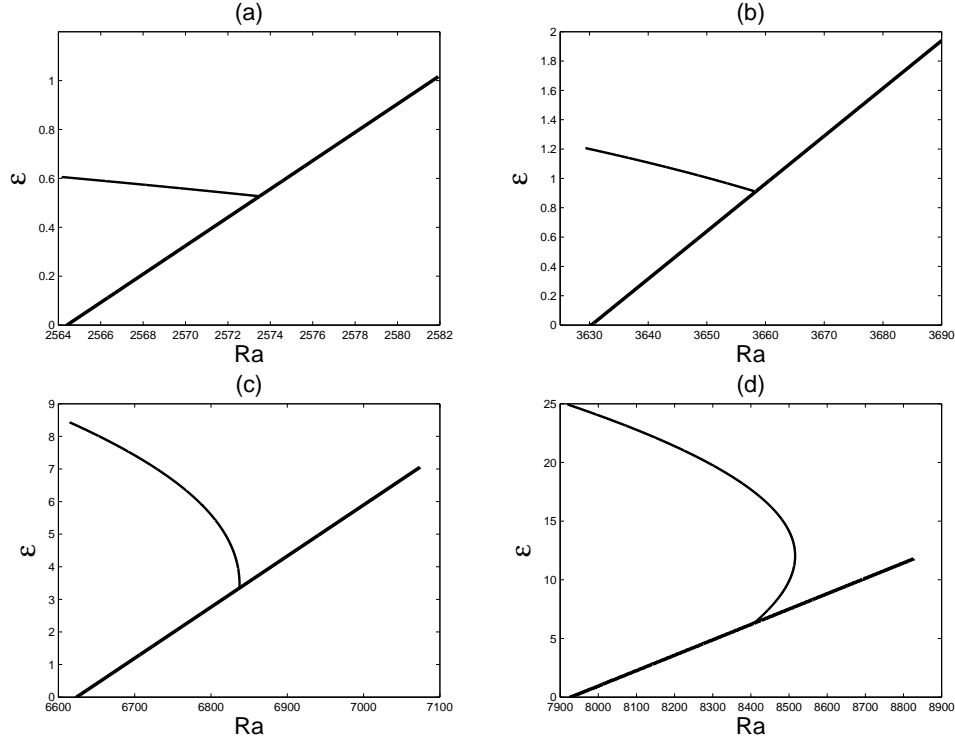


Figure 3.8: Bifurcation diagrams showing stationary solutions of Eq. (3.20) with $\phi_X = 0$ satisfying NBC for $\sigma = 0.6$ and $\Gamma = 10\lambda_c$. Thick solid lines: $k = 0$ primary state (periodic convection). Thin solid lines: modulated states (convectons). (a) $Ta = 50$ ($\xi^2 = 0.7032$, region (2)). (b) $Ta = 70$ ($\xi^2 = 0.5882$, region (2)). (c) $Ta = 120$ ($\xi^2 = 0.4269$, region (2)). (d) $Ta = 140$ ($\xi^2 = 0.3877$, region (3)). The periodic state is stable up to the secondary bifurcation; in (d) the modulated state is stable up to the saddle-node.

In the strongly modulated case with large domain size ($\Gamma'\sqrt{-r'} \gg 1$), the solutions with $\phi_X = 0$ can be approximated by the sech function [18, 19],

$$\rho = \sqrt{\frac{-4r'}{3\xi^2 - 1}} \operatorname{sech}\left(\sqrt{-r'}X\right), \quad (3.33)$$

where

$$r' = -\tilde{r} \left(1 \pm \sqrt{1 - \frac{r}{\tilde{r}}}\right)^2, \quad r < \tilde{r} \equiv \frac{16\xi^4}{\Gamma'^2(3\xi^2 - 1)^2};$$

the $+$ solution exists for all $r < \tilde{r}$ while the $-$ solution exists for $0 < r < \tilde{r}$ only. The resulting solutions are homoclinic to $\rho = 0$ and so represent fully localized convectons. It should be noted that due to finite domain size, $\langle \rho^2 \rangle$ is nonzero. The length of such a convecton is thus

$$L/\Gamma' \approx \frac{\log(2\Gamma'\sqrt{-r'})}{\Gamma'\sqrt{-r'}}. \quad (3.34)$$

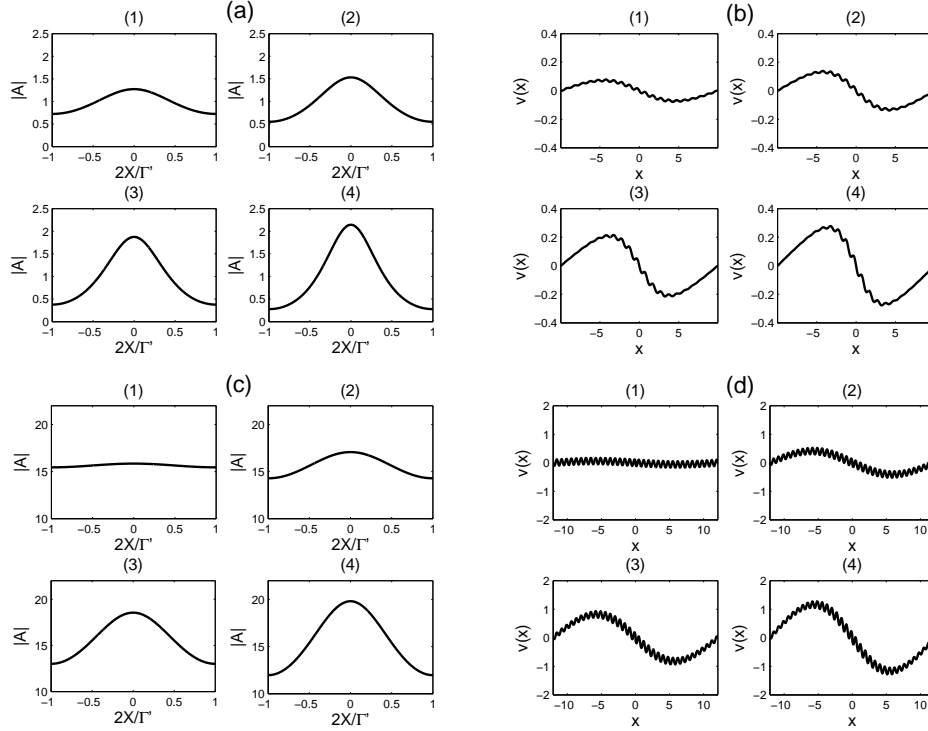


Figure 3.9: Sample profiles of the stationary solutions of Eq. (3.20) when $\Gamma = 10\lambda_c$. The amplitude $|A|$ is shown as function of a scaled variable while the z -average of the zonal velocity, $V(x)$, is shown in terms of the original variable x . (a,b) $\sigma = 0.1$, $Ta = 20$ ($\xi^2 = 33.3308$). (1) $Ra = 1174.3$. (2) $Ra = 1171.8$. (3) $Ra = 1166.8$. (4) $Ra = 1161.7$. (c,d) $\sigma = 0.6$, $Ta = 50$ ($\xi^2 = 0.7032$). (1) $Ra = 2573.5$. (2) $Ra = 2573.3$. (3) $Ra = 2572.6$. (4) $Ra = 2571.6$. Note that the spatial frequency of $V(x)$ is double that of $\psi(x)$.

The stability of the solutions (3.30) on a finite domain was studied rigorously by [59] in the case $\eta > 0$. In conjunction with Appendix F these results confirm that for $1/3 < \xi^2 < 3/7$ the secondary branch is supercritical and stable in the interval between the bifurcation point and a saddle-node on the right and unstable thereafter. For $\xi^2 > 3/7$ the secondary branch is subcritical and unstable throughout (figure 3.8).

In RC, we can use the above results to calculate the local shear at the maximum of the amplitude modulation. For the $n = 1$ secondary branch we obtain

$$s = -\frac{8Ta\pi^3}{3p^2k^2\sigma\Gamma} \sqrt{\frac{Ra - Ra_1}{(3\xi^2 - 1)(3 - 7\xi^2)}} + O(|Ra - Ra_1|), \quad (3.35)$$

where $Ra = Ra_1$ denotes the location of the secondary bifurcation. To obtain this result we include a nonzero constant of integration in Eq. (3.10), as required by PBC, and choose this constant to cancel the mean Reynolds stress associated with periodic wavetrains. With this

shear the critical wavenumber \tilde{k}_c for instability of the sheared base state $(\psi, \theta, v) = (0, 0, sx)$ differs from k_c in Eq. (3.7) by

$$\tilde{k}_c - k_c \approx \frac{Ta\pi^2 s}{12p k^3 \sigma} = -\frac{2Ta^2\pi^5}{9p^3 k^5 \sigma^2 \Gamma} \sqrt{\frac{Ra - Ra_1}{(3\xi^2 - 1)(3 - 7\xi^2)}} + O(|Ra - Ra_1|), \quad (3.36)$$

showing that the wavelength of the instability of the sheared state will be larger than that of the unsheared state $(\psi, \theta, v) = (0, 0, 0)$. Numerical measurements of the convection wavelength near onset (not shown) are consistent with the predicted square root behavior. Although not exact this approach represents an attempt towards a self-consistent determination of the convection wavelength in the weakly nonlinear regime in a system where no spatial Hamiltonian is available to set the wavelength.

Figure 3.9 shows the profiles of the resulting convectons for (a,b) $\xi^2 > 1$ (the subcritical case) and (c,d) $\xi^2 < 1$ (the supercritical case). The results are in excellent qualitative agreement with the continuation results in figures 3.2 and 3.4.

3.3 Modulation equations near a codimension-two point

The leading order theory described in Eqs. (3.15) and (3.16) correctly predicts the bifurcation of periodic states and the subsequent secondary bifurcations to localized states when the domain size is large. However, it cannot describe the stationary patterns near the codimension-two point, i.e., $(r_0, \xi_0^2) = (0, 1/3)$. Moreover, due to the limitation that the theory is of cubic-order certain interesting properties for localized branches such as phase jump and the reconnection to original periodic branch are absent in the theory.

To study the modulation behavior near the codimension-two point we introduce the slower scales $X = \epsilon^2 x$ and $T = \epsilon^6 t$ while retaining the assumption that $A = O(\epsilon)$. To maintain the leading order balance in Eqs. (3.15) and (3.16) we promote the amplitude of the large scale mode, $V = O(1)$, obtaining

$$O(\epsilon^4) = \left(r_2 A - \frac{1}{3} |A|^2 A - 3^{-1/2} A V_X \right) + \epsilon^2 (r_4 A + A_{XX} + f(A, V_X)), \quad (3.37)$$

$$\epsilon^2 V_T = (V_X + 3^{-1/2} |A|^2)_X + \epsilon^2 g(A, V_X)_X, \quad (3.38)$$

Here r_2 and r_4 are parameters depending on Ra and Q (or Ta), and f and g are polynomials in A and V_X and their derivatives. Explicit expressions for f and g are given below.

For MC we assume the following asymptotic expansion

$$\psi \sim \sum_{n=1}^{\infty} \epsilon^n \psi_n, \quad \theta \sim \sum_{n=1}^{\infty} \epsilon^n \theta_n, \quad A \sim A_0 + \sum_{n=1}^{\infty} \epsilon^n A_n, \quad (3.39)$$

where A_0 is a function of X and T alone while the remaining quantities are functions of x , X , z , and T . The parameters Ra and Q are expanded with respect to the critical numbers Ra_c and Q_c (determined by $(r_0, \xi_0^2 = (0, 1/3))$) in the form $Ra = Ra_c + \epsilon^2 r_2 + \epsilon^4 r_4$ and $Q = Q_c + \epsilon^2 q$, where $Ra_c = 2p^3\pi^2$, Q_c satisfies relation (3.7), and the critical wavenumber k is defined by the relation

$$pk^4\zeta^2 = \pi^2(2k^2 - \pi^2)(k^2 + 3\pi^2). \quad (3.40)$$

Figure 3.7 shows the dependence of Q_c on ζ . We see that Q_c exists only when $\zeta \lesssim 1.4238$ and that within this region there are two critical numbers Q_c^\pm of which Q_c^+ lies below the fold and Q_c^- lies above the fold.

Under the expansion, the linear system $O(\epsilon)$ of the equations allows the same marginal mode as in section 3.2 except X and T are scaled differently. Proceeding to higher order (see Appendix G) one obtains

$$\begin{aligned} O(\epsilon^4) = & \frac{k^2 r_2 - p\pi^2 q}{2} a - Q_c p\pi^2 a A_{0,X} - \frac{Q_c \pi^4}{4\zeta^2} |a|^2 a + \epsilon^2 \left\{ (\tilde{\mu}_0 + \tilde{\mu}_1 A_{0,X} + \tilde{\mu}_2 A_{0,X}^2) a \right. \\ & \left. + \tilde{d} a_{XX} + i(\tilde{\gamma} + \tilde{a}_{10}|a|^2) a_X + i\tilde{a}_{20} a^2 a_X^* + \left(\tilde{b}_0 + \tilde{b}_1 A_{0,X} \right) |a|^2 a - \tilde{c}_0 |a|^4 a \right\}, \end{aligned} \quad (3.41)$$

$$\epsilon^2 A_{0,T} = \left(A_{0,X} + \frac{\pi^2 |a|^2}{4p\zeta^2} \right)_X + \epsilon^2 \left(\frac{\pi^2}{4p\zeta} A_{0,X} |a|^2 - \frac{\pi^4}{32p^2\zeta^3} |a|^4 + \frac{k\pi^2}{2p^2\zeta} \text{Im}[aa_X^*] \right)_X. \quad (3.42)$$

Explicit expressions for the coefficients are also given in Appendix G.

The scaling for RC is the same as in MC. The dimensionless numbers Ra and Ta are expanded around the corresponding critical numbers as

$$Ra = Ra_c + \epsilon^2 r_2 + \epsilon^4 r_4, \quad Ta = Ta_c + \epsilon^2 \delta, \quad (3.43)$$

where Ra_c and Ta_c satisfy

$$Ra = 3p^2, \quad Ta_c = Ta_c^\pm \equiv \frac{\sigma\pi^2(2 \pm \sqrt{1 - \sigma^2})}{(1 \pm \sqrt{1 - \sigma^2})^2}. \quad (3.44)$$

Thus Ta_c exists only when $\sigma \leq 1$. The detailed calculations for RC can be found in the supplementary material to [17] and here we simply present the results

$$\begin{aligned} O(\epsilon^4) = & \left(\frac{k^2 r_2}{2} - T_c \pi^2 \delta \right) a - \frac{pk^2}{2} a v_{0,X} - \frac{pk^4}{8} |a|^2 a + \epsilon^2 \left\{ (\tilde{\mu}_0 + \tilde{\mu}_1 v_{0,X} + i\tilde{\mu}_2 v_{0,XX}) a + \tilde{d} a_{XX} \right. \\ & \left. + i(\tilde{\gamma}_0 + \tilde{\gamma}_1 v_{0,X} + \tilde{a}_{10}|a|^2) a_X + i\tilde{a}_{20} a^2 a_X^* + \left(\tilde{b}_0 + \tilde{b}_1 v_{0,X} \right) |a|^2 a - \tilde{c}_0 |a|^4 a \right\}, \end{aligned} \quad (3.45)$$

$$\frac{\epsilon^2 v_{0,T}}{\sigma} = \left(v_{0,X} + \frac{k^2}{4} |a|^2 \right)_X + \epsilon^2 \left(\frac{k^3}{2p} \text{Im}[aa_X^*] + \frac{\pi^2 |a|^2 (v_{0,X} + \delta\sigma)}{4p\sigma^2} - \frac{k^2 \pi^2 |a|^4}{32p\sigma^2} \right)_X. \quad (3.46)$$

Here v_0 denotes the large scale zonal velocity. Explicit expressions of the coefficients are given in Appendix H.

3.4 Stationary nonlocal Ginzburg-Landau equation

The modulation equations derived in the previous section can be used to describe the bifurcation near the codimension-two point $(Ra, Q) = (Ra_c, Q_c)$ or $((Ra, Ta) = (Ra_c, Ta_c))$. In the stationary case, the large scale mode can be eliminated in favor of the amplitude function resulting in a nonlocal fifth order Ginzburg-Landau equation. To demonstrate this, let us focus on Eqs. (3.42) and (3.46) in the stationary case

$$\left(A_{0,X} + \frac{\pi^2 |a|^2}{4p\zeta^2} \right)_X + \epsilon^2 \left(\frac{\pi^2}{4p\zeta} A_{0,X} |a|^2 - \frac{\pi^4}{32p^2\zeta^3} |a|^4 + \frac{k\pi^2}{2p^2\zeta} \text{Im}[aa_X^*] \right)_X = 0, \quad (3.47)$$

$$\left(v_{0,X} + \frac{k^2}{4} |a|^2 \right)_X + \epsilon^2 \left(\frac{k^3}{2p} \text{Im}[aa_X^*] + \frac{\pi^2 |a|^2 (v_{0,X} + \delta\sigma)}{4p\sigma^2} - \frac{k^2\pi^2 |a|^4}{32p\sigma^2} \right)_X = 0. \quad (3.48)$$

These equations can be integrated once with respect to X and leave the integration constants to be determined. Before doing so we note that each equation consists of two parts with different orders in ϵ . We use this fact to solve for $A_{0,X}$ and $v_{0,X}$ iteratively. The integration constants are then determined imposing periodic boundary conditions. The calculation gives

$$A_{0,X} = \frac{\pi^2 (\langle |a|^2 \rangle - |a|^2)}{4p\zeta^2} + \frac{\pi^2 \epsilon^2}{p^2 \zeta} \left\{ \frac{k}{2} \text{Im} [\langle aa_X^* \rangle - aa_X^*] + \frac{\pi^2}{32\zeta^2} (3|a|^4 - 2|a|^2 \langle |a|^2 \rangle + 2 \langle |a|^2 \rangle^2 - 3 \langle |a|^4 \rangle) \right\}, \quad (3.49)$$

$$v_{0,X} = \frac{k^2 (\langle |a|^2 \rangle - |a|^2)}{4} + \frac{\epsilon^2}{p} \left\{ \frac{k^3}{2} \text{Im} [\langle aa_X^* \rangle - aa_X^*] + \frac{\delta\pi^2}{4\sigma} (\langle |a|^2 \rangle - |a|^2) + \frac{k^2\pi^2}{32p\sigma^2} (3|a|^4 - 2|a|^2 \langle |a|^2 \rangle + 2 \langle |a|^2 \rangle^2 - 3 \langle |a|^4 \rangle) \right\}. \quad (3.50)$$

After substituting these relations into the equations of a we arrive at

$$k^2 r_2 - p\pi^2 q = \frac{Q_c \pi^4 \langle |a|^2 \rangle}{2\zeta^2} \quad (\text{MC}), \quad r_2 - 2p\sigma\delta = \frac{pk^2 \langle |a|^2 \rangle}{4} \quad (\text{RC}) \quad (3.51)$$

at leading order, and at

$$\tilde{\mu}a + \tilde{d}a_{XX} + i(\tilde{\gamma}a_X + \tilde{a}_1|a|^2a_X + \tilde{a}_2a^2a_X^*) + \tilde{b}|a|^2a - \tilde{c}|a|^4a = 0 \quad (3.52)$$

at next order. Equation (3.52) is nonlocal and of fifth order in a ; expressions for the coefficients can be found in Appendices G and H. Note that $r_2 \neq 0$ even when $a = 0$; this is a consequence of the fact that Ra_c is determined at $Q = Q_c$ and not at Q and similarly for RC . The shift of Q and Ta from their critical values also changes the critical wavenumber by $\frac{\epsilon^2 q \pi^4}{6pk^3}$ in MC and $\frac{\epsilon^2 \delta \sigma}{6k}$ in RC. This effect is responsible for the nonzero value of $\tilde{\gamma}_0$ in the coefficient $\tilde{\gamma}$.

Equation (3.52) can be written in the simpler form

$$\mu A + A_{XX} + i(\gamma A_X + a_1 |A|^2 A_X + a_2 A^2 A_X^*) + b |A|^2 A - \text{sgn}(\tilde{c}) |A|^4 A = 0, \quad (3.53)$$

where A is the scaled amplitude function

$$A(X) = \left(|\tilde{c}|/\tilde{d} \right)^{1/4} a(X) \exp \left(\frac{i\tilde{\gamma}_0 X}{2\tilde{d}} \right) \quad (3.54)$$

and the exponential factor offsets the shift in critical wavenumber. The coefficients in Eq. (3.53) are defined as

$$\begin{aligned} \mu &= \frac{\tilde{\mu}}{\tilde{d}} - \left(\frac{\tilde{\gamma}_0}{2\tilde{d}} \right)^2, & b &= \frac{\tilde{b}}{(|\tilde{c}|\tilde{d})^{1/2}} + \frac{\tilde{\gamma}_0}{2\tilde{d}}(a_1 - a_2), \\ \gamma &= \frac{\tilde{\gamma} - \tilde{\gamma}_0}{\tilde{d}}, & a_1 &= \frac{\tilde{a}_1}{(|\tilde{c}|\tilde{d})^{1/2}}, & a_2 &= \frac{\tilde{a}_2}{(|\tilde{c}|\tilde{d})^{1/2}}, \end{aligned}$$

implying that

$$\begin{aligned} \mu &= \mu_0 + \mu_1 \langle |A|^2 \rangle + \mu_2 \langle |A|^2 \rangle^2 + \mu_3 \langle |A|^4 \rangle + \mu_4 \langle \text{Im}[AA_X^*] \rangle, \\ \gamma &= \gamma_1 \langle |A|^2 \rangle, & b &= b_0 + b_1 \langle |A|^2 \rangle, \end{aligned}$$

where μ_n , γ_n , and b_n are constant coefficients that are independent of the nonlocal terms while \tilde{c} , a_1 , and a_2 are intrinsic coefficients independent of the parameters r_2 , r_4 , q (or δ) and of nonlocal contributions. The dependence of a_1 and a_2 on the parameters ζ and σ in MC and RC are given in figures 3.10 and 3.11.

Equation (3.53) is valid only when \tilde{c} and preferably positive. In MC, \tilde{c} is independent of the Prandtl number σ and is always positive when $Q_c = Q_c^+$. But for $Q_c = Q_c^-$, \tilde{c} is positive when $1.0300 \lesssim \zeta \lesssim 1.4238$ and negative when $0 < \zeta \lesssim 1.0300$. In RC, \tilde{c} is always positive when $Ta_c = Ta_c^+$. But for $Ta_c = Ta_c^-$, \tilde{c} is negative when the Prandtl number lies within $0.59796 \lesssim \sigma < 1$ and negative otherwise. These conditions limit the applicability of Eq. (3.53).

To study the bifurcation properties of Eq. (3.53) in the presence of PBC, we pick r_4 as the control parameter. The parameter r_2 is determined by the spatial average of $|A|^2$. Equation (3.53) can be solved by quadrature under polar coordinate $A(X) \equiv \rho(X)e^{i\phi(X)}$ with the aid of the spatially conserved quantities

$$E_1 = \rho^2 \phi_X + \frac{\gamma}{2} \rho^2 + \frac{a_1 + a_2}{4} \rho^4, \quad E_2 = \frac{1}{2} (\rho_X)^2 + U[\rho], \quad (3.55)$$

where

$$U[\rho] = \frac{E_1^2}{2\rho^2} + \left(\mu + \frac{\gamma^2}{4} + \frac{3a_2 - a_1}{2} E_1 \right) \frac{\rho^2}{2} + \left(b + \frac{a_1 - a_2}{2} \gamma \right) \frac{\rho^4}{4} + \frac{\beta \rho^6}{2} \quad (3.56)$$

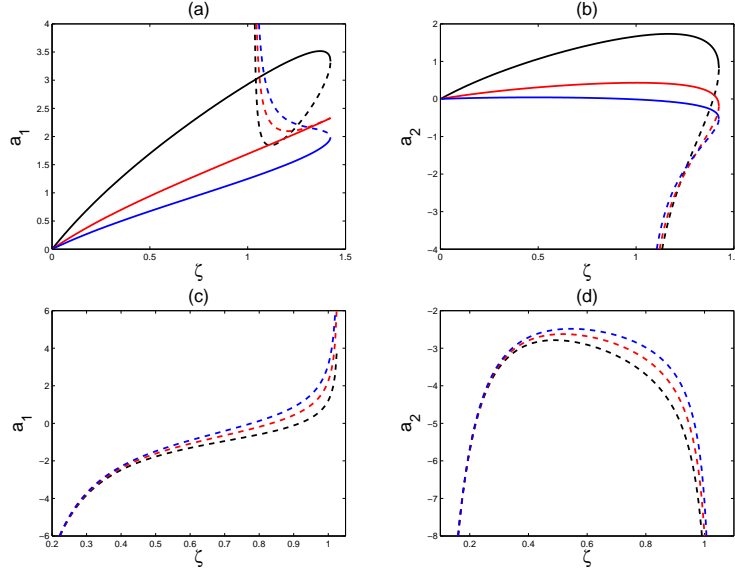


Figure 3.10: Dependence of a_1 and a_2 on ζ for different σ when (a,b) $\tilde{c} > 0$ and (c,d) $\tilde{c} < 0$. Black line: $\sigma = 0.2$. Red line: $\sigma = 0.4$. Blue line: $\sigma = 2$. $Q_c = Q_c^+$ is indicated in a solid line while $Q_c = Q_c^-$ is indicated in a dashed line.

with $\beta \equiv \frac{(a_1+a_2)(3a_1-5a_2)}{48} - \frac{1}{3}\text{sgn}(\tilde{c})$. Thus constant amplitude ($\rho_X = 0$) phase-winding ($\phi_X = K_0$, a constant) solutions have amplitude ρ_0 given by

$$\rho_0^2 = \rho_{\pm}^2 \equiv \frac{b' \pm \sqrt{b'^2 + 4c\mu'}}{2c} > 0, \quad (3.57)$$

where $c \equiv \text{sgn}(\tilde{c}) - b_1 - \mu_2 - \mu_3$, $b'(K_0) \equiv b_0 + \mu_1 + K_0(a_2 - a_1 - \gamma_1 - \mu_4)$, and $\mu'(K_0) \equiv \mu_0 - K_0^2$.

As known in [20] in the absence of nonlocal coupling localized solutions of Eq. (3.53) exhibit protosnaking behavior around the Maxwell point $\mu = \mu_M \equiv \frac{b^2}{16\beta}$, which is defined as the parameter value of μ for the existence of a stationary front solution. This solution is characterized by $E_1 = 0$ and serves as a connection between the zero state and a periodic state with wavenumber $k_M = (a_1 + a_2)\mu_M$. But here due to the presence of nonlocal terms in Eq. (3.53) the Maxwell point is replaced by a Maxwell curve satisfying

$$16\beta \left(\mu + \frac{\gamma^2}{4} \right) = \left(b + \frac{a_1 - a_2}{2} \gamma \right)^2. \quad (3.58)$$

Here γ and b depend of μ through their dependence on $\langle |A|^2 \rangle$ as computed from the front solution at each μ . In figure 3.12 we show the resulting Maxwell curve in the (Ra, Q) plane (MC) and in the (Ra, Ta) plane (RC) for fixed ζ and σ . The asymptotic periodic state has amplitude square $-\frac{1}{4\beta} \left[b + \frac{(a_1 - a_2)\gamma}{2} \right]$ and wavenumber $\frac{a_1 + a_2}{16\beta} \left(b + \frac{\gamma a_2}{3} \right) + \frac{\gamma}{6\beta} \text{sgn}(\tilde{c})$. The relation (3.58) can be used to predict the location of localized states but the nonlocal terms

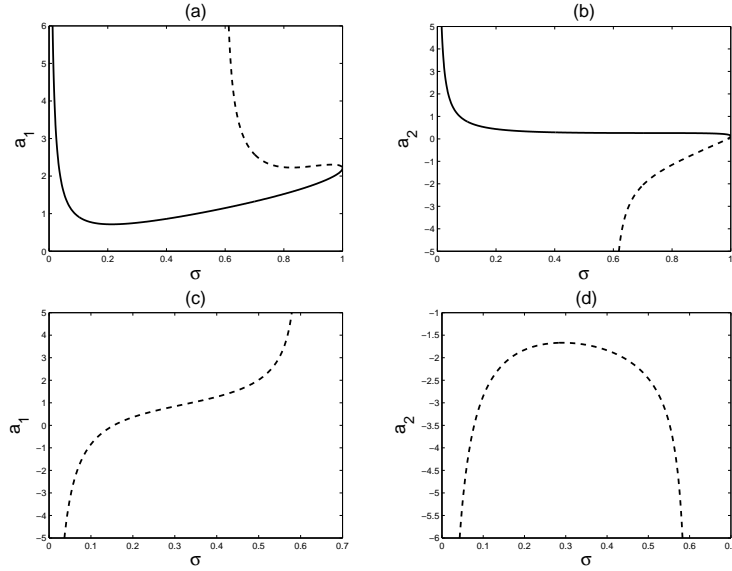


Figure 3.11: Coefficients (a) a_1 and (b) a_2 as functions of σ when (a,b) $\tilde{c} > 0$ and (c,d) $\tilde{c} < 0$. Solid line: $Ta_c = Ta_c^+$. Dashed line: $Ta_c = Ta_c^-$.

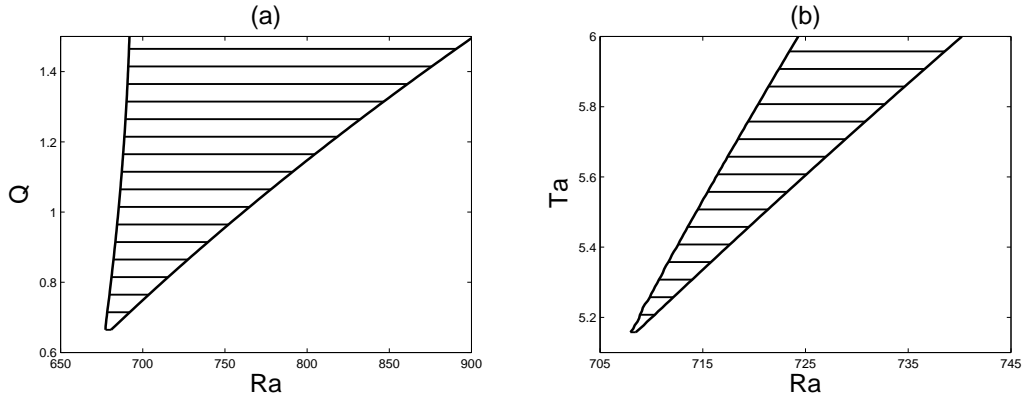


Figure 3.12: The existence region of Maxwell curve in (a) MC with $\zeta = 0.5$ and $\sigma = 1$ and (b) RC with $\sigma = 0.6$.

should be taken into account. A case that yields simple albeit approximate result is when the domain size $\epsilon^2\Gamma$ is large and the regions of periodic state and zero state are large compare with the transition region between the two states. If the periodic state occupies a portion $e \equiv l/(\epsilon^2\Gamma)$ of the whole spatial domain (l is the length of the periodic state), the nonlocal terms are approximately equal to

$$\langle |A|^2 \rangle = e\rho_0^2, \quad \langle |A|^4 \rangle = e\rho_0^4, \quad \langle \text{Im}[AA_X^*] \rangle = e\rho_0^4 \left(\frac{e\gamma_1}{2} + \frac{a_1 + a_2}{4} \right). \quad (3.59)$$

The occupation portion e can be determined by the requirement $\rho_0^2 = -\frac{1}{4\beta} \left[b + \frac{(a_1 - a_2)\gamma}{2} \right]$ which gives

$$e\rho_0^2 = -\frac{b_0 + 4\beta\rho_0^2}{b_1 + \frac{a_1 - a_2}{2}\gamma_1}. \quad (3.60)$$

The relation for the Maxwell curve can then be determined by substituting these relations into Eq. (3.58).

Another important property of the localized states is the onset of secondary bifurcation. The bifurcation of secondary branches from the periodic states only occur at the point which $U_{\rho\rho}$ is nonnegative with spatial period $2\pi/U_{\rho\rho}^{1/2}$. It can be shown $U_{\rho\rho}$ takes the form

$$U_{\rho\rho} = 4K_0^2 + 2[b_0 + K_0(a_1 + a_2 + 2\gamma_1)]\rho^2 + (a_1^2 - a_2^2 + \gamma_1^2 + 2a_1\gamma_1 + 2b_1 - 4\text{sgn}(\tilde{c}))\rho^4 \quad (3.61)$$

on the periodic state. For systems of finite domain, the spatial period of the modulated solution should fit the size of domain thus leads to discrete bifurcation points instead of continuous bands along the periodic branches when the domain size is infinite. According to this we can define a number n which corresponds to the number of spatial modulations across the whole domain.

In the followings, we study the bifurcation under physical coefficients using numerical continuation package AUTO. The bifurcation diagrams are plotted with respect to the Rayleigh number Ra in the horizontal and the H_1 norm of ϵA in the vertical. Here the H_1 norm is defined as

$$\|u\|_{H^1} = \left(\frac{1}{\Gamma} \int_0^\Gamma |u|^2 + |u_X|^2 dX \right)^{1/2}. \quad (3.62)$$

Due to spatially reversibility in Eq. (3.53), instead of imposing periodic boundary conditions we perform the computation on half domain $[0, \epsilon^2\Gamma/2]$ with

$$\text{Re}[A_X] = 0, \quad \text{Im}[A] = 0$$

at both ends. The effect of nonlocal contributions can be included by introducing auxiliary variables. As an illustration, in order to get the spatial average of $f = f(X)$ we include two variables u_1 and u_2 which satisfy

$$u_{1,X} = u_2, \quad u_{2,X} = -f_X$$

with boundary conditions $u_1 = 0$ at both ends. The spatial average of f is then equal to $u_2 + f$. Under this setting AUTO is able to detect and switch to the modulated branches and the locations of secondary branching agree with analytical prediction.

Here we focus on $K_0 = 0$, i.e., the band center. The twice derivative of U takes the following form along the primary branch

$$U_{\rho\rho} = 2b_0\rho^2 + (a_1^2 - a_2^2 + \gamma_1^2 + 2a_1\gamma_1 + 2b_1 - 4\text{sgn}(\tilde{c}))\rho^4. \quad (3.63)$$

The coefficient b_0 , which is proportional to $Q - Q_c$ in MC and $Ta - Ta_c$ in RC, has its importance in determining the bifurcation behavior. When the coefficient of ρ^4 in Eq. (3.63) is positive, there are countably infinite number of secondary bifurcations with each modulated branch of different $n = 1, 2, 3 \dots$ and appears exactly once. The locations of the branching points move into larger amplitude as b_0 decreases. However, when the coefficient of ρ^4 in Eq. (3.63) is negative there is no secondary bifurcation if b_0 is negative. As b_0 becomes positive, the secondary bifurcation points appear in pairs while b_0 increases and each pair have the same modulation number n .

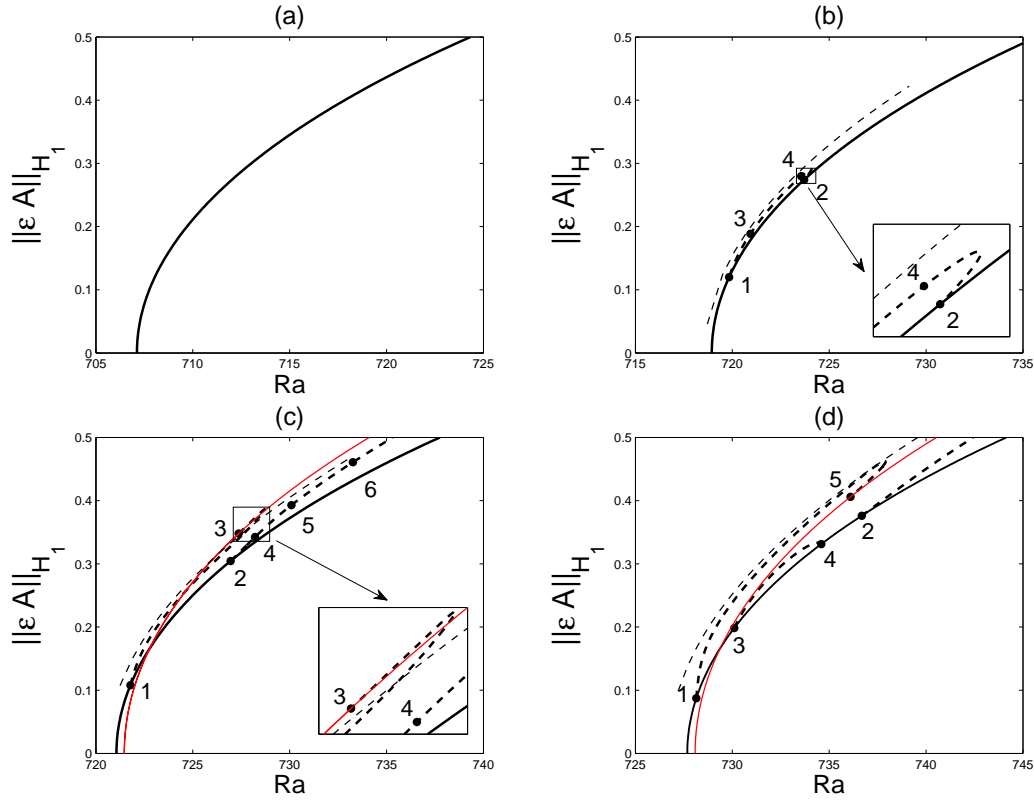


Figure 3.13: Bifurcation diagrams of $K_0 = 0$ primary branch in rotating convection with $\sigma = 0.6$ and $\Gamma = 50\lambda_c$. (a) $Ta = Ta_c = 5.1176$. (b) $Ta = 5.7176$. (c) $Ta = 5.8176$. (d) $Ta = 6.1176$.

We demonstrate these two bifurcation scenarios under RC since the behavior in MC is qualitatively the same. The bifurcation diagrams and solution profiles are shown in figures 3.13–3.15. The bifurcation of primary branches are all strongly supercritical due to the codimension-two point is located in the supercritical region. In figure 3.13, the primary branches ($K_0 = 0$) has the coefficient of ρ^4 in Eq. (3.63) negative and b_0 has the same sign as $Ta - Ta_c$. The Maxwell curves are indicated as thin-dashed lines in the figures. As expected there is no secondary bifurcation when Ta is less than critical Taylor number Ta_c which

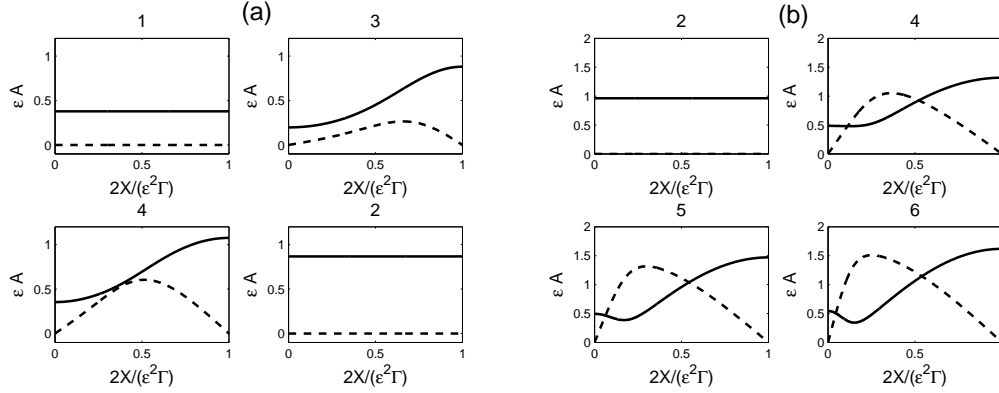


Figure 3.14: Spatial profiles of solutions in (a) figure 3.13(b) and (b) figure 3.13(c). Solid line: $\text{Re}[\epsilon A]$. Dashed line: $\text{Im}[\epsilon A]$.

agrees with the bifurcation picture depicted in section 3.2. Secondary bifurcations appear as Ta increases above Ta_c and the modulated branches first appear at small amplitude and then reconnect back at larger amplitude. These branches appear in (b), which connects point 1 to point 2 ($n = 1$), and (d), which connects point 3 to point 4 ($n = 2$). As Ta increases these branches break up as shown in (c) and the ones bifurcate at small amplitude (point 1) undergo phase jump and terminate on primary branches with $K_0 \neq 0$ (point 3 with $n = 2$) while the ones bifurcate at larger amplitude (point 2) evolve into defect states as Ra increases.

In figure 3.15, the coefficient of ρ^4 in Eq. (3.63) is positive. In contrast with figure 3.13, b_0 and $Ta - Ta_c$ take different sign thus in (a) $Ta < Ta_c = 311.7656$ the location of secondary bifurcation is lower compare with (b) $Ta > Ta_c$. This bifurcation behavior does not coincide with the prediction in section 3.2 but however as Ta increases to value far above Ta_c the secondary bifurcation move up to larger amplitude and thus no secondary bifurcation can be observed at $O(1)$ amplitude. All the secondary branches (bifurcate from points 1–3) undergo phase jump and terminate on primary branches with nonzero wavenumber ($K = \frac{\epsilon^2 \Gamma}{n}$, $n = 1, 2, 3$). In figure 3.15 we only show the primary branches with $K_0 = 0$ and $\epsilon^2 \Gamma$. It appears that all these secondary branches bifurcate subcritically from the $K_0 = 0$ primary branch. The direction of branching can be inferred by a local analysis around the branching point. The change of bifurcation parameter Ra_c is dominated by the change of r_2 which is linearly related to $\langle |A|^2 \rangle$. In order to get the branching direction of secondary branches, we need to figure out how $\langle |A|^2 \rangle$ changes after the bifurcation. A sketch of this calculation can be found in Appendix I which agrees well with the numerical result.

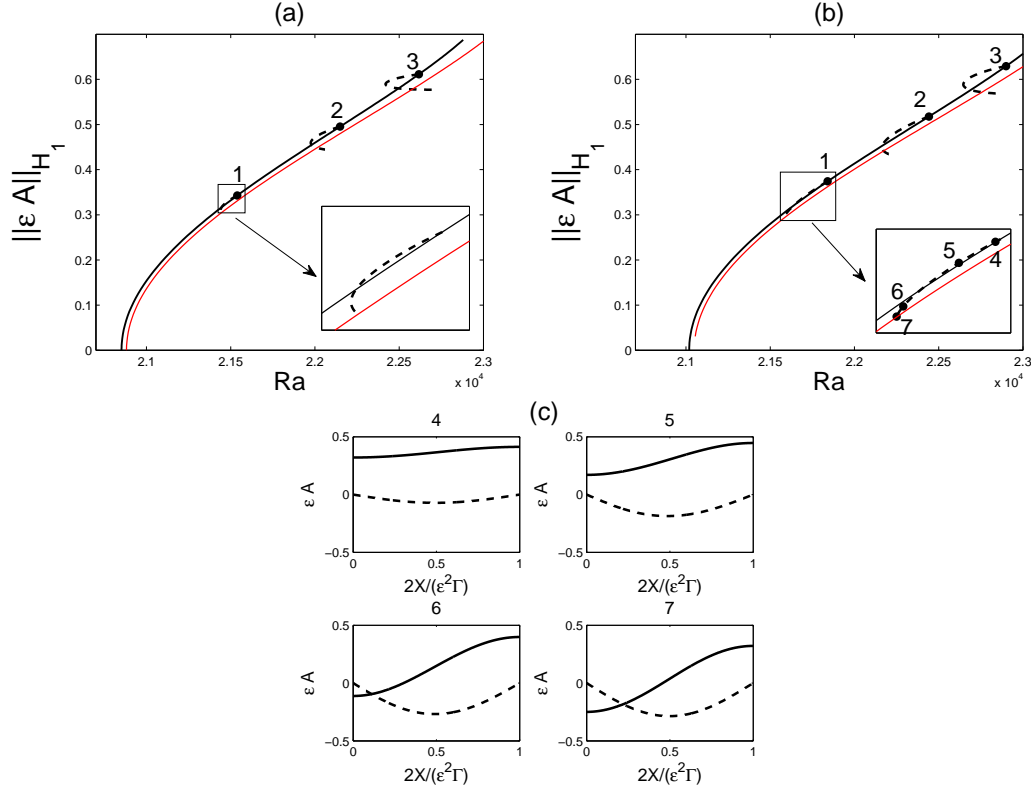


Figure 3.15: Bifurcation diagrams of $K_0 = 0$ primary branch in rotating convection. $\sigma = 0.5$. $\Gamma = 50\lambda_c$. (a) $Ta = 310.7656$. (b) $Ta = 312.7656$. (c) Spatial profiles of solutions in (b). Solid line: $Re[\epsilon A]$. Dashed line: $Im[\epsilon A]$.

3.5 Temporal stability of the stationary solutions

To study the stability of the solutions obtained in section 3.4, we consider the dynamical equations Eqs. (3.42) and (3.46). These relations indicate the time dependence of $|A|$ should be of the form

$$(|A|^2)_T = -[A^{-1}(A_{XX} + i\gamma A_X) + i(a_1 A^* A_X + a_2 A A_X^*) + b|A|^2 - \text{sgn}(\tilde{c})|A|^4]_{XX}. \quad (3.64)$$

Combining Eq. (3.64) with spatial periodicity, the imaginary part implies the gradient of phase ϕ_X is slaved by ρ^2 as

$$\phi_X = \frac{E_1}{\rho^2} - \frac{\gamma}{2} - \frac{a_1 + a_2}{4}\rho^2, \quad (3.65)$$

where E_1 is the spatial constant introduced in the previous section but is time dependent here in this section. This time dependent spatial constant can be determined by spatial periodicity which gives

$$E_1 = \left[\left(\frac{\gamma_1}{2} + \frac{a_1 + a_2}{4} \right) \langle \rho^2 \rangle + \frac{\Delta\phi}{\epsilon^2\Gamma} \right] / \langle \rho^{-2} \rangle, \quad (3.66)$$

where $\Delta\phi$ is the phase change of A across the domain and is equal to integer multiples of 2π . The real part of Eq. (3.64) can thus be written as

$$(\rho^2)_T = - \left\{ \frac{\rho_{XX}}{\rho} - \frac{E_1^2}{\rho^4} + \left(b + \frac{a_1 - a_2}{2} \gamma \right) \rho^2 + 3\beta\rho^4 \right\}_{XX}, \quad (3.67)$$

or equivalently

$$s_T = - \left\{ \frac{s_{XX}}{2s} - \frac{s_X^2}{4s^2} - \frac{E_1^2}{s^2} + \left(b + \frac{a_1 - a_2}{2} \gamma \right) s + 3\beta s^2 \right\}_{XX} \quad (3.68)$$

with $s \equiv \rho^2$. The coefficients are defined as in section 3.4 and T is redefined suitably to include the overall factor. It is clear that $\langle \rho^2 \rangle$ is time independent. If E_1 remains zero at all time, as indicated in [49], the equation has Lyapunov functional

$$F \equiv \left\langle \rho_X^2 - \frac{1}{2} \left(b + \frac{a_1 - a_2}{2} \gamma \right) \rho^2 - \beta \rho^6 \right\rangle \quad (3.69)$$

which decreases monotonically over time.

The temporal stability of stationary solutions can be obtained via studying the eigenvalue problem of the linearized equation. Consider $s = s_0 + \delta s$ where s_0 is the amplitude square of the stationary solution. The linearized equation can be written as

$$\begin{aligned} \delta s_T = & - \left\{ \left[\frac{s_{X,0}^2 + 4E_{1,0}^2}{2s_0^3} - \frac{s_{XX,0}}{2s_0^2} + \left(b + \frac{a_1 - a_2}{2} \gamma \right) + 6\beta s_0 \right] \delta s \right. \\ & \left. + \frac{\delta s_{XX}}{2s_0} - \frac{s_{X,0}\delta s_X}{2s_0^2} - \frac{2E_{1,0}^2}{s_0^2 \langle s_0^{-1} \rangle} \left\langle \frac{\delta s}{s_0^2} \right\rangle \right\}_{XX}, \end{aligned} \quad (3.70)$$

where $E_{1,0}$ is E_1 evaluated at the stationary solution. This equation can be further simplified for stationary solutions with constant amplitude in space

$$2s_0\delta s_T = - \left(U_{\rho\rho}|_{\rho=s_0^{1/2}} \delta s + \delta s_{XX} \right)_{XX}, \quad (3.71)$$

where $U_{\rho\rho}$ is given in Eq. (3.61). This indicates the primary branch is temporally unstable in the region where $U_{\rho\rho}|_{\rho=s_0^{1/2}} > \left(\frac{2\pi}{\epsilon^2\Gamma} \right)^2$ (the domain is finite periodic). The temporal instability of the primary branch always accompanies with the secondary bifurcation and the number of unstable eigenvalues either increases or decreases by 2 while passing through the branching points. According to this the primary branch is stable in figure 3.13(a), twice unstable between point 1 and point 2 in figure 3.13(b,c) and point 1 and point 3, point 4 and point 2 in figure 3.13(d), and quadrice unstable between point 3 and point 4 in figure 3.13(d). For the primary branches in figure 3.15, they are stable only at small amplitude and the number of unstable eigenvalues increases by 2 while passing through each successive branching point along the primary branch from below.

For stationary modulated solutions, we compute their temporal stability numerically based on Eq. (3.70) and focus on the solutions given in figures 3.13 and 3.15. Spectral method with Fourier basis functions is used to construct the spectral matrix and the modes included are $k = 0, \pm \frac{2\pi}{\epsilon^2\Gamma}, \dots, \pm \frac{256\pi}{\epsilon^2\Gamma}$. We have examined this by including more modes (up to $512 \times 2 + 1$) in the calculation but the result on the stability is identical. In figure 3.13(b), the modulated branch is stable along the lower part of the branch and becomes once unstable after passing through the saddle-node before reconnecting back to the primary branch. The same property holds for modulated branches bifurcate from point 1 in figure 3.13(c,d) but however all the other modulated branches, including the ones in figure 3.15, are temporally unstable.

There exists no stable modulated state when \tilde{c} is negative and the only stable solutions are periodic states occur before the onset of secondary bifurcation. But when \tilde{c} is positive, besides stable periodic states there exist also stable modulated states on the first secondary branch ($n = 1$) while the other solutions are all unstable. Furthermore, the stable region (in Ra) of the modulated states overlaps with the stable region of the periodic states as shown in figure 3.13 which indicates a bistability between these two states.

3.6 Effects of boundary conditions

The presence of the large scale phase-like mode in MC can be attributed to the definition of magnetic flux, but in RC the zonal velocity v is itself a physical variable and the phase-like property is due to the stress-free boundary conditions. According to this, it would be worth to see how the bifurcation behavior changes under weakly broken of stress-free boundary conditions. In this section, we examine this effect by imposing mixed boundary conditions of Robin type, with the stress-free boundary conditions in RC replaced by a linear interpolation between stress-free ($\beta = 0$) and no-slip ($\beta = 1$) boundary conditions:

$$(1 - \beta)\psi_{zz} \pm \beta\psi_z = 0, \quad (1 - \beta)v_z \pm \beta v = 0, \quad (3.72)$$

where β is in between $[0, 1]$ and the plus sign is chosen at the upper boundary while the minus sign is for the lower one. All the other boundary conditions remain unchanged. Under these boundary conditions, the two reflection symmetries mentioned in section 3.1 still hold and the choice of sign agrees with the physical intuition in which the fluid velocity at the boundary is in the same direction as the fluid stress. These boundary conditions can be regarded as the first order approximation of slip boundary conditions.

A direct consequence of these boundary conditions is a change in the critical Rayleigh number when β becomes nonzero. To analyze this we consider the linearized version of Eqs. (3.3) and (3.4)

$$\sigma^{-1}\nabla^2\psi_t = Ra\theta_x - Tav_z + \nabla^4\psi, \quad (3.73)$$

$$\theta_t = \psi_x + \nabla^2\theta, \quad \sigma^{-1}v_t = Ta\psi_z + \nabla^2v. \quad (3.74)$$

Assume ψ , θ , and v have horizontal wavenumber equal to k . In the case of steady convection the linear equations can be combined into a single equation of ψ which takes the form

$$[(\partial_{zz} - k^2)^3 + Rak^2 + Ta^2 \partial_{zz}] \psi = 0. \quad (3.75)$$

The corresponding characteristic equation is

$$(\lambda^2 + k^2)^3 + Ta^2 \lambda^2 = Rak^2. \quad (3.76)$$

While treating Eq. (3.76) as a polynomial of degree 3 with respect to λ^2 , the three roots are $(\lambda_0^2, \lambda_1^2, \lambda_1^{*2})$, where λ_0^2 is real positive and $(\lambda_1^2, \lambda_1^{*2})$ is a complex conjugate pair. Steady convection first occurs with even parity thus we restrict our attention to solutions that are even in z . The general form of even solutions is

$$\psi = A \cos(\lambda_0 z) + \{B \cos(\lambda_1 z) + c.c.\}, \quad (3.77)$$

$$\theta = i \left[\frac{Ak \cos(\lambda_0 z)}{p_0} + \left\{ \frac{Bk \cos(\lambda_1 z)}{p_1} + c.c. \right\} + \frac{CTa^2 \cosh(kz)}{Ra} \right], \quad (3.78)$$

$$v = -Ta \left[\frac{A\lambda_0 \sin(\lambda_0 z)}{p_0} + \left\{ \frac{B\lambda_1 \sin(\lambda_1 z)}{p_1} + c.c. \right\} + C \sinh(kz) \right], \quad (3.79)$$

where $p_n \equiv k^2 + \lambda_n^2$, and A, B, C are constants to be determined. Here we define a matrix \mathbf{M} as $\mathbf{M} = (\mathbf{M}_0, \mathbf{M}_1, \mathbf{M}_1^*, \mathbf{N})$ with

$$\mathbf{M}_n = \begin{pmatrix} \cos(\lambda_n/2) \\ (1 - \beta)\lambda_n^2 \cos(\lambda_n/2) + \beta\lambda_n \sin(\lambda_n/2) \\ [(1 - \beta)\lambda_n^2 \cos(\lambda_n/2) + \beta\lambda_n \sin(\lambda_n/2)] / p_n \\ \cos(\lambda_n/2) / p_n \end{pmatrix},$$

$$\mathbf{N} = \begin{pmatrix} 0 \\ 0 \\ (1 - \beta)k \cosh(k/2) + \beta \sinh(k/2) \\ \frac{Ta^2}{Rak} \cosh(k/2) \end{pmatrix},$$

In order to satisfy the boundary conditions at $z = \pm 1/2$, the linear homogeneous system

$$\mathbf{M}(A, B, B^*, C)^T = 0 \quad (3.80)$$

must have nontrivial solutions. This implies the determinant of \mathbf{M} is zero. With these relations we can obtain the critical Rayleigh number Ra_c by minimizing Ra via varying k for given values of Ta and β . Figure 3.16 shows the dependence of the critical wavenumber k_c and the critical Rayleigh number Ra_c on β when $Ta = 20, 60, 100$, and 140 . As shown in the figure, Ra_c increases as β increases for small Taylor numbers but Ra_c decreases as β increases for Taylor numbers greater than 60 and the minimum value of Ra_c occurs at a value of β less than but close to 1.

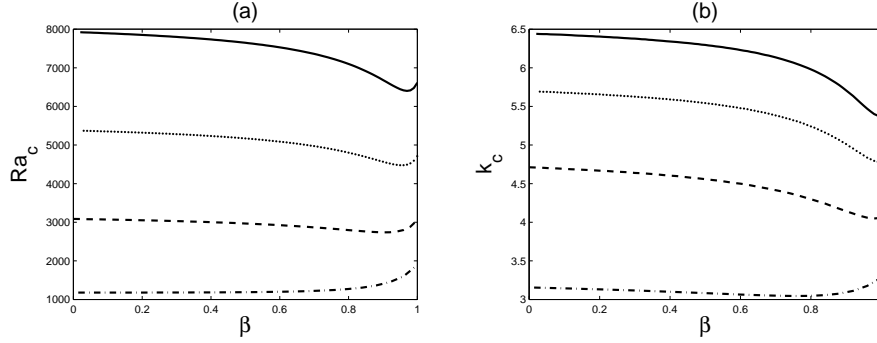


Figure 3.16: Dependence of (a) Ra_c and (b) k_c on β . Solid line: $Ta = 140$. Dotted line: $Ta = 100$. Dashed line: $Ta = 60$. Dashed-dotted line: $Ta = 20$.

The large scale mode is no longer marginal with mixed boundary conditions. Regarding this, we calculate the corresponding temporal eigenvalue to find out the dependence of growth rate on β . When β is nonzero, the large scale mode is referred as the mode with nonzero v component and is non-oscillatory in the horizontal direction ($k = 0$). As shown in section 3.1, the phase-like mode $(\psi, \theta, v) = (0, 0, 1)$ is marginal when $\beta = 0$ but this is no longer true as β becomes nonzero. Let μ be the growth rate of the large scale mode. According to Eqs. (3.3) and (3.4) these modes should satisfy

$$-Tav_z + \partial_{zz}(\partial_{zz} - \sigma^{-1}\mu)\psi = 0, \quad (3.81)$$

$$(\partial_{zz} - \mu)\theta = 0, \quad Ta\psi_z + (\partial_{zz} - \sigma^{-1}\mu)v = 0. \quad (3.82)$$

Here θ is independent of v and ψ hence we can ignore it in the later computation. Combining Eqs. (3.81) and (3.82) together we have

$$Ta^2v_{zz} = -(\partial_{zz} - \sigma^{-1}\mu)^2v_{zz}. \quad (3.83)$$

There are six linearly independent solutions in Eq. (3.83) but only the even modes of v in z are relevant in the calculation. In this case the general form of the solution is

$$\psi = \frac{\sigma^{-1}\mu}{Ta}Az + \{i\lambda_1^{-1}B \sin(\lambda_1 z) + c.c.\}, \quad (3.84)$$

$$v = A + \{B \cos(\lambda_1 z) + c.c.\}, \quad (3.85)$$

where $\lambda_1^2 = -\sigma^{-1}\mu + iTa$. The boundary conditions at $z = \pm 1/2$ imply that

$$\begin{aligned} \frac{\sigma^{-1}\mu A}{2Ta} + \left\{ \frac{i \sin(\lambda_1/2)B}{\lambda_1} + c.c. \right\} &= 0, \\ \beta\sigma^{-1}\mu A + \left\{ iTa \left[(\beta - 1)\lambda_1 \sin\left(\frac{\lambda_1}{2}\right) + \beta \cos\left(\frac{\lambda_1}{2}\right) \right] B + c.c. \right\} &= 0, \\ \beta A + \left\{ \left[(\beta - 1)\lambda_1 \sin\left(\frac{\lambda_1}{2}\right) + \beta \cos\left(\frac{\lambda_1}{2}\right) \right] B + c.c. \right\} &= 0. \end{aligned}$$

Applying the solvability condition (determinant of the matrix vanishes) for this linear homogeneous system again we can obtain the dependence of μ on other parameters, which is shown in figure 3.17. The growth rate is always negative when β becomes nonzero and decreases monotonically as β increases. The slope of μ with respect to β when $\beta \approx 0$ is approximately equal to -2σ .

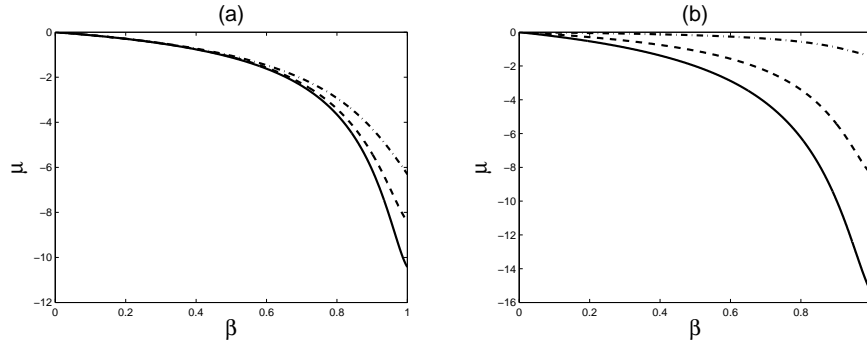


Figure 3.17: The dependence of μ on β . (a) $\sigma = 0.6$. Solid line: $Ta = 100$. Dashed line: $Ta = 60$. Dashed-dotted line: $Ta = 20$. (b) $Ta = 60$. Solid line: $\sigma = 1.1$. Dashed line: $\sigma = 0.6$. Dashed-dotted line: $\sigma = 0.1$.

From the calculations above, the weakly nonlinear theory should include a damping term in the large scale mode whenever the stress free boundary conditions are weakly broken. Under the same scaling as in [18], together with $\beta = \epsilon^2 \beta_2$, the scaled modulation equations are

$$\eta A_T = rA + A_{XX} - \frac{1 - \xi^2}{2} |A|^2 A - \xi A V_X, \quad (3.86)$$

$$V_T = -\lambda V + V_{XX} + \xi (|A|^2)_X, \quad (3.87)$$

where $\lambda = 24p\beta_2$. In the stationary case, the gradient of the large scale mode is given by

$$V_X = \xi \left(\frac{1}{2} \int_{\mathbb{R}} e^{-|y|} |A(X + \lambda^{-1/2} y)|^2 dy - |A|^2 \right). \quad (3.88)$$

Here the domain of integration is extended to the whole real line due to periodicity in X . The presence of λ provides another length scale in the problem and acts as a connection between local and nonlocal coupling. When λ is large or equivalently the magnitude of β is larger than $O(\epsilon^2)$, the large scale mode becomes irrelevant and the governing modulation equation reduces into the cubic real Ginzburg-Landau equation as in Eq. (2.1).

Figure 3.18 shows the bifurcation diagrams of Eqs. (3.86) and (3.87) for several different values of β with the primary branches all located at the band center. The thin lines correspond to $n = 1$ modulated solutions. The solution branches with $\beta \neq 0$ are shifted such that the primary branches all lie at the same location for comparison. The cubic real Ginzburg-Landau equation only allows stationary modulated solution when the primary bifurcation is

subcritical ($\xi^2 > 1$). The secondary bifurcation point in the subcritical case converges to the location $r = -\frac{2\pi^2}{\epsilon^2\Gamma^2}$ predicted by Eq. (2.1) as λ increases, while the branching point moves up to infinity in the supercritical case ($\xi^2 < 1$).

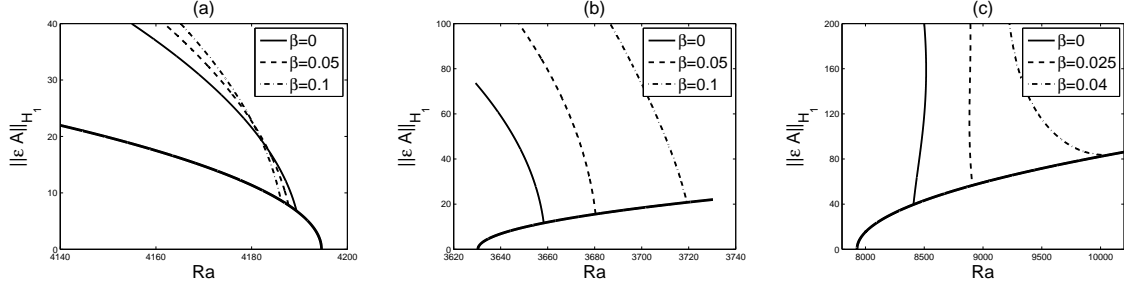


Figure 3.18: Bifurcation diagrams of $K_0 = 0$ primary branch in rotating convection for the mixed boundary conditions (3.72). $\Gamma = 10\lambda_c$. (a) $\sigma = 0.4$, $Ta = 80$ ($\xi^2 = 1.2263$). (b) $\sigma = 0.6$, $Ta = 70$ ($\xi^2 = 0.5882$). (c) $\sigma = 0.6$, $Ta = 140$ ($\xi^2 = 0.3877$).

On the effect of slanted snaking, since the large scale mode becomes linearly damped as β increases it can be expected that the structure of slanted snaking will reduce into regular homoclinic snaking. Figure 3.19 [60] shows the snaking behavior of RC for the parameter values given in figure 3.1 ($Ta = 20$, $\sigma = 0.1$ and $\Gamma = 10\lambda_c$) except that the boundary conditions are now given by the relation (3.72). Notice that the snaking becomes less slanted as β increases and is nearly vertical for $\beta = 0.6$.

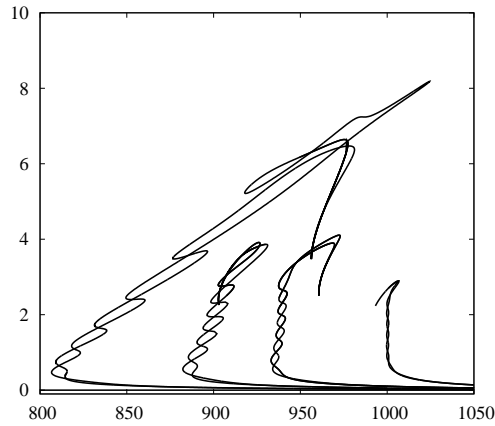


Figure 3.19: Bifurcation diagram showing the average poloidal kinetic energy \mathcal{E} (vertical axis) as a function of the Rayleigh number Ra (horizontal axis) for slanted snaking when $Ta = 20$, $\sigma = 0.1$, and $\Gamma = 10\lambda_c$ for the mixed boundary conditions (3.72). From left to right, the snaking branches correspond to $\beta = 0, 0.2, 0.4$, and 0.6 . These results are provided by Dr. Beaume [60].

3.7 Discussion

In this chapter we have described strongly nonlinear solutions of the equations describing two-dimensional RC. Localized solutions are present regardless of whether the primary branch of periodic states is subcritical or supercritical, provided only that $\xi^2 > 1/3$. The localized structures are embedded in a self-generated zonal shear layer with a compensating shear profile outside the structure. The shear rate $V' < 0$ inside the convection while $V' > 0$ outside, implying that the convection locally reduces the angular velocity by expelling angular momentum; this angular momentum increases the angular velocity outside the convection and creates a shear layer. Similar symbiotic coexistence between anticyclonic shear and localized vortex structures is familiar from other rotating fluid systems [61, 62, 63, 64].

The convections can be present over a substantial range of Rayleigh numbers in contrast to other fluid systems exhibiting localized states [9, 12]. This is a consequence of the large scale mode in the presence of stress-free boundary conditions at the top and bottom boundaries. Because of this conserved quantity the amplitude equations describing the localized structure are nonlocal, and the spatially periodic states are unstable at small amplitude even when they bifurcate supercritically. This nonlocal aspect of the problem has four consequences: (i) it leads to slanted snaking of the localized structures, (ii) it permits localized structures to be present outside the region of bistability between the conduction state and periodic convection, (iii) it destabilizes the spatially periodic convection at small amplitude even when the bifurcation to convection is supercritical, and (iv) it permits localized states even when periodic convection bifurcates supercritically.

Based on weakly nonlinear analysis, we derived the modulation equations for two-dimensional RC and MC for stress-free boundary conditions near a codimension-two point. In both cases, the modulation equation takes the form of a nonlocal fifth order Ginzburg-Landau equation. Extensive study of the bifurcation and stability properties of this equation indicates that the higher order theory we derived can capture important phenomena that are not present in the leading order theory [18]. The bifurcation scenario can be qualitatively separated into two classes, $\tilde{c} < 0$ and $\tilde{c} > 0$. When $\tilde{c} < 0$, the primary branch is only stable at small amplitude. The instability sets in at larger amplitude and leads to countably infinite number of unstable modulation branches all of which undergo phase jumps to $K_0 \neq 0$ periodic states. However, when $\tilde{c} > 0$, the region of instability of the primary branch is bounded within certain range of Rayleigh numbers and the first modulation branch that bifurcates closest to the primary bifurcation is stable before reaching a saddle node. There is also a region of bistability between periodic and modulated states. These results suggest a possible investigation of the full problem near the codimension-two point focusing on dynamical aspects such as coarsening type behavior which could exist in the system.

We also examined the case when the stress-free boundary conditions are weakly broken. Mixed boundary conditions of Robin type were introduced to destroy the marginal stability property of the large scale mode. But when the boundary conditions are close to free-slip, they permit the interpolation between nonlocal to local coupling connecting Cox and Matthew's equation [18] to the cubic real Ginzburg-Landau equation. Moreover, the snaking

behavior is changed from slanted snaking to regular homoclinic snaking as β increases. These results indicate that the formation of localized states in two-dimensional RC is sensitive to the chosen boundary conditions.

Chapter 4

Exact solutions of the cubic-quintic Swift-Hohenberg equation

In this chapter, we study the Swift-Hohenberg equation with cubic-quintic nonlinearity (SH35), which takes the form

$$u_t = \mu u - (1 + \partial_{xx})^2 u + bu^3 - cu^5. \quad (4.1)$$

Here u is a real-valued scalar function and the coefficients are also real. In our consideration, both b and c are positive which $b > 0$ is responsible for the subcritical bifurcation of periodic states and $c > 0$ is responsible for saturating the growth of the instability. In principle, we can set $c = 1$ by rescaling u and b but here we retain the coefficient c for later convenience. Equation (4.1) is equivariant under

$$R_1 : x \rightarrow -x, \quad u \rightarrow u, \quad R_2 : x \rightarrow x, \quad u \rightarrow -u \quad (4.2)$$

together with translations $T_\ell : x \rightarrow x + \ell, \quad u \rightarrow u$, and these symmetries will prove important in what follows.

The bifurcation of Eq. (4.1) has been studied in [70] and [74, 37] with the former focusing on the spatially localized states on an extended domain and the later focusing on the modulated structures formed on a finite domain. But there remains the question whether there are nontrivial $O(1)$ solutions that are not related to the states which bifurcate from the periodic solutions that originate from the homogeneous state $u = 0$. To investigate this possibility we adopt a method developed in [75, 76] to construct exact meromorphic solutions of related equations and use the resulting exact solutions as initial conditions for numerical continuation. The approach has also been used to search for exact meromorphic solutions of the standard Swift-Hohenberg equation [77] and for the quadratic-cubic Swift-Hohenberg equation (SH23) with a dispersive term u_{xxx} [78].

Another aspect that will be covered is SH23 with a dispersive term u_{xxx} . Some preliminary estimate on the traveling solutions is given and a modulation equation approach is applied to study the small amplitude bifurcation behavior near the onset. The chapter builds upon works that appear in [80].

4.1 Exact meromorphic solutions

In this section we give a brief overview of the method of deriving exact meromorphic solutions of ordinary differential equations (ODEs) in the complex plane. Consider an autonomous algebraic ODE of order n defined on a neighborhood of $z = z_0$ in the complex plane,

$$\sum_j a_j \Pi_{k=0}^n (w^{(k)})^{j_k} = 0, \quad (4.3)$$

where the superscript (k) denotes the k -th derivative with respect to z , $j = (j_1, \dots, j_n)$ is a multi-index and $a_j \in \mathbb{C}$ are constants. The degree of a monomial is defined as $\sum_{k=0}^n j_k$. We seek a solution in the form of a formal Laurent series,

$$w(z) = \sum_{k=-p}^{\infty} c_{k+p} (z - z_0)^k, \quad (4.4)$$

with a finite principal part. Here $z_0 \in \mathbb{C}$ is an arbitrary constant and p is a positive integer indicating the order of the pole at $z = z_0$. Substitution of Eq. (4.4) into Eq. (4.3) allows one to solve for the coefficients $\{c_0, c_1, \dots\}$ recursively. For $j \geq 1$ one obtains relations of the form

$$P(c_0, j) c_j = Q_j(\{c_l | l < j\}), \quad (4.5)$$

where $P(c_0, j)$ are polynomials in c_0 and j , while Q_j are polynomials in $\{c_l | l < j\}$. Fuchs indices are the values of j for which $P = 0$. If one of the Fuchs indices is a positive integer k , say, the corresponding $Q_k = 0$ and the coefficient c_k is undetermined. Note that $k = -1$ is always a Fuchs index, reflecting the arbitrariness of z_0 .

Equation (4.3) is said to have the finiteness property if it only admits finitely many formal Laurent series with finite principal part and degree $p \geq 1$. If this property holds and the equation contains only one monomial of the highest degree, all meromorphic solutions fall into one of three classes [75]: (A) elliptic solutions, (B) singly periodic solutions, or (C) rational solutions. Each solution is periodic in \mathbb{C} with a fundamental cell: a periodic parallelogram in (A), a periodic stripe in (B), and the whole complex plane in (C). Owing to the finiteness property each periodic cell contains at most N poles, where N is the number of different formal Laurent series. This classification is a consequence of Nevanlinna theory and the restriction on the number of poles is a consequence of the uniqueness of solutions of ODEs. Meromorphic solutions of these three types will be referred as belonging to class W in later discussion. If an equation does not possess the finiteness property (this is the case if one of the Fuchs indices is a positive integer), we may still look for solutions that belong to class W although we are no longer guaranteed that all meromorphic solutions are of this class.

It follows that meromorphic solutions in W can be written as linear superpositions of functions with poles of suitable order. In case (A) these are the Weierstrass ζ function $\zeta(z - z_i; \omega_1, \omega_2)$ (order 1 pole), the Weierstrass \wp function $\wp(z - z_i; \omega_1, \omega_2)$ (order 2 pole) and their

derivatives, in case (B) the appropriate functions are the cotangent function $\cot(\pi(z - z_i)/\omega)$ (order 1 pole) and its derivatives, while in case (C) the functions are $\{1/(z - z_i)^n | n \in \mathbb{N}\}$. Here z_i are the locations of the poles, ω_1, ω_2 are the periods of the elliptic solutions in case (A), while ω is the period of the singly periodic functions in case (B). To obtain these solutions the locations of the poles z_i need to be determined. This can be done by matching the general expressions with the formal Laurent series obtained above. The procedure requires the use of addition formulae and the knowledge of Laurent expansions of Weierstrass and trigonometric functions [79]. For convenience we list here the relevant formulae for Weierstrass functions. The addition formula for the Weierstrass ζ function is

$$\zeta(z - z_i) = \zeta(z) - \zeta(z_i) + \frac{1}{2} \frac{\wp'(z) + \wp'(z_i)}{\wp(z) - \wp(z_i)}. \quad (4.6)$$

Here \wp is the Weierstrass \wp function and solves the ODE

$$\wp'(z)^2 = 4\wp(z)^3 - g_2\wp(z) - g_3. \quad (4.7)$$

The Weierstrass \wp function has the Laurent expansion

$$\wp(z) = z^{-2} + \frac{g_2 z^2}{20} + \frac{g_3 z^4}{28} + O(|z|^6) \quad (4.8)$$

around the pole at $z = 0$. The constants g_2 and g_3 are elliptic invariants defined by

$$g_2 \equiv \sum_{m,n \neq (0,0)} \frac{60}{(m\omega_1 + n\omega_2)^4}, \quad g_3 \equiv \sum_{m,n \neq (0,0)} \frac{140}{(m\omega_1 + n\omega_2)^6},$$

where ω_1 and ω_2 represent the two periods of the function.

4.2 Meromorphic solutions of stationary SH35

In the stationary case, i.e., $u(x, t) = w(x)$, Eq. (4.1) reduces to

$$w'''' + 2w'' - aw - bw^3 + cw^5 = 0. \quad (4.9)$$

This equation can be integrated once by multiplying w' and gives

$$w''''w' - \frac{w''^2}{2} + w'^2 - \frac{aw^2}{2} - \frac{bw^4}{4} + \frac{cw^6}{6} - E = 0, \quad (4.10)$$

where E is an integration constant. Here $a \equiv \mu - 1$ and c is set equal to $3/2$ to simplify the calculations that follow. To recover the usual case $c = 1$, we may rescale w and the coefficient b as $w \rightarrow (2/3)^{1/4} w$ and $b \rightarrow \sqrt{3/2} b$. In the following we extend the domain of w to the whole complex plane, and demand that $w(z)$ is meromorphic and hence locally

representable in terms of a formal Laurent series as in Eq. (4.4). The parameters a and b are assumed to be real although the results that follow hold when a and b are complex numbers.

Before proceeding we note that the autonomous ODE Eq. (4.9) is equivariant with respect to two different reflections,

$$R_1 : z \rightarrow -z, \quad w \rightarrow w, \quad R_2 : z \rightarrow z, \quad w \rightarrow -w. \quad (4.11)$$

However, in the complex domain there is a third symmetry

$$R_3 : z \rightarrow z^*, \quad w \rightarrow w^*. \quad (4.12)$$

Under this operation, $R_3 w$ remains a function of z but the coefficients c_k of the Laurent series transform to c_k^* . If a and b are complex, we also transform $(a, b) \rightarrow (a^*, b^*)$ so that $R_3 w$ remains a function of z and solves Eq. (4.9) with parameters (a, b) .

The degree of the pole at $z = 0$ and the coefficient c_0 can be determined by balancing $w'''w' - \frac{w''^2}{2}$ and the sextic term in Eq. (4.10),

$$p = 1, \quad c_0^4 = -16. \quad (4.13)$$

The Fuchs indices are

$$j_1 = -1, \quad j_{2,3} = \frac{5 \pm i\sqrt{39}}{2}. \quad (4.14)$$

Since there is no positive integer Fuchs index and only one monomial of highest degree, w^6 , the finiteness property holds and all meromorphic solutions belong to class W . Equation (4.10) admits four different Laurent series all of which are odd functions of z :

$$w_1(z) = \sqrt{2}(1+i) \left\{ \frac{1}{z} + \frac{1-bi}{30}z + \frac{2ib-4-15a-2b^2}{1800}z^3 \right\} + \dots, \quad (4.15)$$

$$w_2(z) = R_2 w_1(z), \quad (4.16)$$

$$w_3(z) = \sqrt{2}(1-i) \left\{ \frac{1}{z} + \frac{1+bi}{30}z - \frac{2ib+4+15a+2b^2}{1800}z^3 \right\} + \dots, \quad (4.17)$$

$$w_4(z) = R_2 w_3(z). \quad (4.18)$$

The Laurent series w_1 and w_3 are related by the symmetry R_3 , i.e., $w_3 = R_3 w_1$.

In the following subsections, we seek solutions belonging to class W and derive explicit expressions for the corresponding meromorphic solutions. There are at most four poles within each periodic cell. Moreover, the symmetries relating $\{w_n | n = 1, 2, 3, 4\}$ imply that if w has Laurent expansions w_n and w_m with $n \neq m$ around the poles z_n and z_m , then w is periodic with period $2(z_n - z_m)$. To see this explicitly, assume $n = 1$ and $m = 2$ so that

$$w(z - z_1) = w_1(z) = R_2 w_2(z) = R_2 w(z - z_2). \quad (4.19)$$

Thus $w(z) = R_2 w(z + z_1 - z_2) = w(z + 2z_1 - 2z_2)$ with period $2(z_1 - z_2)$. Since the ODE is autonomous and the Laurent series are related to one another by the symmetries, we may assume that w has Laurent expansion w_1 around $z = 0$.

We remark that traveling solutions of the form $u(x, t) = w(x - Ct)$, $C \in \mathbb{R}$, do not have a Laurent series for $C \neq 0$.

Elliptic solutions

Elliptic functions are meromorphic functions w defined on \mathbb{C}/Γ satisfying

$$w(z) = w(z + \omega_1) = w(z + \omega_2), \quad \omega_1, \omega_2 \in \mathbb{C}, \quad \omega_1/\omega_2 \notin \mathbb{R}, \quad (4.20)$$

where ω_1 and ω_2 are the two periods of the function $w(z)$ and Γ is the lattice generated by these two periods. Due to double periodicity,

$$\oint w dz = 0 \quad (4.21)$$

over the fundamental parallelogram and the sum over the residues vanishes. Expansions (4.15)–(4.18) imply that elliptic solutions of Eq. (4.10) can only have two or four distinct poles within the fundamental parallelogram.

For the case of four distinct poles, one pole may be placed at the origin ($z_0 = 0$) with the remaining poles located at z_1, z_2 , and z_3 . The general form of the elliptic solution is thus

$$\begin{aligned} w(z) &= \tilde{h} + 2e^{i\pi/4} \sum_{m=0}^3 i^m \zeta(z - z_m) \\ &= h + e^{i\pi/4} \sum_{m=1}^3 i^m \frac{\wp'(z) + \wp'(z_m)}{\wp(z) - \wp(z_m)}, \end{aligned} \quad (4.22)$$

where the relation (4.6) was used to obtain the second expression. Here \tilde{h} and h are constants. By comparing the Laurent expansion of Eq. (4.22) with w_1 at $z = 0$, we obtain $h = 0$ together with

$$\sum_{m=1}^3 i^{m-1} \wp(z_m)^n = f_n, \quad \sum_{m=1}^3 i^{m-1} \wp(z_m)^{n-1} \wp'(z_m) = 0, \quad (4.23)$$

where $n \in \{1, 2, 3\}$ and

$$f_1 = \frac{i+b}{30}, \quad f_2 = \frac{(b-i)b + \frac{15a}{2} - 90g_2 + 2}{900i}, \quad f_3 = \frac{c_6(1+i)}{2\sqrt{2}} + \frac{g_2(i+b)}{200} + \frac{3ig_3}{28}.$$

In addition $\wp(z_m)$ and $\wp'(z_m)$ are related by Eq. (4.7). Owing to the symmetries we know, without solving the algebraic equations, that the poles are located at points of half-period which are $\omega_1/2$, $\omega_2/2$, and $(\omega_1 + \omega_2)/2$. Hence $\wp'(z_m) = 0$ for all m and $\wp(z_m) = e_m$, where e_m are the roots of the polynomial

$$4\wp^3 - g_2\wp - g_3 = 0. \quad (4.24)$$

After some manipulations, it can be shown that

$$e_1 = \frac{(b+i)(i+2) + (1-i)f}{180}, \quad e_2 = \frac{1+i(f-b)}{90}, \quad e_3 = \frac{(b+i)(i-2) - (1+i)f}{180},$$

and

$$g_2 = \frac{ib - 2 - b^2 - 15a/2 + (i + b)f}{810}, \quad g_3 = 4e_1e_2e_3,$$

where

$$f = \pm \left(\frac{11b^2 - 8ib + 19 + 75a}{2} \right)^{1/2}.$$

The periods ω_1 and ω_2 can be obtained numerically from g_2 and g_3 .

Since $\oint w dz = 0$, the general expression for the case of two distinct poles is

$$\begin{aligned} w(z) &= \sqrt{2} \{ (1+i)\zeta(z) - (1+i)\zeta(z - z_2) \} + \tilde{h}, \\ &= - \left(\frac{1+i}{\sqrt{2}} \right) \frac{\wp'(z) + \wp'(z_2)}{\wp(z) - \wp(z_2)} + h, \end{aligned} \quad (4.25)$$

where the second equality again follows from relation (4.6). Here \tilde{h} and h are constants and z_2 is the location of the pole with Laurent expansion w_2 . By comparing the Laurent expansion of Eq. (4.25) with w_1 at $z = 0$, we obtain $h = 0$ together with

$$\begin{aligned} \wp'(z_2) &= 0, \quad \wp(z_2) = e_1 = \frac{1 - ib}{30}, \\ g_2 &= \frac{1 - ib}{30} + \frac{a}{12}, \quad g_3 = 4e_1^3 - g_2e_1. \end{aligned}$$

Singly periodic solutions

Singly periodic functions are meromorphic functions w defined on $\mathbb{C}/\{n\omega \mid n \in \mathbb{Z}\}$ that satisfy

$$w(z) = w(z + \omega), \quad \omega \in \mathbb{C} \setminus \{0\}. \quad (4.26)$$

Here ω is the period of the singly periodic function. Meromorphic solutions of this type only admit either one or two poles within each periodic stripe (a third distinct pole would provide an additional period and hence break the assumption of single periodicity). In the following, we assume the Laurent expansion around $z = 0$ is of the form w_1 .

In the one pole case, the general form of the meromorphic solution is

$$w(z) = \frac{\sqrt{2}\pi(1+i)}{\omega} \cot\left(\frac{\pi z}{\omega}\right) + h, \quad (4.27)$$

where ω is the period and h is a constant. Comparing the Laurent expansion of Eq. (4.27) with w_1 , we obtain $h = 0$ together with

$$a = -\frac{2(b+i)(2b-3i)}{25}, \quad \omega = \pi \sqrt{\frac{10}{ib-1}}. \quad (4.28)$$

If there are two poles within a single periodic stripe, three possible cases arise since the pole with Laurent expansion w_1 can only pair with either w_2 , w_3 , or w_4 . The general expressions in these three cases are

$$w_{12}(z) = \frac{2\sqrt{2}\pi(1+i)}{\omega} \csc\left(\frac{2\pi z}{\omega}\right) + h, \quad (4.29)$$

$$w_{13}(z) = \frac{2\sqrt{2}\pi}{\omega} \left[\cot\left(\frac{2\pi z}{\omega}\right) + i \csc\left(\frac{2\pi z}{\omega}\right) \right] + h, \quad (4.30)$$

$$w_{14}(z) = \frac{2\sqrt{2}\pi}{\omega} \left[\csc\left(\frac{2\pi z}{\omega}\right) + i \cot\left(\frac{2\pi z}{\omega}\right) \right] + h, \quad (4.31)$$

where w_{1n} is the general expression for two pole singly periodic solutions with Laurent series w_1 and w_n . Comparing Eqs. (4.29)–(4.31) with w_1 at $z = 0$, we obtain $h = 0$ in all three cases, together with

$$\begin{aligned} w_{12} \quad : \quad a &= -\frac{(b+i)(b-9i)}{25}, \quad \omega = 2\pi\sqrt{\frac{5i}{b+i}}, \\ w_{13} \quad : \quad a &= \frac{(97+21i)(i+b)}{123125} (-197b+105+288i), \quad \omega = 2\pi\sqrt{\frac{5(i-2)}{(1-i)(b+i)}}, \\ w_{14} \quad : \quad a &= -\frac{(97-21i)(b+i)}{123125} (197b+105-288i), \quad \omega = 2\pi\sqrt{\frac{5(1-2i)}{(1-i)(b+i)}}. \end{aligned}$$

Rational solutions

Rational functions are meromorphic functions w defined on $\mathbb{C} \cup \{\infty\}$ that satisfy

$$w(z) = \frac{Q_1(z)}{Q_2(z)} \quad (4.32)$$

with Q_1 and Q_2 polynomials in z and $Q_2 \not\equiv 0$. Since the solution is nonperiodic only one pole can be present and the general expression for meromorphic solutions of this type is

$$w(z) = \frac{\sqrt{2}(1+i)}{z} + P(z), \quad (4.33)$$

where P is a polynomial in z . Since there is only one monomial of highest degree in Eq. (4.10), P can only be a constant and by comparing with w_1 we have $P = 0$. It is straightforward to see that $w(z) = \frac{\sqrt{2}(1+i)}{z}$ is a rational solution only when $a = 0$ and $b = -\frac{i}{2}$.

4.3 Real meromorphic solutions

In the previous section, we obtained exact solutions of the stationary SH35 equation by considering meromorphic solutions belonging to class W . But solutions of interest in

applications are those for which w is real when z is restricted to the real line. A meromorphic solution is said to be real if

$$\{w(z + z_0) \mid z \in \mathbb{R}\} \subset \mathbb{R} \quad (4.34)$$

for some $z_0 \in \mathbb{C}$. Evidently there is no real rational solution so that in the following we may focus on the elliptic and singly periodic cases. Before proceeding to find exact real solutions, we remark that we have shown in section 4.2 that exact elliptic solutions are of codimension zero in the parameter space (a, b) while exact singly periodic solutions are of codimension one. It follows that exact real solutions are generically of codimension one in the elliptic case and of codimension two in the singly periodic case. Owing to the symmetries R_1 , R_2 , and spatial translations in x , each exact real solution is embedded in a larger family of real exact solutions.

In order that a real elliptic solution exists, the periodic lattice Γ must admit one set of generators $\{\omega_1, \omega_2\}$ with ω_1 real, for otherwise the set $\{z_0 + \mathbb{R}\}/\Gamma$ will be dense in \mathbb{C}/Γ and no real solution is possible. To seek real solutions in the elliptic case, we suppose that the periodic lattice Γ is real rectangular, i.e., that there exists a pair of generators $\{\omega_1, \omega_2\}$ with ω_1 real and ω_2 imaginary. For this to be the case g_2 and g_3 must be real and the modular discriminant

$$\Delta \equiv g_2^3 - 27g_3^2 \quad (4.35)$$

must be positive. If there are four poles in the periodic parallelogram, Γ is real rectangular when

$$b^2 = -\frac{25a}{3} - 3, \quad a \in I_1 \cup I_2, \quad (4.36)$$

where $I_1 \equiv (-\infty, -\frac{36}{25})$ and $I_2 \equiv (-\frac{36}{25}, -\frac{9}{25})$. The corresponding elliptic invariants are

$$g_2 = -\frac{a}{108}, \quad g_3 = \frac{1}{6750} + \frac{a}{3240}. \quad (4.37)$$

In the following we shall be interested in $b > 0$, i.e., the hysteretic regime, implying that $a < -9/25$. In this case a one parameter family of real exact periodic solutions parametrized by a can be found by a translation of $z_0 = \omega_2/4$ (ω_2 is pure imaginary) and the solutions can be represented as

$$w(z) = e^{i\pi/4} \sum_{m=1}^3 \frac{i^m \wp'(z + \omega_2/4)}{\wp(z + \omega_2/4) - e_m}, \quad (4.38)$$

where

$$e_1 = \frac{b-1}{60}, \quad e_2 = \frac{1}{30}, \quad e_3 = -\frac{b+1}{60}.$$

Sample profiles of the resulting exact solutions are shown in figure 4.1 for $a \in I_1$ and in figure 4.2 for $a \in I_2$. In the former case the exact solutions are invariant under the symmetry R_1 . In the latter case they are invariant under R_2 followed by a translation in z by the half period $\omega_1/2$, i.e., under the symmetry TR_2 . The modular discriminant Δ

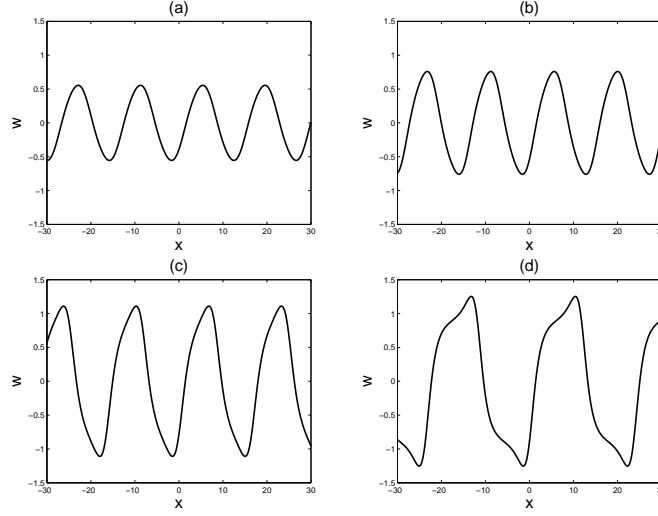


Figure 4.1: Solution profiles of the exact real elliptic solution (4.38) when $a \in I_2$ and $b = (-\frac{25a}{3} - 3)^{1/2}$. The solutions are TR_2 -symmetric. (a) $a = -0.4$. (b) $a = -0.5$. (c) $a = -1$. (d) $a = -1.4$.

vanishes when $a = -36/25$, $-9/25$ and the solution becomes degenerate as a approaches these two points. When a increases to $-9/25$ from below in I_2 , $(\omega_1, \omega_2) \rightarrow (2\sqrt{5}\pi, i\infty)$ and the solution decreases to zero in the supremum norm. In contrast, when $a \rightarrow -36/25$ from either side, it is ω_1 that tends to infinity and the solution approaches a front (heteroclinic solution) that is discussed further below. Figure 4.3 shows the spatial average of w , i.e., $\langle w \rangle \equiv L^{-1} \int_0^L w(x) dx$, the spatial period $L \equiv \omega_1$, and the free energy F/L of the solutions as a function of $\mu \equiv a + 1$. Here F is defined as

$$F[u] \equiv \int_0^L \left\{ \frac{1}{2} |(1 + \partial_{xx})u|^2 - \frac{1}{2} \mu u^2 - \frac{1}{4} b u^4 + \frac{1}{6} c u^6 \right\} dx \quad (4.39)$$

and Eq. (4.1) has been rewritten in variational form, $u_t = -\frac{\delta F}{\delta u}$. We found no real solutions in the two pole case.

In the singly periodic case the only situation that yields a nontrivial real solution is w_{13} with a purely imaginary ω , i.e., $\omega = iT$, $T \in \mathbb{R}$. By shifting the origin to $\omega/4$ as in the elliptic case, w_{13} can be rewritten as

$$w_{13}(z) = \frac{2\sqrt{2}\pi}{T} \left[-\tanh\left(\frac{2\pi z}{T}\right) + \operatorname{sech}\left(\frac{2\pi z}{T}\right) \right], \quad (4.40)$$

where $T = \pi\sqrt{10}$ and the parameters $(a, b) = (-36/25, 3)$. These parameter values correspond to the degenerate point separating the intervals I_1 and I_2 in the four pole elliptic case. This front solution connects two unstable (with respect to time) flat states $u = \pm 2/\sqrt{5}$ as shown in figure 4.4.

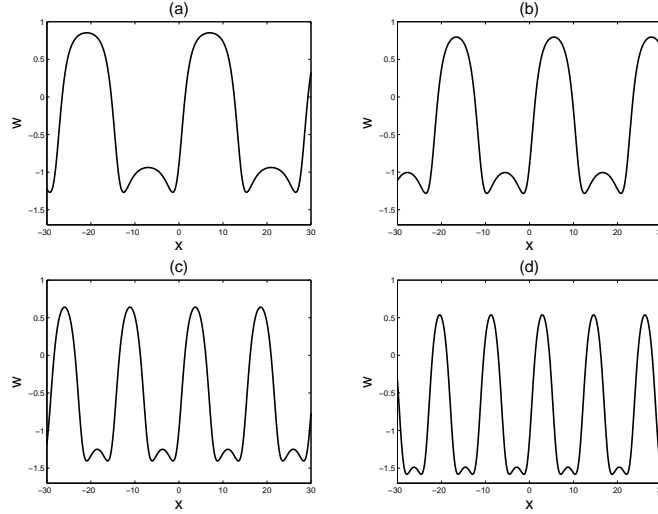


Figure 4.2: Solution profiles of the exact real elliptic solution (4.38) when $a \in I_1$ and $b = \left(-\frac{25a}{3} - 3\right)^{1/2}$. The solutions are R_1 -symmetric. (a) $a = -1.45$. (b) $a = -1.5$. (c) $a = -2$. (d) $a = -3$.

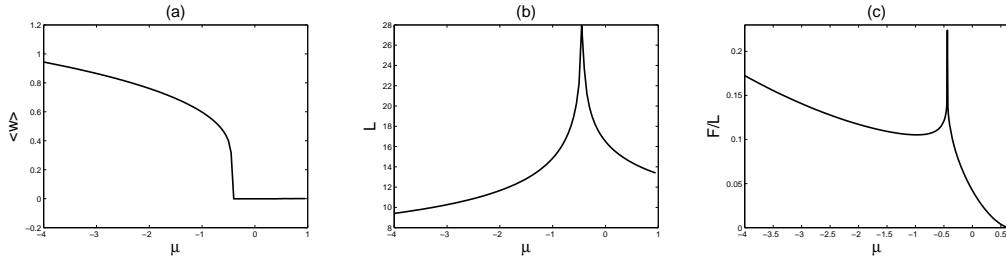


Figure 4.3: (a) The spatial average $\langle w \rangle \equiv \frac{1}{L} \int_0^L w(x) dx$, (b) the spatial period L , and (c) the free energy F/L of the exact real solutions as functions of $\mu \equiv a + 1$.

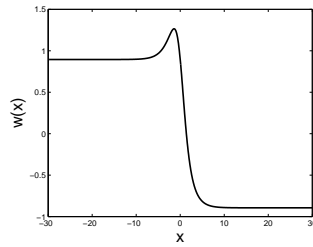


Figure 4.4: Exact front solution (4.40) for $a = -\frac{36}{25}$, $b = 3$.

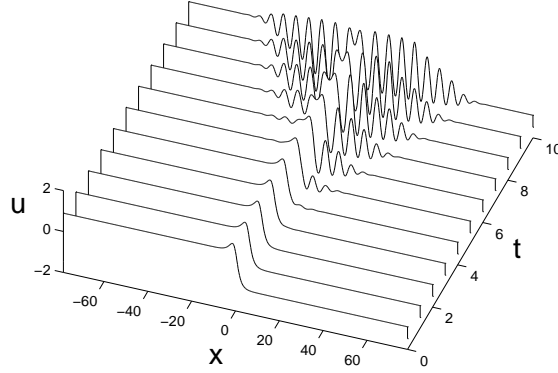


Figure 4.5: Time evolution of the front solution (4.40) perturbed in the middle at $t = 0$ with $O(10^{-3})$ random noise.

Similar results can be derived for SH23 with dispersion, viz.,

$$u_t = (\alpha + 1)u - (1 + \partial_{xx})^2 u + \sigma u_{xxx} + \beta u^2 - \gamma u^3. \quad (4.41)$$

Meromorphic traveling solutions of Eq. (4.41) of class W were studied for $\gamma < 0$ in [78]; the corresponding results for $\gamma > 0$ are summarized in Appendix J.

Linear stability properties of the exact real solutions determined in the preceding section are obtained using a spectral method with Fourier basis functions. When $a \in I_2$ the solutions are always unstable and the number of unstable modes increases with decreasing a . The stationary front solution is always unstable since the asymptotic states $w(+\infty)$ and $w(-\infty)$ are both unstable flat states. Time evolution of this solution with $O(10^{-3})$ random noise superposed in the middle at $t = 0$ is shown in figure 4.5. The solution breaks down in the middle and leads to a spatially periodic state at both ends.

The simulation was carried out in a domain of size $L = 50\pi$ with Neumann boundary conditions using the time stepper ETD4RK [40] with cosine basis functions. In contrast, when $a \in I_1$ the number of unstable modes decreases with decreasing a and the solutions acquire stability with respect to perturbations with spatial period L when a decreases below $a \approx -4.15$.

4.4 Numerical bifurcation analysis

In this section we use the exact real solutions derived in section 4.3 to initialize numerical continuation. The parameter μ (or equivalently a) is taken as the control parameter. To implement AUTO [36], the spatial dynamical ODE is written as

$$w'_0 = Lw_1, \quad w'_1 = Lw_2, \quad w'_2 = Lw_3, \quad (4.42)$$

$$w'_3 = L(-2w_2 + aw_0 + bw_0^3 - cw_0^5), \quad (4.43)$$

where w_n is the n -th spatial derivative of u , each scaled with the domain length L so that the system is defined on the interval $[0, 1]$. Periodic boundary conditions are applied on variables w_0, w_1, w_2 with L fixed and equal to the period of the starting solution (the normalization $c = 3/2$ is retained). The phase fixing condition

$$\int_0^1 (w_0 - w_{0,old}) w'_{0,old} dx, \quad (4.44)$$

is implemented to eliminate translates of the solution. Here $w_{0,old}$ is the solution at the previous continuation step. The bifurcation diagrams below show the H_2 norm

$$\|w\|_{H_2} = \left(\frac{1}{L} \sum_{n=0}^2 \int_0^L |w^{(n)}(x)|^2 dx \right)^{1/2} \quad (4.45)$$

of the solution as a function of μ . In all cases we maintain the spatial period L selected by the exact solution.

The relative position between the saddle-node (computed numerically) of the primary branch with wavenumber $k = 1$ ($L = 2\pi$) and the exact real solutions is shown in figure 4.6 in the (μ, b) plane. A bound $\mu > -\frac{3b^2}{10}$ for the presence of either periodic or pulse-like solutions is derived in [69]. This bound can be improved as follows. Multiply Eq. (4.9) by w and integrate it over Γ to obtain

$$\mu \int_{\Gamma} w^2 dx = \int_{\Gamma} [(1 + \partial_{xx})w]^2 - bw^4 + \frac{3}{2}w^6 dx \geq \int_{\Gamma} w^2 \left(\frac{3}{2}w^4 - bw^2 \right) dx, \quad (4.46)$$

where Γ is either the whole real line for the pulse solution or a single period for the periodic solution. Since $\frac{3}{2}w^4 - bw^2 \geq -\frac{b^2}{6}$ it follows that $\mu > -\frac{b^2}{6}$. The comparison between this bound and the actual location of the $k = 1$ saddle-node is also shown in the figure. All the exact real solutions lie to the right of the saddle-node of the $k = 1$ primary branch.

The exact solutions with $a \in I_2$ are symmetric with respect to TR_2 and the branches obtained by continuation share this symmetry. When $a = -0.4$ (i.e., $b = 0.5774$) the corresponding exact solution has $L = 14.1492$ and lies on a secondary branch that bifurcates from a primary branch with wavenumber $k = 0.4441$; this primary branch is the third branch that bifurcates from $u = 0$ as μ increases. This secondary branch bifurcates from the primary branch above the saddle-node and reconnects back to it as shown in figure 4.7. Similar behavior is also present for $a = -0.9$ ($b = 2.1213, L = 15.9311$) as shown in figure 4.8. In the latter case there are two additional secondary branches (the upper of these is indicated in red (gray) in figure 4.8(a)) that also connect the primary branch to itself. Both consist of solutions with R_1 symmetry. With further decrease in the value of $a \in I_2$, the spatial period of the initial solution increases and the bifurcation diagram becomes increasingly complicated. Figure 4.9 shows the bifurcation diagram for $a = -1.35$ ($b = 2.8723, L = 21.1801$). The

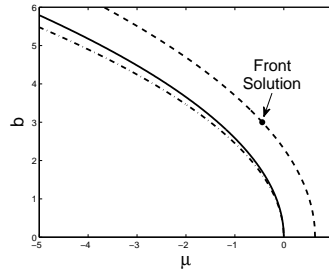


Figure 4.6: The (μ, b) plane showing the location of the exact real solutions obtained in section 4.3 (dashed line) together with the position of the saddle-node of the primary branch with $k = 1$ (solid line). The dashed-dotted line corresponds to the bound $\mu > -\frac{b^2}{6}$ for the existence of periodic or pulse-like solutions. The solid dot indicates the location of the front solution (4.40).

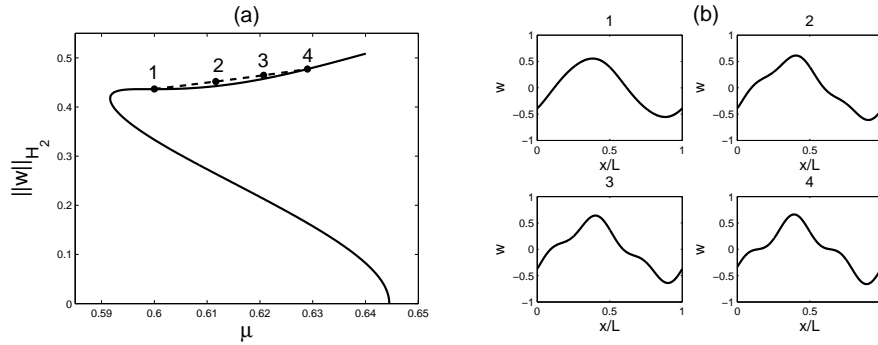


Figure 4.7: (a) Bifurcation diagram for stationary periodic solutions with $b = 0.5774$, $c = 3/2$ and period $L = 14.1492$. Point 1 corresponds to the exact real solution when $a = -0.4$. (b) Sample profiles along the black dashed line.

inset in (a) indicates the bifurcation behavior near the first appearance of secondary branches and shows there are in fact three branches that bifurcate from the primary branch in close succession. The dashed and dotted branches consist of states with TR_2 and R_1 symmetries, respectively, while the red (gray) branch consists of asymmetric states generated through a parity-breaking bifurcation. In nongradient systems states of this type travel, although here they correspond to stationary states. The asymmetric states do not reconnect to the primary branch. The exact solution (point 1) lies on the dashed branch.

As the parameter a approaches the critical value $a = -36/25$ from above the exact real solutions fall on isolas instead of secondary branches. Figure 4.10 shows an example of such an isola when $a = -1.43 > -36/45$. In addition to the isola there is also a crosslink (dashed curve in figure 4.10(a)) consisting of asymmetric stationary solutions. The structure of these isolas becomes more and more complex as a decreases through the critical value $a = -36/25$ (figure 4.11). However, for $a \in I_1$ (i.e., $a < -36/45$) the exact solutions are symmetric with

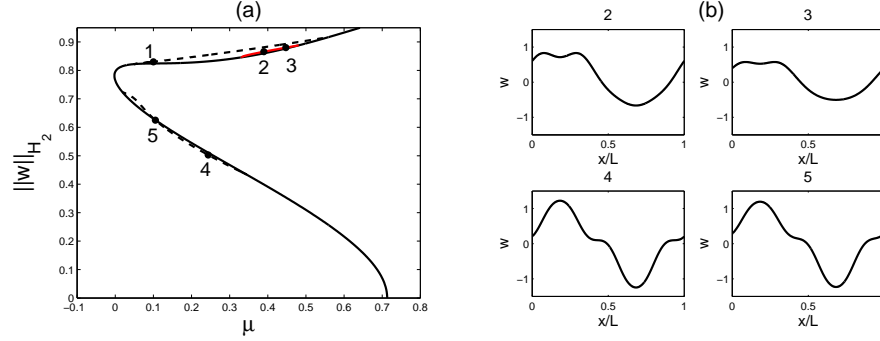


Figure 4.8: (Color online) (a) Bifurcation diagram for stationary periodic solutions with $b = 2.1213$, $c = 3/2$ and period $L = 15.9311$. Point 1 corresponds to the exact real solution with $a = -0.9$. (b) Sample profiles along the red (gray) and black dashed lines.

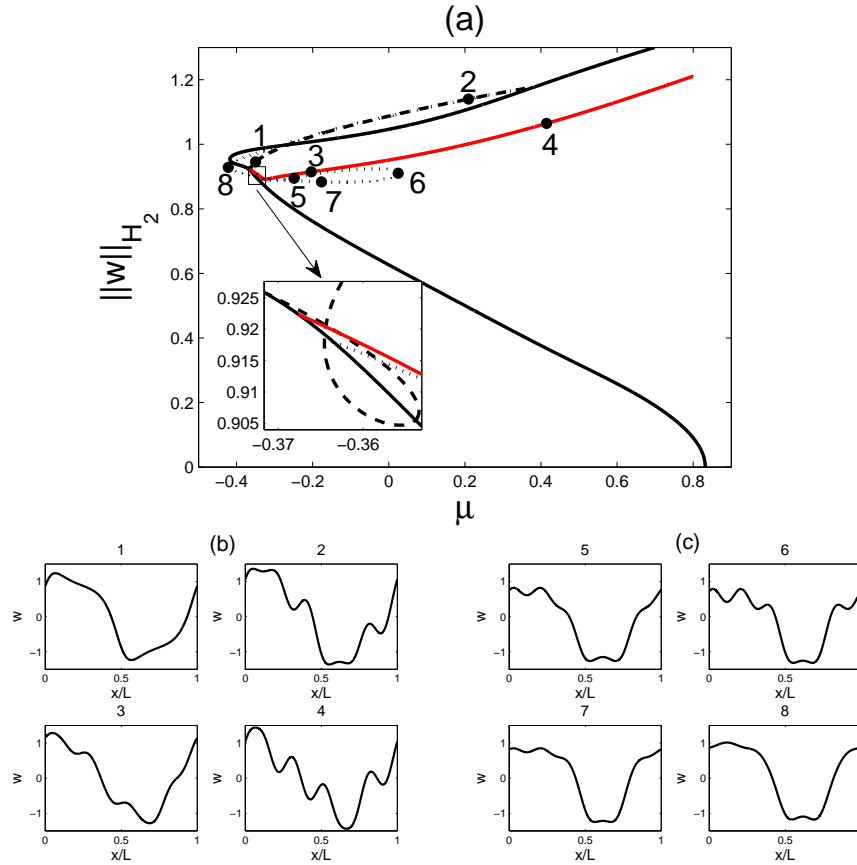


Figure 4.9: (Color online) (a) Bifurcation diagram for stationary periodic solutions with $b = 2.8723$, $c = 3/2$ and period $L = 21.1801$. Point 1 corresponds to the exact real solution with $a = -1.35$. (b) Sample profiles along the dashed and red (gray) branches. (c) Sample profiles along the dotted branch.

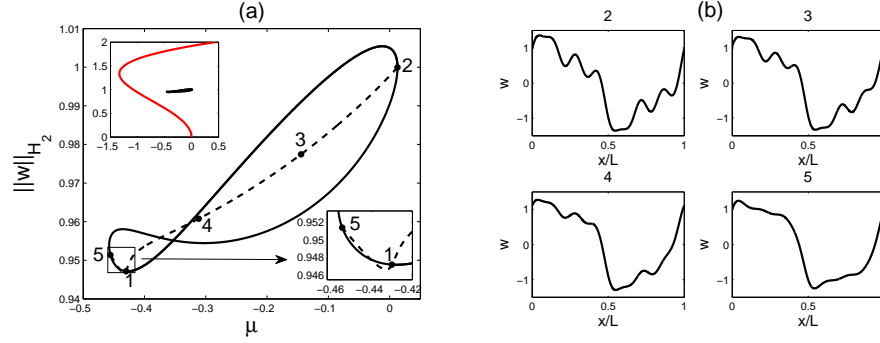


Figure 4.10: (a) Bifurcation diagrams for stationary periodic solutions with $b = 2.9861$, $c = 3/2$ and period $L = 27.9881$. Point 1 corresponds to the exact real solution with $a = -1.43 > -36/25$ and lies on an isola. The inset at top left indicates the relative position between the primary branch of 2π periodic states and the isola of periodic states with $L = 27.9881$. (b) Sample profiles along the secondary branch connecting points 2 and 5 (dashed line, panel (a)).

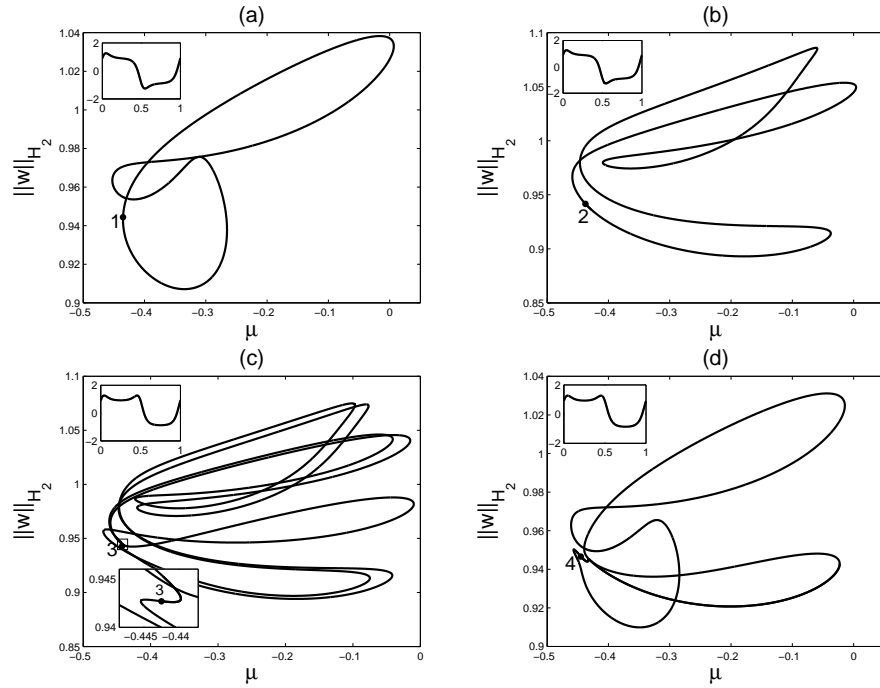


Figure 4.11: Bifurcation diagrams for stationary periodic solutions $c = 3/2$ and (a) $b = 2.9930$, $L = 30.1667$, (b) $b = 2.9965$, $L = 32.3511$, (c) 3.0035 , $L = 32.3321$, and (d) $b = 3.0069$, $L = 30.1327$. The points labeled 1, 2, 3, 4 correspond to the exact real solutions (shown in the insets with x/L as the horizontal coordinate) at (a) $a = -1.435$, (b) $a = -1.4375$, (c) $a = -1.4425$, and (d) $a = -1.445$, respectively; all lie on isolas. Secondary crosslinks consisting of asymmetric solutions are omitted.

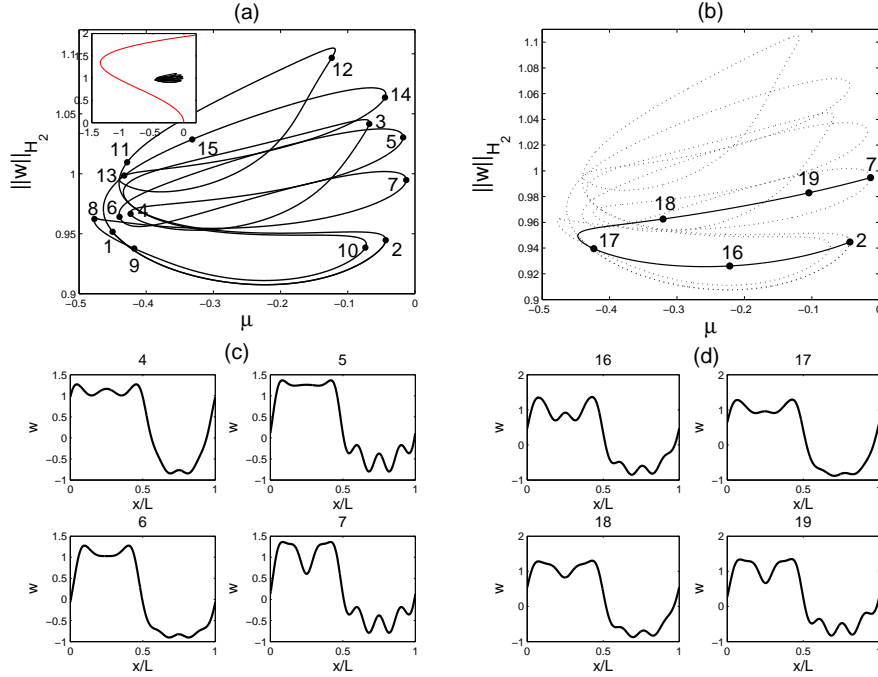


Figure 4.12: (a) Bifurcation diagrams for stationary periodic solutions with $b = 3.0139$, $c = 3/2$ and period $L = 27.9276$. Point 1 corresponds to the real exact solution with $a = -1.45 < -36/25$. The inset at top left indicates the relative position between the primary branch of 2π periodic states and the isola of periodic states with $L = 27.9276$. (b) Bifurcation diagram for the stationary asymmetric states connecting points 2 and 7. (c) Sample profiles along the isola (solid line, panel (a)). (d) Sample profiles along the asymmetric branch connecting points 2 and 7 (solid line, panel (b)).

respect to R_1 instead of TR_2 and the solutions obtained from these solutions by numerical continuation share this symmetry. Figure 4.12(a) shows details of the bifurcation diagram obtained from such an exact solution at $a = -1.45$ for comparison with figure 4.11(c). Here, too, the exact solution lies on an isola consisting of seven leaves but this time we have seven crosslinks consisting of asymmetric states. These crosslinks connect the pairs of points (2, 7), (3, 6), (4, 5), (8, 11), (9, 10), (12, 15) and (13, 14); the (2, 7) crosslink is highlighted in figure 4.12(b). The corresponding solutions are shown in figures 4.12(c,d).

A similar but rather more complex example obtains for $a = -2$ as shown in figure 4.13. Figure 4.13(a) shows a branch of R_1 -symmetric states obtained by continuation from the exact solution at point 1. The entire branch connects point 2 to point 3 and consists of R_1 -symmetric solutions about $x = L/4, 3L/4$. At both end points the solutions acquire an additional TR_2 symmetry, and both points lie on the branch of $R_1 \times TR_2$ -symmetric states shown in red (gray) in figure 4.13(b). Thus the bifurcation at point 2 is a symmetry-breaking bifurcation on the red (gray) branch that breaks the TR_2 symmetry; figure 4.13(b) reveals

that this point lies very close to a fold of this branch. The bifurcation at point 8 is also a symmetry-breaking bifurcation that lies close to a fold but this time it breaks R_1 symmetry. The branch of TR_2 -symmetric states that results (dashed line in figure 4.13(b)) connects to the vicinity of a fold on the primary branch of $R_1 \times TR_2$ symmetric states (thin black line in figure 4.13(b)) that bifurcates from $u = 0$ at $\mu = 0.6739$. With $L = 14.8473$ (the period of the exact solution at point 1) this branch is the first primary branch and the branches shown in figure 4.13(a,b) are therefore associated with the first nonzero states with this period as μ increases. It is unclear why the various symmetry-breaking bifurcations occur so close to folds.

As already mentioned point 3 does not lie on the black branch in figure 4.13(a) or close to a fold but lies on the red (gray) branch in figure 4.13(b) and represents a pitchfork bifurcation of the $R_1 \times TR_2$ -symmetric states on this branch. This bifurcation creates a pair of branches of solutions with R_1 symmetry. However, because of the remaining TR_2 symmetry the two branches coincide in the bifurcation diagram. Figure 4.14 represents a blowup of the region near this bifurcation.

Figure 4.13(d) shows sample solutions along the red (gray) branch at larger values of μ . The figure reveals that as μ increases both ends of the branch evolve into front-like states. The solution with the smaller H_2 norm (lower panels) takes the form of a front connecting a pair of symmetry-related spatially uniform states while the solution with the larger H_2 norm (upper panels) takes the form of a “nonmonotonic” front [81] connecting the same states. These states resemble the heteroclinic orbits computed in Ref. [81] for a system with the same symmetry properties, the forced Ginzburg-Landau equation with 2:1 resonance, although here they are of course computed on a finite domain. The possibility exists therefore that such heteroclinic orbits are indeed present when Eq. (4.1) with $a = -2$, $b = 3.6968$, $c = 3/2$ is posed on the real line, suggesting that continuation in L could also be worthwhile. We have not carried out a systematic study of crosslinks consisting of asymmetric states such as that shown in figure 4.13(a), dashed line.

When the value of a is decreased to $a = -4.5$, the branch of R_1 -symmetric states obtained by continuation from the exact solution is still a secondary branch of the first primary branch albeit somewhat less convoluted (figure 4.15, dashed line). As shown in the inset in figure 4.15(a) this secondary branch connects to the primary branch (solid line) already at small amplitude and does so in a supercritical bifurcation. It follows that the dashed branch is initially once unstable and hence can easily acquire stability at secondary bifurcations. Stability calculation with periodic boundary conditions shows that the solutions on this branch are indeed stable between the first and second folds and again between the third and fourth folds.

A further destabilization of the primary periodic branch occurs via the red (gray) branch (figure 4.15(a), inset). This branch is initially twice unstable but becomes only once unstable after a tertiary bifurcation (point 6 in figure 4.15(a)) prior to the first fold. As a result solutions on this branch also acquire stability at the first fold and these remain stable until the second fold. Sample solutions are shown in figure 4.15(b,c).

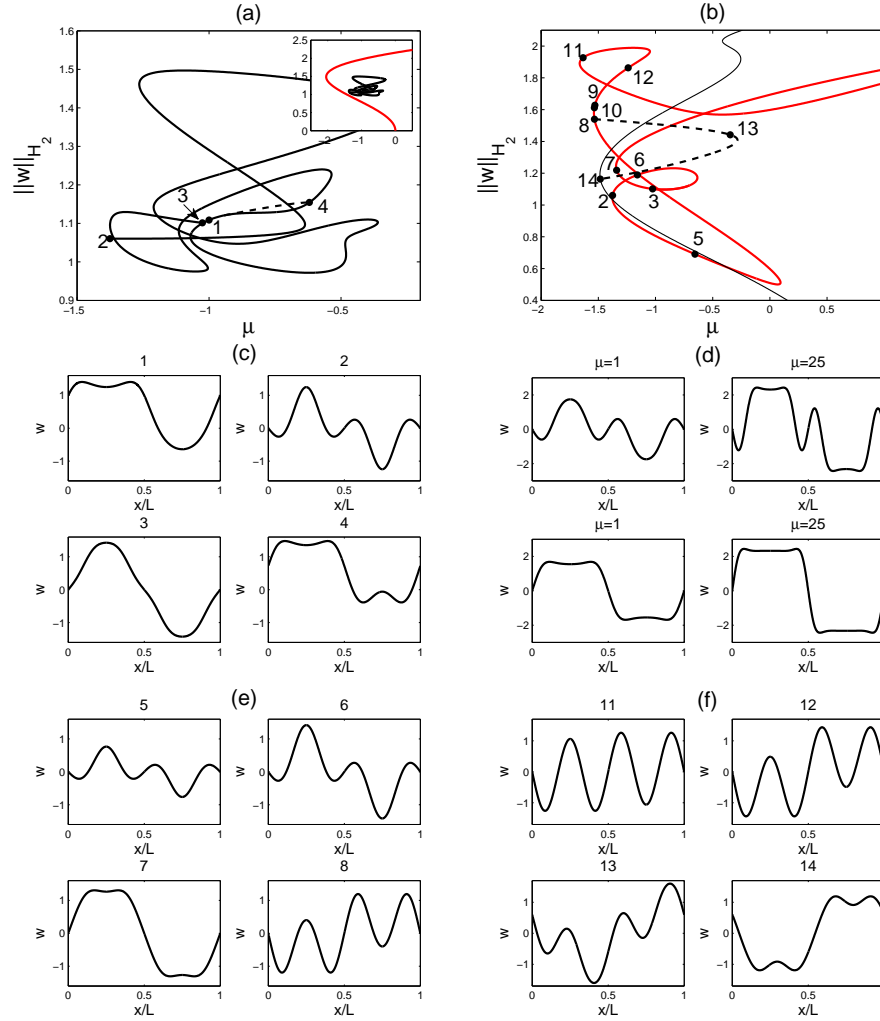


Figure 4.13: (a) Bifurcation diagram for stationary R_1 -symmetric solutions (solid line) with $b = 3.6968$, $c = 3/2$ and period $L = 14.8473$. Point 1 corresponds to the exact solution with $a = -2$. The inset indicates the relative position between the branch of 2π periodic states and the branch originating from the exact solution with the period held at $L = 14.8473$. The dashed line shows one of the crosslinks consisting of asymmetric solutions. (b) The branch of $R_1 \times TR_2$ -symmetric front-like states that bifurcate from the branch in panel (a) at points labeled 2 and 3 together with a second branch of $R_1 \times TR_2$ -symmetric states that bifurcates from $u = 0$ at $\mu = 0.6739$. The two branches are connected at points 8 and 14, respectively, by a branch of asymmetric states (dashed line). (c) Sample profiles at the points indicated in panel (a). (d) Sample profiles at $\mu = 1$ and $\mu = 25$ along the red (gray) branch in panel (b) (top row: upper branch; bottom row: lower branch). (e,f) Sample profiles at the points indicated in panel (b); points (2, 3), (5, 6), (9, 11), (10, 12) are connected by crosslinks (not shown). The fold labeled 7 indicates the transition to front-like states at larger μ .

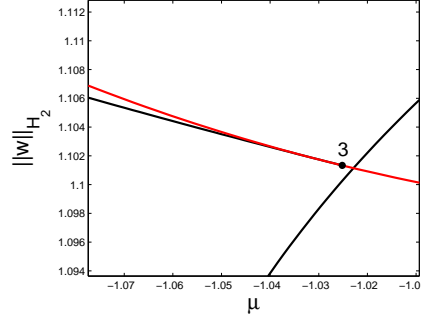


Figure 4.14: A blowup of the bifurcation diagram near point 3 showing the termination of the branch of R_1 -symmetric states in figure 4.13(a) on the branch of $R_1 \times TR_2$ -symmetric states shown in red (gray) in figure 4.13(b). The close passage of a part of the R_1 -symmetric branch near point 3 is a projection effect.

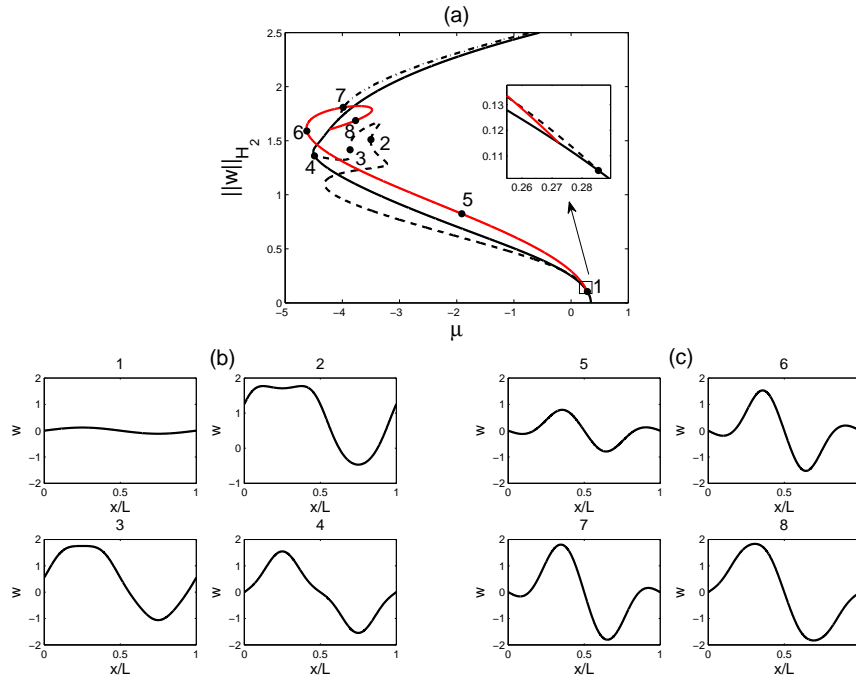


Figure 4.15: (a) Bifurcation diagrams for stationary periodic solutions with $b = 5.8737$, $c = 3/2$ and period $L = 9.7914$. Point 2 corresponds to the exact solution with $a = -4.5$. Point 6 on the red (gray) branch is a tertiary bifurcation point. The dashed line shows one of the R_1 -symmetric branches connecting the original periodic branch to itself, with the inset showing details of its appearance at small amplitude. (b) Sample profiles along the dashed branch. (c) Sample profiles along the red (gray) branch.

4.5 Discussion

In this chapter we have explored in detail of obtaining exact meromorphic solutions of SH35 and show that no other solutions of the same class can be found. Based on results of exact meromorphic solutions, two one-parameter families of exact real solutions were identified. These consist of elliptic solutions with different symmetries and are separated, at $a = -36/25$, by an exact real solution in the form of a front, i.e., a heteroclinic solution. The solutions for $a < -36/25$ (parameter interval I_1) are R_1 -symmetric, while those for $-36/25 < a < -9/25$ (parameter interval I_2) are TR_2 -symmetric. Explicit expressions for these exact solutions are given in section 4.3. Numerical continuation with periodic boundary conditions shows that when $a \equiv \mu - 1$ is close to $-9/25$ the amplitude of the exact solution is small and the branches identified using continuation lie on primary branches of periodic solutions, generally above a fold. In contrast, when a is close to $-36/25$ the solution branches obtained from the exact solutions can exhibit a variety of complex bifurcation behavior. In particular, the exact solution may lie on a secondary branch or an isola depending on the value of a . The discovery of these isolas is a nontrivial consequence of the exact solutions we have identified. We conjecture that the appearance of these isolas is associated with the passage of the parameter a through the critical value $a = -36/25$. Indeed, we believe that the plethora of periodic solutions present near this parameter value is directly associated with the presence of the heteroclinic orbit at $a = -36/25$, cf. [82].

Of the great variety of solutions we have identified stable solutions were typically found only for larger negative values of a for which the exact solutions are associated with secondary branches bifurcating from the first primary branch of periodic states that bifurcates from $u = 0$ as a increases.

The technique used in this chapter and in earlier work [75, 76, 78, 77] could be useful for studies of other one-dimensional partial differential equations arising in simple models of physical systems since in these cases waves of constant form (periodic, homoclinic or heteroclinic) are usually described by nonlinear ODEs of algebraic type. As an example we obtained in Appendix J analogous results for the SH23 with dispersion, thereby extending the results given in [78]. The technique provides a different approach to finding exact solutions, one that is independent of additional structure such as a Hamiltonian structure or spatial reversibility that are required of other approaches, and hence has a potentially far greater range of applicability. In addition, since the method is not perturbative, the solutions found are fully nonlinear. On the other hand not all physically interesting solutions have meromorphic extensions to the entire complex plane, and such solutions cannot be identified using the present approach.

Chapter 5

Conclusions

5.1 Summary of results

This thesis focuses on the formation of spatially modulated structures in convective systems, especially in the codimension-two bifurcation region. The modulation equation and spatial dynamics approaches substantially enhance our understanding of these degenerate bifurcation points. The presented theories are of higher order and take the form of fifth order local or nonlocal Ginzburg-Landau equations. The study of these fifth order equations is of great value since they are generic when the underlying system is translation invariant and reflection symmetric in horizontal direction. The genericity implies they have wide applications not only in convective systems but also in other pattern forming systems that share the same bifurcation properties.

Chapter 2 is the study of the canonical amplitude equation (1.6) that describes the bifurcation of stationary weakly subcritical and supercritical patterns. With control parameters μ and b , the system is characterized by the coefficients of the nonlinear gradient terms a_1 and a_2 . These two coefficients allow us to predict and classify the properties of weakly subcritical or supercritical pattern forming systems. Several codimension-one curves in the (a_1, a_2) plane are discovered and each corresponds to different bifurcation behaviors. These two coefficients also have significant influence on the dynamics, especially the presence of gradient structure ($a_2 = 0$). Nonvariational dynamics are present when $a_2 \neq 0$ and are elucidated in the numerical results. Among the stationary solutions, the front solution which connects zero state to a spatially periodic state plays the most important role. The location of the front in parameter μ is treated as a Maxwell point. The spatially modulated solutions which bifurcate from the periodic solutions demonstrate protosnaking behavior near this point. These results allow us to locate the parameter region of localized states and also shed light on their behavior in general pattern forming systems.

Chapter 3 is the study of two-dimensional convective systems with a large scale mode (rotating convection and magnetoconvection) in which the localized states form a slanted snaking structure in the bifurcation diagram. To study the formation of such localized states,

I examined the behavior near the codimension-two point $(r, \xi^2) = (0, 1/3)$ (described in section 3.2) described by a fifth order Ginzburg-Landau equation with nonlocal terms. With periodic boundary conditions, two possible bifurcation pictures are discovered. When $\tilde{c} > 0$ (cf. section 3.53), the primary branch at the band center allows only a finite number of secondary branches and the number of secondary branches increases as the Taylor number Ta (or Chandrasekhar number Q) increases. Regarding stability, among the modulated solutions, only the ones lying on the secondary branch closest to the onset of primary bifurcation are stable while the others are all unstable. The primary branch itself is stable before the first and after the last secondary branching points. There are also regions of bistability between modulated and periodic states. When $\tilde{c} < 0$ the primary branch at the band center allows an infinite number of secondary branches but all the secondary branches are unstable. The effects of boundary conditions on the large scale mode and slanted snaking are examined at the end of the chapter. With mixed boundary conditions (3.72), the large scale mode becomes linearly damped and we observe a transition from slanted to regular homoclinic snaking.

Chapter 4 is the study of stationary SH35 (4.9), a fourth order nonlinear ODE. This chapter is different from the previous two chapters in several aspects. The motivation is to explore the solution space of stationary SH35 by deriving nontrivial exact solutions of the equation. Instead of relying only on the standard bifurcation theory approach, I applied techniques from complex analysis to the nonlinear ODE and discovered all the possible classes of meromorphic solution and found exact expressions for them. Based on these results, a one parameter family of real exact solutions was obtained. These solutions are of two types, differing in their symmetry properties, and are connected via an exact heteroclinic solution. The real exact solutions are then used as initial conditions for a numerical bifurcation analysis. Most of the exact solutions lie on modulated branches that bifurcate from $k \neq 1$ periodic states. But as the parameter b approaches the value corresponding to the exact heteroclinic solution, a plethora of isolas is observed.

5.2 Ongoing work

There are several ongoing projects which I am currently studying. One of these is the study of SH23 with a dispersive term which breaks spatial reversibility

$$u_t = \mu u + \gamma u_{xxx} - (1 + \partial_{xx})^2 u + bu^2 - u^3. \quad (5.1)$$

This equation has been studied before in [83] which is mainly a numerical investigation of localized states. The effect of breaking spatial reversibility occurs in convective systems when the direction of gravity is not exactly aligned with the direction of applied temperature difference. Here the dispersive term u_{xxx} leads to drifting patterns and no stationary localized or periodic solution exists when $\gamma \neq 0$. The system is no longer variational due to the presence of u_{xxx} and there could be interesting dynamics associated with this. I analyze the dependence of the drift speed of the traveling solutions on γ and use these results to

demonstrate the nonexistence of traveling periodic solutions in certain parameter regions. More precisely, there is no periodic solution with period Γ less than $\sqrt{2}\pi$ when $\mu < 1 - b^2/4$ and $2\pi/\sqrt{1 + \sqrt{\mu + b^2/4}}$ when $\mu > 1 - b^2/4$. This condition holds as the speed c and γ tend to zero. In addition, I also show the localized and periodic solutions exist only when $\mu > -\frac{b^2}{4}$. This result yields a better bound compared with the one given in [69].

The modulation equation approach is also applied in Eq. (5.1). The periodic wavetrain moves at velocity γ while the amplitude modulation moves at group velocity 3γ . The small amplitude solutions thus take the asymptotic form

$$u(x, t) \sim \{A(\eta, t_2)e^{i(x-\gamma t)} + c.c.\} + h.o.t., \quad (5.2)$$

where $\eta \equiv \epsilon(x - 3\gamma t)$ and $t_2 \equiv \epsilon^2 t$. When the parameter b is chosen away from the transition region between subcritical and supercritical bifurcation, the amplitude function A satisfies

$$\begin{aligned} A_{t_2} = & [\mu_2 + (4 + 3i\epsilon\gamma_1)\partial_\eta^2 - 4i\epsilon\partial_\eta^3] A \\ & + \left(\frac{38}{9}b^2 - 3 - \frac{4i\epsilon b^2\gamma_1}{27}\right) |A|^2 A + \frac{32i\epsilon b^2}{27} |A|^2 A_\eta + O(\epsilon^2), \end{aligned} \quad (5.3)$$

where $\mu_2 \equiv \epsilon^{-2}\mu$ and $\gamma_1 \equiv \epsilon^{-1}\gamma$. The steady solution of this equation can be compared with the perturbed 1:1 resonance normal form with broken reversibility.

When b is close to the transition region, i.e., $b^2 = 27/38 + \epsilon^2 b_2$, a different scaling needs to be considered and the small amplitude solutions now take the form

$$u(x, t) \sim \{A(\eta, t_4)e^{i(x-\gamma t)} + c.c.\} + h.o.t., \quad (5.4)$$

where $\eta \equiv \epsilon^2(x - 3\gamma t)$ and $t_4 \equiv \epsilon^4 t$. Here the amplitude function A is governed by

$$A_{t_4} = (\mu_4 + 4\partial_\eta^2) A + \frac{16i}{19} |A|^2 A_\eta + \left(\frac{38}{9}b_2 - \frac{2i\gamma_2}{19}\right) |A|^2 A - \frac{8820}{361} |A|^4 A, \quad (5.5)$$

where $\mu_4 \equiv \epsilon^{-4}\mu$ and $\gamma_2 \equiv \epsilon^{-2}\gamma$. Through the study of these amplitude equations, we can obtain useful information about the bifurcation behavior and explore new dynamics which are not present in the case $\gamma = 0$. The results have useful implications for convective systems with broken reflection symmetry.

Another topic is the investigation of the generalized Swift-Hohenberg equation under non-homogeneous forcing. In the practical setup of convection experiments, it is extremely difficult to achieve the condition of homogeneous forcing due to various practical and physical limitations. It will be useful to see how spatially dependent forcing alters the behavior of convection, and especially of localized structures. I consider SH35 with two different types of spatially dependent forcing:

$$\mu(x) = r(1 + \alpha \cos x), \quad (5.6)$$

$$\mu(x) = r \left[1 + \alpha \exp\left(-\frac{x^2}{2\sigma^2}\right) \right]. \quad (5.7)$$

The first forcing corresponds to a periodic forcing with mean r and relative oscillation amplitude α . The cosine profile in the forcing allows a resonance with the intrinsic wavelength. The second forcing models a homogeneous forcing locally perturbed by a Gaussian bump with width σ .

When $\alpha = 0$, there are two types of localized solutions, each satisfying either even or odd parity. Figures 5.1 and 5.2 show the bifurcation results with periodic forcing with $\alpha = \pm 0.1$, ± 0.4 , and ± 0.7 . For even states, the snaking structure persists and increasing $|\alpha|$ leads

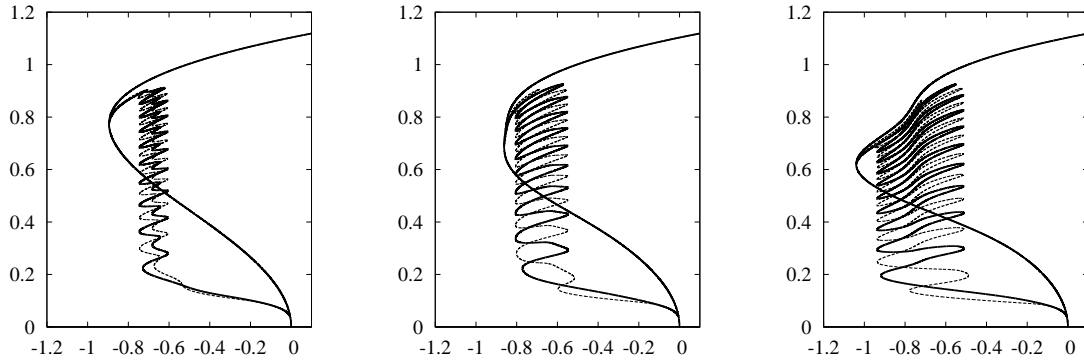


Figure 5.1: Bifurcation diagrams showing the L^2 -norm (vertical) of u as a function of r (horizontal) for even parity branches with $\alpha = \pm 0.1$, ± 0.4 , and ± 0.7 (from left to right) in SH35 with periodic forcing. Localized branches represented in a solid line have $\alpha > 0$ while those in a dashed line have $\alpha < 0$.

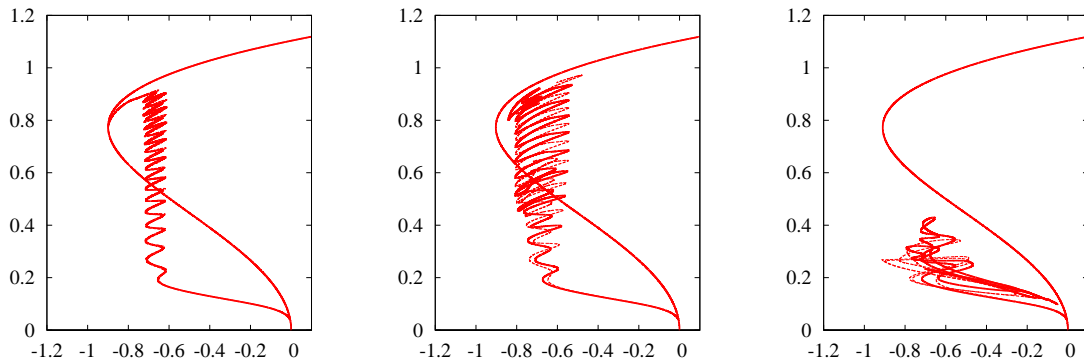


Figure 5.2: Bifurcation diagrams showing the L^2 -norm (vertical) of u as a function of r (horizontal) for odd parity branches with $\alpha = \pm 0.1$, ± 0.4 , and ± 0.7 (from left to right) in SH35 with periodic forcing. Localized branches represented in a solid line have $\alpha > 0$ while those in a dashed line have $\alpha < 0$.

to a broadening of the snaking region. When $|\alpha|$ is small, instead of lying on two specific values of r , the saddle-nodes appear at sequential locations $r_1 \rightarrow r_4 \rightarrow r_2 \rightarrow r_3 \rightarrow r_1 \dots$ for positive α , or $r_2 \rightarrow r_3 \rightarrow r_1 \rightarrow r_4 \rightarrow r_2 \dots$ for negative α . These values have relative order $r_i < r_j$ if $i < j$. As $|\alpha|$ increases further, the branches connecting the saddle-nodes between r_2 and r_3 annihilate and the number of oscillations in r decreases by half.

In bump forcing, the localized branches bifurcate directly from the trivial state as shown in figure 5.3. These localized branches do not reconnect back to any other branch after snaking but rather continue their way to larger amplitude states with a defect at the location of the bump. Figure 5.3 shows the bifurcation diagram of even states with bump forcing when $\alpha = \pm 0.1$ and ± 0.7 . The bifurcation diagram of odd states is qualitatively similar to the bifurcation diagram of even states. The behavior of the solutions depends significantly

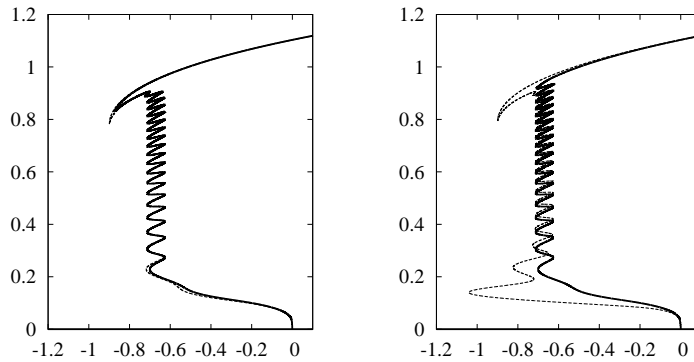


Figure 5.3: Bifurcation diagrams showing the L^2 -norm (vertical) of u as a function of r (horizontal) for the even parity branches for $\alpha = \pm 0.1$ and ± 0.7 (from left to right) in SH35 with bump forcing. Localized branches represented in a solid line have $\alpha > 0$ while those in a dashed line have $\alpha < 0$.

on the sign of α . When α is negative (forcing is larger at the center) we have localized states located at the center but when α is positive (forcing is smaller at the center) the localized states are located at the edge instead.

Future study will focus on the stability of these solutions and the associated dynamics when r is perturbed slightly from the snaking region. I expect the spatial dependence of the forcing selects the localized states and also their spatial locations. If there is a mismatch in location, the localized state will drift and shift to the location with lower free energy. This mechanism allows us to manipulate the localized states to desired length and location dynamically by altering the forcing, which could have interesting applications.

5.3 Future work

The generalized Swift-Hohenberg equation appears to be a good model equation for convection problems, at least it captures the essential mechanism which governs the bifurcation properties observed in the fluid systems. But little is known about the relation between the model equation and the underlying physics. For modulation equations, which are only valid under certain conditions (small amplitude, large domain,...), the derivation can be rigorously justified and the coefficients are physically meaningful. This is not the case for the generalized Swift-Hohenberg equation. For example, how do we pick the nonlinear coefficients in order to match a certain convection problem with given physical parameters? This cannot be answered by the work done in previous literature.

A missing link that should be established is to rigorously derive a lower dimensional equation that effectively captures the bifurcation behavior of convection problems, possibly under certain approximation. This has only been done in the case of classical Rayleigh-Bénard convection [84] but not for other convection problems. The effective equation may not take the same form as the generalized Swift-Hohenberg equation but they should match at least at the linear level. Such a study is definitely important since otherwise the study of the generalized Swift-Hohenberg equation is more of mathematical interest than of physical interest.

A topic I would like to study in the near future is to revisit the problem of inclined layer convection in a more theoretical fashion, especially to establish the connection between the full Navier-Stokes system and the Swift-Hohenberg equation. According to author's knowledge, besides the results from experiments [85], direct numerical simulations [86, 87], and linear stability analysis [88], there has not been any nonlinear analysis performed on such a system. It is surprising that such an important problem has not been well-studied.

Another aspect is the study of two-dimensional Swift-Hohenberg equation. According to [84], in order to describe the three-dimensional convection the Swift-Hohenberg equation should be effectively two-dimensional and the nonlinear terms are nonlocal. This renders the two-dimensional Swift-Hohenberg equation an integro-differential PDE. This fact seems to be overlooked by contemporary researchers. I am interested to study this type of equations and compare them with the local version.

The last aspect I would like to mention is how do physical limitations affect the patterns that can be observed. In a real set-up, there are no idealized boundary conditions such as stress-free boundary conditions and an important question is how to suitably incorporate the experimental boundary conditions. In principle, the properties of the boundaries can be calculated from first principles using techniques like molecular dynamics simulation. But in the theoretical aspect, it will be more useful to derive the effective theory for the boundary conditions from microscopic physics that match with the experimental results and are, at the same time, applicable to the macroscopic formulation. Besides the boundary conditions, the applied temperature difference would be practically impossible to be a constant in both space and time. Due to thermal fluctuation or other physical limitations, the forcing itself will be either stochastic or deterministic but with spatial-temporal dependence. These could

have significant effects of pattern selection as indicated in our modeling result of the Swift-Hohenberg equation (section 5.2) and the study of rotating convection (section 3.6).

The investigation of these topics will lead to better understanding of pattern formation in fluid systems.

Bibliography

- [1] H. BÉNARD, *Les tourbillons cellulaires dans une nappe liquide*, Rev. Gén. Sciences Pure Appl. 11 (1900) 1261–1271.
- [2] B. P. BELOUSOV, *Periodically acting reaction and its mechanism*, Collection of Abstracts on Radiation Medicine 147 (1959) 145–147.
- [3] A. M. TURING, *The chemical basis of morphogenesis*, Phil. Trans. R. Soc. Lond. B 237 (1952) 37–72.
- [4] F. T. ARECCHI, S. BOCCALETTI, AND P. RAMAZZA, *Pattern formation and competition in nonlinear optics*, Phys. Rep. 318 (1999) 1–83.
- [5] F. M. RICHTER, *Experiments on the stability of convection rolls in fluids whose viscosity depends on temperature*, J. Fluid Mech. 89 (1978) 553–560.
- [6] S. CHANDRASEKHAR, *Hydrodynamic and hydromagnetic stability*, Oxford University Press, London (1961).
- [7] J. SWIFT AND P.C. HOHENBERG, *Hydrodynamic fluctuations at the convective instability*, Phys. Rev. A 15 (1977) 319–328.
- [8] L. Y. GLEBSKY AND L. M. LERMAN, *On small stationary localized solutions for the generalized 1D SwiftHohenberg equation*, Chaos 5 (1995) 424–431.
- [9] O. BATISTE, E. KNOBLOCH, A. ALONSO, AND I. MERCADER, *Spatially localized binary-fluid convection*, J. Fluid Mech. 560 (2006) 149–156.
- [10] P. ASSEMAT, A. BERGEON, AND E. KNOBLOCH, *Spatially localized states in Marangoni convection in binary mixtures*, Fluid Dyn. Res. 40 (2008) 852–876.
- [11] A. BERGEON AND E. KNOBLOCH, *Spatially localized states in natural doubly diffusive convection*, Phys. Fluids 20 (2008) 034102.
- [12] C. BEAUME, A. BERGEON, AND E. KNOBLOCH, *Homoclinic snaking of localized states in doubly diffusive convection*, Phys. Fluids 23 (2011) 094102.

- [13] J. BURKE AND E. KNOBLOCH, *Localized states in the generalized Swift-Hohenberg equation*, Phys. Rev. E 73 (2006) 056211.
- [14] Y. POMEAU, *Front motion, metastability and subcritical bifurcations in hydrodynamics*, Physica D 23 (1986) 3–11.
- [15] S. J. CHAPMAN AND G. KOZYREFF, *Exponential asymptotics of localised patterns and snaking bifurcation diagrams*, Physica D 238 (2009) 319–354.
- [16] D. LO JACONO, A. BERGEON, AND E. KNOBLOCH, *Magnetohydrodynamic convections*, J. Fluid Mech. 687 (2011) 595–605.
- [17] C. BEAUME, A. BERGEON, H.-C. KAO, AND E. KNOBLOCH, *Convectons in a rotating fluid layer*, J. Fluid Mech. 717 (2013) 417–448.
- [18] S. M. COX AND P. C. MATTHEWS, *New instabilities in two-dimensional rotating convection and magnetoconvection*, Physica D 149 (2001) 210–229.
- [19] P. C. MATTHEWS AND S. M. COX, *Pattern formation with a conservation law*, Nonlinearity 13 (2000) 1293–1320.
- [20] H.-C. KAO AND E. KNOBLOCH, *Weakly subcritical stationary patterns: Eckhaus stability and homoclinic snaking*, Phys. Rev. E 85 (2012) 026207.
- [21] H.-C. KAO AND E. KNOBLOCH, *Instabilities and dynamics of weakly subcritical patterns*, accepted for the special issue "Bifurcation" of Mathematical Modeling of Natural Phenomena.
- [22] R. HOYLE, *Pattern formation*, Cambridge University Press, Cambridge (2006).
- [23] L. KRAMER AND W. ZIMMERMANN, *On the Eckhaus instability for spatially periodic patterns*, Physica D 16 (1985) 221–232.
- [24] L. S. TUCKERMAN AND D. BARKLEY, *Bifurcation analysis of the Eckhaus instability*, Physica D 46 (1990) 57–86.
- [25] L. S. TUCKERMAN, *The Eckhaus Instability*, <http://www.pmmh.espci.fr/~laurette/highlights/eckhaus.pdf>.
- [26] W. ECKHAUS AND G. IOOSS, *Strong selection or rejection of spatially periodic patterns in degenerate bifurcations*, Physica D 39 (1989) 124–146.
- [27] A. DOELMAN AND W. ECKHAUS, *Periodic and quasi-periodic solutions of degenerate modulation equations*, Physica D 53 (1991) 249–266.
- [28] J. DUAN AND P. HOLMES, *Fronts, domain walls and pulses in a generalized Ginzburg-Landau equation*, Proc. Edinburgh Math. Soc. 38 (1995) 77–97.

- [29] A. SHEPELEVA, *Modulated modulations approach to the loss of stability of periodic solutions for the degenerate Ginzburg-Landau equation*, Nonlinearity 11 (1998) 409–429.
- [30] A. SHEPELEVA, *On the validity of the degenerate Ginzburg-Landau equation*, Math. Method Appl. Sci. 20 (1997) 1239–1256.
- [31] H. BRAND AND R. DEISSLER, *Eckhaus and Benjamin-Feir instabilities near a weakly inverted bifurcation*, Phys. Rev. A 45 (1992) 3732–3736.
- [32] W. VAN SAARLOOS, *Front propagation into unstable states. II. Linear versus nonlinear marginal stability and rate of convergence*, Phys. Rev. A 39 (1989) 6367–6390.
- [33] J. BURKE AND J. H. P. DAWES, *Localised states in an extended Swift-Hohenberg equation*, SIAM J. Appl. Dyn. Syst. 11 (2012) 261–284.
- [34] J. DUAN, P. HOLMES, AND E. S. TITI, *Global existence theory for a generalized Ginzburg-Landau equation*, Nonlinearity 5 (1992) 1303–1314.
- [35] E. KNOBLOCH AND D. MOORE, *Chaotic travelling wave convection*, Eur. J. Mech. B/Fluids 10 (1991) 37–42.
- [36] E. J. DOEDEL, A. R. CHAMPNEYS, T. FAIRGRIEVE, Y. KUZNETSOV, B. OLDEMAN, R. PAFFENROTH, B. SANDSTED, X. WANG, AND C. ZHANG, *AUTO-07p: Continuation and Bifurcation Software for Ordinary Differential Equations*, available for download from <http://indy.cs.concordia.ca/auto/> (2007).
- [37] J. H. P. DAWES, *Modulated and localized states in a finite domain*, SIAM J. Appl. Dyn. Syst. 8 (2009) 909–930.
- [38] A. BERGEON, J. BURKE, E. KNOBLOCH AND I. MERCADER, *Eckhaus instability and homoclinic snaking*, Phys. Rev. E 78 (2008) 046201.
- [39] J. D. CRAWFORD AND E. KNOBLOCH, *On degenerate Hopf bifurcation with broken $O(2)$ symmetry*, Nonlinearity 1 (1988) 617–652.
- [40] S. M. COX, P. C. MATTHEWS, *Exponential time differencing for stiff systems*, J. Comp. Physics 176 (2002) 430–455.
- [41] L. J. BOYA, *Supersymmetric quantum mechanics: two simple examples*, Eur. J. Phys. 9 (1988) 139–144.
- [42] C. M. ELLIOTT AND S. ZHENG, *On the Cahn-Hilliard equation*, Arch. Rational Mech. Anal. 96 (1986) 339–357.
- [43] E. KNOBLOCH AND J. DELUCA, *Amplitude equations for travelling wave convection*, Nonlinearity 3 (1990) 975–980.

- [44] E. KNOBLOCH, *Oscillatory convection in binary mixtures*, Phys. Rev. A 34 (1986) 1538–1549.
- [45] D. HENRY, *Geometric theory of semilinear parabolic equations*, Springer-Verlag, Berlin (1981).
- [46] E. BEN-JACOB, H. BRAND, G. DEE, L. KRAMER, AND J. S. LANGER, *Pattern propagation in nonlinear dissipative systems*, Physica D 14 (1985) 348–364.
- [47] H.-C. KAO AND E. KNOBLOCH, *Spatial localization in rotating convection and magnetoconvection*, in preparation.
- [48] J. H. P. DAWES, *Localized pattern formation with a large scale mode: slanted snaking*, SIAM J. Appl. Dyn. Syst. 7 (2008) 186–206.
- [49] M. R. E. PROCTOR, *Finite amplitude behaviour of the Matthews-Cox instability*, Phys. Lett. A 292 (2001) 181–187.
- [50] S. M. COX, *The envelope of a one-dimensional pattern in the presence of a conserved quantity*, Phys. Lett. A 333 (2004) 91–101.
- [51] H. F. GOLDSTEIN, E. KNOBLOCH AND M. SILBER, *Planform selection in rotating convection*, Phys. Fluids A 2 (1990) 625–627.
- [52] T. CLUNE AND E. KNOBLOCH, *Pattern selection in rotating convection with experimental boundary conditions*, Phys. Rev. E 47 (1993) 2536–2550.
- [53] J. H. P. DAWES AND S. LILLEY, *Localized states in a model of pattern formation in a vertically vibrated layer*, SIAM J. Appl. Dyn. Syst. 9 (2010) 238–260.
- [54] G. VERONIS, *Cellular convection with finite amplitude in a rotating fluid*, J. Fluid Mech. 5 (1959) 401–435.
- [55] P. HALL, *Evolution equations for Taylor vortices in the small-gap limit*, Phys. Rev. A 29 (1984) 2921–2923.
- [56] F. J. ELMER, *Nonlinear and nonlocal dynamics of spatially extended systems: Stationary states, bifurcations and stability*, Physica D 30 (1988) 321–342.
- [57] J. NORBURY, J. WEI, AND M. WINTER, *Existence and stability of singular patterns in a Ginzburg-Landau equation coupled with a mean field*, Nonlinearity 15 (2002) 2077–2096.
- [58] J. M. VEGA, *Instability of the steady states of some Ginzburg-Landau-like equations with real coefficients*, Nonlinearity 18 (2005) 1425–1441.

- [59] J. NORBURY, J. WEI, AND M. WINTER, *Stability of patterns with arbitrary period for a Ginzburg-Landau equation with a mean field*, Euro. J. Appl. Math. 18 (2007) 129–151.
- [60] C. BEAUME, private communication.
- [61] J. MARSHALL AND F. SCHOTT, *Open-ocean convection: observations, theory, and models*, Rev. Geophys. 37 (1999) 1–64.
- [62] P. S. MARCUS AND T. KUNDU AND C. LEE, *Vortex dynamics and zonal flows*, Phys. Plasmas 7 (2000) 1630–1640.
- [63] M. EVONUK AND G. A. GLATZMAIER, *The effects of rotation rate on deep convection in giant planets with small solid cores*, Planetary and Space Sci. 55 (2007) 407–412.
- [64] M. R. PETERSEN AND K. JULIEN AND G. R. STEWART, *Baroclinic vorticity production in protoplanetary disks. I. Vortex formation*, Astrophys. J. 658 (2007) 1236–1251.
- [65] J. LEGA, J. V. MOLONEY, AND A. C. NEWELL, *Swift-Hohenberg equation for lasers*, Phys. Rev. Lett. 73 (1994) 2978–2981.
- [66] S. LONGHI AND A. GERACI, *Swift-Hohenberg equation for optical parametric oscillators*, Phys. Rev. A 54 (1996) 4581–4584.
- [67] Y. POMEAU AND P. MANNEVILLE, *Wavelength selection in cellular flows*, Phys. Lett. A 75 (1980) 296–298.
- [68] G. J. B. VAN DEN BERG, *Dynamics and equilibria of fourth order differential equations*, Ph.D. Thesis, Leiden University (2000).
- [69] L. A. PELETIER AND W. C. TROY, *Spatial Patterns*, Birkhäuser, Basel (2001).
- [70] J. BURKE AND E. KNOBLOCH, *Snakes and ladders: Localized states in the Swift-Hohenberg equation*, Phys. Lett. A 360 (2007) 681–688.
- [71] H. SAKAGUCHI AND H. R. BRAND, *Stable localized solutions of arbitrary length for the quintic Swift-Hohenberg equation*, Physica D 97 (1996) 274–285.
- [72] D. BENSIMON, B. I. SHRAIMAN, AND V. CROQUETTE, *Nonadiabatic effects in convection*, Phys. Rev. A 38 (1988) 5461–5464.
- [73] A. A. NEPOMNYASHCHY, M. I. TRIBELSKY, AND M. G. VELARDE, *Wave number selection in convection and related problems*, Phys. Rev. E 50 (1994) 1194–1197.
- [74] Y. HIRAOKA AND T. OGAWA, *Rigorous numerics for localized patterns to the quintic Swift-Hohenberg equation*, Japan J. Indust. Appl. Math. 22 (2005) 57–75.

- [75] A. EREMENKO, *Meromorphic travelling wave solutions of the Kuramoto-Sivashinsky equation*, J. Math. Phys. Anal. Geom. 2 (2006) 278–286.
- [76] M. V. DEMINA AND N. A. KUDRYASHOV, *Explicit expressions for meromorphic solutions of autonomous nonlinear ordinary differential equations*, Commun. Nonlinear Sci. Numer. Simulat. 16 (2011) 1127–1134.
- [77] R. CONTE, T.-W. NG, AND K.-K. WONG, *Exact meromorphic stationary solutions of the real cubic Swift-Hohenberg equation*, Stud. Appl. Math. 129 (2012) 117–131.
- [78] N. A. KUDRYASHOV AND D. I. SINELSHCHIKOV, *Exact solutions of the Swift-Hohenberg equation with dispersion*, Commun. Nonlinear Sci. Numer. Simulat. 17 (2012) 26–34.
- [79] M. ABRAMOWITZ AND I. A. STEGUN, *Handbook of Mathematical Functions with Formulas, Graphs, and Mathematical Tables*, 9th printing, New York: Dover (1972).
- [80] H.-C. KAO AND E. KNOBLOCH, *Exact solutions of cubic-quintic Swift-Hohenberg equation and their bifurcations*, Dyn. Syst., in press (2013).
- [81] A. YOCHELIS, J. BURKE, E. KNOBLOCH *Reciprocal oscillons and nonmonotonic fronts in forced nonequilibrium systems*, Phys. Rev. Lett. 97 (2006) 254501.
- [82] A. R. CHAMPNEYS AND J. F. TOLAND, *Bifurcation of a plethora of multi-modal homoclinic orbits for autonomous Hamiltonian systems*, Nonlinearity 6 (1993) 665–772.
- [83] J. BURKE, S. M. HOUGHTON, AND E. KNOBLOCH, *Swift-Hohenberg equation with broken reflection symmetry*, Phys. Rev. E 80 (2009) 036202.
- [84] Y.-P. MA AND E. A. SPIEGEL, *A diagrammatic derivation of (convective) pattern equations*, Physica D 240 (2011) 150–165.
- [85] K. E. DANIELS, B. B. PLAPP, AND E. BODENSCHATZ, *Pattern formation in inclined layer convection*, Phys. Rev. Lett. 84 (2000) 5320–5323.
- [86] F. H. BUSSE AND R. M. CLEVER, *Three dimensional convection in an inclined layer heated from below*, J. Eng. Math. 12 (1992) 1–19.
- [87] F. H. BUSSE AND R. M. CLEVER, *Bursts in inclined layer convection*, Phys. Fluids 12 (2000) 2137–2140.
- [88] R. M. CLEVER AND F. H. BUSSE, *Instabilities of longitudinal convection rolls in an inclined layer*, J. Fluid Mech. 81 (1977) 107–127.

Appendix A

The generalized Swift-Hohenberg equation near the subcritical to supercritical transition

We start from the generalized Swift-Hohenberg equation

$$u_t = ru - (1 + \partial_{xx})^2 u + f(u), \quad (\text{A.1})$$

where $u = u(x, t)$ is a real-valued function and $f(u)$ is a smooth function with Taylor expansion

$$f(u) = f_2 u^2 + f_3 u^3 + f_4 u^4 + f_5 u^5 + O(u^6). \quad (\text{A.2})$$

Here r is the bifurcation parameter and the transition from subcriticality to supercriticality occurs at $r = 0$ when $27f_3 + 38f_2^2 = 0$.

To focus on the vicinity of this transition we write $r = \epsilon^4 \mu$ and $f_3 = -\frac{38}{27}f_2^2 + \epsilon^2 b$, where μ and b are $O(1)$ unfolding parameters, and consider the following multiscale asymptotic expansion

$$u(x, t) \sim \sum_{n=1}^{\infty} \epsilon^n u_n(x, X \equiv \epsilon^2 x, T \equiv \epsilon^4 t). \quad (\text{A.3})$$

Substitution of this expansion into Eq. (A.1) leads to the following sequence of linear problems

$$\begin{aligned} Mu_1 &= 0, \\ Mu_2 &= f_2 u_1^2, \\ Mu_3 &= -4(u_{1,xx} + u_1)_{Xx} - \frac{38}{27} f_2^2 u_1^3 + 2f_2 u_2 u_1, \\ Mu_4 &= -4(u_{2,xx} + u_2)_{Xx} - \frac{38}{9} f_2^2 u_1^2 u_2 + 2f_2 u_1 u_3 + f_2 u_2^2 + f_4 u_1^4, \end{aligned}$$

$$\begin{aligned} Mu_5 = & -4(u_3 + u_{3,xx})_{Xx} + 2f_2(u_1u_4 + u_2u_3) + bu_1^3 - \frac{38}{9}(u_2^2 + u_1u_3)f_2^2u_1 \\ & + \mu u_1 - u_{1,T} - 2u_{1,XX} - 6u_{1,XXxx} + f_5u_1^5 + 4f_4u_1^3u_2. \end{aligned}$$

Here M is the linear self-adjoint operator $M \equiv (1 + \partial_{xx})^2$.

At each order the homogeneous problem $Mu = 0$ has four independent solutions, two that are periodic in x and two that diverge as $|x| \rightarrow \infty$. Thus at each order the homogeneous solutions must take the form $A_n(X, T)e^{ix} + c.c.$, where the A_n denote the corresponding amplitude. Without loss of generality we set $A_1 = A(X, T)$ and $A_n = 0$ for $n > 1$, and seek an evolution equation for $A(X, T)$.

The solutions u_n for $n = 1, \dots, 4$ are

$$\begin{aligned} u_1 &= Ae^{ix} + c.c., \\ u_2 &= f_2 \left\{ \frac{A^2}{9} e^{2ix} + c.c. \right\} + 2f_2|A|^2, \\ u_3 &= -\frac{f_2^2 A^3}{54} e^{3ix} + c.c., \\ u_4 &= \left\{ \left(f_4 - \frac{40f_2^3}{81} \right) \frac{A^4 e^{4ix}}{225} + \left(4f_4 - \frac{727f_2^3}{81} \right) \frac{|A|^2 A^2 e^{2ix}}{9} + \frac{16if_2 A A_X e^{2ix}}{27} + c.c. \right\} \\ &\quad + \left(6f_4 - \frac{1118f_2^3}{81} \right) |A|^4. \end{aligned}$$

At $O(\epsilon^5)$ the solvability condition yields the amplitude equation

$$A_T = \mu A + 4A_{XX} + \frac{32if_2^2}{27}|A|^2 A_X + 3b|A|^2 A - 2 \left(\frac{1960f_2^4}{81} - \frac{58f_2 f_4}{3} - 5f_5 \right) |A|^4 A. \quad (\text{A.4})$$

This equation can be identified with Eq. (1.6) after a rescaling, yielding

$$a_1 = \frac{4f_2^2}{21\sqrt{5}} \left(f_2^4 - \frac{783}{980} f_2 f_4 - \frac{81}{392} f_5 \right)^{-1/2}, \quad a_2 = 0, \quad (\text{A.5})$$

provided $f_2^4 - \frac{783}{980} f_2 f_4 - \frac{81}{392} f_5 > 0$.

Appendix B

Heteroclinic and homoclinic solutions in GL35

When $E = L = 0$ and $\mu = \mu_M$, if $b > 0$ and $\beta < 0$, the heteroclinic solution connecting the states $A = 0$ and $A = R_M \exp(ik_M x)$ can be found explicitly:

$$R^2 = -\frac{b}{4\beta} \frac{1}{\exp\left(\mp \frac{bx}{2\sqrt{-\beta}}\right) + 1}, \quad \phi = \mp \frac{a_1 + a_2}{8\sqrt{-\beta}} \log \left[\frac{1 + \exp\left(\pm \frac{bx}{2\sqrt{-\beta}}\right)}{2} \right]. \quad (\text{B.1})$$

Here and hereafter we have omitted arbitrary constants x_0 and ϕ_0 determining the location of the front and its phase at this location. The resulting solution is shown in figure 2.7. This solution remains valid when $\mu_{sn} = \mu_M$, i.e., when the condition (2.19) holds and the heteroclinic orbit connects the origin to a non-hyperbolic equilibrium (in time).

When $L = 0$ the amplitude R can take on both positive and negative values since the phase ϕ jumps by π each time the amplitude R passes through zero. Thus homoclinic orbits are present in figures 2.5(a)–(f) provided the energy E is selected to coincide with the local maximum of the potential $U(R; \mu, L)$. There are three type of homoclinic orbits when $L = 0$:

- (1) Homoclinic orbit to the origin: This type of solution occurs when $E = 0$ and $\mu < 0$, and has the form

$$R^2 = \frac{\xi_1 \xi_2}{\xi_1 + (\xi_2 - \xi_1) \cosh^2(\sqrt{-\mu}x)}, \quad (\text{B.2})$$

where $\xi_1 = \frac{-b + \sqrt{b^2 - 16\mu\beta}}{4\beta}$, and $\xi_2 = \frac{-b - \sqrt{b^2 - 16\mu\beta}}{4\beta}$. When $\beta < 0$, the coefficient b must satisfy $b > 4\sqrt{\mu\beta}$. The phase varies according to

$$\phi = -\frac{a_1 + a_2}{4\sqrt{\beta}} \tan^{-1} \left(\sqrt{\frac{\xi_1}{-\xi_2}} \tanh \sqrt{-\mu}x \right), \quad \text{if } \beta > 0; \quad (\text{B.3})$$

$$\phi = -\frac{a_1 + a_2}{4\sqrt{-\beta}} \tanh^{-1} \left(\sqrt{\frac{\xi_1}{\xi_2}} \tanh \sqrt{-\mu}x \right), \quad \text{if } \beta < 0. \quad (\text{B.4})$$

The potential $U(R; \mu, 0)$ for $\beta > 0$ is shown in figure 2.5(a) while that for $\beta < 0$ is shown in figure 2.5(c). In the degenerate case $\mu = 0$, there is a homoclinic orbit that decays algebraically to the origin. This occurs when $E = 0$, $b < 0$, and $\beta > 0$:

$$R^2 = -\frac{b}{2\beta} \left(1 + \frac{b^2 x^2}{4\beta}\right)^{-1}, \quad \phi = \frac{a_1 + a_2}{4\sqrt{\beta}} \tan^{-1} \left(\frac{bx}{2\sqrt{\beta}}\right). \quad (\text{B.5})$$

A typical solution of this form is shown in figure 2.8.

(2) Homoclinic orbit to a nonzero equilibrium crossing $R = 0$:

$$R^2 = \frac{\xi_1 \xi_2 \sinh^2 \left(\sqrt{\mu + \frac{b\xi_1}{2}} x \right)}{\xi_2 \cosh^2 \left(\sqrt{\mu + \frac{b\xi_1}{2}} x \right) - \xi_1}. \quad (\text{B.6})$$

Here $\xi_1 = \frac{-b - \sqrt{b^2 - 12\mu\beta}}{6\beta}$, $\xi_2 = \frac{-b + 2\sqrt{b^2 - 12\mu\beta}}{6\beta}$, and $E = U(\sqrt{\xi_1})$ corresponding to the local maximum of U . When $\beta > 0$, μ must be positive with $b < -2\sqrt{3\mu\beta}$. When $\beta < 0$, μ can be either positive or negative. But if μ is negative, b must satisfy $b > 4\sqrt{\mu\beta}$. The phase varies according to

$$\phi = -\frac{(a_1 + a_2)}{4} \left[\xi_1 x - \frac{1}{\sqrt{\beta}} \tan^{-1} \left(\frac{\tanh \sqrt{\mu + (b\xi_1)/2} x}{\sqrt{(\xi_2/\xi_1) - 1}} \right) \right], \quad \text{if } \beta > 0; \quad (\text{B.7})$$

$$\phi = -\frac{(a_1 + a_2)}{4} \left[\xi_1 x - \frac{1}{\sqrt{-\beta}} \tanh^{-1} \left(\frac{\tanh \sqrt{\mu + (b\xi_1)/2} x}{\sqrt{1 - (\xi_2/\xi_1)}} \right) \right], \quad \text{if } \beta < 0. \quad (\text{B.8})$$

The relevant potential $U(R; \mu, 0)$ for $\beta > 0$ is shown in figure 2.5(d,f) and for $\beta < 0$ in figures 2.5(b,c).

(3) Homoclinic orbit to a nonzero equilibrium which does not cross $R = 0$:

$$R^2 = \frac{\xi_1 \xi_2 \cosh^2 \left(\sqrt{\mu + \frac{b\xi_1}{2}} x \right)}{\xi_1 + \xi_2 \sinh^2 \left(\sqrt{\mu + \frac{b\xi_1}{2}} x \right)}. \quad (\text{B.9})$$

Here ξ_1 and ξ_2 are as in (2) above, and $E = U(\sqrt{\xi_1})$ again corresponds to the local maximum of U . When $\beta > 0$, μ must be positive with $b < -2\sqrt{3\mu\beta}$. When $\beta < 0$, μ must be negative with $2\sqrt{3\mu\beta} < b < 4\sqrt{\mu\beta}$. The phase varies according to

$$\phi = -\frac{(a_1 + a_2)}{4} \left[\xi_1 x + \frac{1}{\sqrt{\beta}} \tan^{-1} \left(\sqrt{\frac{\xi_2}{\xi_1}} - 1 \tanh \sqrt{\mu + \frac{b\xi_1}{2}} x \right) \right], \quad \text{if } \beta > 0; \quad (\text{B.10})$$

$$\phi = -\frac{(a_1 + a_2)}{4} \left[\xi_1 x - \frac{1}{\sqrt{-\beta}} \tanh^{-1} \left(\sqrt{1 - \frac{\xi_2}{\xi_1}} \tanh \sqrt{\mu + \frac{b\xi_1}{2}} x \right) \right], \quad \text{if } \beta < 0. \quad (\text{B.11})$$

The relevant potential $U(R; \mu, 0)$ for $\beta > 0$ is shown in figures 2.5(d,f) and for $\beta < 0$ in figure 2.5(e).

When $L \neq 0$, only homoclinic orbits are present (figures 2.6(a,c)). For such an orbit the energy E again coincides with the local maximum of the potential $U(R; \mu, L)$, assumed to be located at $R_1 = \sqrt{\xi_1}$. With ξ_2 and ξ_3 as the other two roots of the polynomial $\xi [E - U(\sqrt{\xi})]$, assumed distinct and different from ξ_1 , a homoclinic orbit with a turning point at $\sqrt{\xi_2}$ has the form:

$$R^2 = \xi_1 + \frac{(\xi_2 - \xi_1)(\xi_3 - \xi_1)}{\xi_2 - \xi_1 + (\xi_3 - \xi_2) \cosh^2 \left[\sqrt{\beta(\xi_3 - \xi_1)(\xi_1 - \xi_2)} x \right]} \quad (\text{B.12})$$

with the phase

$$\begin{aligned} \phi = -\frac{(a_1 + a_2)}{4} \left\{ \xi_1 x - \frac{1}{\sqrt{\beta}} \tan^{-1} \left[\left(\frac{\xi_1 - \xi_2}{\xi_3 - \xi_1} \right)^{1/2} \tanh \sqrt{\beta(\xi_3 - \xi_1)(\xi_1 - \xi_2)} x \right] \right\} \\ + \left(k_\infty + \frac{a_1 + a_2}{4} \xi_1 \right) \left\{ x + \frac{\tan^{-1} \left[\sqrt{\frac{\xi_3(\xi_1 - \xi_2)}{\xi_2(\xi_3 - \xi_1)}} \tanh \sqrt{\beta(\xi_3 - \xi_1)(\xi_1 - \xi_2)} x \right]}{\sqrt{\beta \xi_2 \xi_3}} \right\}, \quad \text{if } \beta > 0; \end{aligned} \quad (\text{B.13})$$

$$\begin{aligned} \phi = -\frac{(a_1 + a_2)}{4} \left\{ \xi_1 x - \frac{1}{\sqrt{-\beta}} \tanh^{-1} \left[\left(\frac{\xi_1 - \xi_2}{\xi_1 - \xi_3} \right)^{1/2} \tanh \sqrt{\beta(\xi_3 - \xi_1)(\xi_1 - \xi_2)} x \right] \right\} \\ + \left(k_\infty + \frac{a_1 + a_2}{4} \xi_1 \right) \left\{ x + \frac{\tan^{-1} \left[\sqrt{\frac{\xi_3(\xi_1 - \xi_2)}{\xi_2(\xi_3 - \xi_1)}} \tanh \sqrt{\beta(\xi_3 - \xi_1)(\xi_1 - \xi_2)} x \right]}{\sqrt{\beta \xi_2 \xi_3}} \right\}, \quad \text{if } \beta < 0. \end{aligned} \quad (\text{B.14})$$

Here k_∞ is the wavenumber at the equilibrium. The relevant potential $U(R; \mu, L)$ for $\beta > 0$ is shown in figure 2.6(c) and for $\beta < 0$ in figure 2.6(a).

Appendix C

Bifurcation analysis near $\mu = 1$ in GL35

As already noted that the first primary bifurcation occurs at $\mu = 0$ generates steady spatially homogeneous states characterized by wavenumber $k = 0$. Here we study the second primary instability, characterized by states with wavenumber $k = \pm 1$.

C.1 The case $a_1 = a_2 = 0$

When $a_1 = a_2 = 0$ Eq. (1.6) has the symmetry $O(2) \times O(2)$ with the first $O(2)$ generated by the operations $x \rightarrow x + x_0, A \rightarrow A$ and $x \rightarrow -x, A \rightarrow A$, and the second $O(2)$ generated by the operations $x \rightarrow x, A \rightarrow A \exp i\phi_0$ and $x \rightarrow x, A \rightarrow A^*$. At $\mu = 1$ the trivial state $A = 0$ loses stability at a steady state bifurcation to modes with wavenumber $k = \pm 1$. Over \mathbb{C} the multiplicity of the zero eigenvalue is therefore two while over \mathbb{R} its multiplicity is four. The bifurcation is thus properly analyzed as a mode interaction problem and we write

$$A(x, t) = v(t)e^{ix} + w(t)e^{-ix} + h.o.t. \quad (\text{C.1})$$

The symmetries of the problem act on the amplitudes (v, w) as follows:

$$x \rightarrow x + x_0 : (v, w) \rightarrow (ve^{ix_0}, we^{-ix_0}), \quad x \rightarrow -x : (v, w) \rightarrow (w, v); \quad (\text{C.2})$$

$$A \rightarrow e^{i\phi_0} A : (v, w) \rightarrow (ve^{i\phi_0}, we^{i\phi_0}), \quad A \rightarrow A^* : (v, w) \rightarrow (\bar{w}, \bar{v}). \quad (\text{C.3})$$

It follows, cf. [44], that the normal form near $\mu = 1$ is

$$\dot{v} = \lambda v + b_1|v|^2v + b_2|w|^2v + h.o.t., \quad \dot{w} = \lambda w + b_2|v|^2w + b_1|w|^2w + h.o.t., \quad (\text{C.4})$$

where $\lambda = \mu - 1$ and the coefficients $b_1 = b, b_2 = 2b$ are real. It follows that near $\mu = 1$ there are two distinct nontrivial solutions corresponding to $(v, w) = (v, 0)$ and $(v, w) = (v, v)$. We refer to these solutions as RW: $A = v \exp ix$ and SW: $A = 2v \cos x$. The stability of these solutions is determined by the coefficients b_1, b_2 [44].

C.2 Nonzero a_1 or a_2 (or both)

When a_1 or a_2 is nonzero Eq. (1.6) has the smaller symmetry $O(2) \times SO(2)$ generated by the operations $x \rightarrow x + x_0, A \rightarrow A$ and $x \rightarrow x, A \rightarrow A \exp i\phi_0$ and the reflection $x \rightarrow -x, A \rightarrow A^*$. Since the linear problem is unchanged the multiplicity of the zero eigenvalues remains four over \mathbb{R} , but the amplitude equations must now respect the symmetries:

$$x \rightarrow x + x_0 : (v, w) \rightarrow (ve^{ix_0}, we^{-ix_0}), \quad A \rightarrow e^{i\phi_0} A : (v, w) \rightarrow (ve^{i\phi_0}, we^{i\phi_0}), \quad (\text{C.5})$$

together with

$$x \rightarrow -x, A \rightarrow A^* : (v, w) \rightarrow (\bar{v}, \bar{w}). \quad (\text{C.6})$$

Thus

$$\dot{v} = \lambda v + b_{11}|v|^2 v + b_{12}|w|^2 v + h.o.t., \quad \dot{w} = \lambda w + b_{21}|v|^2 w + b_{22}|w|^2 w + h.o.t., \quad (\text{C.7})$$

where $\lambda = \mu - 1$ and the coefficients $b_{11} = b - a_1 + a_2$, $b_{12} = 2(b - a_2)$, $b_{21} = 2(b + a_2)$, and $b_{22} = b + a_1 - a_2$ are real. These equations admit a pair of distinct RW solutions $(v, w) = (v, 0)$ and $(v, w) = (0, w)$, hereafter RW^+ : $A = v \exp ix$ and RW^- : $A = w \exp -ix$, both of which bifurcate from $\mu = 1$. The equations, in addition, admit mixed modes of the form (v, w) , $vw \neq 0$, hereafter MW: $A = v \exp ix + w \exp -ix$, given by

$$|v|^2 = -\lambda(b - a_1 - a_2)/\Delta, \quad |w|^2 = -\lambda(b + a_1 + a_2)/\Delta. \quad (\text{C.8})$$

Here $\Delta \equiv 3b^2 + (a_1 - 3a_2)(a_1 + a_2)$ is assumed to be nonzero. These expressions imply that the MW only exist for $|a_1 + a_2| < |b|$, in agreement with the calculation in Appendix D. In particular, when $|a_1 + a_2| = |b|$ the MW degenerate into one or other RW. In contrast, when $a_1 = a_2 = 0$ the RW^\pm branches become identical and the MW branch becomes SW in agreement with the preceding section. In the special case $a_1 = a_2$ the RW^\pm branches become identical (cf. Eq. (2.18)) while in the case $a_1 + a_2 = 0$ the MW become SW with $|v| = |w|$. These results explain the absence of an MW branch in figures 2.17(a,b) and the presence of an SW branch in figure 2.18. They also explain the presence of an MW branch in figure 2.19, where the MW branch bifurcates simultaneously with the RW^\pm . The stability of the above solutions is determined by the coefficients b_{11} , b_{12} , b_{21} , b_{22} , although the branches are initially all unstable owing to the inherited unstable $k = 0$ eigenvalue.

The above results describe fully the bifurcation behavior near the $k = 1$ primary bifurcation and are readily generalized to $k \neq 0, 1$. Global results based on the particle-in-a-potential formulation are summarized in the corresponding bifurcation diagrams.

Appendix D

Calculation of $\frac{dE}{d\mu}$ and $\frac{dL}{d\mu}$ on primary branches

The direction of branching at the bifurcation point is determined by the sign of the quantity $\frac{dE}{d\mu} - U_{0,L} \frac{dL}{d\mu} - U_{0,\mu}$. This quantity measures the parameter dependence of the energy difference between that of the periodic orbit and the minimum of the potential $U(R; \mu, L)$ and must be of the same sign as $\mu - \mu_0$ for a periodic orbit to be created as μ changes. Here μ_0 is the value of μ at the bifurcation point. Hence to determine the direction of branching, we need to compute $\frac{dE}{d\mu}$ and $\frac{dL}{d\mu}$. At the bifurcation point, the following conditions hold:

$$U(R_0; \mu_0, L_0) = E_0, \quad U_R(R_0; \mu_0, L_0) = 0, \quad U_{RR}(R_0; \mu_0, L_0) = \frac{2\pi^2 n^2}{\Gamma^2}. \quad (\text{D.1})$$

The subscript 0 indicates that the quantity is evaluated on the primary branch. If μ is changed by a small amount, $\mu_0 \rightarrow \mu_0 + \delta\mu$, then $E_0 \rightarrow E_0 + \delta E$, $L_0 \rightarrow L_0 + \delta L$, and the position of the local minimum of U will be shifted from R_0 to $R_0 + \delta R_0$. Since $U_R = 0$ along the primary branch, it follows that $\partial_R U(R_0 + \delta R_0; \mu_0 + \delta\mu, L_0 + \delta L) = 0$, and hence that

$$\frac{\delta R_0}{\delta\mu} = -U_{RR}^{-1} \left(U_{RL} \frac{\delta L}{\delta\mu} + U_{R\mu} \right). \quad (\text{D.2})$$

To calculate the period of amplitude modulation under small perturbation, we need to expand the potential energy locally up to fourth order in $r \equiv R - (R_0 + \delta R_0)$. To simplify expressions, let $U_0 = U(R; \mu_0, L_0)$ with U representing $U(R; \mu_0 + \delta\mu, L_0 + \delta L)$ unless otherwise specified. The potential can be expressed in the form

$$\begin{aligned} U(R) = & U(R_0 + \delta R_0) + \frac{U_{RR}(R_0 + \delta R_0)}{2!} r^2 + \frac{U_{RRR}(R_0 + \delta R_0)}{3!} r^3 \\ & + \frac{U_{RRRR}(R_0 + \delta R_0)}{4!} r^4 + O(r^5), \end{aligned} \quad (\text{D.3})$$

and this expansion employed in the computation of the half period of amplitude modulation: $\int_{R_{min}}^{R_{max}} \frac{dR}{\sqrt{E_0 + \delta E - U(R)}}$. To calculate the integral, consider the change of variable

$$\Delta s^2 = U(R) - U(R_0 + \delta R_0), \quad (\text{D.4})$$

where $\Delta \equiv E_0 + \delta E - U(R_0 + \delta R_0)$. Then

$$r = \sqrt{\frac{2\Delta}{U_{RR}}} \left[s - \frac{U_{RRR}\Delta^{1/2}}{3\sqrt{2}U_{RR}^{3/2}} s^2 + \frac{(5U_{RRR}^2 - 3U_{RRRR}U_{RR})\Delta}{36U_{RR}^3} s^3 \right] + O(\Delta^2). \quad (\text{D.5})$$

Substituting this expression into the integral yields

$$\sqrt{\frac{U_{RR}}{U_{0,RR}}} - 1 = \frac{5U_{RRR}^2 - 3U_{RRRR}U_{RR}}{24U_{RR}^3} \Delta + O(\Delta^{3/2}), \quad (\text{D.6})$$

and hence

$$\begin{aligned} & U_{0,RRR} \frac{\delta R_0}{\delta \mu} + U_{0,RRL} \frac{\delta L}{\delta \mu} + U_{0,RR\mu} \\ &= \left(\frac{\delta E}{\delta \mu} - U_{0,L} \frac{\delta L}{\delta \mu} - U_{0,\mu} \right) \frac{5U_{0,RRR}^2 - 3U_{0,RRRR}U_{0,RR}}{12U_{0,RR}^2}. \end{aligned} \quad (\text{D.7})$$

A similar calculation to match the change of phase $\int_{R_{min}}^{R_{max}} \frac{k dR}{\sqrt{E - U(R)}}$ yields

$$2 \left(\sqrt{\frac{U_{RR}}{U_{0,RR}}} k_0 - k \right) = \left(\frac{5U_{RRR}^2 - 3U_{RRRR}U_{RR}}{12U_{RR}^3} k_0 - \frac{k_R U_{RRR}}{U_{RR}^2} + \frac{k_{RR}}{U_{RR}} \right) \Delta + O(\Delta^{3/2})$$

and hence

$$2 \left(k_R \frac{\delta R_0}{\delta \mu} + \frac{1}{R_0^2} \frac{\delta L}{\delta \mu} \right) = \left(\frac{\delta E}{\delta \mu} - U_{0,L} \frac{\delta L}{\delta \mu} - U_{0,\mu} \right) \left[\frac{U_{0,RRR}}{U_{0,RR}^2} k_R - \frac{k_{RR}}{U_{0,RR}} \right], \quad (\text{D.8})$$

where $k \equiv \phi_x$ is a function of R and L . The derivatives in these two relations are all evaluated at the bifurcation point $\mu = \mu_0$. From the three relations above, we obtain the quantity $\frac{dE}{d\mu} - U_{0,L} \frac{dL}{d\mu} - U_{0,\mu}$ and thereby determine the direction of branching.

The direction of branching of SW can be calculated in the same way. Since the SW are characterized by $L = k = 0$ and are only present as primary bifurcations when $a_1 + a_2 = 0$ the direction of branching is only determined by $\frac{dE}{d\mu}$, where

$$\frac{dE}{d\mu} = U_{0,\mu} + \frac{12U_{0,RR}^2 (U_{0,RR\mu} - U_{0,RRR}U_{0,RR}^{-1}U_{0,R\mu})}{5U_{0,RRR}^2 - 3U_{0,RRRR}U_{0,RR}} = -\frac{4\mu}{3b}. \quad (\text{D.9})$$

Since μ must be positive in order that the bifurcation be from $A = 0$ the direction of branching is determined solely by the sign of b (subcritical if $b > 0$, supercritical if $b < 0$).

The direction of branching of quasiperiodic states that bifurcate from $A = 0$ can also be calculated. These branches appear at $\mu_0 > 0$ when $a_1 + a_2 \neq 0$. The condition $\mu_0 > 0$ implies that $R = 0$ is a local minimum for U when $L = 0$. As L becomes nonzero, U becomes singular at $R = 0$. But since $\mu_0 > 0$, a local minimum of U appears close to $R = 0$. With the change of variable

$$\rho = \frac{R^2}{|L|} - \frac{E}{2\mu'|L|}, \quad (\text{D.10})$$

the half period of amplitude modulation and the corresponding phase change can be written as:

$$\int_{R_{min}}^{R_{max}} \frac{dR}{\sqrt{E-U}} = \frac{1}{2} \int_{\rho_{min}}^{\rho_{max}} \frac{d\rho}{\sqrt{\mu'\gamma^2 - 1 - u(\rho; \mu, L, \gamma)}}, \quad (\text{D.11})$$

$$\int_{R_{min}}^{R_{max}} \frac{k dR}{\sqrt{E-U}} = \frac{1}{2} \int_{\rho_{min}}^{\rho_{max}} \frac{\text{sgn}(L) (\rho + \gamma)^{-1} - \frac{a_1+a_2}{4}|L| (\rho + \gamma)}{\sqrt{\mu'\gamma^2 - 1 - u(\rho; \mu, L, \gamma)}} d\rho, \quad (\text{D.12})$$

where $\mu' = \mu + \frac{3a_2-a_1}{2}L$, $\gamma = \frac{E}{2\mu'|L|}$ and

$$u(\rho; \mu, L, \gamma) = \mu' \rho^2 + \frac{b|L|}{2} (\rho + \gamma)^3 + \beta L^2 (\rho + \gamma)^4. \quad (\text{D.13})$$

As L tends to 0, these integrals equal to $\frac{\pi}{2\sqrt{\mu_0}}$ and $\frac{\pi}{2}$, respectively, and are independent of γ . To compute the asymptotic behavior of these integrals for small L , we assume that $L = \epsilon \tilde{L}$, $\mu = \mu_0 + \epsilon \tilde{\mu}$ with $\mu_0 = k^2$, and $\gamma = \gamma_0 + \epsilon \tilde{\gamma}$, where $\epsilon \ll 1$. We next define ρ_ϵ by the following relation:

$$\mu' \rho_\epsilon^2 = \mu' \rho^2 + \frac{b|L|}{2} [(\rho + \gamma)^3 - \gamma^3] + \beta L^2 [(\rho + \gamma)^4 - \gamma^4],$$

with the property that $\lim_{\epsilon \rightarrow 0} \rho(\epsilon) = \rho$. When ϵ is small,

$$\rho = \rho_\epsilon - \frac{\epsilon b |\tilde{L}|}{4\mu_0} (\rho_\epsilon^2 + 3\rho_\epsilon \gamma + 3\gamma^2) + O(\epsilon^2).$$

Substituting this into the integrals (D.11)–(D.12), we see that the $O(\epsilon)$ terms give

$$2\tilde{\mu} + (3a_2 - a_1)\tilde{L} + 3\gamma_0 b |\tilde{L}| = 0, \quad \text{sgn}(L)b + \mu_0 \gamma_0 (a_1 + a_2) = 0. \quad (\text{D.14})$$

Since $\gamma_0 > 0$, $\mu_0 > 0$ the sign of L must be the same as $-b(a_1 + a_2)$. As $\epsilon \rightarrow 0$, $\mu_0 \gamma_0^2 - 1$ must be positive implying that $|b| > \sqrt{\mu_0} |a_1 + a_2|$ in order that a branch of quasiperiodic states exists. Substituting γ into the first relation in Eq. (D.14), we obtain a relation between μ and L along the branch, viz.,

$$L = -\frac{2(\mu - \mu_0)}{3a_2 - a_1 - \frac{3b^2}{\mu_0(a_1+a_2)}} + O(|\mu - \mu_0|^2).$$

This prediction agrees with the result shown in figure 2.19.

Appendix E

Derivation of the nonlinear phase equation in GL35

Here we present the derivation of the nonlinear phase equation as described in section 2.5. Before presenting the calculations, we remark that at the onset of phase instability $f = 0$ is equivalent to $2g_0 = -b_+b_-$, where b_{\pm} are given in Eq. (2.56). This relation will be used several times in the calculation to simplify expressions. Applying the scaling assumption introduced in Eq. (2.54) the $O(\epsilon^2)$ equation yields

$$2g_0r^{(0)} = b_-\phi_X^{(0)}, \quad (\text{E.1})$$

indicating that the perturbed amplitude is slaved to the gradient of the phase. The relation at $O(\epsilon^3)$ is automatically satisfied. At $O(\epsilon^4)$ and $O(\epsilon^5)$ one obtains, after using the relation in Eq. (E.1),

$$\begin{aligned} -2g_0r^{(1)} + b_-\phi_X^{(1)} &= \partial_X^3\phi^{(0)}/b_+ + \phi_X^{(0)2} [(8k_0 + b_-)/(2b_+) + (2R_{0,+}^2b')/b_+^2 + 1] \\ &\quad + \mu_2\phi_X^{(0)} [(a_1 - a_2)\partial_\mu R_{0,+}^2 - 2(b'\partial_\mu R_{0,+}^2 + 2)/b_+], \end{aligned} \quad (\text{E.2})$$

$$b_+r_X^{(1)} + \phi_{XX}^{(1)} = \phi_T^{(0)} + \partial_\mu R_{0,+}^2\mu_2(a_1 + a_2)\phi_{XX}^{(0)}/b_+ + (b_+ + 4k_0)\phi_{XX}^{(0)}\phi_X^{(0)}/b_+^2. \quad (\text{E.3})$$

Since $2g_0 = -b_+b_-$ we see that Eq. (E.3) is proportional to the spatial derivative of Eq. (E.2). The nonlinear phase equation (2.55) now follows on eliminating $r^{(1)}$ between these two equations.

Appendix F

Branching direction of the convection branches

We begin with Eqs. (3.15) and (3.16) and compute the secondary branch of stationary modulated solutions using weakly nonlinear theory, following [19]. These equations have the stationary equilibrium $(A, V) = (A_0, 0)$, where without loss of generality $A_0 = \sqrt{2r/(1 - \xi^2)}$. We seek nearby solutions in the form

$$A = A_0(1 + \tilde{A}(X, \tau; \epsilon)), \quad V = \tilde{V}(X, \tau; \epsilon), \quad (\text{F.1})$$

where $\tau = \epsilon^2 T_2$ and $\tilde{A} = \epsilon \tilde{A}_1 + \epsilon^2 \tilde{A}_2 + \epsilon^3 \tilde{A}_3 + \dots$, $\tilde{V} = \epsilon \tilde{V}_1 + \epsilon^2 \tilde{V}_2 + \epsilon^3 \tilde{V}_3 + \dots$. Here ϵ is defined implicitly by the relation $r = r_1 + \epsilon^2 \tilde{r}$, where $r = r_1$ denotes the location of the secondary bifurcation. Since the imaginary part of \tilde{A} decays to zero we take \tilde{A} to be real. At $O(\epsilon)$ we obtain a linear eigenvalue problem for r_1 with solution $\tilde{A}_1 = \tilde{A}_{11} \cos lX$, $\tilde{V}_1 = \tilde{V}_{11} \sin lX$, where

$$r_1 = \frac{l^2}{2} \left(\frac{1 - \xi^2}{3\xi^2 - 1} \right), \quad \tilde{V}_{11} = -\frac{4\xi r_1}{l(1 - \xi^2)} \tilde{A}_{11}. \quad (\text{F.2})$$

In the following we assume that $\xi^2 < 1$ so that the periodic state $(A_0, 0)$ is supercritical. Thus a secondary bifurcation requires that $3\xi^2 - 1 > 0$.

Second order

At $O(\epsilon^2)$ we obtain

$$\tilde{A}_{2XX} - 2r_1 \tilde{A}_2 - \xi \tilde{V}_{2X} = 3r_1 \tilde{A}_1^2 + \xi \tilde{A}_1 \tilde{V}_{1X}, \quad (\text{F.3})$$

$$\tilde{V}_{2X} + \frac{4\xi r_1}{1 - \xi^2} \tilde{A}_2 = -\frac{2\xi r_1}{1 - \xi^2} \tilde{A}_1^2 + C_2, \quad (\text{F.4})$$

where C_2 is a constant of integration. The requirement that $\langle \tilde{V}_{2X} \rangle = 0$ determines C_2 and leads to the solution

$$\tilde{A}_2 = \tilde{A}_{20} + \tilde{A}_{22} \cos 2lX, \quad \tilde{V}_{2X} = \tilde{V}_{22} \cos 2lX, \quad (\text{F.5})$$

where

$$\tilde{A}_{20} = \frac{7\xi^2 - 3}{4(1 - \xi^2)} \tilde{A}_{11}^2, \quad \tilde{A}_{22} = \frac{1}{4} \tilde{A}_{11}^2, \quad \tilde{V}_{22} = -\frac{2\xi r_1}{1 - \xi^2} \tilde{A}_{11}^2. \quad (\text{F.6})$$

Third order

At $O(\epsilon^3)$ we obtain

$$\tilde{A}_{3XX} - 2r_1 \tilde{A}_3 - \xi \tilde{V}_{3X} = 2\tilde{r} \tilde{A}_1 + 6r_1 \tilde{A}_1 \tilde{A}_2 + r_1 \tilde{A}_1^3 + \xi \tilde{A}_2 \tilde{V}_{1X} + \xi \tilde{A}_1 \tilde{V}_{2X}, \quad (\text{F.7})$$

$$\tilde{V}_{3X} + \frac{4\xi r_1}{1 - \xi^2} \tilde{A}_3 = -\frac{4\xi \tilde{r}}{1 - \xi^2} \tilde{A}_1 - \frac{4\xi r_1}{1 - \xi^2} \tilde{A}_1 \tilde{A}_2 + C_3. \quad (\text{F.8})$$

The requirement $\langle \tilde{V}_{3X} \rangle = 0$ establishes that $C_3 = 0$. Elimination of terms proportional to $\cos lX$ from the equation for \tilde{A}_3 leads to the solvability condition

$$\tilde{r} = \frac{l^2}{4} \left(\frac{3 - 7\xi^2}{3\xi^2 - 1} \right) \tilde{A}_{11}^2, \quad (\text{F.9})$$

where $l = 2\pi/\Gamma'$ and Γ' is defined in Eq. 3.31. It follows that the secondary branch is supercritical ($\tilde{r} > 0$) if $\xi^2 < 3/7$ and subcritical ($\tilde{r} < 0$) if $\xi^2 > 3/7$, in agreement with the numerical results in section 3.2. These results can also be obtained from a careful study of the conditions (3.26) using the potential $U[\rho]$ given in Eq. (3.25) with $K_1 = 0$ [20].

Appendix G

Derivation of the modulation equations for magnetoconvection near the codimension-two point

Here we apply the scaling assumption given in section 3.3 for the perturbation expansion. To simplify expressions, we use in the following notation

$$\begin{aligned}\nabla^2 &\equiv \partial_{xx} + \partial_{zz}, & J(u, v) &\equiv u_x v_z - u_z v_x, & \tilde{J}(u, v) &\equiv u_X v_z - u_z v_X, \\ p_{nm} &\equiv -(n^2 k^2 + m^2 \pi^2)^3 + Ra_c n^2 k^2 - Q_c m^2 \pi^2 (n^2 k^2 + m^2 \pi^2).\end{aligned}$$

The equation takes the following form at each order of ϵ

$$\mathbf{M}\Psi_n = \begin{pmatrix} \nabla^4 & Ra_c \partial_x & Q_c \zeta \partial_z \nabla^2 \\ \partial_x & \nabla^2 & 0 \\ \partial_z & 0 & \zeta \nabla^2 \end{pmatrix} \Psi_n = \mathbf{f}_n, \quad (\text{G.1})$$

where Ψ_n represents $(\psi_n, \theta_n, A_n)^T$ and \mathbf{f}_n is a vector with components as a polynomials of $\psi_1, \dots, \psi_{n-1}, \theta_1, \dots, \theta_{n-1}, A_0, \dots, A_{n-1}$, and their derivatives. Eq. (G.1) can also be written as a single equation with respect to ψ_n ,

$$M\psi_n \equiv (\nabla^6 - Ra_c \partial_{xx} - Q_c \partial_{zz} \nabla^2) \psi_n = \nabla^2 f_{n1} - Ra_c \partial_x f_{n2} - Q_c \partial_z \nabla^2 f_{n3}. \quad (\text{G.2})$$

We solve this equation for ψ_n and determine the corresponding θ_n and A_n from Eq. (G.1).

First & second order

At $O(\epsilon)$, $\mathbf{f}_1 = 0$. The resulting homogeneous problem has a solution of the form

$$\begin{aligned}\psi_1 &= \frac{a}{2} e^{ikx} \sin(\pi z) + c.c., \\ \theta_1 &= \frac{ika}{2p} e^{ikx} \sin(\pi z) + c.c., \\ A_1 &= \frac{\pi a}{2p\zeta} e^{ikx} \cos(\pi z) + c.c.\end{aligned}$$

Note that the linear operator M in Eq. (G.2) is self-adjoint with kernel $e^{\pm ikx} \sin(\pi z)$. This facts simplifies the solvability condition at each subsequent order.

At $O(\epsilon^2)$ \mathbf{f}_2 is given by

$$\begin{aligned} f_{21} &= \sigma^{-1} J(\psi_1, \nabla^2 \psi_1) - Q_c \zeta J(A_1, \nabla^2 A_1), \\ f_{22} &= -J(\theta_1, \psi_1), \\ f_{23} &= -J(A_1, \psi_1). \end{aligned}$$

The solvability condition for ψ_2 is always satisfied at this order and Ψ_2 is given by

$$\begin{aligned} \psi_2 &= 0, \\ \theta_2 &= -\frac{k^2 |a|^2 \sin(2\pi z)}{8\pi p}, \\ A_2 &= A_{20}(X, T) + \left\{ \frac{i\pi^2 e^{2ikx} a^2}{16k\zeta^2 p} + c.c. \right\}. \end{aligned}$$

The homogeneous term A_{20} plays an important part in what follows.

Third order

At $O(\epsilon^3)$ \mathbf{f}_3 is given by

$$\begin{aligned} f_{31} &= -4\nabla^2 \psi_{1,Xx} - Ra_c \theta_{1,X} - q\zeta \nabla^2 A_{1,z} + \sigma^{-1} [J(\psi_2, \nabla^2 \psi_1) + J(\psi_1, \nabla^2 \psi_2)] \\ &\quad - Q_c \zeta [2A_{1,Xxz} + J(A_1, \nabla^2 A_2) + J(A_2, \nabla^2 A_1) + A_{0,X} \nabla^2 A_{1,z}] - r_2 \theta_{1,x}, \\ f_{32} &= J(\psi_1, \theta_2) + J(\psi_2, \theta_1) - \psi_{1,X} - 2\theta_{1,Xx}, \\ f_{33} &= J(\psi_1, A_2) + J(\psi_2, A_1) - 2\zeta A_{1,Xx} - \psi_{1,z} A_{0,X}. \end{aligned}$$

The solvability condition for ψ_3 gives

$$\frac{k^2 r_2 - p\pi^2 q}{2} a - Q_c p \pi^2 a A_{0,X} - \frac{Q_c \pi^4}{4\zeta^2} |a|^2 a = 0, \quad (\text{G.3})$$

which corresponds to the $O(\epsilon^3)$ terms in Eq. (3.37). The solution Ψ_3 is

$$\begin{aligned} \psi_3 &= \frac{a_1^3 e^{3ikx} Q_c \pi^4 (9k^2 + \pi^2)(k^2 - \pi^2) \sin(\pi z)}{8p^2 \zeta^2 p_{31}} - \frac{|a_1|^2 a_1 e^{ikx} Ra_c k^4 \sin(3\pi z)}{16pp_{13}} + c.c., \\ \theta_3 &= \frac{ik^3 |a|^2 e^{ikx} a (p_{13} - Ra_c k^2) \sin(3\pi z)}{16pp_{13}(k^2 + 9\pi^2)} + \frac{3iQ_c k \pi^4 e^{3ikx} a^3 (k^2 - \pi^2) \sin(\pi z)}{8p^2 p_{31} \zeta^2} \\ &\quad - \frac{a_X e^{ikx} (k^2 - \pi^2) \sin(\pi z)}{2p^2} - \frac{ik^3 |a|^2 e^{ikx} a \sin(\pi z)}{16p^2} + c.c., \\ A_3 &= \frac{\pi e^{ikx} A_{0,X} a \cos(\pi z)}{2\zeta p} + \frac{ik\pi e^{ikx} a_X \cos(\pi z)}{p^2 \zeta} - \frac{e^{ikx} |a|^2 a \pi^3 \cos(\pi z)}{16p^2 \zeta^3} - \frac{3Ra_c k^4 \pi e^{ikx} |a|^2 a \cos(3\pi z)}{16pp_{13} \zeta (k^2 + 9\pi^2)} \\ &\quad + \frac{a^3 e^{3ikx} \cos(\pi z) \pi^3 [2Q_c \pi^2 (9k^4 - 8k^2 \pi^2 - \pi^4) - pp_{31}]}{16p^2 \zeta^3 p_{31} (9k^2 + \pi^2)} + c.c. \end{aligned}$$

Fourth order

At $O(\epsilon^4)$ \mathbf{f}_4 is given by

$$\begin{aligned}
 f_{41} &= \sigma^{-1} \left[2J(\psi_1, \psi_{1,Xx}) + \tilde{J}(\psi_1, \nabla^2 \psi_1) + \sum_{n=1}^3 J(\psi_n, \nabla^2 \psi_{4-n}) \right] \\
 &\quad - Ra_c \theta_{2,X} - q\zeta (\nabla^2 A_{2,z} + J(A_1, \nabla^2 A_1)) - 2Q_c \zeta A_{2,Xxz} - 4\nabla^2 \psi_{2,Xx} - r_2 \theta_{2,x} \\
 &\quad - Q_c \zeta \left[A_{0,X} \nabla^2 A_{2,z} + 2J(A_1, A_{1,Xx}) + \tilde{J}(A_1, \nabla^2 A_1) + \sum_{n=1}^3 J(A_n, \nabla^2 A_{3-n}) \right], \\
 f_{42} &= -\psi_{2,X} - 2\theta_{2,Xx} - \tilde{J}(\theta_1, \psi_1) - \sum_{n=1}^3 J(\theta_n, \psi_{4-n}), \\
 f_{43} &= -2\zeta A_{2,Xx} - \zeta A_{0,XX} - A_{0,X} \psi_{2,z} - \tilde{J}(A_1, \psi_1) - \sum_{n=1}^3 J(A_n, \psi_{4-n}).
 \end{aligned}$$

The solvability condition for ψ_4 is always satisfied. But while solving A_4 , the Laplace operator gives another solvability condition that corresponds to the $O(\epsilon^4)$ terms in Eq. (3.38)

$$\left(A_{0,X} + \frac{\pi^2 |a|^2}{4p\zeta^2} \right)_X = 0. \quad (\text{G.4})$$

The solution Ψ_4 is

$$\begin{aligned}
 \psi_4 &= -\frac{k^2 \pi (|a|^2)_X \sin(2\pi z) (4\zeta \sigma^{-1} p^2 \pi^2 + Ra_c \zeta p + 12Q_c \pi^4)}{2p^2 \zeta p_{02}} \dots \\
 \theta_4 &= \frac{k^4 |a|^4 \sin(2\pi z) (p_{13} - Ra_c k^2) (k^2 + 5\pi^2)}{32p^2 p_{13} \pi (k^2 + 9\pi^2)} + \left\{ \frac{ik\pi a^* a_X \sin(2\pi z)}{8p^2} + c.c. \right\} + \dots \\
 A_4 &= -\frac{(|a|^2)_X \cos(2\pi z) k^2 (8\zeta \sigma^{-1} p^2 \pi^2 + 2Ra_c \zeta p + 24Q_c \pi^4 + p_{02})}{8p^2 p_{02} \zeta^2} + \left\{ -\frac{\pi^2 e^{2ikx} a a_X (3k^2 + \pi^2)}{16p^2 \zeta^2 k^2} \right. \\
 &\quad + \frac{i\pi^4 e^{2ikx} |a|^2 a^2 (5k^2 + \pi^2) (18Q_c k^4 \pi^2 - 16Q_c k^2 \pi^4 - 2Q_c \pi^6 - pp_{31})}{64kp^3 p_{31} \zeta^4 (9k^2 + \pi^2)} \\
 &\quad \left. + \frac{i\pi^2 e^{2ikx} a^2 A_{0,X}}{16kp\zeta^2} + c.c. \right\} + \dots
 \end{aligned}$$

Here we only list the terms which are relevant to the solvability conditions at $O(\epsilon^5)$ and $O(\epsilon^6)$.

Fifth & sixth order

At $O(\epsilon^5)$ and $O(\epsilon^6)$, \mathbf{f}_5 and f_{63} are given by

$$f_{51} = \sigma^{-1} \left\{ 2 \sum_{n=1}^2 \left[J(\psi_n, \psi_{3-n,Xx}) + \tilde{J}(\psi_n, \nabla^2 \psi_{3-n}) \right] + \sum_{n=1}^4 J(\psi_n, \nabla^2 \psi_{5-n}) \right\}$$

$$\begin{aligned}
 & -4\psi_{1,XXxx} - 2\nabla^2\psi_{1,XX} - 4\nabla^2\psi_{3,XX} - Ra_c\theta_{3,X} - r_2\theta_{1,X} - r_2\theta_{3,x} - r_4\theta_{1,x} \\
 & -\zeta [q(\nabla^2 A_{3,z} + 2A_{1,XXz}) + Q_c(A_{1,XXz} + 2A_{3,XXz} + 2A_{1,XXz}A_{0,X} + A_{0,X}\nabla^2 A_{3,z})] \\
 & -Q_c\zeta \left\{ \sum_{n=1}^2 \left[\tilde{J}(A_n, \nabla^2 A_{3-n}) + 2J(A_n, A_{3-n,XX}) \right] + \sum_{n=1}^4 J(A_n, \nabla^2 A_{5-n}) \right\} \\
 & -q\zeta [J(A_1, \nabla^2 A_2) + J(A_2, \nabla^2 A_1) + A_{0,X}\nabla^2 A_{1,z}], \\
 f_{52} &= -\psi_{3,X} - \theta_{1,XX} - 2\theta_{3,XX} - \sum_{n=1}^4 J(\theta_n, \psi_{5-n}) - \sum_{n=1}^2 \tilde{J}(\theta_n, \psi_{3-n}), \\
 f_{53} &= -\zeta(A_{1,XX} + 2A_{3,XX}) - \sum_{n=1}^4 J(A_n, \psi_{5-n}) - \sum_{n=1}^2 \tilde{J}(A_n, \psi_{2-n}) - A_{0,X}\psi_{3,z}, \\
 f_{63} &= A_{0,T} - \zeta(A_{2,XX} + 2A_{4,XX}) - \sum_{n=1}^5 J(A_n, \psi_{6-n}) - \sum_{n=1}^3 \tilde{J}(A_n, \psi_{3-n}) - A_{0,X}\psi_{4,z}.
 \end{aligned}$$

The solvability conditions for ψ_5 and A_6 are

$$\begin{aligned}
 & (\tilde{\mu}_0 + \tilde{\mu}_1 A_{0,X} + \tilde{\mu}_2 A_{0,X}^2) a + \tilde{d} a_{XX} + i(\tilde{\gamma} a_X + \tilde{a}_1 |a|^2 a_X + \tilde{a}_2 a^2 \bar{a}_X) \\
 & + \left(\tilde{b}_0 + \tilde{b}_1 A_{0,X} \right) |a|^2 a - \tilde{c}_0 |a|^4 a - Q_c p \pi^2 a A_{20,X} = 0,
 \end{aligned} \tag{G.5}$$

and

$$A_{0,T} = \left(A_{20,X} + \frac{\pi^2}{4p\zeta} A_{0,X} |a|^2 - \frac{\pi^4}{32p^2\zeta^3} |a|^4 + \frac{k\pi^2}{2p^2\zeta} \text{Im}[aa_X^*] \right)_X. \tag{G.6}$$

These two relations correspond to the $O(\epsilon^5)$ and $O(\epsilon^6)$ terms in Eq. (3.37) and (3.38). The phase-like variable A_0 can be redefined suitably to garner the A_{20} terms hence A_0 contains both the contribution of $O(1)$ and $O(\epsilon^2)$. The coefficients given in Eq. (G.5) are

$$\begin{aligned}
 \tilde{\mu}_0 &= \frac{k^2 r_4}{2}, & \tilde{\mu}_1 &= -p\pi^2 q, & \tilde{\mu}_2 &= -\frac{Q_c p \pi^2}{2}, & \tilde{d} &= 6k^2 p, \\
 \tilde{\gamma} &= -k\pi^2 r_2/p, & \tilde{b}_0 &= \frac{2q\pi^4(\pi^2 - k^2) - r_2 k^4 \zeta^2}{16p\zeta^2}, & \tilde{b}_1 &= \frac{Q_c \pi^4(\pi^2 - k^2)}{4p\zeta^2}, \\
 \tilde{a}_{10} &= \frac{k^3(4\zeta p^2 \pi^2 + R_c \sigma \zeta p + 12Q_c \sigma \pi^4)[3Q_c \pi^4 \sigma + p\zeta(k^2 \pi^2 + 2p\sigma k^2 - 3\pi^4)]}{4p^2 p_{02} \sigma^2 \zeta^2} \\
 &\quad + \frac{pk^3(9\pi^2 - k^2)}{16\pi^2} + \frac{Q_c k \pi^4(2k^2 + 3\pi^2)}{4p^2 \zeta^2}, \\
 \tilde{a}_{20} &= \frac{k^3(4\zeta p^2 \pi^2 + R_c \sigma \zeta p + 12Q_c \sigma \pi^4)[3Q_c \pi^4 \sigma + p\zeta(k^2 \pi^2 + 2p\sigma k^2 - 3\pi^4)]}{4p^2 p_{02} \sigma^2 \zeta^2} \\
 &\quad + \frac{pk^3(\pi^2 - k^2)}{16\pi^2} + \frac{3Q_c k^3 \pi^4}{4p^2 \zeta^2}, \\
 \tilde{c}_0 &= \frac{Q_c^2 \pi^8 (k^2 - \pi^2)(3k^4 - 16k^2 \pi^2 - 3\pi^4)}{32p_{31} p^3 \zeta^4} + \frac{k^8 p^4 (3k^2 + 19\pi^2)}{32p_{13} \pi^4 (k^2 + 9\pi^2)}
 \end{aligned}$$

$$-\frac{k^6 p(k^2 + 5\pi^2)}{32\pi^2(k^2 + 9\pi^2)} - \frac{Q_c \pi^6 (21k^4 - 14k^2\pi^2 - 3\pi^4)}{64\zeta^4 p^2 (9k^2 + \pi^2)}.$$

The coefficients for the stationary nonlocal Ginzburg-Landau equation Eq. (3.52) are

$$\begin{aligned}\tilde{\mu} &= \tilde{\mu}_0 + \frac{\tilde{\mu}_1 \pi^2}{4p\zeta^2} \langle |a|^2 \rangle - \frac{Q_c \pi^4}{2p\zeta} \left(k \text{Im}[\langle a a_X^* \rangle] - \frac{3\pi^2}{16\zeta^2} \langle |a|^4 \rangle + \left(\frac{\pi^2}{8\zeta^2} - \frac{\tilde{\mu}_2}{8p\zeta^3 Q_c} \right) \langle |a|^2 \rangle^2 \right), \\ \tilde{a}_1 &= \frac{Q_c k \pi^4}{4p\zeta} + \tilde{a}_{10}, \quad \tilde{a}_2 = -\frac{Q_c k \pi^4}{4p\zeta} + \tilde{a}_{20}, \quad \tilde{\gamma} = -\frac{k \pi^2 r_2}{p} = -\frac{\pi^4}{k} \left(q + \frac{Q_c \pi^2 \langle |a|^2 \rangle}{2p\zeta^2} \right), \\ \tilde{b} &= -\frac{\tilde{\mu}_1 \pi^2}{4p\zeta^2} + \frac{k^2 r_2 - p \pi^2 q}{2p Q_c \pi^2} \left(\tilde{b}_1 - \frac{\tilde{\mu}_2 \pi^2}{2p\zeta^2} + \frac{Q_c \pi^4}{4\zeta} \right) + \tilde{b}_0 \\ &= -\frac{\tilde{\mu}_1 \pi^2}{4p\zeta^2} + \frac{\pi^2}{4p\zeta^2} \left(\tilde{b}_1 - \frac{\tilde{\mu}_2 \pi^2}{2p\zeta^2} + \frac{Q_c \pi^4}{4\zeta} - \frac{Q_c \pi^2 k^2}{8} \right) \langle |a|^2 \rangle + \frac{q \pi^4 (\pi^2 - k^2)}{8p\zeta^2} - \frac{k^2 \pi^2 q}{16}, \\ \tilde{c} &= \frac{3Q_c \pi^6}{32p\zeta^3} + \frac{\tilde{b}_1 \pi^2}{4p\zeta^2} - \frac{\tilde{\mu}_2 \pi^4}{16p^2 \zeta^4} + \tilde{c}_0.\end{aligned}$$

Appendix H

Coefficients of the modulation equation for rotating convection near the codimension-two point

Here we give the explicit expressions of coefficients in Eq. (3.45).

$$\begin{aligned}
p_{nm} &= -(n^2 k^2 + m^2 \pi^2)^3 + Ra_c n^2 k^2 - Ta_c^2 m^2 \pi^2, \\
\tilde{\mu}_0 &= \frac{k^2 r_4 - \delta^2 \pi^2}{2}, \quad \tilde{\mu}_1 = -\frac{\delta \pi^2}{2\sigma}, \quad \tilde{d} = 6k^2 p, \quad \tilde{\gamma}_0 = -\frac{k\pi^2(r_2 + 2Ta_c \delta)}{p}, \\
\tilde{\mu}_2 &= \tilde{\gamma}_1 = -k^3, \quad \tilde{b}_0 = \frac{2p\delta\pi^2 - k^2 r_2 \sigma}{16p\sigma} k^2, \quad \tilde{b}_1 = \frac{k^2 \pi^2}{16\sigma^2}, \\
\tilde{a}_{10} &= \frac{k^3 p(4k^2 + 2\pi^2 + 3p\sigma)(2k^4 - 9\pi^4 + 7k^2 \pi^2 + 6k^2 \pi^2 \sigma)}{8p_{02}\sigma^2} + \frac{9k^3(3\pi^2 + k^2)}{32} + \frac{k^7}{16\pi^2}, \\
\tilde{a}_{20} &= \frac{k^3 p(4k^2 + 2\pi^2 + 3p\sigma)(2k^4 - 9\pi^4 + 7k^2 \pi^2 + 6k^2 \pi^2 \sigma)}{8p_{02}\sigma^2} + \frac{k^3(3\pi^2 + k^2)}{32} + \frac{k^7}{16\pi^2}, \\
\tilde{c}_0 &= \frac{p^2 k^8(19k^2 + 3\pi^2)}{128p_{31}(9k^2 + \pi^2)} + \frac{k^4 \pi^2(5k^2 + \pi^2)}{64\sigma^2(9k^2 + \pi^2)} + \frac{9k^8 p^2}{128p_{13}} - \frac{3k^6(k^2 + 5\pi^2)(p_{13} - 3k^2 p^2)}{64p_{13}(k^2 + 9\pi^2)}.
\end{aligned}$$

The coefficients for the stationary nonlocal Ginzburg-Landau equation Eq. (3.52) are

$$\begin{aligned}
\tilde{\mu} &= \tilde{\mu}_0 + \frac{\tilde{\mu}_1 k^2}{4} \langle |a|^2 \rangle - \frac{k^4}{8} \left(2k \text{Im}[\langle aa_X^* \rangle] + \frac{\delta \pi^2}{k^2 \sigma} \langle |a|^2 \rangle - \frac{3\pi^2}{8\sigma^2} \langle |a|^4 \rangle + \frac{\pi^2}{4\sigma^2} \langle |a|^2 \rangle^2 \right), \\
\tilde{a}_1 &= \frac{k^2}{4} \left(\frac{k^3}{2} - \tilde{\mu}_2 - \tilde{\gamma}_1 \right) + \tilde{a}_{10}, \quad \tilde{a}_2 = -\frac{k^5}{8} - \frac{\tilde{\mu}_2 k^2}{4} + \tilde{a}_{20}, \\
\tilde{\gamma} &= \frac{r_2(\tilde{\gamma}_1 - k\pi^2)}{p} - 2\delta\sigma(\tilde{\gamma}_1 + k^3) = -2pk\sigma\delta + \left(\frac{\tilde{\gamma}_1 k^2}{4} - \frac{k^3 \pi^2}{4} \right) \langle |a|^2 \rangle, \\
\tilde{b} &= \frac{k^2}{4} \left(\frac{\delta \pi^2}{\sigma} - \frac{\delta k^2 \sigma}{2} - \tilde{\mu}_1 \right) + \left(\frac{r_2}{p} - 2\sigma\delta \right) \left(\tilde{b}_1 - \frac{k^4}{16} + \frac{\pi^2 k^2}{8\sigma^2} \right)
\end{aligned}$$

$$\begin{aligned}
 &= \frac{k^2}{4} \left(\frac{\delta\pi^2}{\sigma} - \frac{\delta k^2 \sigma}{2} - \tilde{\mu}_1 \right) + \frac{k^2}{4} \left(\tilde{b}_1 - \frac{k^4}{16} + \frac{\pi^2 k^2}{8\sigma^2} \right) \langle |a|^2 \rangle, \\
 \tilde{c} &= \frac{3k^4 \pi^2}{64\sigma^2} + \frac{\tilde{b}_1 k^2}{4} + \tilde{c}_0.
 \end{aligned}$$

Appendix I

Direction of branching in the fifth order nonlocal Ginzburg-Landau equation

In order for a modulated branch to bifurcate from the primary state, the "energy" E_2 should increase above the local minimum of $U[\rho]$. This provides a route to compute the change of $\langle |A|^2 \rangle$. To see this, first note that at the branching point we have

$$U_0 = E_{2,0}, \quad U_{0,\rho} = 0, \quad U_{0,\rho\rho} = \left(\frac{2n\pi}{\epsilon^2\Gamma} \right)^2. \quad (\text{I.1})$$

The subscript 0 indicates the quantity is evaluated on the primary branch. If μ is changed by a small amount, i.e., $\mu_0 \rightarrow \mu_0 + \delta\mu$, the quantities E_1 , E_2 , ρ_e , $\langle |A|^2 \rangle$, $\langle |A|^4 \rangle$, and $\langle \text{Im}[AA_X^*] \rangle$ will change accordingly by δE_1 , δE_2 , $\delta \rho_e$, $\delta \langle |A|^2 \rangle$, $\delta \langle |A|^4 \rangle$, and $\delta \langle \text{Im}[AA_X^*] \rangle$ and are of the same order as $\delta\mu$. Here ρ_e corresponds to the local minimum of $U[\rho]$ which satisfies $U_\rho|_{\rho=\rho_e} = 0$. A leading order expansion of the condition $U_\rho|_{\rho=\rho_e} = 0$ around the branching point takes the form

$$\begin{aligned} 0 = & U_{0,\rho\mu}\delta\mu + U_{0,\rho E_1}\delta E_1 + U_{0,\rho\rho}\delta\rho_e + U_{0,\rho\langle |A|^2 \rangle}\delta\langle |A|^2 \rangle + U_{0,\rho\langle |A|^4 \rangle}\delta\langle |A|^4 \rangle \\ & + U_{0,\rho\langle \text{Im}[AA_X^*] \rangle}\delta\langle \text{Im}[AA_X^*] \rangle. \end{aligned} \quad (\text{I.2})$$

The modulated solutions are subjected to the constraints

$$\int_{\rho_{min}}^{\rho_{max}} \frac{d\rho}{\sqrt{2(E_2 - U)}} = \frac{\epsilon^2\Gamma}{2n}, \quad \int_{\rho_{min}}^{\rho_{max}} \frac{\phi_X d\rho}{\sqrt{2(E_2 - U)}} = 0, \quad (\text{I.3})$$

where ρ_{min} and ρ_{max} are the minimum and maximum of the modulated amplitude. To evaluate these integrals and the perturbation of nonlocal terms $\delta \langle |A|^2 \rangle$, $\delta \langle |A|^4 \rangle$, and $\delta \langle \text{Im}[AA_X^*] \rangle$, we introduce the change of variable

$$\Delta s^2 = U[\rho] - U[\rho_e], \quad (\text{I.4})$$

where $\Delta \equiv E_2 - U[\rho_e]$ is small and of the same order as $\delta\mu$. The dependence of ρ on s has the form

$$\rho - \rho_e = \left(\frac{2\Delta}{U_{\rho\rho}} \right)^{1/2} \left(s - \frac{U_{\rho\rho\rho}\Delta^{1/2}s^2}{3\sqrt{2}U_{\rho\rho}^{3/2}} + \frac{5U_{\rho\rho\rho}^2 - 3U_{\rho\rho\rho\rho}U_{\rho\rho}}{36U_{\rho\rho}^3}\Delta s^3 \right) + O(\Delta^2). \quad (\text{I.5})$$

Substituting these into the integrals yield

$$\begin{aligned} & U_{0,\rho\rho\mu}\delta\mu + U_{0,\rho\rho E_1}\delta E_1 + U_{0,\rho\rho\rho}\delta\rho_e + U_{0,\rho\rho\langle|A|^2\rangle}\delta\langle|A|^2\rangle + U_{0,\rho\rho\langle|A|^4\rangle}\delta\langle|A|^4\rangle \\ & + U_{0,\rho\rho\langle\text{Im}[AA_X^*]\rangle}\delta\langle\text{Im}[AA_X^*]\rangle - \frac{5U_{0,\rho\rho\rho}^2 - 3U_{0,\rho\rho\rho\rho}U_{0,\rho\rho}}{12U_{0,\rho\rho}^2}\Delta = 0, \end{aligned} \quad (\text{I.6})$$

$$\begin{aligned} & \frac{\delta E_1}{\rho_0^2} - \frac{\gamma_1}{2}\delta\langle|A|^2\rangle - (\gamma_1 + a_1 + a_2)\rho_0\delta\rho_e \\ & + \left[(\gamma_1 + a_1 + a_2)\frac{U_{0,\rho\rho\rho}\rho_0}{U_{0,\rho\rho}} + 3\gamma_1 + a_1 + a_2 \right] \frac{\Delta}{2U_{0,\rho\rho}} = 0, \end{aligned} \quad (\text{I.7})$$

$$\delta\langle|A|^2\rangle = 2\rho_0\delta\rho_e + \left(1 - \frac{U_{0,\rho\rho\rho}\rho_0}{U_{0,\rho\rho}} \right) \frac{\Delta}{U_{0,\rho\rho}}, \quad (\text{I.8})$$

$$\delta\langle|A|^4\rangle = 4\rho_0^3\delta\rho_e + 6\rho_0^2 \left(1 - \frac{U_{0,\rho\rho\rho}\rho_0}{3U_{0,\rho\rho}} \right) \frac{\Delta}{U_{0,\rho\rho}}, \quad (\text{I.9})$$

$$\delta\langle\text{Im}[AA_X^*]\rangle = \gamma_1\rho_0^2\delta\langle|A|^2\rangle + \frac{a_1 + a_2}{4}\delta\langle|A|^4\rangle - \delta E_1 \quad (\text{I.10})$$

when $K_0 = 0$. Here we ignore the terms higher than $\delta\mu$. With Eq. (C2) and relations (I.6)–(I.10), we can determine how the conserved quantities and the nonlocal terms change while varying parameter μ locally at the leading order. But to get the dependence of $\delta\langle|A|^2\rangle$ on Δ , only Eq. (C2) and relations (I.6)–(I.8) are needed. After some calculations we have

$$\begin{aligned} & [5U_{0,\rho\rho\rho}^2 - 3U_{0,\rho\rho\rho\rho}U_{0,\rho\rho} - 6(\rho^{-1}U_{0,\rho\rho} - U_{0,\rho\rho\rho})^2 + 24\rho^2U_{0,\rho\rho}(2\gamma_1 + a_1 + a_2)^2] \frac{\Delta}{12U_{0,\rho\rho}^2} \\ & + 2(b_0 - \rho^{-2}U_{0,\rho\rho})\delta\langle|A|^2\rangle = 0. \end{aligned} \quad (\text{I.11})$$

Since Δ becomes positive right after branching we can thus determine the sign of $\delta\langle|A|^2\rangle$ and obtain the branching direction.

Appendix J

Exact real solutions of SH23 with dispersion

Here we study exact real solutions of SH23 with dispersion, Eq. (4.41), based on general expressions for meromorphic traveling solutions presented in [78]. Traveling solutions of Eq. (4.41) satisfy the ODE [83]

$$w'''' - \sigma w''' + 2w'' - Cw' - \alpha w - \beta w^2 + \gamma w^3 = 0, \quad (\text{J.1})$$

where $w(z) = u(x, t)$, $z \equiv x - Ct$ and C is the speed of the traveling solution. Meromorphic traveling solutions require $\sigma \neq 0$; no such solutions are present when $\sigma = 0$ [78] although traveling fronts are of course present in this case, too. As before, we are primarily interested in the physically more relevant case $\gamma > 0$; the destabilizing case ($\gamma < 0$) considered in [78] can be transformed into the stabilizing case using the transformation

$$w \rightarrow -iw, \quad \beta \rightarrow i\beta. \quad (\text{J.2})$$

We assume that all coefficients are real with $\sigma, \beta \geq 0$ and set $\gamma = 30$. Equation (J.1) yields two Laurent series with different principal parts,

$$w_1(z) = \frac{2}{z^2} + \frac{\sigma}{7z} + O(1), \quad w_2(z) = -\frac{2}{z^2} - \frac{\sigma}{7z} + O(1). \quad (\text{J.3})$$

When $\sigma \neq 0$ exact real elliptic solutions, periodic on the real axis, are present. These possess two poles within the periodic parallelogram when $\frac{28}{\sqrt{127}} < \sigma < \sqrt{7}$ or $\sqrt{7} < \sigma \lesssim 3.015$ and take the form

$$\begin{aligned} w(z) = & \frac{1}{2i} \left[\frac{\wp'(z + \frac{\omega}{2})}{\wp(z + \frac{\omega}{2}) - \wp(z_1)} \right]^2 + \frac{\sigma}{14i} \frac{\wp'(z + \frac{\omega}{2})}{\wp(z + \frac{\omega}{2}) - \wp(z_1)} + 4i\wp\left(z + \frac{\omega}{2}\right) \\ & + i\frac{23\sigma^2 - 196}{2940} + \frac{\sqrt{42(13384\sigma^2 - 43904 - 941\sigma^4)}}{5880}, \end{aligned} \quad (\text{J.4})$$

where

$$\begin{aligned} \wp(z_1) &= \frac{23\sigma^2 - 196}{5880}, \quad C = -\frac{\sigma(3627\sigma^4 - 38640\sigma^2 + 21952)}{1372(93\sigma^2 - 56)}, \\ g_2 &= \frac{2311\sigma^4 - 38024\sigma^2 + 153664}{6914880}, \quad g_3 = -\frac{(23\sigma^2 - 196)(9439\sigma^4 - 154056\sigma^2 + 614656)}{203297472000}, \\ \beta &= \frac{3\sqrt{42(13384\sigma^2 - 43904 - 941\sigma^4)}}{196}, \quad \alpha = \frac{\beta^2}{135}. \end{aligned}$$

The modular discriminant Δ vanishes when $\sigma = 28/\sqrt{127}$, $\sqrt{7}$, $\sqrt{833/89}$, and $\sqrt{32/41}$. The periodic lattice Γ is rectangular when $\frac{28}{\sqrt{127}} < \sigma < \sqrt{7}$ and rhombic (Γ admits a basis $\{\omega_1, \omega_1^*\}$) when $\sqrt{7} < \sigma \lesssim 3.015$. In the former case, ω is chosen as one half of the pure imaginary period; in the latter case ω is set equal to ω_1 . The solutions decrease to zero in supremum norm as σ approaches $28/\sqrt{127}$. When σ tends to $\sqrt{7}$, the real period increases to infinity and the solutions become homoclinic (pulse or hole, depending on the sign of $\text{Im}[\omega]$). These solutions take the form

$$w(z) = \pm \frac{\cosh(\sqrt{7}z/14) + \sinh(\sqrt{7}z/14)}{14 \cosh^2(\sqrt{7}z/14)} + \frac{1}{4\sqrt{14}}. \quad (\text{J.5})$$

At this value of σ the speed $C = 17/(28\sqrt{7})$ while $\alpha = -15/56$, $\beta = 45/(2\sqrt{14})$.

Stationary ($C = 0$) real meromorphic solutions of Eq. (J.1) with $\sigma = 0$ obtain when $\beta = 0$ (i.e., the standard Swift-Hohenberg equation) and $\alpha \in (-\frac{16}{25}, \frac{11}{25}) \cup (\frac{11}{25}, \infty)$ in the two poles case. These take the form

$$w(z) = \frac{\wp'(z + \frac{\omega}{2})}{2i(\wp(z + \frac{\omega}{2}) + \frac{1}{30})^2} + 4i\wp\left(z + \frac{\omega}{2}\right) - \frac{i}{35}, \quad (\text{J.6})$$

with

$$g_2 = \frac{4 - 5\alpha}{540}, \quad g_3 = \frac{8 - 25\alpha}{81000}. \quad (\text{J.7})$$

The modular discriminant Δ vanishes when $\alpha = -16/25$ and $11/25$. The periodic lattice Γ is rectangular when $-\frac{16}{25} < \alpha < \frac{11}{25}$ and rhombic when $\alpha > 11/25$. As before, ω is chosen as half of the pure imaginary period in the rectangular case and as the generator of the lattice in the rhombic case. The solutions decrease to zero in supremum norm when α approaches $-16/25$. As $\alpha \rightarrow 11/25$, the solutions become homoclinic and take the form

$$w(z) = \pm \frac{2 \sinh(z/\sqrt{5})}{5 \cosh^2(z/\sqrt{5})}. \quad (\text{J.8})$$

The elliptic solutions and the homoclinic solution computed in Eqs. (J.6), (J.8) have also been derived in [77]. Sample solution profiles for $\sigma \neq 0$ and $\sigma = 0$ are shown in figures J.1 and J.2, respectively.

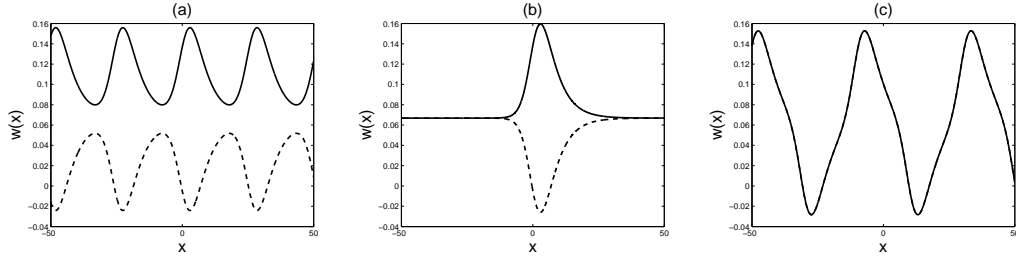


Figure J.1: Solutions of Eq. (J.1) when $\sigma \neq 0$ as given by (J.4). (a) $\sigma = 2.5$. (b) $\sigma = \sqrt{7}$. (c) $\sigma = 2.8$. The solid (dashed) line corresponds to $\text{Im}[\omega] > 0$ ($\text{Im}[\omega] < 0$). The solid and dashed lines coincide in (c).

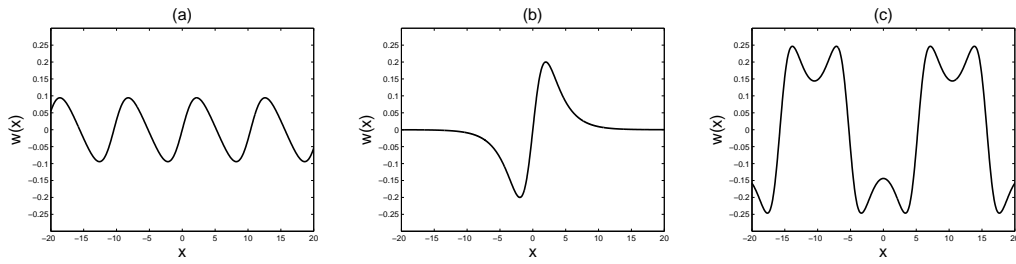


Figure J.2: Solutions of Eq. (J.1) when $\sigma = 0$, $\beta = 0$ as given by (J.6). (a) $\alpha = -0.4$. (b) $\alpha = \frac{11}{25}$. (c) $\alpha = 1$.